Versatile and Tunable Transparent Conducting Electrodes Based on Doped Graphene

Dissertation by

Ahmed Esam Mansour

In Partial Fulfillment of the Requirements

For the Degree of

Doctor of Philosophy

King Abdullah University of Science and Technology

Thuwal, Kingdom of Saudi Arabia

The dissertation of Ahmed Esam Mansour is approved by the examination committee.

Committee Chairperson: Aram Amassian

Committee Member: Husam Alshareef

Committee Member: Iain McCulloch

Committee Member: Paolo Samorì

ABSTRACT

Versatile and Tunable Transparent Conducting Electrodes Based on Doped Graphene

Ahmed E. Mansour

The continued growth of the optoelectronics industry and the emergence of wearable and flexible electronics will continue to place an ever increasing pressure on replacing ITO, the most widely used transparent conducting electrode (TCE). Among the various candidates, graphene shows the highest optical transmittance in addition to promising electrical transport properties. The currently available large-scale synthesis routes of graphene result in polycrystalline samples rife with grain boundaries and other defects which limit its transport properties. Chemical doping of graphene is a viable route towards increasing its conductivity and tuning its work function. However, dopants are typically present at the surface of the graphene sheet, making them highly susceptible to degradation in environmental conditions. Few-layers graphene (FLG) is a more resilient form of graphene exhibiting higher conductivity and performance stability under stretching and bending as contrasted to single-layer graphene. In addition FLG presents the advantage of being amenable bulk doping by intercalation.

Herein, we explore non-covalent doping routes of CVD FLG, *such as surface doping, intercalation and combination thereof*, through in-depth and systematic characterization of the electrical transport properties and energy levels shifts. The intercalation of FLG with Br_2 and $FeCl_3$ is demonstrated, showing the highest improvements of the figure of merit of TCEs of any doping scheme, which results from up to a five-fold increase in

conductivity while maintaining the transmittance within 3% of that for the pristine value. Importantly the intercalation yields TCEs that are air-stable, due to encapsulation of the intercalant in the bulk of FLG. Surface doping with novel solution-processed metal-organic molecular species (n- and p-type) is demonstrated with an unprecedented range of work function modulation, resulting from electron transfer and the formation of molecular surface dipoles. However, the conductivity increases compared modestly to intercalation as the electron transfer is limited to the uppermost graphene layers. Finally, a novel and universal multi-modal doping strategy is developed, thanks to the unique platform offered by FLG, where surface and intercalation doping are combined to mutually achieve high conductivity with an extended tunability of the work function. This work presents doped-FLG as a prospective and versatile candidate among emerging TCEs, given the need for efficient and stable doping routes capable of controllably tuning its properties to meet the criteria of a broad range of applications.

ACKNOWLEDGEMENTS

The beauty of doing a Ph.D. lies in the obstacles, challenges, and the achievements involved. I have to admit that my Ph.D. has been full of frustration moments and equally joyful pleasures of achievements, and it wouldn’t have been completed without the continuous support my family, friends, and colleagues.

First of all, I would like to thank my advisor Prof. Aram Amassian for his confidence and complete trust in my abilities, and continuous support for my achievements and progression towards the successful completion of my Ph.D.

My parents are the reason for everything I’m now! Their continuous prayers, support and pride in me have been persistently strengthening me throughout this journey. My father Esam Mansour is my role model, I always look up to him as inspiration for hard work, persistence and ethical conduct. My mother Hanan Kamal has been calling me almost every day during the past five years, to check on me and support me with prayers. I can’t thank them enough and appreciate their understanding of my absence during several family events and gatherings during my Ph.D.

My beautiful and loving wife Ghada Albeik has equally contributed to my degree and this thesis, as I did. She has lived every single moment with me during this Ph.D., sharing and soothing my frustrations of a rejected manuscript or a non-working experiment, and celebrating every milestone and achievement I have come along. Her smile, the proud look in her eyes, and patience have been strengthening me. She has been completely understanding for my late nights in the lab and continuously supplying me with Ph.D.

survival kit (meals, snacks, and coffee) directly to my office when I’m unable to be at home. I fully dedicate this Ph.D. thesis to her and to my son Esam, who since he was born has given a meaning to everything I do in life, especially my Ph.D.

I would also like to thank a key influencer and mentor who have accompanied me through my graduate studies journey, Prof. Husam Alshareef. His door was the first that I would knock for advice and support. He has taught me various courses, and supported several of my extracurricular activities. I have learned from him the importance of loyalty to our newly established institute, KAUST, and that my achievements as a student will have a huge impact on its reputation and progression.

Finally, I would like to acknowledge every single member of our laboratory, the Organic Electronics and Photovoltaics Lab (OEPV). We have been through a lot together, which has reflected in our interactions to act as a family rather than just colleagues. I would like to specifically mention Dr. Guy Olivier Ngongang Ndjawa, who has accompanied me throughout thesis writing and preparation for the defense.

TABLE OF CONTENTS

Page

LIST OF ILLUSTRATIONS

LIST OF TABLES

CHAPTER 1
Introduction

Transparent conductive electrodes (TCE) are materials which are characterized by their high electrical conductivity and optical transmittance. These characteristics enable a wide range of applications including, low-emissivity windows, electrically controlled smart windows, defrosting windows, touch screens, photovoltaics and displays.[1] TCEs form a crucial part of any optoelectronic and photovoltaic device, acting as a window for light to enter or exit while simultaneously providing or collecting electrical current. In conventional thin film photovoltaics, including organic, quantum dot and perovskite solar cells, light is transmitted through the TCE into the light absorber layer where either excitons or free carriers are generated. Transparent hole and electron transporting layers (HTL and ETL) selectively transport holes and electrons to the anode and cathode, respectively, while also blocking the opposite charge from reaching the electrode.[2,3]

Applications and technologies relying on TCEs are persistently increasing, placing a continuous demand for such materials. Touch panels have been produced at a rate of more than 3.5 million units in 2010 with annual growth of 20% through 2013,while E-paper displays have seen 30 fold increase from 2008 to 2014, and sales are expected to exceed $13 billion by 2017 highlighting the ever increasing demand on TCEs.[4] Similarly, the market of wearables using smart textiles is expected to grow at a rate of 132% between 2016 and 2022 which translates into a $70 billion dollars potential market.[5] Furthermore, the paradigm shift in the electronics industry from being technology-oriented (faster, smaller and larger capacity) towards user-oriented (wearable, flexible and novel human-interfacing methods) has further increased the demand on TCEs and motivated their development to satisfy the additional requirements of being flexible, bendable and producible with tunable optoelectronic and energetic properties.[6]

Historically, transparent conductive oxides (TCO) were the first TCEs used, with indium tin oxide (ITO) being the most popular due to its conductivity being the highest among all TCOs and since it has become a mature material that has been extensively studied and developed since its discovery in 1947.[1,4] ITO exhibits a sheet resistance as low as a few tens of Ohms per square and transmittance of around 80% in the visible range, making it suitable for various optoelectronic, photovoltaics and touch screen technologies.[7,8]

The incumbent transparent conducting electrode still today is ITO, occupying 93% of the of the market share as of the year 2013 at $1.6 billion sales in the touch screen technology alone,[9] and the market is expected to grow to $6.3 billion in 2024.[10] This continuous growth in demand combined with the scarcity of indium has led to an ever-increasing cost of ITO. As shown in **Figure 1.1A**, indium currently sells at $745 per kg as compared to ~ $200 per kg in the early 1990s.[11] Furthermore, indium has been flagged as a critical energy element by APS-MRS study panel and the U.S. DOE, defined as elements required for emerging sustainable energy sources and are forecast to encounter supply disruptions (**Figure 1.1B**).[12] In addition, ITO has shown chemical stability issues[13] and a degraded performance under bending and stretching conditions.[14]

Even though analysts predict a continuous dominance of ITO during the next 20 years, immense research is directed towards seeking alternative materials, which would match its performance while being mechanically flexible and chemically stable.[4,9,15,16] Emerging TCEs include metal nanowires, carbon nanotubes, conductive polymers, and graphene, which combined are forecast to sell more than $220 million in 2026, forming more than 25% of the market share of TCEs.[10]

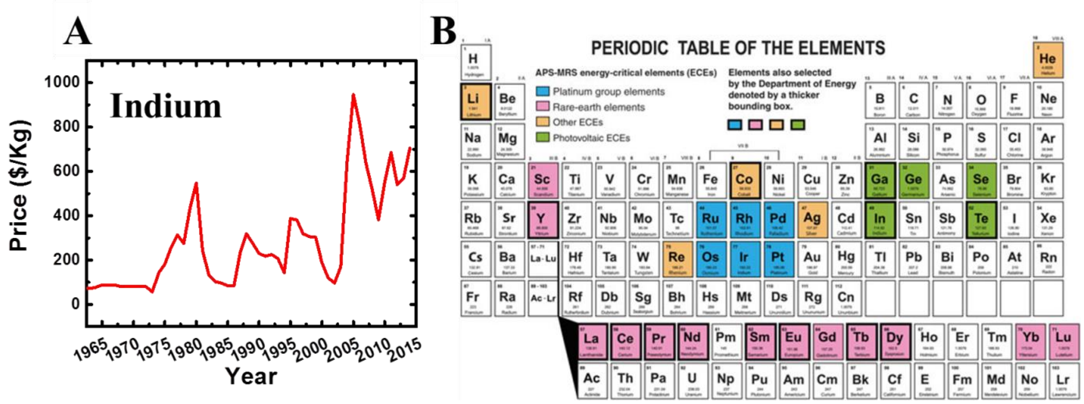

Figure 1.1: (A) Fluctuations and the overall increase in the prices of indium. The cyclic trend characterized by various sharp rises in the price in 1980, 1988, 1995 and 2005 are attributed to factors related to the economy, resource availability, and introduction of new technological innovations factors. The recent price decrease in 2009 was driven by a recession in the global economy. The increasing demand of ITO after 2009 is the reason for the continuous increase in indium price since then.[17] *Data are obtained from U.S. Geological Survey (USGS).*[11] *(B) The periodic table with highlighted energy critical elements.*[12]

Since its discovery in 2004,[18] graphene‘s unique properties have sparked tremendous interest and interdisciplinary research aimed towards integrating it a wide range of emerging applications including TCEs.[19] Mechanically, it is the strongest known material with a Young’s modulus of 1 TPa and intrinsic strength of 130 GPa.[20] Moreover, charge transport in graphene is ballistic on the submicron scale with a fundamental limit of carrier mobility of 200000 $cm^2/(Vs)$ and a carrier density on the order of 10^{12} cm^{-2}. [21] Optically, graphene is also remarkably transparent, as a single layer absorbs only 2.3% of white light and reflects less than 0.1% at all wavelengths.[22]

This leads graphene to exhibit the highest transmittance among other existing and emerging TCE such as metal nanowires and carbon nanotube.[14]

The combination of the remarkable electrical transport and optical transmittance of graphene, in addition to being atomically flat and continuous, which beats the nanowires and tubes structure with respect to surface roughness and high local resistance at tubes/wires junctions,[4,23–26] has led to increased interest in utilizing graphene as TCE and various demonstrations in optoelectronic and photovoltaics applications as schematically shown in **Figure 1.2**.

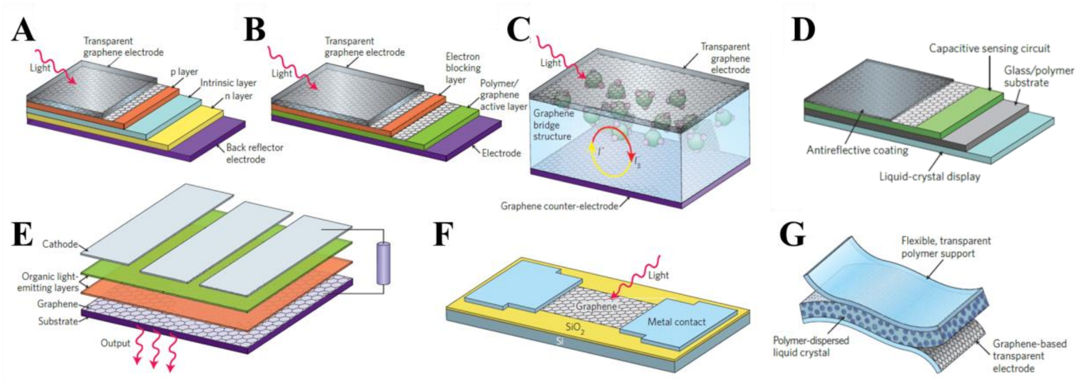

Figure 1.2: Schematic illustration of potential applications of Graphene TCEs. (A) Inorganic, (B) organic, and (C) dye-sensitized solar cells. (D) Capacitive touch screen, (E) organic light emitting diode, (F) photodetector, and (G) smart screen window.[14]

However, the enabling of industrial applications based on graphene TCE requires the availability of large-scale production routes, for which much research effort has been invested, as will be discussed in details in **Chapter 2.2**. Chemical vapor deposition (CVD) of graphene on metals is currently the most promising route towards large-scale production, which is currently used to grow either single layer graphene (SLG) or few layer graphene (FLG). CVD graphene, in general, has outperformed graphene synthesized by any other scalable route such as solution-processed reduced graphene oxide as shown in **Table 1.1**.[6] However, CVD typically yields polycrystalline samples, which become more defective and impure after the required transfer step, resulting in inferior conductivity as compared to theoretical predictions and the conductivity of mechanically exfoliated graphene.[27] This has hindered the industrial realization of CVD graphene as a TCE. To tackle this, the research community has followed two main directions; (1) understanding and optimizing the growth of CVD graphene and the subsequent transfer method,[27–31] and (2) the engineering of grown CVD graphene to increase its conductivity without sacrificing its optical transmission, which have been generally done through layers stacking and doping.[6,32–36] This second route has the added advantage of the ability to modulate the work function of graphene TCEs so that it better interfaces by forming energetically favorable paths for electron extraction and injection. This dissertation adds to the efforts along the second route, for which an extensive literature review is provided in **Chapter 2.4**.

Table 1.1: Various routes of graphene production compared based on their scalability and other properties.[6]

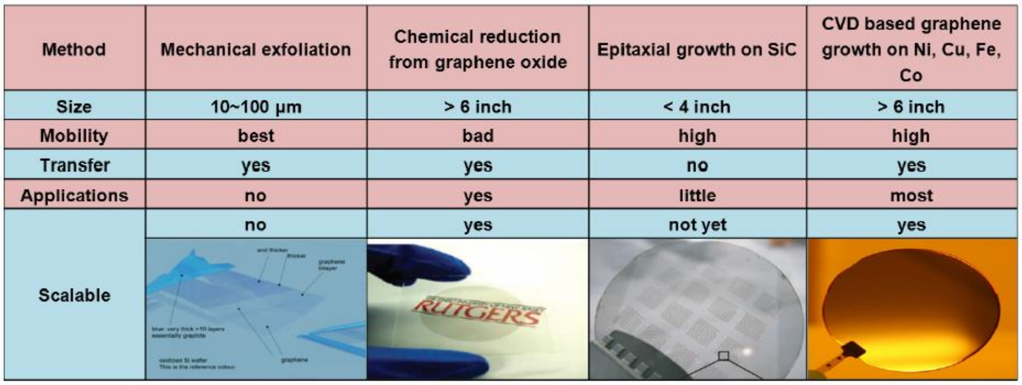

Method	Mechanical exfoliation	Chemical reduction from graphene oxide	Epitaxial growth on SiC	CVD based graphene growth on Ni, Cu, Fe, Co
Size	10~100 μm	> 6 inch	< 4 inch	> 6 inch
Mobility	best	bad	high	high
Transfer	yes	yes	no	yes
Applications	no	yes	little	most
Scalable	no	yes	not yet	yes

Our literature survey demonstrates that most of the work done in this area has focused on using surface molecular dopants on SLG, which being exposed on the surface can reduce the long-term stability of doped graphene TCEs. In addition, benefits of molecular doping result from interplay between increasing the carrier density in graphene and reducing the mobility attributed to Coulomb scattering by the charged molecules of the dopant as detailed in **Chapter 2.3**. On the other hand, several groups have adopted interlayer doping of graphene, in which cumbersome sequential cycles of SLG doping and transfer took place, to form an artificial structure similar to graphite intercalation compounds (GIC) so that long-term stability is enhanced. Few reports on spontaneous intercalation of FLG in a similar manner to GIC have appeared more recently, where the small guest molecule would intercalate and provide an efficient doping for the bulk of FLG. However, this effort has mainly been focused on the non-scalable mechanically exfoliated FLG.

In this dissertation, we focus on the chemical doping of CVD graphene as the most promising route towards industrial realization of graphene TCEs, aiming to provide a better understanding of the doping process, in addition to providing means to enhance the figure of merit (FoM) of graphene TCEs through the development of efficient and novel doping strategies. We adopt FLG grown on nickel thin films because they are more resilient, and exhibit favorable stability under stretching and bending conditions, which to a large extent is in contrast to SLG. FLG intrinsically inherits the advantages of the layer stacking strategy, thus eliminating the need for the cumbersome process of sequential transfer that includes additional defects and contaminations into graphene. With respect to chemical doping of FLG, larger benefits are demonstrated from molecular surface doping, as Coulomb scattering of the charged molecules would be screened by the top most layers, and thus causing smaller carrier mobility losses as compared to surface doped SLG, while being amenable to forming large-scale intercalation compounds in a similar manner to GIC, and thus providing an efficient doping of graphene layers in the bulk of FLG. These advantages of FLG are further elaborated in **Section 2.2.6**.

Our approach includes the detailed investigation of the evolution of the electronic, electrical transport, optical and structural properties of CVD FLG using non-covalent chemical dopants that would either adsorb on the surface or spontaneously intercalate in between the sheets of FLG. Followed by the development of a universal hybrid doping approach, where FLG is mutually bulk-doped through intercalation, and surface-doped by large molecular species providing a maximized doping of almost all available graphene layers in FLG. Further details on the methodologies used throughout this thesis are provided in **Chapter 3**, as well as in **Appendices A** and **B**.

The results of this work show that intercalation doping leads to significantly large improvements in the FoM of CVD-FLG based TCEs, which result from the large increase in the conductivity due to the effective doping the bulk of FLG, and the minimal reduction of optical transmittance. In addition, longer air stability is achieved due to the encapsulation of dopants in between the sheets. This is demonstrated in a comparative study of bromine doping of FLG and SLG, where benefits of intercalation are evident through the former as will be discussed in **Chapter 4**. Furthermore, this dissertation provides a guideline for the selection of molecular surface dopants and the need to optimize their coverage in order to achieve a desirable performance of graphene TCEs. This is realized through a systematic study of organic and metal-organic molecules and the effect of their doping strength and coverage on the optoelectronic properties of graphene which is described in **Chapter 5**. Finally, a novel and universal doping strategy has been developed, where increased conductivity and further work function tunability are achieved through the combination of intercalation and surface molecular doping, which effectively work together towards achieving desired properties of graphene TCEs, through maximizing the number of doped graphene layers in FLG. This approach is detailed in **Chapter 6**.

The combination of the scientific aspect presented by the in-depth understanding of the charge transport and energy level adjustments in doped graphene, and the engineering aspect presented by the demonstration of doping strategies that would enhance the FoM of graphene TCE, demonstrates the significant contribution of this work, given the need for effective and stable doping routes for graphene synthesized by the large-scale production methods such as chemical vapor deposition towards application as TCE. Conclusions and future perspective are provided in **Chapter 7**.

CHAPTER 2
Literature Review

2.1 Transparent conductive electrodes (TCE)

The combination of optical transmittance and high electrical conductivity in thin films of materials has enabled several technologies and a broad range of applications such as displays, lighting, electromagnetic shield windows and photovoltaics.[1,15] Materials exhibiting these two properties simultaneously are widely known as transparent conductive electrodes (TCEs), of which transparent conductive oxides (TCOs) were the first to be extensively utilized in the above-mentioned applications.[37–40] In this section, the historical development of TCEs is surveyed, along with applications and general requirements. Next, the shortcomings of the most popular TCE to date, indium tin oxide (ITO) are presented and contrasted to emerging TCEs including graphene. The Figure of Merit (FoM) defining the performance of TCE is then described, followed by discussing the potential of graphene as emerging TCE along with strategies towards it being utilized in applications.

2.1.1 Historical perspective of TCEs

The discovery of thin film transparent metallic compounds in 1907 by Badeker is well recognized as the starting point in history for this field and semiconductor electronics.[41] During his work on electrical conduction in metals, Badeker has successfully demonstrated the synthesis of various transparent conductive metallic compounds by sputtering on glass and mica followed by oxidation in air, such as CdO, Cu_2O and PbO, and precisely determined their thickness and conductivity. Significant development of TCOs has occurred with the advent of quantum mechanics, which has enabled solid understanding of the electronic structures and transport properties of such materials, motivating the improvement of their synthesis process.[15,37] Several investigations on using TCO in optoelectronics such as selenium rectifier based photocells as well as heated and antistatic windows has followed, and was celebrated by the first application in 1947 as a transparent heating layer for cockpit windows in planes using SnO.[42] Later on, with the introduction of flat panel displays in the 1970s, the application of metals oxides as TCEs has grown and ITO became the most commonly used TCO, mainly due to its high electrical conductivity.[15] The discovery of ITO as TCO came unplanned, during experiments on metal oxide insulators at Corning laboratories in1930s,[43] and was later on mentioned clearly in a patent filed in 1947.[44] The increased awareness of the importance of energy conservation and sustainability after the oil crises in 1970[45,46] has generated research opportunities and applications for TCO in the form of low emissivity windows, that controls heat and light flux into buildings, where a metal sandwiched between two TCO layers have dominated the market.[15] In addition, the ever increasing interest in photovoltaics, which utilizes TCEs as a window that allows light into the active materials while being able to transport the photo-generated charges to external circuits, has driven much of the research towards improving TCOs and developing new materials as TCEs.[47]

2.1.2 General requirements for TCEs

The criteria for choosing a specific TCE cannot be universally defined, since every application poses different requirements on the physical properties - defining the performance of the TCE in devices such as electronic, optical and electrical properties - and other practical requirements related to the manufacturing processes involved in these applications, such as chemical durability, ability to be patterned, mechanical hardness and economic feasibility and toxicity.[1] Reference [1] reviews such requirements for TCOs and puts them in perspective for various applications. **Table 2.1** compares the transmittance and sheet resistance requirements for most common display and touch panel electronic devices.[4]

Table 2.1: Requirements of TCEs for various applications. Adapted from Ref [4].

Transparent Electrode Type	Device Type	%T Range	R_s Range (Ω/□)
Touch side	Resistive touch panel	86-90	300-500
Device side	Resistive touch panel	88-90	200-500
Top or Bottom	Projected Capacitive touch panel	88-92	100-300
Primary	Surface Capacitive touch panel	88-90	900-1500
Pixel	LCD	87-90	100-300
Common	LCD	87-90	30-80

Figure 2.1illustrates the wide range of required electrical conductivity of TCEs for different applications. For example, a TCE with ~ 500 Ω/□ is considered sufficient for touch screens and smart windows, however, light emitting diodes and photovoltaics pose more stringent requirement with sheet resistance < 50 Ω/□.[6]

Ideally, a TCE should be highly transparent in the spectral range of interest for the optoelectronic/photovoltaic device as well as highly conducting, and should be energetically aligned with buffer and photoactive layers in order to inject or extract charges with a minimal barrier. Accordingly, the properties of TCEs that directly influence the performance of devices are the sheet resistance (R_s), the transmittance (T) and the work function (Φ). More recently, with stretchable and wearable electronics appearing on the horizon, the additional requirement of flexibility and stretchability has also become relevant.[48,49]

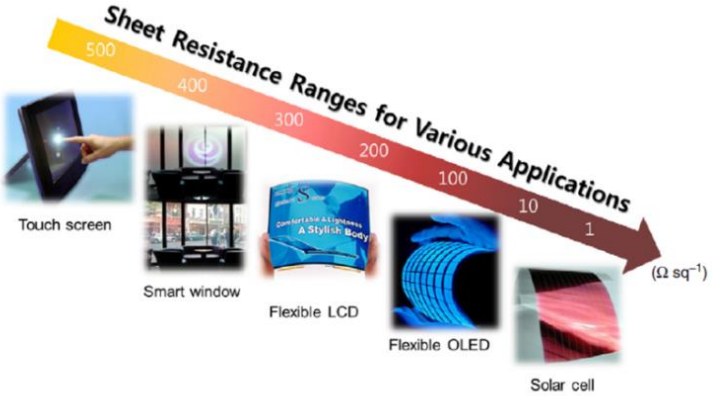

Figure 2.1: Applications of TCE and their posed requirements on the sheet resistance.[6]

2.1.3 Emerging TCEs towards replacing ITO

Currently, indium tin oxide (ITO) is the most popular TCE used owing to its low sheet resistance of few tens of Ohms per square and transmittance of around 80% in the visible range.[7,8] However, due to the relative scarcity of indium in the face of growing demand,[12,50] chemical stability issues[13] and its rigidity,[14] a replacement material that can meet the performance of ITO, and be mechanically flexible and chemically stable has been the subject of much research.[36,48,51] Several candidate TCEs in lieu of ITO have been reported, such as conductive polymers,[52,53] metal nanowires,[51,54] single-walled carbon nanotubes[55,56] and more recently graphene.[57–59] Compared to graphene, most of these alternatives have already achieved good conductivities that are comparable to ITO as shown in **Figure 2.2A**, which plots the transmittance vs. sheet resistance of various TCEs.[14] However, the superiority of graphene lies in its flat transmittance spectrum, which exceeds all of the current TCEs including ITO as shown in **Figure 2.2B**. The shaded area in **Figure 2.2A** shows the calculated limits of graphene performance as TCE using commonly achieved mobility and carrier concentrations of CVD graphene, which is currently the most promising route for large-scale production of highly conductive graphene as will be discussed in details in **Section 2.2.5**.[14] These results show the promising potential of graphene to achieve similar levels of conductivity as ITO but with higher transmittance. The 2D nature of graphene resolves several of the challenges associated with the inherently patchy and rough films of carbon nanotubes and silver nanowires, which decreases the shunt resistance in photovoltaic applications and degrades their performance.[26] In addition, nanowires and nanotubes typically suffer from high resistance at the junctions of overlapping wires or tubes,[23–25] for example, at the junction of the overlap of two carbon nanotubes the resistance can be in the range of 200 kΩ to 20MΩ (as contrasted to the resistance along a single tube being 10 kΩ).[4]

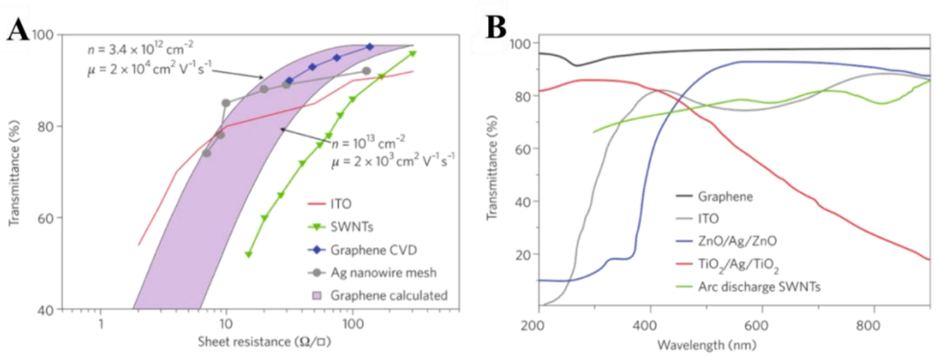

Figure 2.2: (A) Transmittance (550nm) vs. sheet resistance and (B) transmittance spectra for various emerging TCEs.[14]

2.1.4 Figure of Merit (FoM) of TCEs

Among the many requirements of TCEs,[1] high electrical conductivity and optical transmittance are the most crucial, as these directly influence the performance of optoelectronic and photovoltaic devices. However, achieving these two goals in a single material may be challenging due to the fact that they are fundamentally contradicting.[15,60] Direct-current conductivity (σ_{DC}) linearly increases with increasing the charge carrier density (n) and/or mobility (μ), according to $\sigma_{DC} = en\mu$. However, increasing the charge carrier density shifts the plasma frequency (ω_p) to a higher energy, which determines the threshold energy of absorption in materials, below which photons would be absorbed. For example, in metals the carrier density is on the order of 10^{22} cm^{-3}, which puts the plasma frequency in ultra-violate range rendering them opaque and highly reflective in the visible, whereas, the carrier density in graphene is on the order of 10^{19} cm^{-3} resulting in plasma frequency in the far-infrared region, leading graphene to behave as a transparent material in the visible region. Moreover, while increasing the thickness of a TCE reduces its sheet resistance, it can also increase the absorption losses, especially in the context of graphene, whose absorbance scales with the number of graphene layers as will be discussed in **Section 2.3.3**.

Comparison of the performance metrics of various TCE materials is greatly facilitated by the definition of a Figure of Merit (FoM) which takes into account both the sheet resistance and the optical transmittance. The first such FoM was proposed in 1972, and was simply taken as the ratio between the transmittance and sheet resistance, where a higher value would indicate a better performing TCE.[61] However, failure of this FoM was demonstrated due to the dependence of both R_s and T on thickness, which led to a FoM value at the maximum thickness resulting in T = 37%, making it unsuitable for most TCE applications. To address this, Haacke proposed a new FoM in 1976,[60] which used the ratio between T and R_s, however, adding an exponent x ($x > 1$) to the former to balance the contributions of both effects in the FoM as shown in **Equation 2.1**;

$$FoM_{Haake} = \frac{T^x}{R_s} \qquad \textit{Equation 2.1}$$

The exponent x is set to a value limiting the maximum thickness that would maximize the FoM to a value that results in an acceptable T for the specific application. For example, x = 10, 20 or 100 would limit the maximum FoM for a TCE with T = 90%, 95% or 99%, respectively. The value of x can be derived for each application depending on the minimum value of T that would yield the desired performance.

More recently, another approach has been introduced that defines the FoM in terms of more fundamental material properties such as the direct current and optical conductivities, σ_{DC} and σ_{op}, respectively, and thus eliminates extrinsic effects such as thickness.[62] The R_s and T are defined according to following equations,

$$R_s = \frac{1}{\sigma_{DC} t} \qquad \textit{Equation 2.2}$$

$$T = \left[1 + \frac{Z_o}{2}\sigma_{op} t\right]^{-2} \qquad \textit{Equation 2.3}$$

Eliminating the thickness t, and taking $\sigma_{op} \approx 2\alpha/Z_o$, where α is the absorption coefficient and Z_o is the impedance of free space and has the value 377 Ω. A general relation between R_s and T could be defined for a thin continuous conducting film according to,

$$T = \left[1 + \frac{Z_0}{2\,R_s}\frac{\sigma_{op}}{\sigma_{DC}}\right]^{-2} \qquad \textit{Equation 2.4}$$

It is clear from **Equation 2.4**, that the ratio $\frac{\sigma_{DC}}{\sigma_{op}}$ controls the relation between T and R_s, and thus is defined as the FoM for TCEs (**Equation 2.5**). Hence, by measuring the T and R_s for a specific material the FoM can be calculated with ease and used to compare various films with respect to industrial standards for different applications. Transmittance is reported at 550 nm by convention.

$$FoM = \frac{Z_0}{2\,R_S(T^{-0.5}-1)} \qquad \textit{Equation 2.5}$$

2.1.5 Graphene as emerging TCE

The high optical transmittance, electrical conductivity, flexibility and chemical stability of graphene have triggered great interest in its application as a TCE material in optoelectronic devices as a potential replacement for ITO.[14,57,58,63] CVD graphene has emerged in recent years as the most promising route for large-scale industrial production and replacement of the incumbent ITO. However, improving the quality and performance of CVD graphene as well as reducing the energy consumption of the growth and transfer processes continue to be important in order to replace ITO.

The wide range of available routes to synthesis graphene has led to numerous morphological, structural and electronic properties. Moreover, thickness of graphene samples in literature are hardly reported, in addition to difficulties involved in the exact determination of the thickness, making the extraction and comparison of electrical resistivity of graphene a non-reliable property to compare graphene films obtained using various routes. Moreover, even in the case of large-area SLG synthesized using CVD, islands of bilayer and trilayer graphene unavoidably and non-controllably exist.

The optical properties of graphene also depend on the thickness of graphene film being studied. Thus, for a comparison of the performance of graphene based materials with respect to TCEs, a FoM was proposed to combine both the electrical transport properties presented by the sheet resistance, and the optical properties presented by the optical transmittance typically taken at 550 nm. As shown in the equations 2.2 and 2.3, these two parameters are combined by using the thickness as a common factor, which would eliminate the influence of the thickness in such FoM as shown in equation 2.5, and thus provide a reliable metric to compare graphene produced using different methods.

A recent comparison of the FoM of graphene-based materials reveals an upper limit that makes pristine graphene in general not suitable for applications such as TCEs. However, it suggests that doping or layer stacking can push these limits further to meet the industrial standard which was set to be larger than 35 based on $R_s < 100\ \Omega/\square$ and $T > 90\%$.[62] Moreover, as plotted in **Figure 2.3**, CVD graphene have shown the highest FoM (~10) as compared with graphene obtained from other routes, such as the non-scalable mechanically exfoliated graphene (FoM=2.7) and solution-processed graphene and chemically derived graphene, where the latter would result in a significantly low FoM = 0.7 due to junction resistance between overlapping flakes.[62] Theoretical estimation of the FoM of a monolayer graphene leads to a value of 2.55, however, CVD graphene has shown values as high as 11 which can be attributed to unintentional doping from the substrate. With the limit of FoM = 11, graphene-based TCEs fall below the industrial standard of 35. Thus doping of graphene is essential to enhance the FoM, for which an upper limit of 330 was approximated initially for CVD graphene, significantly higher than that of ITO (FoM = 172).[62] A stack of 4 layers of CVD graphene treated with acid doping has already been demonstrated to exhibit a FoM of 118.[63] Moreover, lithium intercalation of mechanically exfoliated graphene has recently beaten the predicted limit for CVD, approaching FoM of 1400 which demonstrates the huge advantage of pursuing bulk doping of optically thin few layers graphene through intercalation, however, this is limited by the industrial scalability of mechanically exfoliated graphene.[64]

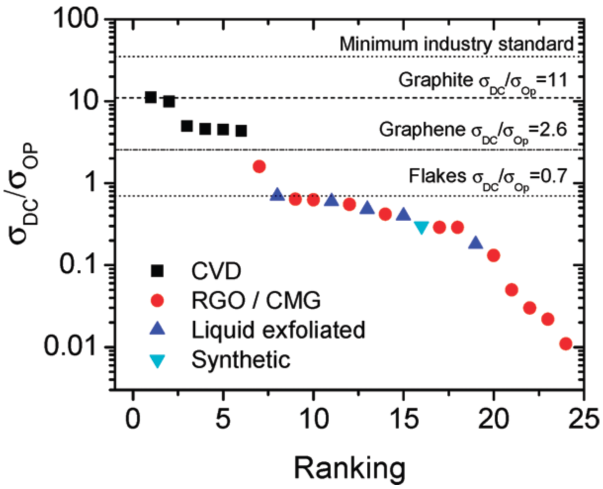

Figure 2.3: FoM of graphene synthesized by various routes and characterized without any deliberate doping.[62]

A recent comparison using Life Cycle assessment method (LCA) of the impact of CVD growth of graphene and ITO production as TCEs on the basis of energy consumption and scarce metal usage, have concluded that the former can indeed have a lower impact than the production of ITO under the best scenario proposed by the authors.[65] Surprisingly, the highest impact on energy consumption for CVD graphene process comes from the production of copper foils rather than high temperature involved in the process. Thus, an opportunity to further reduce the impact would be availed by the reuse the copper foil after the transfer process, which has been demonstrated recently using electrochemical transfer route, or by the recovery of etched copper from the etchant.[66,67]

The main challenge towards using graphene as a TCE in lieu of ITO, is increasing its conductivity to match that of the later. CVD Graphene, however, exhibits higher sheet resistance due to the polycrystalline nature of the obtained samples, in addition to the induced defects during the transfer process. Key strategies to improve the conductivity of CVD graphene are: (1) growing higher quality graphene through increasing the grain size in the polycrystalline films, (2) improve the transfer process to minimize the number of introduced defects and contaminants, (3) engineering of graphene films through layers stacking and (4) chemical doping of graphene. The latter point is the main scope of this dissertation and will be reviewed in details in **Chapter 2.4**.

2.2 Production routes of graphene-based materials

Since the celebrated exfoliation of single layer graphene using the scotch tape method in 2004,[18] immense research effort has gone into developing large-scale production routes that can yield high-quality graphene sheets and thus enable industrial applications of the miracle material.[68] Furthermore, the properties of graphene are highly dependent on the synthesis route, which largely determines the potential applications for each, indicating that there isn't a universal optimum route to synthesis graphene-based materials, and it should always be discussed in the window of a specific application of interest and its required performance metrics.

In this section, efforts to define the nomenclature of graphene are traced, towards the most recent definition of the term graphene and its related materials. The criteria used to develop such terminologies are described, with providing examples to clearly define the various members of graphene-related materials family. The terms outlined in this section is to serve as a reference for the terminologies used in this thesis. Then, routes for synthesizing graphene are surveyed along with their potential applications and limitations. A special emphasize is given to CVD graphene, since it is the most promising method for large-scale production of graphene of sufficient conductivity towards applications as TCE, in addition to being the focus of this thesis.

2.2.1 Nomenclature of graphene

Despite being the most recently discovered carbon allotrope, the term “graphene” has appeared in publications dating back to 1986 in reference to the individual layers of sp^2 hybridized carbon making up graphite and its intercalated compounds (GIC).[69] Around the same period graphene was used to conceptually describe the structure of other carbon-based materials, such as carbon nanotubes,[70] epitaxial graphite,[71] fullerenes[72] and polycyclic aromatic hydrocarbons.[73]

After the successful isolation of a single layer of graphene in 2004,[18] and the associated flurry of research activities on graphene and related materials, the term “graphene” became used broadly to describe a wide range of two-dimensional (2D) or 2D/3D carbon materials with varying thicknesses, lateral sizes, and structures. This has led to inconsistencies in the early literature, some of which continue to persist, but a serious effort by the scientific community has led to the adoption of a nomenclature which precisely describes each member of the graphene family.[74,75]

In 1986 an editorial article aiming to define the nomenclature and terminology of GIC by Boehm et al. registered the term “*graphene layer”* for a single atomic thick carbon sheet within the 3D graphite.[69] After the realization of isolated single layers of graphene, this term was strictly used to describe a single carbon layer in any other carbon material of various dimensionalities, such as graphite (3D), carbon nanotubes (1D), and fullerenes (0D). On the other hand, the term *“graphene”* was reserved to refer to an isolated single layer graphene sheet of extended lateral dimension either suspended or placed on a foreign substrate.[74]

A recent recommendation for the nomenclature of the *graphene-based materials* has been published, to promote a consistent and well-defined usage of terminologies, that precisely describe the material, thus eliminating confusion in the scientific literature.[74] Graphene-based materials have been defined to comprise a family of nanomaterials which inherits the 2D characteristic of a graphene sheet, accordingly it includes multilayered graphene and chemically derived graphene sheets such as Graphene Oxide. It is to be distinguished from the 3D sp^2 carbonaceous materials which are together with graphene-based materials are part of a larger family labeled as Graphenic-carbon-materials. The various categories of graphene-related materials are illustrated in **Figure 2.4**, and will be described in details below.

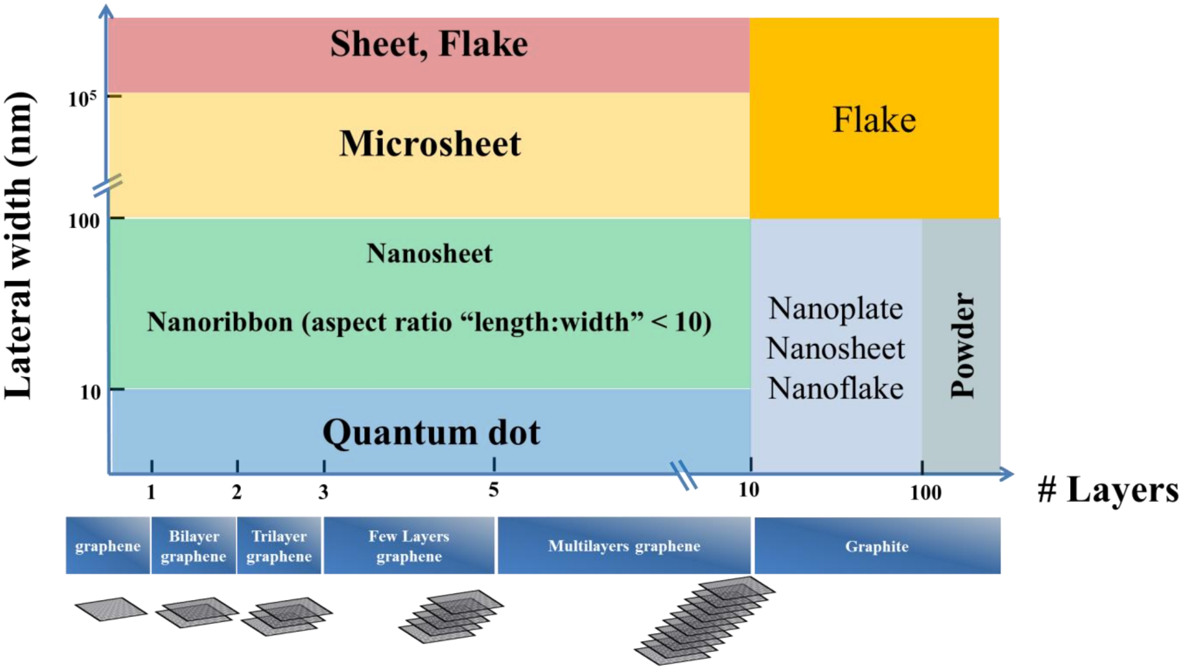

Figure 2.4: Suggested nomenclature of graphene based on the number of layers and lateral size

The suggested recommendations were based on various principles relying on a set of well-defined characteristics which when varied, alters the physical and chemical properties of graphene, so that each terminology would imply a physically and/or chemically different material. The first among these principles enforces the distinction between the terms *graphene* and *graphene layer*, where it clearly defines the use of *graphene* to refer to isolated single atomic thick carbon sheets, arranged hexagonally in a honeycomb structure, and doesn't form part of any other carbon structure. The deviation of any graphene-based material from this definition shall be reflected in the terminology by adding a descriptive suffix or prefix to the term *graphene*. Secondly, graphene has been obtained with lateral dimension ranging from tens of nanometers to several micrometers depending on the synthesis route, and processing conditions. The lateral dimension can significantly alter the electrical transport and other properties in graphene, and thus a clear definition of such parameter in the terminology of graphene-based materials especially those in solutions is highly recommended, such as "graphene nanosheets" or "graphene microsheets". Thirdly, the thickness of graphene is a crucial parameter, as the electronic structure evolves with the number of layers, till it resembles that of bulk graphite once the number of layers exceeds ten.[76] Such statement is only valid in the case where the sheets are electronically coupled through Bernal-ABA or rhombohedral ABCA stacking, however, for randomly stacked (Turbostratic or rotationally faulted) there is no coupling between the sheets and thus the electronic structure resembles that of a monolayer. This makes it important to define the stacking as well as the number of layers in the terminology of the graphene-based material. The in-plane shape is an important feature that should also be included such as Graphene ribbons or quantum dots which have generated a significant amount of research interest. According to the principles just mentioned, graphene-based materials were classified based on the number of well-defined and countable layers in the material. A single layer of graphene is simply referred to as graphene, two layers and three layers are labeled as bilayer and trilayer graphene, respectively. As the number of layers increases, *few layers graphene (FLG)* is reserved to describe graphene with 1 – 5 layers, and *multilayer graphene (MLG)* to describe graphene with 1– 10 layers. For thicker materials with thickness and lateral dimensions less than 100 nm, the term *graphite nanoplates* is to be used, with the "nano-" term included to distinguish from *graphite powders* that are typically more than100 nm thick. This transition from using the term graphene to the term graphite results from the fact that the electronic properties of graphene sheets of more than 10 layers are no longer distinguishable from those of bulk graphite once the layers are stacked in Bernal stacking (ABA).

With the increased industrial and commercial interest of chemically modified graphene and exfoliated graphite, in addition to their different properties and applications as compared to pristine graphene, a clear distinction shall be made when referring to graphene oxide (GO) and reduced graphene oxide (rGO) which are the most common chemically modified graphene materials. The structure of GO is largely altered due to the incorporated oxidation process during the synthesis which renders the material electrically insulating. The reduction of GO can restore the electrical conductivity partially by various chemical and thermal processes, however, in either case, GO and rGO are considered among the most important graphene-based materials. As will be described in details in the next section, the properties of graphene can vary drastically from one synthesis route to another. The synthesis route has been generally used to prefix the term graphene which provides valuable information on what to expect in terms of the physical and chemical properties, such as CVD graphene, epitaxial graphene and mechanically exfoliated graphene.

2.2.2 Mechanically exfoliated Graphene

Monolayer graphene sheets obtained by mechanical exfoliation are by far the highest quality graphene, and have been the favored route by researchers for fundamental studies into its unique physical properties.[76] Starting from a highly oriented pyrolytic graphite crystal (HOPG), a scotch tape can be used to peel flakes of graphene by cleaving them from the crystal via normal force. The flakes commonly attached to the scotch tape are typically few layers graphene and thick graphite platelets, which can be made thinner by attaching them to a Si substrate, and repeatedly peeling them off until a monolayer graphene is obtained **(Figure 2.5A)**.[77] Another variation of the mechanical cleavage process is to apply a shear force to the crystal by drawing it on a target substrate.[78] Samples obtained through mechanical exfoliation are typically on the scale of tens of micrometers – thus typically referred to as micromechanical cleavage – in addition to having a very low throughput, since single layers are buried among thicker ones which obstruct its characterization and detection. Hence, it is unlikely to develop any mature industrial mass production of graphene based on this route.[79] Larger scale production routes of graphene have been developed, generally compromising the high quality of the obtained graphene.

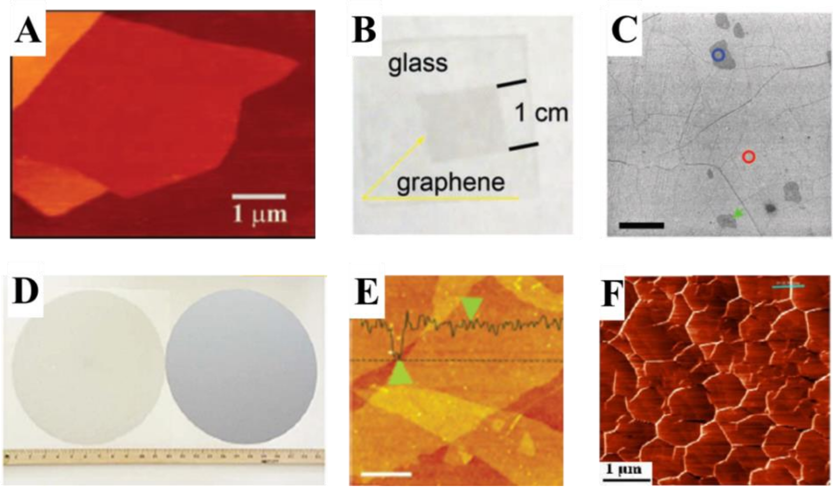

Figure 2.5: Morphological images of graphene synthesized by different methods. (A) AFM image of mechanically exfoliated graphene.[18] *(B) Optical image of monolayer CVD graphene transferred to glass*[80]*, (C) SEM image of monolayer CVD graphene transferred to SiO_2/Si showing wrinkles and multilayer regions, scale bar is 5 µm,*[80] *(D) photograph of large-scale spin-coated graphene oxide on 300 mm wafer and the transferred free-standing graphene oxide membrane (left).*[81] *(E) AFM image of graphene oxide showing a step height of individual flake corresponding to 0.67 nm (across the green dashed line), scale bar is 1 µm.*[81] *(F) epitaxial graphene grown on SiC.*[82]

2.2.3 Epitaxial growth of graphene on SiC

Graphene has been grown epitaxially on SiC wafers. Annealing SiC at ~ 1500 °C leads to the segregation of graphitized islands of carbon, as the Si desorbs from the surface at around 1000 °C **(Figure 2.5F)**.[83–86] Epitaxial growth of graphene on SiC is a two-step process; first the wafer is annealed in a hydrogen environment aiming towards removing contamination and minimizing surface roughness to provide a high-quality platform for graphene growth, followed by annealing at an increased temperature to sublime Si and grow graphene layers.[86] This process has been demonstrated to hold in ultra-high vacuum (1×10^{-10} Torr)[86] or ambient pressure conditions; [84] with the former generally leading to higher quality, wafer size monolayer graphene with smoother morphology and larger crystalline domains.

Several limitations for this route are related to the use of SiC substrate since the lateral size of obtained graphene is limited to that of the available standard wafer size, i.e. ≤ 4 inches. In addition to posing difficulty and additional cost related to the required transfer of graphene to arbitrary substrates for various technological applications.

2.2.4 Solution processed graphene oxide (GO) and reduced graphene oxide (rGO)

The development of methods to disperse graphene sheets in solution and rendering its solution processability has been extensively investigated. However, graphene is hydrophobic and tends to aggregate in aqueous and organic solvents. To overcome this, modifying the basal plane of graphene with functional groups that would increase its solubility and stability in solutions has been a subject of much interest.[87] The presence of oxygen based functionalities has led to hydrophilic graphene which is highly soluble in aqueous and common polar solvents. However, the oxidation of graphene would induce significant defects to its basal plane, so that it loses its high conductivity and becomes insulating.

Oxidation of graphite using the Hummers methods,[88] followed by exfoliation in water by sonication was used to produce solutions of single layer and few layers graphene oxide sheets, which can be solution-processed onto large-area substrates as shown in (**Figure 2.5D** and **E**). GO sheets are then reduced either by annealing at high temperature or using various chemical reducing agents such as hydrazine. The reduction step is needed to restore the electrical conductivity in rGO. Even after the reduction process, the obtained sheets have the lowest conductivity when compared to all other routes of graphene production due to the large amount of defects present. The conductivity is further reduced by the interlayer junction resistance of obtained films, diminishing the opportunity of using it in electronic applications.[81] This, in addition to environmental and cost impacts of the various chemical reducing agents, forms a major barrier in the face of its industrial production.

2.2.5 Chemical Vapor Deposited (CVD) graphene

Synthesis of CVD graphene

The growth of thick graphitic films by the decomposition of hydrocarbons on the surface of crystalline[89] or polycrystalline[90] transition metals using CVD has been known for more than 50 years.[91] The search for large-scale production routes of single layer graphene has led the community to revisit this approach, attempting to grow single to few layers graphene films on various transition metals such as Ru,[92,93] Pt,[94–96] Co,[97] Ni[98–101] and Cu.[80,102] Graphene-based materials of varying morphology, thickness, and quality were obtained depending on the processing conditions and the metal of choice. This variation was ascribed to two different growth mechanisms shown in **Figure 2.6**, which are classified based on the solubility of carbon in the transition metal of choice: (1) surface thermal decomposition of the hydrocarbon precursor which typically occur on metals with low carbon solubility (**Figure 2.6A**) and (2) diffusion and segregation of the carbon species from the bulk of the metal and metastable metal carbides during the cooling process, occurring in metals with high carbon solubility (**Figure 2.6B**).[27] The catalytic behavior of transition metals is attributed to the partially filled *d*-orbitals which allow for reactions either by changes in their oxidation states or by forming intermediates that are appropriate for the growth.[27]

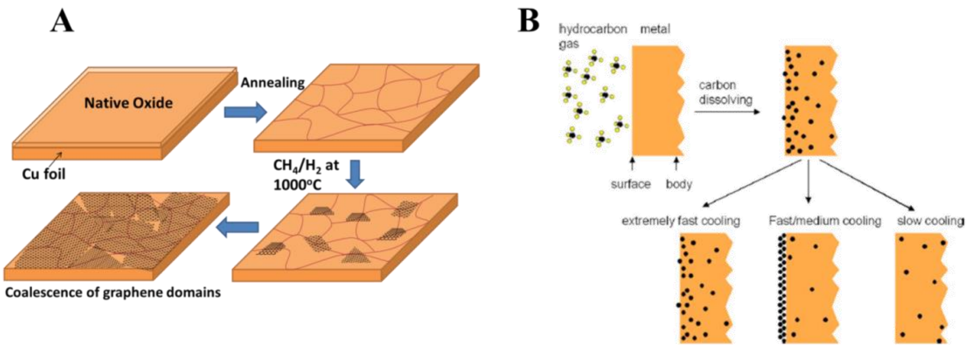

Figure 2.6: Growth mechanisms of CVD graphene. (A) surface thermal decomposition[103] *and (B) diffusion and segregation.*[98]

In general, CVD growth of graphene is a three step process, (1) starting with loading of a transition metal into a tube furnace, feeding of hydrogen while heating up to around 1000 °C allowing for recrystallization of the metal to larger grains and the reduction of any metal oxide on the surface, (2) and then a hydrocarbon precursor such as methane is introduced into the reaction chamber along with the hydrogen flow at specific pressure and duration, during which it thermally decomposes into reactive species that forms graphene nuclei growing and coalescing into a continuous graphene film (3) followed by controlled cooling of the system. The last step becomes important only when diffusion and segregation mechanism (**Figure 2.6B**) dominates, and the cooling rate should be carefully controlled to determine the quality and the thickness of graphene films.[98] Initially, large-scale FLG and MLG were reported by various groups in 2008,[100,101] using Ni as the catalytic metal under ambient pressure. Carbon exhibits a relatively high solubility in Ni ~0.6 weight% at 1326 ^{o}C,[27] and hence the growth mechanism is dominated by carbon diffusion and segregation during the cooling process. Thus, both nickel film thickness and the cooling rate had to be optimized to control the thickness of grown graphene. Typically 300 nm thick e-beam evaporated nickel film on SiO_2/Si yields the highest quality FLG films composed of 4-12 layers. Lower thicknesses have been reported to affect the morphology of the Ni film during the growth, where the high temperature of the process would cause its aggregation and dewetting into clusters with negative consequences on the quality of graphene.[100] The cooling rate has been systematically studied and has been identified as a key factor in thickness and continuity of grown FLG. Extremely fast cooling (>50 ^{o}C/s) reduces the mobility of the carbon atoms in the C-Ni solution, and results in poor film continuity, whereas, the optimum cooling rate (10 – 20 ^{o}C/s) has achieved high quality and continuous FLG films. Slow cooling rates (<0.1 ^{o}C/s) provide sufficient time for carbon to diffuse into the bulk and prevent any film formation as shown in **Figure 2.6B**.[98]

In 2009, it was reported that graphene with more than 95% single layer (SLG) coverage can be grown on a copper foil (~25 μm thick) used as the catalytic metal substrate.[80] The growth of graphene on copper is a self-limiting surface process, where thermal decomposition of hydrocarbon precursors occurs at 1000 ^{o}C in the presence of hydrogen at the surface of the copper catalyst. The absence of the precipitation mechanism seen on other metals was an important advantage. This is due to the low affinity of copper to carbon, which has a solubility of ~0.008 weight% at 1084 ^{o}C. This removes the need for controlling the cooling rate and substrate thickness in order to control the quality of the grown monolayers.[104,105] Indeed, similar graphene quality was obtained despite cooling rates varying from 20 to 300 ^{o}C/min and using foil thicknesses of 12.5, 25 and 50 μm, indicating the growth process is dominated by surface catalysis effects.[80] CVD growth of graphene on thin copper films (<500 nm) on SiO_2/Si has been attempted in a similar manner to FLG growth on Ni. However, the resulting graphene is generally defective[106] and exhibits lower carrier mobility[105] than those obtained on thick copper foils. This has been attributed to changes in the morphology of thin polycrystalline metal films, including their de-wetting at high-temperature and low-pressure conditions.

Roll-to-roll CVD growth of graphene was first attempted in ambient conditions on a one meter strip copper foil, leading to the growth of few layers graphene.[107] The annealing and growth regimes of the process were carefully controlled by tuning the rolling speed and utilizing a specially engineered gas diffusion system that is able to directly flow the gasses at the heated zone which is shown in **Figure 2.7A**. More recently a concentric tube CVD furnace was developed for the synthesis of CVD graphene at low pressure, by helically wrapping the copper foil on the internal quartz tube which was inserted into the main tube of the furnace as shown in **Figure 2.7B**. The gas is supplied to the central zone of the furnace through holes on the internal tube that would allow two different zones for annealing and growth on the furnace. Continuous monolayer graphene has been successfully synthesized using this process.[108]

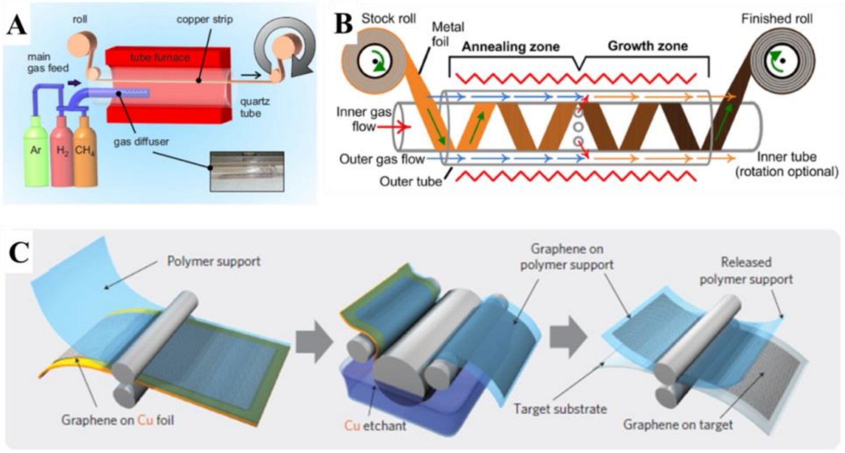

Figure 2.7: Roll-to-Roll processing of CVD graphene. (A) Growth of FLG using a diffusion system for the gasses at the heated zone[107]*, (B) Continuous monolayer growth using concentric tube CVD system,*[108] *and (C) Transfer of large are CVD SLG to PET substrates using roll-to-roll processing.*[63]

Transfer of CVD-grown graphene

CVD has proven to be a successful route for the synthesis of large-area graphene films on transition metals. However, most applications require the graphene (SLG or FLG) to be transferred to another substrate for device fabrication. Successful transfer of graphene is not a trivial task. The main criterion for a successful transfer process is that it should not damage the CVD-grown graphene and thus result in a smooth and defect-free graphene free of residues associated with the transfer.[109]

However, the transfer process can cause significant degradation of the quality of CVD graphene due to tearing and folding of the sheet.[109] Significant effort has therefore been put in place in order to improve transfer processes to the point that they can maintain the quality of the as-grown samples.

Transfer methods of CVD graphene generally employ a support layer placed on top of the graphene, which provides mechanical support during the chemical etching of the underlying metal film or substrate. After the etching process is complete, the graphene/support bilayer is transferred to the destination substrate, at which time the support layer is removed. Depending on the support layer used, transfer methods are generally classified either as carrier or stamp methods.[110] Carrier transfer methods utilize a support layer that adheres strongly to graphene and requires aggressive chemical or thermal treatments to be removed. Examples of carrier transfer processes include the use of popular Poly-(methyl methacrylate) PMMA film or thermal release tapes. The main issue with such methods is that residues of the support layer are difficult to remove completely. This negatively impacts the ability to make contacts to graphene. In addition, the harsh chemical and thermal treatments used in the removal of the support layer are likely to be incompatible with the destination substrate or device. In this regard, the stamp transfer method which utilizes an elastomeric support layer that picks up the graphene layer and stamps it onto the destination substrate has advantages. Stamping methods typically utilize polydimethylsiloxane (PDMS) as support layer because of its weak adhesion to most materials. Removal of the stamp layer relies on the thermodynamics of the interfacial adhesion forces at the stamp/graphene and graphene/substrate (destination) interfaces. The stamp support layer is removed simply via mechanical peeling, which would leave the graphene film intact on the destination substrate and leave no residues on the surface. However, mechanical stresses during the release step can introduce cracks into the graphene sample.

A) Carrier transfer methods: PMMA support layer

The PMMA-mediated transfer has been successfully demonstrated in the context of carbon nanotubes,[111] and has been shown to transfer CVD graphene from the catalyst metal to a wide range of target substrates.[80,101] The process consists of a thick spin-cast polymer layer on graphene, followed by chemical etching of the metal support leaving the PMMA/graphene floating on the surface of the etchant. After washing with DI water, the stack is scooped up by the target substrate, forming a PMMA/graphene/substrate stack. The PMMA is dissolved and washed away with acetone leaving graphene on the target substrate. However, the existence of covalent bonds between the PMMA layer and graphene complicates the transfer.[109] Some PMMA residues always remain on the surface of graphene – even with intense washing, increasing its roughness, introducing unintentional p-doping, reducing its conductivity and impacting the quality of contacts between graphene and other materials. Removal of PMMA residues requires additional annealing in vacuum[112] or under an H_2/Ar mixture[113] at 300 ^{o}C, which is quite effective at removing residues.

The PMMA transfer method has been fine-tuned by Ruoff et al.,[114] who introduced a second layer of PMMA on the PMMA/Graphene stack after scooping with the target substrate. Processing the second PMMA layer is believed to partially dissolve the first one, allowing an easier release of graphene and its internal stresses built up during the etching and transfer processes. This method has been shown to improve the contact between graphene and the target substrate.

B) Stamp transfer methods: PDMS support layer

Stamp transfer methods most commonly utilize PDMS layer to mechanically support graphene, a concept borrowed from soft-lithography, where a microstructure can be replicated using pre-patterned elastomer masks. The PDMS stamp is attached to the graphene sample, followed by chemical etching on the underlying metal catalyst, the PDMS/Graphene can be lifted off using a tweezer, washed and dried and then stamped on the target substrate. The PDMS stamp can be peeled off leaving the graphene on the substrate. This is in contrast to the scooping step in the PMMA transfer method, which is less desirable when the target substrate or device is sensitive to moisture, acetone and/or heating. As PDMS is durable, unreactive and binds to graphene via weak van der Waals interactions, the transfer process tends to be cleaner and the surface of graphene can be free of residues. This method has been demonstrated to transfer continuous and patterned SLG[115] and FLG[100] graphene onto SiO_2/Si. The only requirement for a successful stamp transfer process is that the work of adhesion – defined as the energy needed to separate two solids at the interface into their respective free surfaces – between the graphene and PDMS (source) to be lower than that between the graphene and the target substrate.

$$W_{G-S} < W_{G-D}$$

The work of adhesion is a function of the surface energy of the materials in contact; hence this equation can be represented as a comparison between the surface energies of PDMS and the target substrate. The former's surface energy is 20 mJ/m^2, which tends to be lower than many materials.[116]

The transfer process can also be adapted to roll-to-roll CVD graphene and has successfully led to the transfer of CVD graphene onto flexible PET substrates.[63,67,107] Large-scale transfer of a 30 inch (diagonal) SLG from a copper foil to PET has also been made possible by the use of thermal release tapes which are attached to the graphene/copper by applying soft pressure between two rollers, and finally removed after the etching of copper and stacking on PET by applying moderate heating (90 – 120 ^{o}C) as shown in **Figure 2.7C**.[63] In addition to various advantages offered by CVD graphene in terms of quality, scalability, and throughput; the adaptation of the growth process and the subsequent transfer to batch and continuous manufacturing, including roll-to-roll processing, have positioned the CVD route as a front runner for the industrialization and commercialization of graphene into electronic and optoelectronic applications.

2.2.6 CVD single-layer vs. few-layer graphene

Our literature survey indicates that FLG, which typically refers to an as-grown stack of 2-5 layers of graphene,[74] is a more mechanically and chemically resilient form of graphene with demonstrated advantages over SLG,[117] including superior performance in various applications such as gas sensors,[118] flash memory[119] and electrical interconnects.[120,121] FLG electrodes exhibit only a slight variation in conductivity upon stretching and bending with full recovery to the original performance when the strain is removed,[100] whereas the conductivity of SLG decreases significantly and irreversibly in similar conditions as shown in **Figure 2.8**,[114,122] making FLG a particularly interesting TCE candidate from the perspective of emerging applications, such as flexible electronics, optoelectronics, and photovoltaics.

The increased number of layers in FLG not only increases the conductivity of graphene films, but also makes them more resistant to adverse effects from the substrate, such as charged impurities, and decreases the contact resistance in devices due to screening effect of the additional layers.[120,123] In addition, the fact that at least one graphene layer is buried beneath the surface makes FLG more robust and less prone to performance degradation due to contamination and defects during processing.[117] Moreover, as we will show in this thesis, FLG is amenable to intercalation by very small dopant molecules in a similar manner as graphite can be intercalated to form graphite intercalation compounds (GIC) with small redox-active guests.

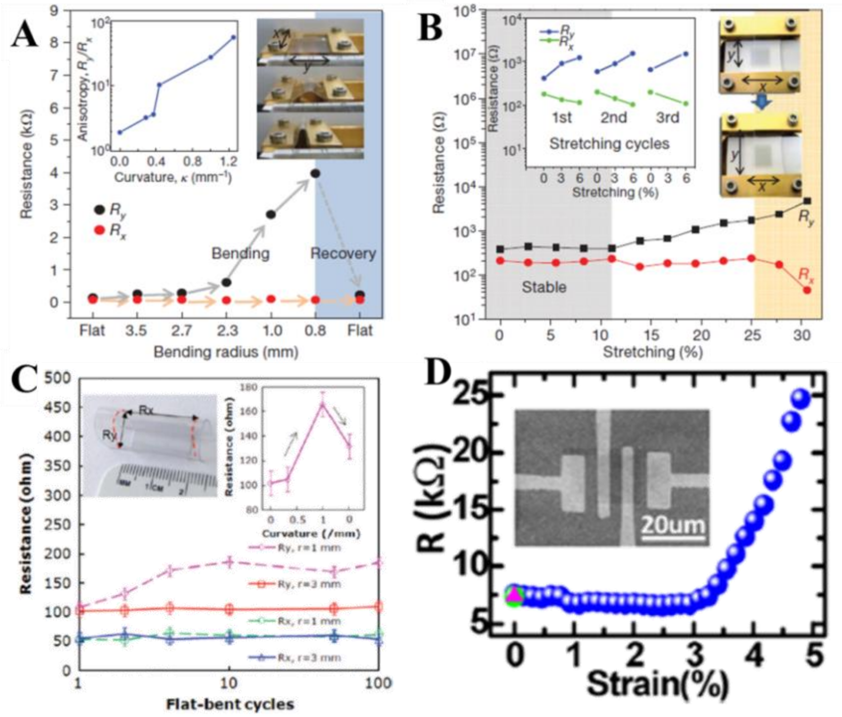

Figure 2.8: Comparison of the variation of the electrical transport of FLG and SLG under mechanical bending and stretching. Variation of the resistance of FLG as a function of (A) bending radius, and (B) lateral stretching (strain).[100]*And the variation of the resistance of SLG as a function of (C)flat-fold cycles and for various bending radii,*[114] *and (D) lateral stretching (strain).*[122]

The intercalated dopant molecules are thus encapsulated by graphene overlayers resulting in a more stable bulk doping, as has been shown for few-layer and multilayer graphene with various intercalants such as Br_2,[124] $FeCl_3$[125] and Li.[64] This potential nexus between graphene and GICs offers a tremendous opportunity to independently tune the properties of graphene via surface and/or bulk doping, a direction which has yet to be explored and is the main topic of this thesis.

2.3 Electronic structure and optoelectronic properties of graphene

In this section, the electronic band structure of graphene, along with the resulting unique physical phenomena are introduced. The electrical transport properties and the various carrier scattering mechanisms in graphene are described while comparing ideal graphene sheets to the polycrystalline graphene typically obtained in large-scale production routes. Then the optical properties of graphene relevant to applications as TCE are discussed.

2.3.1 Electronic structure of graphene

The extraordinary electronic properties and charge transport in graphene arise from its unique band structure that was predicted in 1947 for a single graphene layer in graphite. This band structure has been subsequently used as the basis for describing the electronic structure of a wide range of sp^2 carbon allotropes, including nanotubes and Buckminsterfullerenes.[126] Graphene is described as a hexagonal honeycomb lattice of carbon atoms lying flat in one plane. Carbon atoms are bonded covalently to each other by sp^2 hybridized bonds with a C-C distance of 0.142 nm and an exact atomic thickness of one carbon atom, equivalent to 0.335 nm. Hybridization of the filled *2s* and *2p* orbitals of carbon atoms leads to three planar sp^2 orbitals which align with the basal plane of the graphene sheets forming the strong covalent σ bond responsible for the high in-plane mechanical strength in graphene, leaving behind one orbital (*2p*) that aligns orthogonally to the basal plane which gets occupied by the delocalized π-electrons.

The π-electrons are responsible for the unique electronic band structure of graphene, where non-interacting π-states from the valence band and π^*-states from the conduction band touch at six points known as the Dirac points. These are typically reduced to an independent pair (K and K' points) having a linear and symmetric dispersion relations around the Dirac point which is generally illustrated in literature as two cones touching at E_{Dirac} (**Figure 2.9**).[127] Consequently, graphene is a zero-gap semiconductor, with electrons and holes exhibiting the same properties leading to the ambipolar field effect transport.[18] In addition, the charge carriers in graphene are relativistic and hence described by the Dirac equations - rather than the Schrödinger equation - as zero-mass quasiparticles called massless Dirac fermions, moving with an effective speed equal to the speed of light ($\upsilon_F=10^6$ m s^{-1}).[76,127]

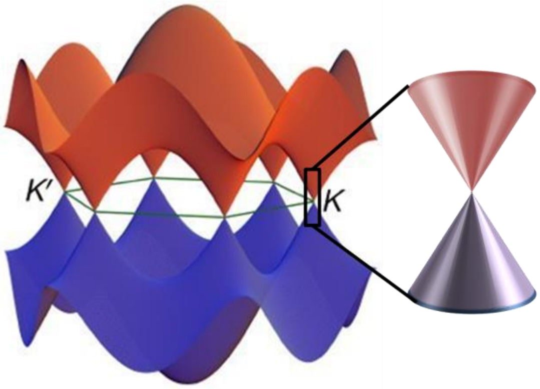

Figure 2.9: Electronic Structure of Graphene and the reduced representation of the linear dispersion relation at the K point.[128]

2.3.2 Electrical transport properties of graphene

Theoretical and experimental studies have shown graphene to exhibit a minimum conductivity on the order of e^2/h at vanishing carrier concentration at the Dirac point, which extends over a plateau independent of carrier concentration.[129–131] The minimum conductivity is an intrinsic property of electronic structures described by the Dirac equation and a direct consequence of the massless Dirac fermion charge carriers in graphene. And thus it was initially attributed to the fact that such carriers show no localization effects in the presence of disorder, thus validating Mott's argument that the mean free path of charge carrier cannot be smaller than their wavelengths and hence the conductivity cannot be smaller than e^2/h.[129] Later, the minimum conductivity and the accompanying plateau in carrier density were associated with charge density inhomogeneity at low carriers concentration forming networks of electron rich and hole rich regimes which were termed as the electron-hole puddles.[132] Thus, changing the carrier concentration via electric field gating or chemical doping would be limited to the redistribution of charges without increased conductivity.[133]

As the carrier density increases in graphene, the system moves away from the inhomogeneous electron-hole puddle regime to a homogeneous 2D system for which the electrical transport has been theoretically explained by the semiclassical Boltzmann transport equations.[132,134,135] Experimentally, the transition between these two regimes have been accessible through applying a gate voltage (V_g) to graphene on SiO_2; that can vary the surface charge density in graphene according to **Equation 2.6**[77]

$$n = \frac{\varepsilon_o \varepsilon V_g}{te} \qquad \textit{Equation 2.6}$$

Here, ε_o and ε are the permittivities of free space and the SiO_2 substrate, respectively, e is the electron charge and t is the thickness of the SiO_2 layer. The modulation of the carrier density by electric field gating has been considered as electrical doping of graphene and has been extensively used to study the electrical transport properties and electronic structure in doped graphene.[136–138] At $V_g = 0$, the electrical transport is at the electron-hole puddles regime, where the Fermi energy lies at the Dirac point for intrinsic graphene, and the resistivity exhibits a maximum. Sweeping the gate voltage across this point yields a sharp reversal in the Hall coefficient $R_H = \frac{1}{en}$, and initially very small changes in the conductivity, indicating the substitution of one type of the carriers to the other moving towards the homogeneous transport regime. In doped graphene, the resistivity peak at (originally at $V_g = 0$) would be shifted towards a negative or positive gate voltage for n- and p- doping respectively.[139]

Scattering mechanisms in the homogeneous carrier regime

Various scattering mechanisms have been proposed to take place in the homogeneous carrier regime and were investigated both theoretically and experimentally (**Table 2.2**). It was theorized that transport in graphene is limited by short-range scattering, which is independent of the carrier density. However, experimental observations of the carrier density dependence of graphene's conductivity, have led to the introduction of Coulomb long-range impurity scattering, which turned out to be the dominant scattering mechanism in graphene.[132,135] Both long-range Coulomb scattering by impurity centers (n_i) and short-range scattering by point defects (n_d) can be treated theoretically by the Boltzmann transport equations, which predicts the carrier density dependence of either and has shown a quantitative agreement with transport properties obtained experimentally in the high carrier density regime ($n > n_i$).[132]

The conductivity (σ) at zero temperature is defined by **Equation 2.7**.

$$\sigma = \frac{e^2}{2} \upsilon_F D(E_F) \tau(E_F) \qquad \textit{Equation 2.7}$$

Here, υ_F is the Fermi velocity of carriers, $D(E_F)$ is the density of states and $\tau(E_F)$ is the scattering time. The scattering rate $\frac{1}{\tau}$ is a function of the density of the scattering centers and the matrix element of the scattering potentials $\langle V_{kk'}(Z)\rangle$, which varies with the energy of carriers for Coulomb scattering and is constant for short-range disorder scattering. The dependence of the scattering time (τ) on the carrier density for each scattering mechanism is different, and is defined according to **Equation 2.8**, [132]

$$\tau \propto \begin{cases} \sqrt{n}, & Coulomb\ scattering \\ \frac{1}{\sqrt{n}}, & Short\ range\ scattering \end{cases} \qquad \text{Equation 2.8}$$

The density of states for monolayer graphene is defined as

$$D(E_F) = \frac{2E_F}{\pi(\hbar\upsilon_F)} \qquad \text{Equation 2.9}$$

Here, E_F is the Fermi energy for monolayer graphene $(E_F = \hbar\upsilon_F\sqrt{\pi n})$. Thus, $D(E_F) \propto \sqrt{n}$, leading to the conductivity dependence on carrier density based on **Equation 2.10**;

$$\sigma \propto \begin{cases} n\ , & Coulomb\ scattering \\ n^0, & Short\ range\ scattering \end{cases} \qquad \text{Equation 2.10}$$

Fitting of the Boltzmann equations to various results in the literature has shown that the Coulomb scattering is the dominant scattering mechanism by showing the linear conductivity dependence on carrier density for $n>n_i>n_d$, with the impurity density in typically supported graphene samples is of the order of $n_i \sim 10^{12}$cm^{-2}. Furthermore, this analysis explained the sublinear conductivity regime observed for high-quality samples,[131] which was referred to as a crossover between impurity scattering dominant transport to that increasingly affected by point defects leading to a flattening of the curve when $n_d/n_i \sim 0$. The Boltzmann transport predictions break down in the low carrier density regime, where the conductivity is predicted to vanish linearly to zero. However, as mentioned earlier, graphene conductivity at low density ($n<n_i$) becomes density-

independent and stabilizes at a constant value on the order of e^2/h due to the formation of electron-hole puddles.

The fact that long-range Coulomb scattering by impurity centers is the limiting factor of transport in graphene has been verified experimentally by several groups.[131,140] A systematic comparison of various mechanically exfoliated graphene devices on SiO_2, with a varying degree of impurity density, led to two different electrical transport behaviors. Higher mobility samples (>10000 cm^2/Vs) exhibited lower charge impurity density and sublinear carrier density dependence of the conductivity in the high-density regime indicating the importance of the short-range scattering mechanism in this regime, in agreement with theory.[131] On the other hand, increasing the charge impurity density has led to samples with lower mobility (<5000 cm^2/Vs), where a linear carrier density dependence of the conductivity is an indication of the dominance of the long-range Coulomb scattering. In addition, asymmetry of the electron and hole branches was observed in this regime, which has been inferred to the interaction of the random impurity charges (electron-hole puddles) with the applied gate voltage of different polarity.

The effect of Coulomb scattering was shown to extend to the low carrier density regime, where a higher minimum conductivity, wider voltage plateau around the Dirac point and larger shift of the Dirac voltage has been correlated with a higher impurity density, due to interactions with the electron-hole puddles.[131,140] The significant role played by the density of charged impurities at the low-density limit was found to affect the position and value of the minimum conductivity in addition to the plateau width (carrier density at which the minimum conductivity is constant), concluding that charged impurities obscure the Dirac point physics predicted theoretically. The minimum conductivity was found to occur at a carrier density that nullifies the potential of the charge impurities, rather than the simple expectations of $n=n_i$. In addition, its value was shown to be higher than theoretical predictions.[133,140]

Lattice vibrations comprise another scattering mechanism in graphene including either graphene phonons (intrinsic) or the surface polar phonons from the underlying substrate (extrinsic). The latter have been shown to set the fundamental limit of carrier mobility at room temperature.[21,135,141] Temperature dependent studies of conductivity, have shown a carrier density independent component of the resistivity, that scales linearly with T<150 K. Such component is characteristic of intravalley (q=0) longitudinal acoustic phonons in graphene[142] which has been reported to set the intrinsic limit of transport properties in graphene. Carriers mobility could be higher than 200000 cm^2/Vs if all other scattering mechanisms are eliminated.[21,141] Other phonons in graphene are believed not to contribute significantly to the transport properties,[135] where the intravalley (q=0) optical and intervalley (q=K) acoustic phonons have been ruled out since both modes are out-of-plane and do not couple strongly to the electrons.[141]

At higher temperatures (>150 K), a nonlinear dependence of resistivity has been generally observed, that is also carrier density-dependent. The latter dependence results in the rejection of the optical phonon scattering mechanism in graphene which is expected to show a weak dependence on the carrier density. This regime was attributed to scattering by remote interfacial phonons (RIP) in the underlying substrate

(SiO_2),[133,143,144] which generates an electric field that couples with the charge carriers. Fitting resistivity due to SiO_2 surface optical phonons (with hω = 59 and 155 meV) to experimentally measured data have shown general agreement explaining that its magnitude is temperature- and charge carrier density-dependent.[141] The mobility limited by the RIP from the substrates yields a limiting mobility of 40000 cm^2/Vs, confirming the fact the scattering by the extrinsic charged impurity in currently obtained samples is the limiting scattering mechanism in graphene.

Table 2.2: Electron scattering Mechanisms in Graphene

Scattering mechanism	References
Coulomb scattering by charged impurities	[131,140,145]
Short-range scattering	[132,135,146]
Phonon scattering by graphene	[141,147]
Substrate surface polar phonons scattering	[141,143]
Surface Roughness	[21]

Transport properties in suspended graphene

Aiming to experimentally access the intrinsic transport properties of graphene and better understand the unique physical phenomena near the Dirac point, the transport properties of high-quality suspended graphene sheet were attempted in 2008 by two different groups.[133,148] By suspending graphene, substrate effects on the electrical transport are eliminated, by mitigating surface charge traps and removing the effects of interfacial polar phonons, substrate roughness and the potential of forming ripples in graphene in addition to fabrication residues on or under the graphene sheets. Bolotin et al.[148] have successfully suspended mechanically exfoliated graphene about 150 nm above SiO_2 substrate and studied its electrical transport at low temperature (5 K). They observed relatively low mobility of 28000 cm^2/Vs at a carrier density of 2×10^{11} cm^{-2}, similar to that reported for supported graphene.[18] However, by applying an electric current heating, they have raised the mobility substantially to 230000 cm^2/Vs, due to the removal of impurity contaminations. Being suspended allows such impurities to be effectively removed from both top and bottom surfaces of the graphene sheet. Similar annealing treatments on supported graphene did not show any improvement in the carrier mobility.[149] Du et al.[133] have reported near ballistic transport in suspended graphene sheets in the low carrier density regime ($<5\times10^9$ cm^{-2}) at T=4.2 K, achieving a mobility as high as 200000 cm^2/Vs. Such observations were correlated to the diminished effect of electron-hole puddles once the substrate was removed. The effect of the electron-hole puddle was quantified by the average deviation of the Dirac point from the Fermi energy defined as E_f, below which the gating of graphene would be limited to the redistribution of carriers between electrons and holes without significantly changing the carrier density. It was estimated to be less than 10 meV for suspended samples as compared to nearly 40 meV for supported samples. Moving away from the Dirac point, carrier mobility as high as 185000 cm^2/Vs was reported at low temperature (T= 20 K).

Electrical transport in polycrystalline graphene

The electrical transport properties discussed thus far have focused on high quality mechanically exfoliated graphene, in which large single crystal domains are obtained. The large-scale production methods of graphene such as epitaxial growth on SiC and CVD on transition metals typically lead to inferior transport properties as discussed in **Chapter 2.2**. Such large-scale synthetic graphene is typically polycrystalline consisting of several single grains that coalesce together into single or multiple grain boundaries, which are defective by nature consisting of periodic pentagons and heptagons of carbon atoms. The impeded electrical conductivity and mobility of such samples have been attributed to such grain boundaries, which gained significant research interest to address the electron scattering at the boundaries and providing strategies to optimize the growth process to control them.[30,66,150–154]

First principle calculations on polycrystalline graphene have identified two distinct behaviors of carriers across a grain boundary; depending on the periodicity of defects in the direction of the one-dimensional interface between two domains. Electrons could be either totally transmitted through via tunneling or totally reflected impeding the charge transport.[154]Total reflection occurs at grain boundaries with a structure that could introduce a transport gap that prevents the tunneling of carriers. Furthermore, a potential barrier model has been used to describe the mobility in polycrystalline graphene, which can be described as a network of low resistivity regions ρ_1 of dimension l_1 characteristic of transport in a single domain (intra- grain), and a high resistivity regions ρ_2 of dimension l_2 characteristic of transport across a grain boundary (inter- grain). The effective carrier mobility has been modeled according to **Equation 2.11**;

$$\mu^* = \left(\frac{\alpha}{\alpha+\beta}\right)(\mu_1 + 2\beta\mu_2) \qquad \textit{Equation 2.11}$$

where $\alpha = \frac{\rho_1}{\rho_2}$ *and* $\beta = \frac{l_2}{l_1}$. Introducing grain boundaries leads to an increase in β, thus deteriorating the carrier mobility.[153] This model has been used to verify experimental measurements of Hall mobility on large area graphene grown epitaxially on SiC, showing the mobility going down from 5800 cm^2/Vs for single grain graphene (low resistivity region) to 370 cm^2/Vs as a result of inter-grain transport.[82]

Temperature dependent transport studies across grain boundaries in CVD graphene, revealed a plateau of finite conductivity at low temperature (<100 K) indicating a transport limited by tunneling through the grain boundaries, with the majority of the carriers unable to overcome the potential barrier across the boundary. At higher temperature, the conductivity increases with temperature and could be fitted with an Arrhenius relation form $\frac{dI}{dV} \propto e^{\frac{E_a}{2k_BT}}$ where E_a is the activation energy which describes the tunneling barriers the carrier would have to overcome.[150,153]

The deleterious effect of grain boundaries on the mobility of CVD graphene, have also been experimentally verified by studying devices fabricated on two single crystalline domains that coalesce into a single grain boundary, obtained by suppressing the growth process prior to the formation of full coverage. The device terminals were deposited in such a way that allows direct measurement of both inter-grain and intra-grain transport simultaneously.[30] Carrier mobility obtained from measurements across the grain boundary was significantly lower than those obtained from single grains. The series resistance measured between the two grains was 0.9 kΩ, significantly lower than the measured resistance across the boundary (3 kΩ), showing that the grain boundary impedes the transport by 2.1 kΩ.

Potential carrier scattering mechanisms in CVD graphene include point defects and impurities from processing in addition to the grain boundaries. The effect of point defects was systematically investigated by introducing defects into a mechanically exfoliated sheet and comparing its carrier mobility to that of CVD graphene having the same level of defects (quantified by the I_D/I_G peak ratio from Raman spectroscopy). It was observed that the former still exhibits higher mobility (3000 cm^2/Vs) as compared to CVD graphene with an average mobility of 1100 cm^2/Vs)[153], concluding that grain boundaries are indeed the origin of the low carrier mobility in large-scale synthetic graphene.

2.3.3 Optical properties of graphene

The richness of the physics underlying the electronic structure of graphene and its transport mechanisms also results in unique optical properties. Light-matter interactions are manifested through the transition of electrons from an occupied state below the Fermi level to an unoccupied state above the Fermi level. The optical properties and the reflectivity or transmittance of graphene are therefore closely linked to its electronic structure, dielectric function, and optical conductivity. [155]

The optical conductivity σ_{opt} describes the electrical current density in the presence of an alternating electric field with frequency ω and is the key parameter that defines the optical properties of graphene. For example, the transmittance of graphene at normal incidence has been shown to be [22,156,157]:

$$T(\omega) = \left[1 + \frac{2\pi}{c}\sigma(\omega)\right]^{-2} \qquad \textit{Equation 2.12}$$

The optical sheet conductivity in graphene has been theoretically predicted to exhibit a universal value ($\frac{e^2}{4\hbar}$) – that is frequency-independent. Moreover, the universal absorption of a suspended graphene layer has been measured to be 2.3±0.1%, with a reflectance of <0.1%, in general agreement with the theoretical calculation of the optical conductivity.[22,158] Remarkably, the optical absorption of graphene is solely defined by the fundamental fine-structure constant $\alpha = \frac{e^2}{\hbar c} = \frac{1}{137}$, where $(1 - T) \approx \pi\alpha$, which derives from the linear dispersion relation near the Dirac point, and originates from the massless Dirac fermion nature of carriers in graphene, since the fine-structure constant is valid only for coupling between light and relativistic particles.[157] For multilayers graphene, it was observed that the transmittance in the visible region is determined only by the number of layers. The total absorption is proportional to the number of layers where each layer absorbs ~2.3% in the visible range, regardless of the changes in the electronic structure.[22,157] Simulation of different stacking orders (ABA, ABC) which are expected to alter the band structure in multilayer graphene, revealed that the transmittance at 550 nm is identical and is not affected by the interactions between the layers. This has also been shown to be true for CVD multilayer graphene, in which the sheets do not typically show ordered stacking, supporting the fact the each layer would independently absorb 2.3%, with the total transmission at 550 nm determined by the fine structure constant multiplied by the number N of layers, such that [157]

$$T = [1 + 1.13\pi\alpha N/2]^{-2} \qquad \textit{Equation 2.13}$$

The factor 1.13 accounts for deviations from the ideal linear Dirac fermions behavior. **Equation 2.13** can thus be utilized to estimate the number of layers in multilayer graphene samples. This is particularly useful for N > 20, since Raman spectroscopy is capable of accurately counting the number of graphene layers for N < 10.[157]

The flat optical transmittance of graphene in the visible spectrum, irrespective of its band structure, its local environment and photon energy, breaks down at lower photon energy, namely in the mid-infrared. Optical characterization of electrostatically doped (gated) graphene reveals a dependence of the optical conductivity on the carrier density, temperature and chemical potential.[159,160] The deviation from the universal optical conductivity behavior occurs for photons at energies below 0.5 eV, where the measured absorbance (correlated to the optical conductivity) is frequency-dependent and exhibits sample-to-sample variations. These observations can be understood when considering the nature of optical transitions which, in graphene, are divided into interband and intraband transitions. Interband transitions are those in which electrons in an occupied state below the Fermi level gain sufficient energy from the electromagnetic radiation to be excited to an unoccupied state above the Fermi level. These transitions dominate at high photon energies, where the condition $E_{ph} > 2E_F$ is generally met, and where small shifts in the Fermi level do not block the transitions. Intraband transitions correspond to the absorption of electromagnetic waves by free carriers within the conduction band, and dominate the optical response at lower photon energies, and is strongly determined by the scattering mechanisms involved.[158,161] Thus, at low photon energies the optical conductivity loses its universal character, becoming more sensitive to the electronic structure of graphene and to extrinsic effects such as its environment, support substrate, the presence of dopants, etc.[161]

The effects of electrical doping on the optical absorption of graphene have been investigated in the infrared region (0.1 – 1 eV) by electrostatically doping graphene. The transmittance spectra revealed a peak at all doping concentrations, which corresponds to interband optical transitions at ($E_{ph} \sim 2E_F$). The effect of doping was observed through an enhanced intraband absorption in the far infrared, and a shift in the transmission peak towards a higher energy corresponding to changes in E_F which defines the onset of the interband transitions.[159] Since the position of E_F varies with the carrier density, the relative width of the occupied states and unoccupied states changes with doping (with either hole or electrons), thus the energy threshold where the interband transitions are allowed is expected to increase with the doping concentration. This is manifested as an increase in the transmittance of doped graphene in the IR region[160] and in the visible range for heavily doped graphene.[64] In the high photon energy regime, where a universal optical conductivity has been predicted, slight deviations from the ideal Dirac-fermion behavior have been observed in the form of increased absorbance up to 10%.[22,157,161] This behavior has been explained by the possibility of having many-body effects between the carriers rather than the ideal non-interaction massless Dirac fermions,[159] and/or deviation of the linear dispersion relation as we move away from the Dirac point for increased photon energy, which are expected to increase the absorbance at this range.[158,161]

2.4 Doping of graphene towards its application as a TCE material

During the very early experiments on graphene,[18,112,162] it was observed that its electronic structure and electrical transport properties are very sensitive to extrinsic effects and to surface contamination. This is attributed to its 2D nature leading to a large specific surface area of 1315 m^2/g for one side,[163] in addition to the wide-range of reactive sites available[164] making it an ideal platform for various atoms and molecules to attach, and thus modulate its properties and expand its applications. In this section, the various objectives for graphene surface doping and types of dopants is briefly discussed, with the major focus on non-covalent doping for enhancing the electrical conductivity of graphene without significant optical losses towards applications as TCEs. Then, a detailed review of the various chemical non-covalent doping strategies and materials that have been reported in literature is provided. Followed by a discussion of the more stable of bulk doping of graphene, where dopants are sandwiched between graphene layers (interlayer doping). Then this section is concluded with recent advances in intercalation doping of few layers graphene, contrasted to interlayer doping.

2.4.1 Motivation for doping of graphene

Despite the extraordinary properties of graphene, some aspects of this “miracle material” have challenged its wide range industrial applicability in various areas which has motivated the engineering of its structural, electronic and chemical properties through doping. For example, graphene is intrinsically hydrophobic, which renders it insoluble in aqueous and organic solvents, as several sheets spontaneously stack into thick multilayers or agglomerate. To enable large-scale production of graphene, it is favorable to have single sheets of graphene uniformly dispersed in solution allowing for low-cost and room temperature solution processing adaptable with the mainstream industrial techniques in the fabrication of organic electronics and optoelectronics. In addition, the exceptional electrical and mechanical properties of graphene have attracted considerable interest in being used as fillers for polymers, in which an enhanced overall performance of the composite is for graphene (as a filler) to be uniformly dispersed in the composite matrix. This has prompted the need to alter the surface properties of graphene with various functional groups that would prevent their aggregation and stacking. Moreover, forming a uniform interface in electronic devices is key for their successful operation. For graphene to be successfully used in solution-processed organic electronics as an electrode or interlayer on top of which other components are to be deposited from solution, its surface energy has to be modulated through doping to allow for uniform film formation, an issue that has been extensively investigated in organic solar cells, where uniform PEDOT:PSS films could not be deposited with ease on a graphene TCE.[57]

The electronic structure of graphene discussed earlier, indicates that intrinsic graphene is a zero-gap semiconductor exhibiting low carrier density with the existence of non-homogeneous electron-hole puddles resulting from charged impurities at the interface with the substrate, thus leading to a high sheet resistance in pristine SLG of 6000 Ω/□.[15] The modulation of charge carrier’s type and their concentration can be achieved by doping, which has been shown to neutralize the electron-hole puddles and lead to either an n-type or p-type graphene with significantly increased electrical conductivity, which will be reviewed in detail in this section. Moreover, the absence of a band gap leads to a very low on/off currents ratio in graphene-based field effect transistors which hinder its applicability in digital electronic applications.[165] Various doping routes have been demonstrated to induce a band gap in graphene, that allows for its usage in such applications and benefit from its high room temperature mobility. The controlled modulations of the work function of graphene have been enabled by doping, to minimize the potential barrier of charges at the interface during injection or extraction of electrons. The work function of pristine graphene have been reported to be 4.5 eV, which was successfully tuned in the range of 2.1-6 eV with n- and p-doping with various dopants, respectively, thus allowing graphene to be utilized in any device structure.[139,166,167]

For TCE applications, the main objectives for graphene doping that will be discussed in details in this section are: (1) Increasing the conductivity of graphene by increasing carriers density with minimal optical losses and (2) tuning the work function to minimize the energy barrier at the interface between graphene and adjacent layers.

2.4.2 Enhancing the conductivity of graphene through chemical doping

Control over the carrier type and concentration in graphene has been demonstrated through the application of electric field in bottom gated graphene sheet on SiO_2[18,137,166] and through electrochemical gating of graphene sheets with a polymer electrolyte top-gate[138], providing facile experimental procedure to tune doping and understand the effects of doping on the transport properties of graphene. However, these remain temporary and subject to the availability of external electrical sources which are not necessarily suitable for most applications, including TCEs. The term “chemical doping” is used to refer to the permanent modification of the electronic structure and transport properties through chemical interactions with atomic and molecular species, which are distinct from more volatile doping such as through electrical and electrochemical gating. The latter two are therefore excluded from this review and are discussed in the context of understanding the impact of doping on transport properties. Chemical doping in graphene ranges from non-covalent doping which involves graphene-ligand interaction mainly through the π cloud, maintaining the sp^2 hybridization in the basal plane, to covalent doping, which alters the bonding environment of carbon atoms by changing the hybridization state from $sp^2 \rightarrow sp^3$ and severely influences the electronic structure of graphene.[168]

Chemical reactions on graphene can occur either on its basal plane or at its edges, with the latter being more reactive due to the existence of dangling bonds.[169] If we consider an ideal 2D graphene with an infinitely extended sheet (no edges), and perfectly flat honeycomb hexagonal structure (no curvature, vacancy or grain boundaries), we can identify two types of reactions that could potentially occur on the basal plane. The sp^2 characteristic of unsaturated carbon-carbon bonds in graphene, are amenable to forming an additional covalent bond, by $sp^2 \rightarrow sp^3$ hybridization process, towards a saturated state, however, the delocalized π cloud in graphene forms a barrier to covalent addition reactions, which is generally responsible of the chemical inertness in graphene towards covalent bonding. On the other hand, the π cloud acts as a ligand that participates in complexation reactions and charge transfer adsorption with various molecules and atoms.[168,170] Graphene samples typically synthesized are far away from the ideal painting just presented. Practically, graphene includes edges, basal plane fluctuations in the form of curvature, vacancies, and grain boundaries in addition to chemical impurities. All these features promote additional reactive sites on graphene, that can be involved in a reaction either simultaneously or at different stages making it not possible to achieve full control over the doping scheme to be used, and causing a mixed bonding environment for the same dopant as has been observed in various doping experiments.[124]

Covalent functionalization of graphene

Covalent interactions in graphene are generally hindered by its delocalized conjugated π system, which forms an energy barrier for covalent addition reactions. Thus, it requires highly reactive species or radicals that could overcome this barrier and interact directly with the unsaturated carbon bonds in graphene. The most popular covalently functionalized graphene is graphene oxide (GO), which has been demonstrated as a popular synthetic route for the large-scale solution-processed production of graphene, where the oxide functional groups render the initially hydrophobic graphene to become soluble in aqueous solutions and polar solvents thus allowing for uniform solution casting on wafer scale.[81,171] However, GO is insulating due to damaging the basal plane and $sp_2 \rightarrow sp_3$ conversion, which has motivated significant effort toward the reduction of GO with the aim of restoring the high electrical conductivity and mobility for its application as a TCE. Reducing graphene oxide (r-GO) has been achieved by chemical reduction and/or thermal annealing. However, it has not been possible to fully reverse the effects of the oxidation reactions or to restore the intrinsic properties of graphene, limiting the sheet resistance values to the level of kΩ/□. The electrical transport is dominated by hopping of charges between the highly conductive sp^2 regions and the insulating sp^3 regions and exhibits a junction resistance for transport between overlapping sheets.[81,171] Hydrogenation and fluorination of graphene have also been shown to open a large band gap of ~3.0 eV due to symmetry breaking in chemically doped graphene. The opening of a band gap in graphene is not desirable for TCEs, but is essential for transistor applications in digital circuit in preparation for the post-silicon era; as long as the mobility of graphene can be maintained close to it high demonstrate values in pristine graphene. However, both routes have shown inferior mobility and electrical transport properties.[169,172–174]

Substitutional doping of graphene

Doping of graphene either with electrons or holes has been demonstrated by direct atomic incorporation into its lattice, by substituting carbon atoms with either electropositive or electronegative elements, respectively, in a similar manner to the well-established silicon doping, thus providing high stability. The most commonly used atomic substitutes are nitrogen (n-doping) and boron (p-doping), due to their comparable atomic size, and the availability of five and three valence electrons that could bond with carbon atoms, respectively.[175,176] Direct lattice substitution in graphene has been achieved either during the growth process of CVD graphene[175,177,178] or post-growth by inducing vacancies via ion irradiation and subsequent attachments of the atomic substitutes at these sites.[176] Introducing a source of nitrogen such as ammonia[177,178] or urea[175] along to the carbon precursor during the CVD growth process of graphene has resulted in successful substitutional doping of nitrogen atoms in graphene with a concentration approaching 9 at%,[177] on the other hand, using a boron source such as boric acid has resulted in boron incorporation with a ratio of 4.3 at%.[175] It was evident that the sp^2 character of the carbon atoms are not disrupted significantly, where the graphitic peak in the XPS spectra of both N- and B- doped graphene was observed in the usual position of sp^2 carbon.[175,177] Thus the substitute atoms will bond covalently with adjacent carbon atoms in the plane of graphene without significantly affecting the overall conjugation of carbon atoms, while contributing to the π-cloud with either holes or electrons depending on their valency. However, the electrical transport properties of both N- and B-doped graphene were inferior to pristine samples, showing a reduced conductivity and more than 60% drop in the carrier mobility,[175–177] which was caused by the evident topological defects caused by the atomic incorporation process which has been observed from Raman spectroscopy, and to the fact that the presence of the foreign atomic species can break the potential continuum in graphene and act as a scattering center. [168,169]

Non-covalent doping of graphene

Non-covalent doping occurs through interactions with π-cloud (π-complexes) or physical adsorption (van der Waals interactions), without disrupting the sp^2 structure of the basal plane or causing any defects. Thus, the electronic structure of graphene is generally preserved under non-covalent doping, which typically shows a minimal effect on the charge carrier's mobility.[168] Non-covalent doping increases the free carrier density in graphene, which typically occurs via surface charge transfer. The direction and amount of the charge transfer are determined by the relative positions of the electron affinity (EA) and ionization potential (IP) with respect to the Fermi level in graphene. If the energy of the electron affinity of a dopant material is larger than the Fermi energy in graphene, an electron transfer occurs towards the dopant resulting in p-doping of graphene. On the other hand, if the ionization potential of the dopant material is lower than the Fermi energy in graphene, an electron transfer occurs towards graphene resulting in n-doping.[179]

Non-covalent dopants include non-aromatic molecules,[139,180,181] aromatic molecules,[182,183] small gas molecules[162,184] in addition to metal ions,[140,185,186] which attach to the surface of graphene causing a redistribution of charges through charge transfer, and hence increasing the charge carrier density. The remaining species on the surface act as charged impurities, which presents scattering centers in the face of moving electrons according to the coulomb scattering mechanism explained in the previous section. However, scattering effects on the mobility are comparatively small as contrasted to the catastrophic loss due to covalent doping and substitutional doping, albeit not negligible, and can be compensated by the large increase in carrier density, thus having an overall enhanced conductivity. This makes non-covalent doping of graphene an optimal route for transparent conductive electrode applications, provided that it does not cause significant losses in the mobility and the optical transmittance.

Doping with metal adatoms

The adsorption of metals on graphene, whether adatoms, clusters or continuous thin films (e.g., metal contacts), have been shown to alter its electronic structure and cause a strong doping effect that influences the electrical transport properties. The deposition of alkali metals such as K,[140] Rb and Cs[187] have been shown to act as n-dopants to graphene due to their low electron affinity, allowing the charge transfer of their valence electron towards graphene. Similarly, the transition metals Ti, Fe and Pt were demonstrated to act as n-dopants[188], whereas, p-doping has been achieved with atomic metals Bi, Sb, and Au.[189] It is therefore expected that the direction of doping and its extent depend on the relative position of the dopant metal's work function with respect to that of graphene. However, assumptions of doping based solely on the work function difference do not match the experimentally observed shifts in the Fermi level. DFT calculations on the interaction of graphene with metal contacts have found that the work function difference can provide accurate predictions of the sign and the amount of doping only when they are well separated that their orbitals don’t overlap. However, as the equilibrium separation distance between the metal atoms and graphene is approached, the interaction between metals and graphene results in a strong interfacial dipole introducing a potential step that influences the sign and amount of the charge transfer.[190] The effects of the interfacial dipole have been demonstrated experimentally in the case of Pt doping, which is expected to induce a strong p-type doping if we consider the work function position (5.9 eV) relative to graphene (4.5 eV). However, it was observed that the sign and amount of doping of graphene by Pt is coverage dependent, leading to a strong n-doping at low coverages and either weak n- or p-doping at high coverage, which was correlated to a dipole related potential step favoring electron transfer towards graphene that scales down with increased separation at high coverage where it tends to cluster into bulk thin films on the surface.[188]

Vacuum deposition of metals on graphene generally deteriorate its charge mobility, mainly due to long range scattering caused by charged impurities[140,188] and due to short range scattering centers resulting from increased disorder.[191] For example, potassium deposition on mechanically exfoliated graphene has resulted in degraded mobility to around 800 cm^2/Vs[140], and transition metals causing more than 50% reduction in the mobility.[188] Thus, doping graphene with metal atoms and clusters, seem to adversely affect its conductivity, making it a less favorable doping route for graphene TCE.

Doping with solution-processed metal compounds

An alternative route to doping graphene with metals, is the use of solution-processed metal compounds, that would reduce spontaneously on the graphene surface via charge transfer and form neutral metal nanoparticles,[185,192,193] thus minimizing the scattering due to charged impurities and effectively doping graphene through charge transfer. The use of $AuCl_3$ has been extensively reported to p-dope graphene,[185,192–196] and effectively reduces the sheet resistance to values as low as 112 Ω/□ with a transmittance of 83%.[192] However, the doped FLG long-term stability in the air was poor and concentration dependent where the sheet resistance showed an increase of 40% for low concentration after 20 days.

Similarly, chlorides of various metal cations such as Ir, Mo, Os, Pd, Rh and transition metals such as Ni, Cu, Co, Ti and In were also shown to p-dope graphene, with an enhancement of sheet resistance generally correlating with the difference between the work function of the bulk metal and graphene.[185,195] However, it was evident in all cases that the formation of metal nanoparticles on the surface of graphene causes significant optical losses in transmittance which can reach up to 15%. The optical losses could be minimized by reducing the dopant concentration, but at the cost of higher sheet resistance.[195] It is possible to n-dope graphene with chlorides of low work function alkali metals such as Na, K, Ca and Mg, as evident through the decrease in the work function. However, the sheet resistance is found to increase in all cases, probably due to the high reactivity of alkali metals which likely perturb the basal plane of graphene.[194] Improved conductivity of n-doped SLG achieved with silver nitrate ($AgNO_3$) has been reported, which reduced to Ag^0 nanoparticle on the surface of graphene leading to a sheet resistance of 173Ω/□ at 94% transmittance. However, this showed poor stability in air, where an increase of 25% in sheet resistance was observed after 1 month.[186]

The main drawbacks of using metal compounds as dopants for graphene are (1) increase of the surface roughness due to the formation of metal clusters of size ranging between 10 – 100 nm on the surface of graphene[186,192], thus acting as a potential source of electrical shorts in devices. (2) Poor long-term stability in the air due to desorption or further reaction with anions (such as Cl^-) on the surface.[185,192,193] Stability under thermal treatments was also shown to deteriorate due aggregation of metal particles and adsorption of chloride anions, where the sheet resistance of doped graphene was shown to increase from 600 Ω/□ to 10 kΩ/□ after annealing to 400 °C.[197] The stability and degree of doping were correlated to anion in the metal compound, where a higher electronegativity anion and bond strength between Au cation and the counter anion would lead to a more effective and stable p-doping of graphene.[193]

Gas-phase, organic and metal-organic molecular doping

The interaction of gas and organic molecular species with graphene has been a successful route for modulating its transport properties and has seen interest in gas sensing applications.[162] This enhances the charge carrier density through charge transfer without affecting the carrier mobility, unlike covalent doping and metal doping.[32] The high doping efficiency of this route allows for even sub-monolayer coverages to enhance the conductivity of graphene without significantly decreasing its optical transmittance.[139],

The sensitivity of the transport properties of graphene to gas adsorption has gained a wide interest for its potential application as gas sensors,[162] in addition to demonstrating a facile route for its doping.[168] Adsorbed gas molecules were demonstrated to effectively change the carrier concentration of graphene, thus capable of controllably doping it through charge transfer - one by one electron - rendering it a very sensitive gas detector.[162] The doping type (n- or p-doping) depends on the relative positions of the energy of HOMO (IP) and LUMO (EA) of the gas molecule with respect to the Fermi level of graphene. As such, NO_2 and H_2O act as p-dopants, whereas, NH_3, CO and ethanol act as n-dopants. Interestingly, the carrier mobility in graphene does not deteriorate by the adsorption of gas molecules. In fact, it increases contrary to what has been observed when doping graphene with other adsorbates.[136,162] The positive effect of gas molecule adsorption has been attributed to a compensation effect, whereby charge impurities from adsorbed gas molecules neutralize the inhomogeneous charge impurities existing between the graphene and its substrate.[136] Unfortunately, doping with small gas molecules is reversible as the molecules desorb by thermal treatment or UV exposure, making this a more volatile and unstable form of doping not suitable for TCE applications. [162,184]

In this respect, larger and less volatile organic molecules have been proposed as potential non-covalent dopants, including F_4-TCNQ[198] and MeO-DMBI.[199] These molecules generally adsorb on graphene via van der Waals forces and π-interactions without any evidence of structural disruption of graphene. Spontaneous charge transfer between the dopant and graphene increases the free carrier concentration and hence the conductivity of graphene and shifts its Fermi level from the Dirac point, allowing its work function to be tuned. Just as with gas molecules, the relative positions of the LUMO or HOMO of the dopant with respect to the Fermi level of graphene determine whether it acts as p- or n-dopant, respectively. More recently, a new class of metal-organic molecules has been introduced to act as n- or p-dopants for organic semiconductors, as well as surface dopants for metals and 2D-materials including SLG.[139] The large molecular weight of such molecules as compared to other popular organic molecular or gas phase dopants, as well as their versatility and solution processability, motivates their use as potentially stable non-covalent dopants for graphene.

F_4-TCNQ has been a popular p-dopant that has been demonstrated on a wide range of organic semiconductors,[200,201] carbon nanotubes[202] and graphene[198,203] due to its low EA of 5.24 eV, resulting in increased conductivity in addition to significant tuning of the electronic properties of the doped material. Its deposition is only possible through vacuum deposition processes, making it unsuitable for facile solution processing and it has exhibited high diffusivity in organic materials, potentially hindering its use as a stable dopant in other systems, such as graphene.[204,205] Recently, molybdenum tris[1,2-bis(trifluoromethyl)ethane-1,2-dithiolene] denoted as $Mo(tfd)_3$, has been reported to be a powerful metal-organic dopant with EA of 5.59 eV extending its applicability as a p-dopant compared to F_4-TCNQ.[206] It is stable against diffusion up to 110 ºC due to its bulkier non-planar structure as well as the increase in its size upon doping with the formation of its anion.[207] However, the use of $Mo(tfd)_3$ is also limited to thermal evaporation due to its poor solubility. This led to the development of more soluble molybdenum dithiolene derivatives based on the structure of $Mo(tfd)_3$ while replacing the trifluoromethyl groups at each dithiolene ligand to increase the degrees of freedom in addition to eliminating the unfavorable fluoroalkyl-hydrocarbon interactions resulting in molecules that exhibit the same EA as $Mo(tfd)_3$ but with far greater solubility (up to 16 times) in toluene. Examples of these derivatives include molybdenum tris(1-(methoxycarbonyl)-2-(trifluoromethyl)-ethane-1,2-dithiolene) denoted as Mo(tfd-$CO_2Me)_3$ having an EA of 5 eV which has been recently demonstrated to successfully p-dope P3HT and PEDOT:PSS,[208] and molybdenum tris(1-(trifluoroacetyl)-2-(trifluoromethyl)ethane-1,2-dithiolene) denoted as Mo(tfd-$COCF_3)_3$ with EA of 5.6 eV, which has been used to successfully p-dope SLG.[209]

The type of functional groups in a doping molecule, their number and configuration are important factors that control molecular doping through charge transfer in graphene,[179,180,210] since these functional groups contribute directly to the energy of the molecular orbitals (LUMO and HOMO) of the dopant and to its shape and spatial configuration on the surface of graphene.

Density functional theory was used to explore the role of the electron-withdrawing functional group –CN in hexaazatriphyenylene-hexacarbonitril (HATCN) and tetracyanoethylene (TCNE) molecules in the context of graphene doping by systematically replacing –CN groups with a hydrogen atom, one-by-one. It was found that decreasing the number of –CN groups reduces the amount of charge transfer and work function shift of the doped graphene.[210] A similar effect was observed with n-dopant ethylene-amine molecules with a varying number of amine groups, as shown in **Figure 2.10**. Increasing the number of amine groups – a widely used electron donor in chemical reactions – in ethylene amine molecules were shown to influence the charge carrier density of graphene, with molecules having a larger number of amine groups showing the strongest effect.[180,181] Another benefit of dopant molecules with larger molecular size is their greater stability in air and under heating conditions.[181] However, increasing the number of functional groups excessively can increase the number of charge impurity scattering centers, thus causing a strong and undesirable decrease of the mobility of graphene, as seen in **Figure 2.10** for PEI.[180] In addition, effective doping of graphene requires that the electron donating functional groups are able to interact with the surface of graphene so as to maximize charge transfer. In fact, it has been shown that using a polymeric form of ethylene-amine (PEI) results in poor doping despite having the largest number of amine groups, due to steric confinement effects in the polymer.

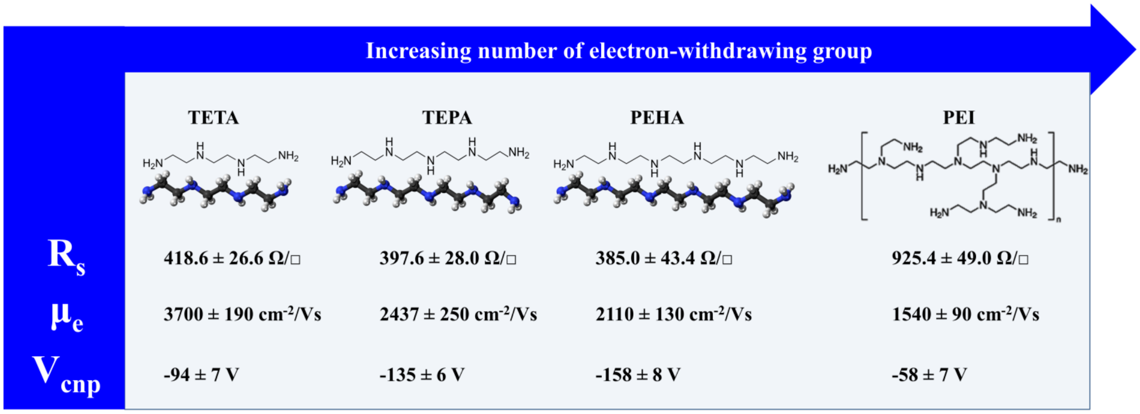

Figure 2.10: Comparison of the properties of graphene doped with ethylene amine molecules with varying number of electron withdrawing groups, with respect to sheet resistance (R_s), electron mobility (μ) and charge neutrality point position (V_{cnp}). Data are taken from ref [180], *where pristine SLG exhibited R_s = 1520.0 ± 67.6 Ω/□, μ = 4060 ± 178 cm^2/Vs and V_{cnp} = 18 ± 5 V.*

Interlayer doping graphene stacks

So far, the doping modalities discussed have been limited to interactions with the surface of a single layer of graphene. As previously discussed in **Section 2.2.6**, there are compelling reasons for stacking graphene sheets in the context of TCE applications, with the most compelling reason being to increase the sheet conductivity by providing additional low-resistance current channels.[35] This can be done without decreasing the optical transmittance too much since it is reduced by 2.3% per layer. In the context of doping of graphene for TCE applications, there are additional compelling reasons for stacking, including the ability to incorporate more dopant molecules and the opportunity to stabilize them further. For example, stacking four layers of CVD graphene by repeating the transfer process can reduce the sheet resistance from 2.1 kΩ/□ (SLG) to 350 Ω/□, while maintaining a transmittance of 90%, which is higher than that of ITO as shown in **Figure 2.11**.[114]

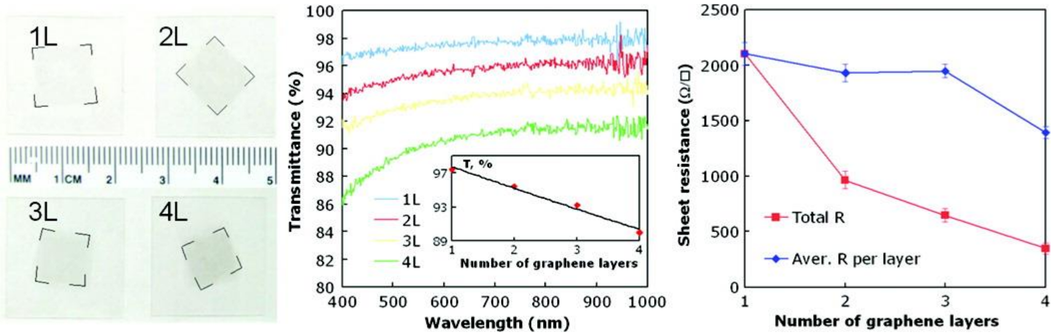

Figure 2.11: Effect of layer stacking of CVD SLG on the sheet resistance and transmittance.[114]

A combination of layer stacking and doping further reduces the sheet resistance of graphene, making it a better performing TCE. Different groups have attempted to produce doped multi-layered graphene film through a repeated sequence of doping SLG - transferring of another SLG on top of the doped layer and then repeating the doping step. This can be repeated until the desired properties are obtained, for example balancing the sheet resistance and the transmittance. This approach has been generally labeled as an interlayer doping and has some similarity with the structure of intercalated graphite compounds shown in **Figure 2.12**.[35,196,211,212] Interlayer doping of eight graphene layers with each p-doped with HNO_3 was compared with a stack of eight layers with doping applied only after the last layer was transferred. The interlayer doped stack showed higher transmittance which was attributed to an additional cleaning step for each graphene layer from residues and contaminants by the acid, however, the reduction in the sheet resistance was not better than without doping (decrease by a factor of 3) in both cases, failing to demonstrate a significant advantage of the interlayer doping approach.[35] The same approach has been used to achieve interlayer p-doping of a stack of 4 layers with $AuCl_3$, leading to a lower sheet resistance and hence a higher FoM of 35 as compared to 30 for only the top-most doped films.[196] In addition to the conductivity enhancement, interlayer doped graphene showed a higher stability in the air due to the encapsulation and protection of the dopants in between the sheets, where the sheet resistance increased by 20% after 3 weeks as compared to 40% for the top most doping. Similarly, the sheet resistance was observed to monotonically decrease by increasing the number of interlayer doped graphene with TCNQ from 850 Ω/□ to 140 Ω/□ for a stack of four graphene layers, consistent with the increase in the carrier density with every TCNQ interlayer.[211] It was, however, pointed out that the use of conventional transfer process with polymer support for every stack can deteriorate the performance of interlayer doped graphene by introducing additional impurities and potentially un-doping the lower layers during the polymer support removal step. The repeated stacking process is indeed quite cumbersome and may inevitably cause defects and contaminants to be introduced in the underlying graphene sheets, leading to many disadvantages which outweigh the mild benefits observed so far.

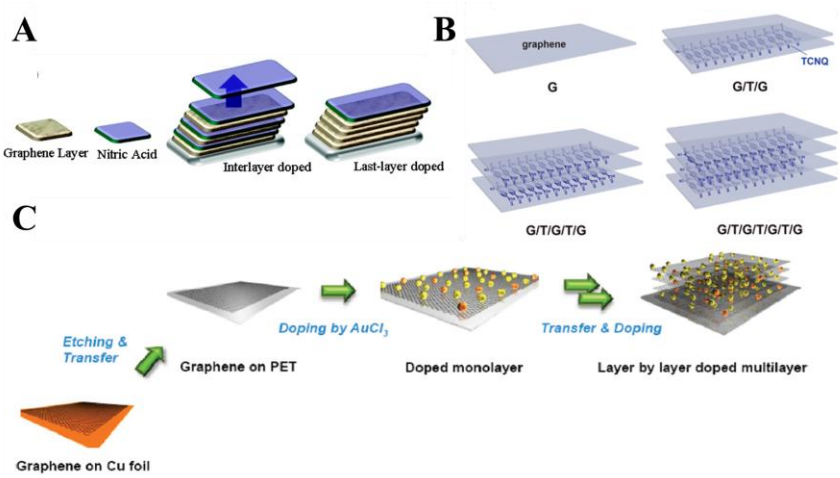

Figure 2.12: Interlayer doped graphene with (A) HNO_3,[35] (B) *TCNQ*[211]*, and (C)*$AuCl_3$.[196]

<u>*Intercalation of dopants*</u>

One way to capture the potential and conceptual advantages of interlayer doping without the drawbacks just mentioned would be to dope via the well-known mechanism of spontaneous intercalation of very small molecules into graphite leading to the formation of graphitic intercalation compounds. Intercalation compounds of graphite have been investigated significantly during the past century revealing more than a hundred chemical species that can be used as intercalates, which are generally classified as donors and acceptors.[213] Intercalation is defined as the insertion of atomic or molecular layers of various chemical species denoted as intercalates into the layers of the host material which is typically highly anisotropic layered materials; with strong in-plane bonding and weak out-of-plane bonding between the layers, such as graphite and transition metal dichalcogenides.[213] The intercalation process initiates around the exposed (outer) basal planes of a graphitic materials and then proceeds to the internal region, provided that intercalant pressure in the reaction chamber is higher than a threshold pressure p_t, which sets up the minimum pressure value required to unpin lattice dislocations and minimize the lattice strain energy required to proceed the intercalation into the interior layers.

GIC has attracted much attention due their relatively higher structural ordering presented by the staging phenomenon which allows long range homogenous intercalation compound to be easily obtained with well-defined stoichiometry, in addition to the diverse sources of the graphite host materials and the appealing applications of GIC as electrodes in batteries, catalyst for a wide range of chemical reactions and light weight electrical conductors.[213–215] For example, alkali metals such as K, Cs, and Li are common donor intercalate, whereas, halogens and their mixtures, metal chlorides and strong acids such as H_2SO_4 and HNO_3 are typically used as acceptor intercalates in graphite.

The significance of intercalation lies in the spontaneous charge transfer process between the intercalant species and large number of layers buried within bulk, which takes place without altering its structure, leading to multiple orders of increase in the magnitude of carrier density which allows a wide variation the physical properties such as the electrical, thermal and magnetic properties.

Extending the well-established lessons from GIC towards doping of optically transparent FLG via intercalation can result in the desired enhancement of their performance as TCE, and results in increased stability. The threshold pressure value is defined by the intercalant material, the temperature under which the intercalation process is done, and the characteristics of the graphitic host materials such as crystallinity, thickness and lateral size. Generally speaking, smaller sample size and thickness reduce the threshold pressure, which means thin sample intercalate more spontaneously than thicker samples which would be expected for FLG. Single crystals exhibit lower threshold pressure as compared to HOPG or less ordered materials such as carbon fibers. Increasing the temperature of graphitic host materials can considerably reduce the threshold pressure of intercalation of a specific system.

An important feature of GIC is the staging phenomena, which is typically defined by the stage index *n* which states the number of graphene layers bound by two intercalate layers in the GIC matrix. The intercalation of FLG with various intercalates have been investigated, using Li,[64] $FeCl_3$[216–219] and Br_2.[220–224] Among the first results on intercalation of FLG is the exposure of mechanically exfoliated stack of graphene (1 – 4 layers) bromine vapor at room temperature,[222] which was motivated by recent achievement of super-metallic conductivity of bromine intercalated HOPG (Br-GIC) where the increase in conductivity was attributed to a parallel integration of weakly coupled p-doped graphene sheets.[225] It is well established that Br-GIC occurs as a stage 2 intercalation compound, meaning that intercalation occurs at every second layer in trilayer or thicker graphene films.[213] Thus for graphene films of 2 layers or less, only physically adsorbed bromine was observed, where intercalation was observed only for films more than 2 layers in thickness.[222] Both mechanisms of adsorption and intercalation were found not to disrupt the basal plane of graphene and led to high p-type doping density as confirmed by DFT studies.[224] Enhancement of the conductivity and increasing the work function for optically opaque multilayered graphene (30 – 60 layers) and thick graphite (10 μm) by bromine vapor exposure was also recently reported, implying a strong thickness dependence of conductivity enhancement as the thick graphite samples exhibited larger improvement than multilayer graphene.[221] Intercalation of mechanically exfoliated FLG with $FeCl_3$ has been demonstrated to yield fully intercalated stage 1 structure, while preserving the sp^2 structure of graphene, using a two-zone vapor transport method.[216,217] DFT calculation indicated a strong charge transfer from FLG, leading to p-doping in addition to the decoupling of the layers due to the increase in the interlayer spacing between the sheets making intercalated ME-FLG similar to SLG, which leads to enhancing electrical transport properties.[217] Due to the smaller size and thickness of FLG, the intercalation process proceeds more easily than $FeCl_3$-GIC as explained earlier, without the need for using chlorine gas, where the latter typically requires a high concentration of Cl_2 gas and takes about 6 days for full intercalation. Thus FLG intercalation with $FeCl_3$ could be beneficial in terms of being environmentally friendly and scalable process for industry.[125,217] Remarkable enhancement in the conductivity of mechanically exfoliated FLG (5 Layers) has been achieved via intercalation with $FeCl_3$, achieving a sheet resistance of 8.8 Ω/□ at an optical transmission of 84%, with a carrier density as high as 8.9×10^{14} cm^2.[125] The same process was also applied to CVD graphene (monolayers and four layers stacked), yielding a sheet resistance of 42 Ω/□ for the 4-layers stack, and 72 Ω/□ for surface doped monolayers. However, these values degraded significantly after exposure to air, probably due the low doping time adopted in this work (1 min) which isn't sufficient to provide full intercalation.[226] A fully intercalated FLG has been demonstrated to have high stability in air up to one year,[125] in addition to unforeseen high temperature (150 ^{o}C in air, and 650 ^{o}C in vacuum) and humidity (up to 100%) stability being reported recently, where the structure and low sheet resistance values were nearly unchanged.[219] Lithium intercalation of mechanically exfoliated ultrathin graphite films has been successfully achieved to produce n-doped graphene, exhibiting a sheet resistance of 3.0 Ω/□ at an optical transmittance of 91% for 19-layers.[64] The striking feature of Li-intercalation is the observed increase in the optical transmittance in the visible range which was attributed to the suppression of the interband optical transition, due to shifting of the Fermi level as a result of the high induced carrier concentration of 6×10^{14} cm^{-2}.

2.4.3 Tuning the work function of graphene by doping

The work function of TCE is an important parameter that determines energy level alignment at interfaces with adjacent components in a device, which in turn determines the energy barrier for charge injection into/out of the optoelectronic devices through the TCE. Thus, the ability to tune the work function of graphene by doping has attracted significant effort towards its universal application as either a cathode or anode in photovoltaics.[57,167,227–229] The work function is defined as the minimum amount of energy required to move an electron from a solid to a point in a vacuum just outside the solid surface, and is generally measured as the energy separation between the Fermi level and the vacuum level of the material.[230] Thus, the work function is determined by two contributions; (1) the chemical potential of the bulk (Fermi level) and (2) the electrostatic contribution across the surface (Vacuum level), hence, the work function is not a bulk property of material, but a function of its surface.[231] For example, a metal exhibits different values of work function depending on the crystalline surface electrons are extracted from due to different surface-dipole on different facets.[230]

A shift in the Fermi level occurs as a result of changing the carrier density of the bulk due either integer or partial charge transfer when interfaced with a dopant molecule. Such a charge transfer would also result in the formation of interfacial surface dipole that leads to a shift in the vacuum level.[139] On the other hand, the vacuum level shift can occur even in the absence of charge transfer by intrinsic molecular dipoles of the interface material, or redistribution of charges at the interface as in the case of adventitious hydrocarbon contaminants on metal surfaces due to the "Push Back effect".[231] Accordingly, the shift in the work function of graphene by molecular dopants has been generally attributed to these two contributions, which typically occurs simultaneously. Charge transfer to/from graphene would decrease/increase the Fermi level energy (n-doping/p-doping, respectively), leaving an electron deficient/rich molecule at the interface which produces an interface dipole that shifts the vacuum level as well. However, these two contributions are rarely quantified clearly in the graphene literature where authors typically attribute the collective shift in the work function to "charge transfer". Few researchers have employed photoelectron spectroscopy (PES) combined with DFT calculations to elucidate both effects. The total shift in the work function in graphene can be calculated using **Equation 2.14**[139]

$$\Delta\Phi = \Delta\Phi_{ET} + \Delta\Phi_{SD} = \hbar\upsilon_F\sqrt{n\pi} + \frac{n}{\varepsilon_0}\int_0^z \frac{q(z)}{\varepsilon_r(z)}dz \qquad \textit{Equation 2.14}$$

Where $\Delta\Phi_{ET}$ and $\Delta\Phi_{SD}$are the shifts in the Fermi level due to the charge transfer *n* and the shift in the vacuum level due to interfacial surface dipole, respectively. q(z) and $\varepsilon_r(z)$ describe the variation in the charge density and effective dielectric constant along the direction normal to the surface, respectively. It can be qualitatively inferred from

Equation 2.14 that the work function shift in doped graphene, would be comprised of a larger contribution due to vacuum level shift as compared to the Fermi level shift contribution, considering their dependence on n and $n^{1/2}$, respectively.

This has been confirmed experimentally through PES for both n-doped and p-doped SLG with $(RhCp^*Cp)_2$ and $Mo(tfd\text{-}COCF_3)_3$, respectively.[139] In the former, the shift in the Fermi level was obtained from the UPS spectra, as the Dirac point was directly deduced from a dip in the spectrum at a binding energy around 0.4 eV higher than the Fermi level (at 0.0 eV), whereas, it was not accessible in the case of p-dopant since it presumably shifts to a lower energy. In this case, the shift of the Fermi level was deduced from the shift of the core levels in XPS. In both cases, the total shift of the work function is obtained from the secondary electron edge of the UPS spectra. The contribution of the shift of the Fermi level $\Delta\emptyset_{ET}$ was reported to dominate at low dopant coverage, however, once the coverage was increased, the contribution of the vacuum level shift due to interfacial dipole dominated the work function shift.[139] However, the coverage dependence of the two contributions is more complex than the qualitative assumption of the carrier's density dependence in **Equation 2.14**, as the orientation of the molecules[232] and/or island growth beyond monolayer coverage[233] can affect the charge transfer characteristics and the resulting interfacial dipole.

The increase in the coverage of the p-dopant "hexaazatiphenylene-hexacarbonitrile" (HATCN) on SLG graphene has resulted in a total increase of the work function by 1.2 eV (from 4.5 eV to 5.7 eV), where the increase was observed to be linear at low coverage and sublinear at higher coverage.[232] This was attributed to the density-dependent reorientation of the HATCN molecules, from flat lying on the graphene surface at low coverage, which causes an abrupt linear increase of the work function by 0.5 eV, to an inclined orientation at 45° at higher coverage, which increases the distance between the negative center of the charged molecules (after charge transfer) and the positively charge center on graphene. This increases the magnitude of the interfacial dipole, which causes an additional 0.7 eV shift in the work function. The sublinear regime at the higher coverage rate was ascribed to the pronounced island growth and the high nominal coverage needed to form a monolayer of vertically inclined molecules.[232]

The relative contribution of the vacuum level shift and the Fermi level shift was recently shown to depend on the underlying substrate supporting graphene.[233] For SLG on quartz, the evaporated electron acceptor 1,3,4,5,7,8-hexafluorotetracyano-naphthoquinodimethane (F6TCNNQ) resulted in a total shift in the work function by 1.0 eV, where a charge transfer from graphene towards the molecules have resulted in a downshift of the Fermi energy level by 0.6 eV, and an interfacial dipole formation which shifts the vacuum level upwards by 0.4 eV. However, in the case of SLG on a copper substrate, the work function was increased to a larger extent at similar coverage of the dopant (1.3 eV), 95% of which was attributed to the vacuum level shifts due to interfacial dipole formation, as confirmed by DFT. The metallic substrate was found to be the main charge donor in the charge transfer process, leading to a stable carrier density in graphene, and thus the Fermi level was mostly invariant.

A commonly used p-dopant is F_4TCNQ, which has been demonstrated to increase the work function of epitaxial FLG graphene by 1.5 eV (from 4.0 eV to 5.3 eV).[198] In addition, solution processed metal-organic molecule Mo(tfd-$COCF_3$)$_3$ has been demonstrated to increase the work function of SLG by 0.7 eV (from 3.9 eV to 4.6 eV) which was attributed to 0.5 eV lowering of the Fermi level energy and 0.2 eV increase of the vacuum level energy.

Decreasing the work function has also been an attractive path to utilizing graphene as anodes in solar cells and potentially in electron emission devices.[166] Chemical doping of graphene with a wide range of n-dopants has been reported to decrease the work function of graphene either by raising the Fermi energy level or lowering the vacuum energy level.[167,199,234–237] In addition, lowering the work function of graphene has been achieved by raising the Fermi energy level through electrostatic doping in gated graphene devices.[137,166] Recently, the combination of these two doping mechanisms has been pursued to maximize the reduction in the work function achieving ultra-low work function of graphene of nearly 1.0 eV.[166]

The electrostatically tuned work function reduction was maximized by using a HfO_2 gate dielectric, which exhibits a higher dielectric constant and higher breakdown electric field than SiO_2, leading to an increase in the Fermi level energy of 0.772 eV, as compared to 0.070 eV in the latter.[137] Then a strong interfacial dipole was induced to the gated graphene through the deposition of Cs/O lowering the vacuum level which in combination with the electric-field raised Fermi level produced SLG with a work function of 1.01 eV.[166] However, the power requirement for gating graphene in addition to the high air sensitivity of Cs would hinder such an approach in applications. A stable chemical doping approach with strong donor molecules has been reported to significantly reduce the work function of graphene. For example, a reduction of 0.7 eV in the work function of graphene (from 4.16 eV to 3.46 eV) has been achieved via spin-coating of 2-(2-Methoxyphenyl)-1,3-dimethyl-2,3-dihydro-1H-benzoimidazole (MeO-DMBI) which has slightly decreased the sheet resistance from 850.6 Ω/□ to 767 Ω/□ of SLG. Solution processed amine-based organic compounds have been demonstrated to reduce the work function by 1.1 eV (from 4.3 eV to 3.2 eV), by spin coating N,N,N′,N′-tetrakis(4-butylphenyl)ethylenediamine (40 mM in Chloroform) on SLG. However, such dopants have generally resulted in an increase in the sheet resistance by few kΩ/□ which would hinder its applicability as TCE.[234] A large reduction in the work function has been also demonstrated using CsF in an aqueous process that could be simultaneously used to transfer and dope graphene in a layer-by-layer scheme, achieving a reduction of 1.25 eV (from 4.5 eV to 3.25 eV) with the added advantage of decreasing the sheet resistance down to 300 Ω/□ from a three layers stacked graphene sheets doped with the CsF.[167]

Typically, n-dopants possess a low IP which makes them highly air-sensitive. Metal-organic molecules based on dimeric sandwich compounds, which are *not* simple one-electron reductants; react with oxidants to form the corresponding monomeric cations that then dope graphene. This coupling of electron-transfer and bond cleavage processes results in materials that are moderately air stable, despite their strongly reducing character which has be demonstrated to reduce the work function by1.30 eV (from 4.10 eV to 2.80 eV), by dipping into solution of pentamethylrhodocene dimer, $(RhCp^*Cp)_2$, which was attributed to 0.7 eV increase in the Fermi energy level, and 0.6 eV reduction of the vacuum level.[139] **Table 2.3** shows a comprehensive list of commonly used n-type and p-type dopants to tune the work function of graphene.

Table 2.3 List of dopants and the respective work function shift in graphene

Dopant	type	ΔΦ (eV)	Reference
N,N,N′,N″,N″-pentamethyldiethylenetriamine - PMDTA (N1)	n-dopants	-0.4 (4.3→3.9)	[234]
N,N,N′,N′-tetraphenylethylenediamine (N2)		-0.5 (4.3→3.8)	
N,N,N′,N′-tetrakis(4-butylphenyl)ethylenediamine (N3)		-1.1 (4.3→3.2)	
N,N,N′,N′-tetrakis(4-benzoylphenyl)ethylenediamine (N4)		-0.7 (4.3→3.6)	
N,N,N′,N′-tetrakis(4-(1-phenyl-2-(4-tolyl)vinyl)phenyl)ethylenediamine (N5)		-0.8 (4.3→3.5)	
1,1' dibenzyl-4,4'-bipyridinium dichloride (BV)		-0.5 (4.5→4)	[235]
CsF		-1.25 (4.5→3.25)	[167]
Cs_2CO_3		-0.8 (4.5→3.7)	
PEIE		-0.3 (4.5→4.2)	
Aminopropyltriethoxysilane (APTES)		-0.31 (4.57→4.26)	[236]
Rhodocene Dimers		-1.29 (4.1→2.81)	[139]
2-(2-Methoxyphenyl)-1,3-dimethyl-2,3-dihydro-1H-benzoimidazole (MeO-DMBI)		-0.7 (4.16→3.46)	[199]
Cs_2CO_3		-0.85 (4.25→3.4)	[237]
Rb_2CO_3		-0.75 (4.25→3.5)	
K_2CO_3		-0.75 (4.25→3.5)	
Li_2CO_3		-0.45 (4.25→3.8)	
PEDOT:PSS	p-dopants	0.6 (4.5→5.1)	[167]
2,3-Dichloro-5,6-dicyanobenzoquinone (DDQ)		0.1 (4.5→4.6)	[235]
Bis(trifluoromethanesulfonyl)amid - (TFSA)		0.7 (4.4→5.1)	[228]
$FeCl_3$ (intercalation)		0.5 (4.6→5.1)	[238]
$AuCl_3$		0.8 (4.2→5.0)	[185]
$MoCl_3$		0.6 (4.2→4.8)	
$OsCl_3$		0.5 (4.2→4.7)	
$IrCl_3$		0.6 (4.2→4.8)	
$PdCl_3$		0.7 (4.2→4.9)	
$RhCl_3$		1.0 (4.2→5.2)	
F4-TCNQ		1.3 (4.0 →5.3)	[198]
F6TCNNQ		1.0 (4.5→5.5)	[233]
HATCN		1.2 (4.5→5.7)	[232]

CHAPTER 3
Methodology

3.1 Design and description of tube furnace assembly

The synthesis of CVD graphene, sample annealing, vacuum drying and doping were performed in a three-zone tube furnace shown in **Figure 3.1**. The furnace can be divided into three main components: (1) Gas supply and control unit, (2) heating unit, and (3) pumping stage and pressure reading utility.

The tube furnace was operated under vacuum conditions (~8.5×10^{-3} mTorr), requiring a tight control of potential leaks at the various joints. This was generally achieved using Swagelok fittings and QF flanges that will be described below.

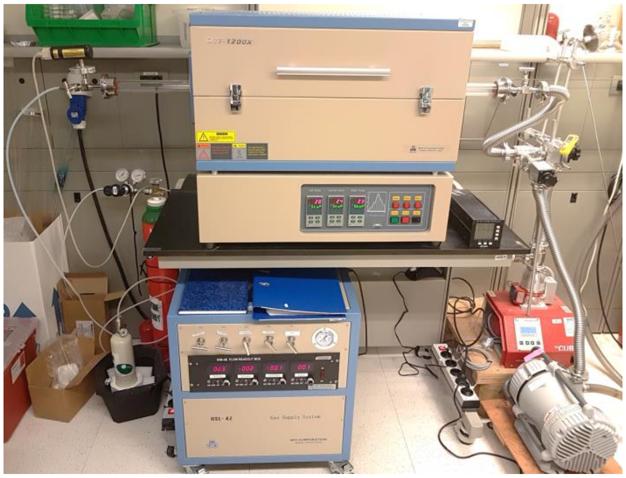

Figure 3.1: Tube furnace system assembly used in this work

3.1.1 Gas supply and control units

Gasses used include methane ‘CH_4’ (99.999%), hydrogen ‘H_2’ (99.9999%), argon ‘Ar’ (99.999%) and nitrogen ‘N_2’ (99.9999%), where the latter was typically used for venting the system prior to loading and unloading samples. The former three gasses were all involved in the graphene synthesis process, while sample annealing was generally done in an atmosphere combining H_2 and Ar. All gasses were supplied through cylinders from a local vendor (Abdullah Hashim Industrial Gases and Equipment co. Ltd), using both 50 liters standard steel cylinders and small standard disposable cylinders.

The cylinders, equipped with gas regulators, were connected to a four channel gas control system (EQ-GSL-4Z) from MTI Corporation US, which allows for precise control of gas mixtures and their flow rates into the heating unit. The gas control system is a heavy duty cart composed of four separate mass flow controllers (MFC), mechanical pressure gauge, gas mixing tank, four channel gas input valves, and a single mixed gas output valve as illustrated **Figure 3.2**. The front panel allows for precise monitoring and control of the gas flow rate and pressure.

MFCs accurately measure and control the amount of gasses flowing into the furnace. Regardless of the amount of gas flowing from the cylinders, and their condition upstream of the furnace in the mixing chamber. The gas volume flow rate at room temperature is expressed in units of standard cubic centimeter per minute (SCCM), calibrated by the manufacturer for N_2, and requires multiplication by a conversion factor when gasses such as Ar, $H_{2,}$ and CH_4 are used, using the equation:

$$\textit{Actual Gas flowing rate} = \textit{flow rate on display } (N_2) \times \textit{conversion coefficient}$$

The conversion coefficients for Ar, $H_{2,}$ and CH_4 are 1.415, 1.010 and 0.719, respectively.[239]

The MFC is equipped with a knob to specify the set value of the flow rate in the process, switch to control the operation mode: OFF – no gas flow, Auto – Sets the flow rate to the set value entered, and Zero Purge – Fully opens the MFC and allows purging of the system.

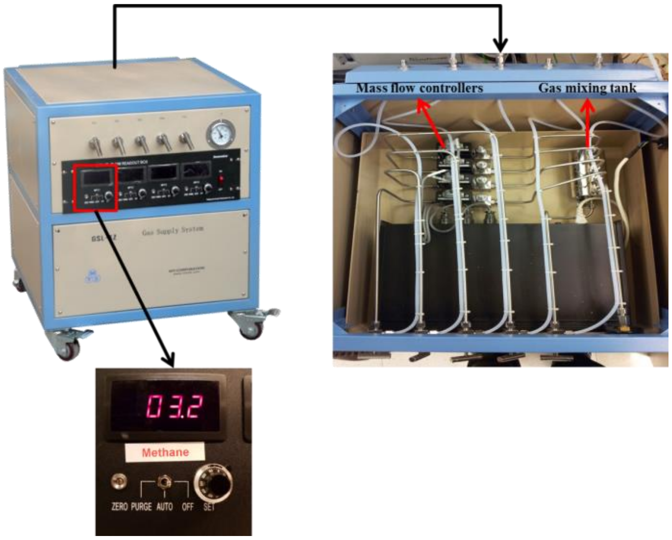

Figure 3.2: Four channel gas control system (EQ-GSL-4Z) with a top view of the internal structure (right) and the control unit for the MFC (bottom)

3.1.2 Heating unit: three-zones tube furnace

For the thermal processing of sample synthesis, annealing, and doping, 610 mm three zones split tube furnace (OTF-1200X-III-S-UL) from MTI corporation US was used (**Figure 3.3**), with a maximum heating temperature of 1200 ^{o}C and a maximum heating rate of 20 ^{o}C/min. The central heating zone of the furnace extends over 304.8 mm offering a constant temperature zone of ±1 ^{o}C accuracy over 260 mm length, and two exterior heating zones of 152.4 mm. Setting all the zones to the same temperature can achieve a ±2 ^{o}C accuracy over 480 mm length as shown in **Figure 3.3B.**

The furnace is contained in a double layer steel case, with two cooling fans to assure low surface temperature. Fe-Cr-Al alloy doped with Mo heating element extends through the furnace which facilitates faster heating and cooling rates, combined with three K-type thermocouples at the center of each zone as shown in the inset of **Figure 3.3A**. Quartz tubes were used for all the processes with 38 mm outer diameter, 35 mm inner diameter, and 1219 mm lengths. Heating only the central zone of the furnace only to 1000 °C leads to thermocouple readings of 400 °C in the first and third zones. The length of the tube was carefully chosen to extend by a sufficient span out of the heating zones to prevent damage to the rubber O-rings used to seal and make upstream and downstream connections to the tube. An alternative approach to protect the O-rings at the edges of the quartz tube is to use alumina foam tube blocks just before the O-rings. However, we chose not to use such a block to avoid potential contamination.

The furnace is equipped with precise temperature controllers based on a proportional-integral-derivative (PID) controller with auto-tune functions. The furnace can be programmed to offer 30 segments of heating and cooling steps with ±1 °C accuracy. Each heating segment is defined by two parameters, the set temperature "C0n" and the duration "T0n" where n identifies the segment order (1 – 30). For example, setting the first segment C01 = 25 °C and T01=°10 mins, and the second segment C02 = 100 °C and T02= 20 mins would increase the temperature of the furnace from 25 to 100 °C in 10 mins. To maintain the temperature of the furnace at 100 °C for 20 mins and then switch of the furnace to cool down, the third segment shall be programmed to have C03 = 100 °C and T03 = -121. The value -121 is a pre-programmed parameter that switches the heating elements off. The various programs used in the course of this dissertation are provided below.

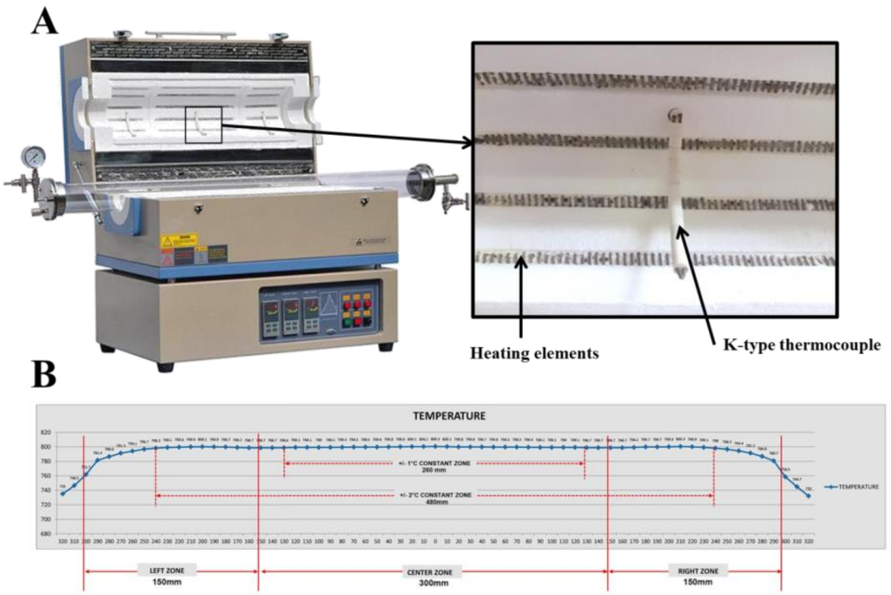

Figure 3.3: (A) Three zones split tube furnace (OTF-1200X-III-S-UL). The inset shows the heating element and the thermocouples. (B) Temperature profile once the temperature is set to 800 ^{o}C in the three zones.

<u>*Production of CVD grown single layer graphene*</u>

The CVD growth process of SLG is mainly divided into three steps, including annealing at 1000 ^{o}C under a flow of Ar and H_2, growth at 1000 ^{o}C under Ar, H_2 and CH_4 environment and cooling down under the same gas flow. All of these steps occur in a single heating zone, namely the central one. In terms of programming the controllers, there are three main heating segments: (1) increasing the temperature to 1000 ^{o}C, (2) maintaining the temperature at 1000 ^{o}C for annealing and growth and (3) cooling down the furnace to room temperature. However, to clearly monitor and distinguish the annealing and growth segments which require different combinations of gasses, we divide the second segment into two constant temperature segments. To maintain the heating rate specified by the manufacturer, we adopted the maximum heating rate of 20 ^{o}C/min to reach the target temperature. The associated temperature profile and various controller parameters are shown in **Figure 3.4**.

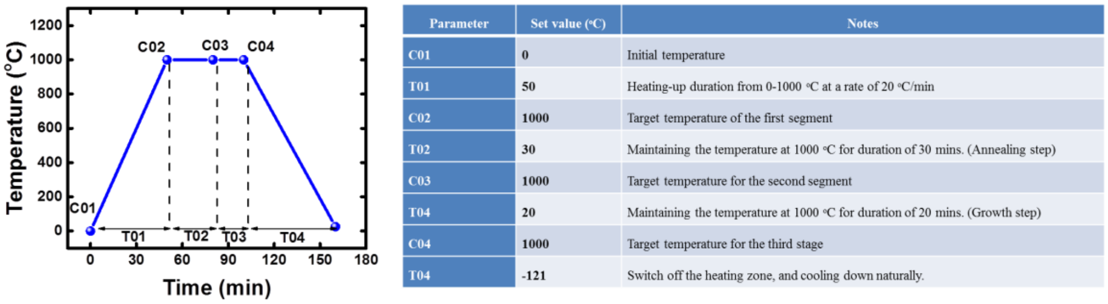

Parameter	Set value (°C)	Notes
C01	0	Initial temperature
T01	50	Heating-up duration from 0-1000 °C at a rate of 20 °C/min
C02	1000	Target temperature of the first segment
T02	30	Maintaining the temperature at 1000 °C for duration of 30 mins. (Annealing step)
C03	1000	Target temperature for the second segment
T04	20	Maintaining the temperature at 1000 °C for duration of 20 mins. (Growth step)
C04	1000	Target temperature for the third stage
T04	-121	Switch off the heating zone, and cooling down naturally.

*Figure 3.4***:** *Temperature profile and controller parameters for production of CVD SLG.*

Sample annealing (transfer process)

Annealing was typically used to clean the surface of transferred SLG/FLG from residual PMMA, a process which has proven to increase the conductivity of the films. Annealing was programmed using three segments: (1) heating up to the desired annealing temperature, (2) maintaining the annealing to the specific duration needed and (3) cooling the furnace naturally. A typical annealing temperature profile used in this work is shown in **Figure 3.5**.

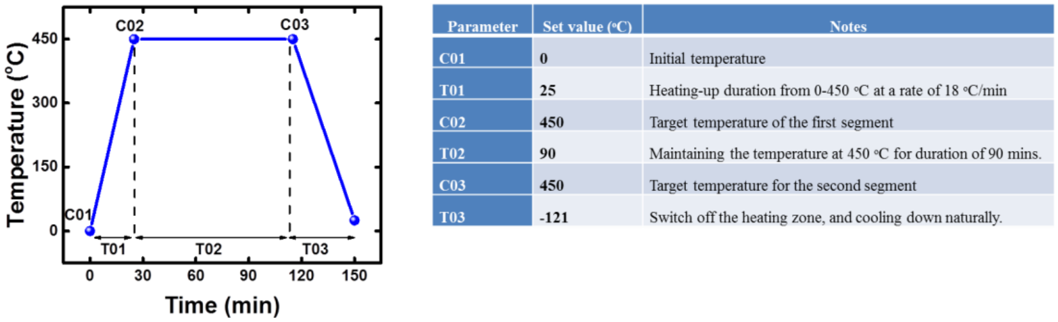

Parameter	Set value (°C)	Notes
C01	0	Initial temperature
T01	25	Heating-up duration from 0-450 °C at a rate of 18 °C/min
C02	450	Target temperature of the first segment
T02	90	Maintaining the temperature at 450 °C for duration of 90 mins.
C03	450	Target temperature for the second segment
T03	-121	Switch off the heating zone, and cooling down naturally.

*Figure 3.5***:** *Temperature profile and controller parameters for sample annealing*

Intercalation experiments requiring a two-zone vapor transport process

A two-zone vapor transport process is a common procedure used in the preparation of GIC, where a temperature gradient is generated between two heating zones, with the intercalate placed in the lower temperature zone and HOPG in the slightly higher temperature zone. For the purpose of intercalating $FeCl_3$ into FLG presented in **chapter 6**, the temperature profile is composed of 3 segments similar to the annealing temperature profile just described, as shown in **Figure 3.6**.

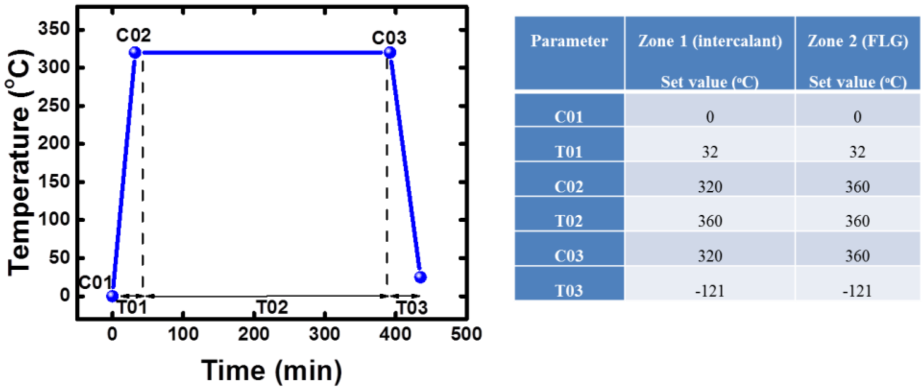

Parameter	Zone 1 (intercalant) Set value (°C)	Zone 2 (FLG) Set value (°C)
C01	0	0
T01	32	32
C02	320	360
T02	360	360
C03	320	360
T03	-121	-121

*Figure 3.6***:** *Temperature profile and controller parameters for two-zone vapor transport doping.*

3.1.3 Pumping station and pressure gauges

Achieving vacuum is essential for removing oxygen, moisture and other potential contaminants that can largely influence the synthesis and annealing processes, especially at high temperatures. We have designed a multi-pumping station, combining in parallel a turbo molecular pumping station (HiCube 80 ECO) from Pfeiffer Vacuum for high vacuum experiments (**Figure 3.7A)** and a dry scroll vacuum pump (XDS 10) from Edwards for low vacuum experiments (**Figure 3.7B)**. The HiCube 80 Eco station is comprised of the turbo molecular pump (HiPace 80), backing diaphragm pump (MVP 015-2), compact full range pressure gauge (PKR 251), electronic drive unit (TC 110) and a display and control unit (DCU 002). The combination of these two pumping modes downstream of the furnace system allows for a better base pressure to be achieved faster. A base pressure of ~8.5×10^{-3} mTorr is achieved in our system. For continuous pumping during various processes which typically involve large gas loading and flow rate into the system and operating pressures up to 10 mTorr, we switched to the scroll dry pump so as not to damage to turbo molecular pump. Using the scroll pump, a base pressure of 2×10^{-2} mTorr can be achieved. The ability to easily switch between pumping modes using gate valves allows for flexibility and reaching a lower base pressure prior to experiments. Two pressure gauges were used to monitor pressure, with a combination Pirani/cold-cathode gauge preinstalled at the turbo molecular pump station (**Figure 3.7C**) downstream of the tube, and a cold cathode gauge (**Figure 3.7D**) installed upstream of the tube furnace.

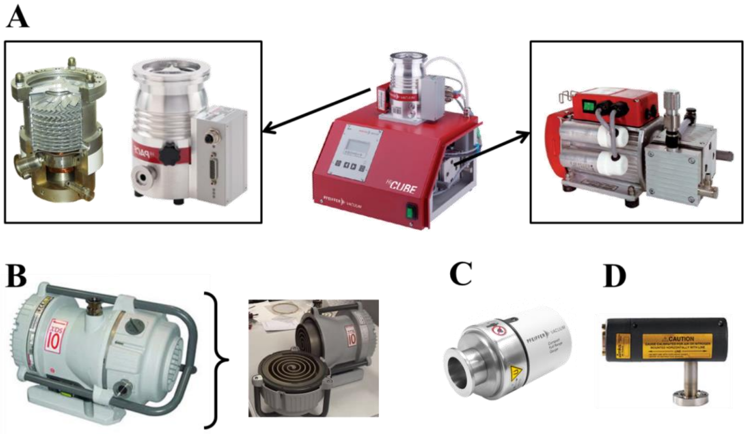

*Figure 3.7***:** *Pumping station and pressure gauges*

3.1.4 Connections and fittings

To assure a tight seal of the furnace and to minimize leakage of contaminants, moisture and oxygen from the ambient in different operating conditions, a careful selection of the fittings and flanges should be made. Connections between gas cylinders, tubes, gas mixer outlets and quartz tube inlet were made using Swagelok standard fittings, the structure of which is shown in **Figure 3.8A**. Their design allows for tight sealing of stainless steel and plastic tubes through pressing the ferrules towards the body. The tube is passed into the nut and both back and front ferrules, which is then seated into the fitting body and then rotating the nut finger tight. A firm tight of one-quarter turn is sufficient to achieve a proper sealed fit. The quartz tube was sealed with O-ring tightening mechanism as shown in **Figure 3.8B**. The open flange is first passed along the quartz tube, followed by two O-rings separated with a pressuring ring and then pressed by the sealing flange by three hexagonal screws. The sealing flange is then connected to the gas mixer by a Swagelok fit. On the pumping side, the quartz tube is connected to a flexible bellow – to facilitate loading and unloading of materials – using QF flanges shown in **Figure 3.8C**. QF flanges are made by two slightly tapered surfaces that are pressed together via a clamp with an O-ring mounted on a centering metallic ring in between.

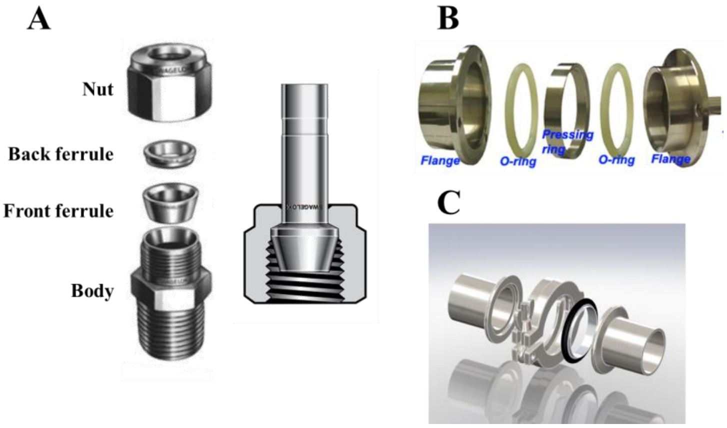

*Figure 3.8***:** *Connections and fitting used for the tube furnace.*

3.2 Synthesis and transfer of CVD graphene

3.2.1 Single-layer graphene (SLG)

Optimization of the growth and transfer processes of graphene is crucial for obtaining high quality and continuous samples with sufficient conductivity for application as TCE. SLG was reproducibly synthesized using a modified CVD process that was developed after a rigorous optimization process as described below (**Figure 3.9**).

Initial attempts to grow graphene in the tube furnace were based on the conventional procedure following the work of Rouff et al.[240] which was described in details in **Section 2.2.5**. As these recipes do not always successfully transfer to other laboratories and equipment, we re-optimized the CVD growth process. The optimization process is described in Appendix A.

The copper foil is cleaned prior to CVD experiments with organic solvents and acetic acid. The latter assists in reducing the copper oxide present on the surface. The cleaned foils were immediately placed inside the tube furnace, which was brought to a base pressure of 2.3×10^{-2} mTorr. Annealing under Ar (30 sccm) and H_2 (30 sccm) step to increase the grain size of the copper foil and further reduce the surface oxides was carried out for 30 minutes before introducing CH_4 (10 sccm) to initiate the graphene growth for 20 minutes. The furnace was switched off and allowed to cool down to room temperature while keeping the same flow rates of the gasses. We found that successful growth of SLG in our furnace required the use of a confining medium around the copper substrate to create a high-pressure region, as described in Appendix A. Without this modification, droplets of copper were found to form on the surface of the foil, causing significant contamination.

3.2.2 Few-layer graphene (FLG)

As commercial sources of graphene and FLG became available mid-way through this PhD, commercial graphene was also acquired for experiments. Commercially available FLG (1×1 cm) from Graphene Laboratories Inc. was used for all FLG-related experiments. FLG was grown via CVD on 300 nm thermally evaporated nickel on

SiO_2/Si substrate. The average number of layers is 4 (ranging between 1 – 7 layers) as specified by the manufacturer. Due to the dissolution-segregation mechanism during graphene growth on nickel, achieving a uniform number of layers is not possible. Thus it forms in the form of sections with different numbers of layers with lateral size in the range of 3 – 10 μm. The sheet stacking for FLG maintained the Bernal AB stacking in small regions, but was mostly rotationally faulted according to the Raman spectra as discussed in details in **Chapters 4 and 5**.

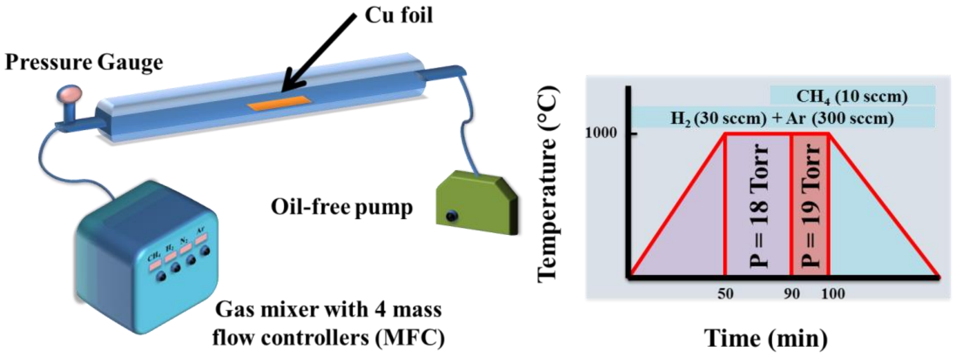

*Figure 3.9***:** *Schematic of CVD graphene growth on copper foil and the optimized growth conditions.*

3.2.3 Transfer of SLG and FLG samples

Transfer of graphene from the support substrate, Cu foil or Ni thin film, is a crucial step in all experiments performed in this thesis. This section describes two transfer methods, namely, PMMA transfer and PDMS stamp transfer, which have been respectively used in **Chapters 4**, **5 and 6**.

PMMA transfer method

SLG and FLG were transferred using a PMMA support layer as reported in literature[114] and shown in **Figure 3.10**. PMMA 950 A6 in anisole from Microchem Inc. was spin-coated on top of graphene at 3500 rpm for 1 min. The PMMA/Graphene/metal stack was then heated on a hotplate at 180 ^{o}C for 1 min to cure PMMA. The next step was to etch the metal film in an aqueous solution of $FeCl_3$, leaving the PMMA/Graphene floating on the surface of the etchant. An important difference in the procedures between SLG and FLG transfer at the etching step is that FLG is dipped in HF acid to etch the SiO_2 first and separate the FLG/Ni from the substrate, which is then washed in DI water and the Ni is subsequently etched using the same procedure described above for copper. The metal etching time ranges from a minute for the thin Ni film supporting FLG to hours for the comparatively thick metal foil supporting SLG. The samples were then scooped from the etchant and placed in a DI water bath for 1 min before being scooped again to another DI water bath for 30 minutes to clean any remaining etchant. Soda-lime glass substrates meant to receive the graphene sample were cleaned by organic solvents and UV-ozone exposure. The glass substrate was used to scoop the PMMA/graphene from the DI water bath. The PMMA/graphene/glass sample was left to dry in air for 6 hours in order to assure conformal adhesion on the substrate. A small amount of PMMA solution, enough to cover the substrate, was dropped on the sample, and was allowed to rest for 3 minutes. This partially dissolves the underlying PMMA layer and releases stress in regions of the sample under stress.[114] The sample was then submerged in acetone overnight at room temperature to remove PMMA resulting in graphene/glass. However, it is difficult to completely get rid of PMMA using solvents alone and the surface of graphene is always contaminated with PMMA residues. Such residues increase the roughness of the surface, the sheet resistance of graphene, and can hinder its ability to be contacted electronically, negatively influencing the device fabrication and performance.

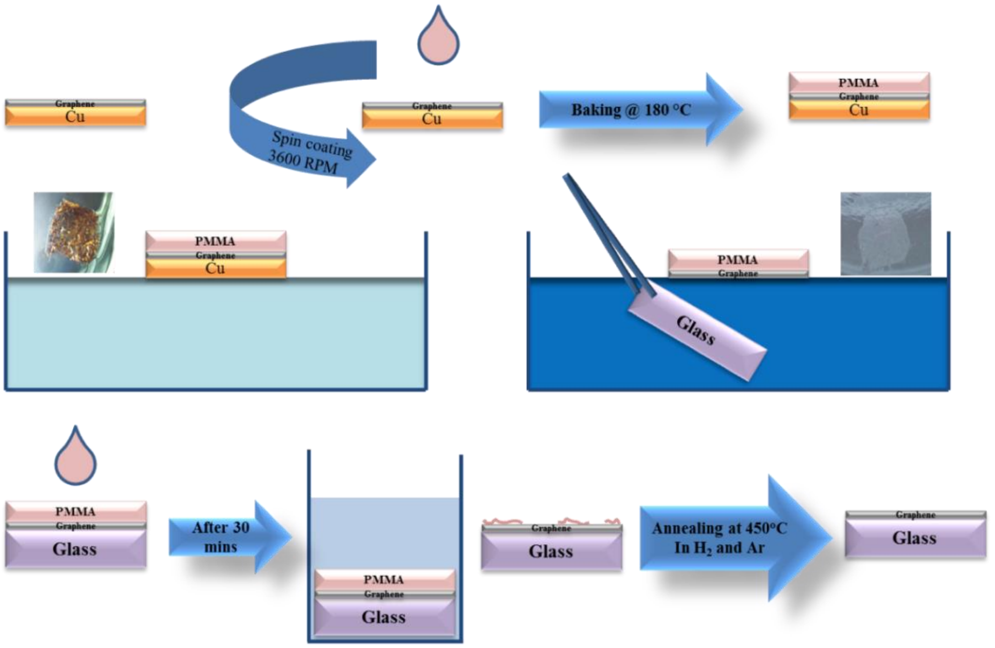

Figure 3.10: PMMA transfer method of graphene from copper foil to target substrate.

A thermal annealing step has therefore been added to the conventional transfer process, whereby the sample is annealed at a temperature of 450 °C under a reducing protective atmosphere of H_2 and Ar in the tube furnace. The process was done at a pressure of 18 Torr for 90 minutes. Surface characterization confirming the suitability of this approach is presented in **Appendix B**.

PDMS transfer process

Some of the disadvantages of the PMMA transfer; including the need for a high-temperature annealing step (see Appendix B) can be addressed by an alternative dry transfer process using a PDMS stamp. PDMS (SYLGRAD 184) from Dow Corning Corporation was used as purchased. The formulation comes in a kit of two liquids; a base prepolymer and a curing agent. PDMS stamps are made by mixing the base with the curing agent at 10:1 weight ratio, followed by vigorous mixing for a two minutes. The mixed solution is then placed in a vacuum desiccator to degas and remove trapped air for around 20 mins. The mixture is gently poured into a petri dish to a height of 3 mm and is placed in a vacuum oven for an hour where it is heated to 70 °C for curing. The cured PDMS can be cut to the desired size and is ready to be used for graphene transfer. The transfer procedure is described in **Section** 2.2.4. A successful transfer of FLG to a glass substrate using PDMS stamp is shown in **Figure 3.11**.

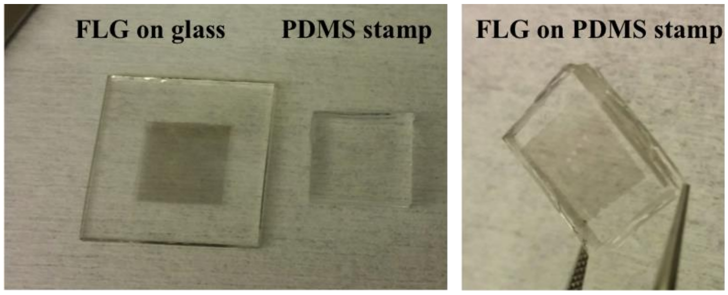

Figure 3.11: Demonstration of PDMS stamping method. PDMS stamp is pressed on top of FLG/Ni/SiO_2, followed by chemical etching of the nickel. The resulting FLG on PDMS can ideally be laminated on any targeted substrate (on glass in this figure)

3.3 Intercalation- and surface-doping of graphene

3.3.1 Experimental environment

The outcomes of doping experiments were observed to be affected by oxygen and moisture contents. For this reason, the environmental conditions were carefully characterized, recorded and controlled, when possible, to ensure a consistent and reproducible outcome of doping experiments. The environmental conditions under which doping experiments were carried out are described in detail in this section and can be used as a reference throughout this thesis.

The term ambient is reserved for conditions where experiments are conducted in the open laboratory environment, at room temperature and at normal atmospheric pressure at sea level. The ambient temperature in our laboratory is defined as ~22 °C and the relative humidity is commonly 50-60%RH.

Environmental control was exercised when needed by performing parts or all of the experimental procedures in enclosure spaces with reduced oxygen and/or moisture content. Enclosures had the benefit of providing protection from toxic chemicals, such as Br_2. Below; we quantify the various enclosed environments used in this thesis. A comparison of the oxygen and moisture content of all enclosures presented is provided in **Figure 3.12**.

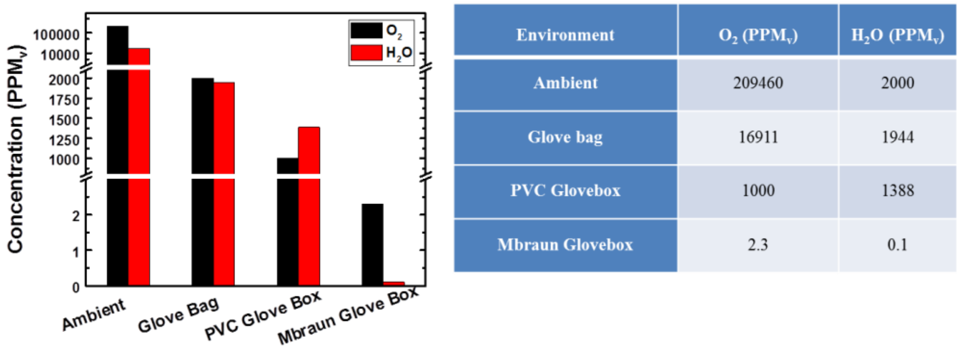

Environment	O_2 (PPM_v)	H_2O (PPM_v)
Ambient	209460	2000
Glove bag	16911	1944
PVC Glovebox	1000	1388
Mbraun Glovebox	2.3	0.1

Figure 3.12: Comparison of oxygen and moisture contents in various enclosures used in this work and contrasted to the ambient conditions.

(A) Glove bag:

Glove bags (Aldrich® AtmosBag) are inflatable polyethylene bags with built-in gloves and zipper-lock closures. These were utilized to provide an environment with moderate oxygen and moisture contents. The bag was connected to in-house vacuum and high purity nitrogen via two separate tubes. An oxygen monitor was connected via a third opening in the glove bag, while a portable moisture monitor (EL-USB-2-LCD) from Lascar electronics was placed inside the glove bag. The oxygen and moisture contents were reduced by repeatedly cycling nitrogen filling and evacuation.

The oxygen and moisture contents are shown in **Figure 3.13**. Representative conditions used in this study in terms of oxygen (2000 ppm$_v$) and moisture (2000 ppm$_v$) contents were obtained after three cycles. The bag was refilled with nitrogen prior to performing the experiment.

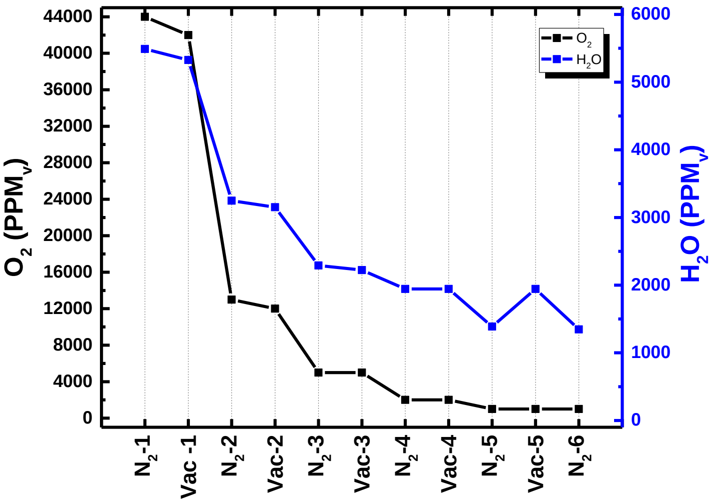

Figure 3.13: Oxygen and moisture content in the nitrogen filled glove bag after various cycles of gas filling and evacuation.

<u>*(B) PVC glove box:*</u>

An isolated non-dissipative transparent PVC glove box from Cleatech Inc. was utilized for a higher level of control over oxygen and moisture contents and especially when using corrosive gasses and vapors. It is equipped with a small antechamber with separate nitrogen and exhaust inlets that served to take tools in and out of the main chamber without disturbing the main chambers environment. Before opening the antechamber to the main chamber, a continuous flow of nitrogen for 10 minutes to minimize oxygen and moisture was followed as the standard procedure. The PVC glove box was mainly used for the bromination experiments and was supplied with a continuous flow of nitrogen at ~

350 Torr and ~ 2000 SCCM. This further reduced the oxygen content to <1000 ppm_v and moisture content to ~1400 ppm_v.

(C) Stainless steel glove box:

The most stringent control of oxygen and moisture is achieved via a closed loop gas circulation in which the gas flows from a stainless steel glove box into the gas purification system composed of a HEPA (class H13) dust filter capable of filtering 99.995% of particles down to 0.2 microns, a reactive agent to remove oxygen and an adsorbent to remove moisture from nitrogen. Such a configuration can achieve <0.1 ppm_v of oxygen and moisture. The glove box in question is built up from a stainless steel interior, polycarbonate windows, and butyl gloves. The system is equipped with antechambers which are evacuated and filled for at least three cycles prior to being opened to the main chamber.

3.3.2 Doping with Bromine

In **Chapter 4** we discuss the intercalation doping of FLG using bromine. Graphene (SLG, layer-by-layer and FLG) samples transferred to glass were exposed to bromine vapor or liquid at room temperature either inside a glove bag filled with nitrogen and placed in a fume hood, in a PVC or a stainless steel glove box, as described above. Bromine (ACS REAGENT, ≥99.5%) from Sigma-Aldrich was used as purchased. For vapor-based bromination, samples were suspended in a sealed container holding liquid bromine at room temperature in either glove bag or glove box as shown in **Figure 3.14**. The bromine reaches its room temperature equilibrium vapor pressure of 270 mbar inside the sealed container.[241] Bromine uptake was controlled by the exposure time inside the sealed container. For liquid-based bromination experiments, we cast a droplet of bromine on the sample inside a fume hood and allowed it to dry in the natural flow of air therein.

All samples were washed with ethanol to remove excess and possibly weakly adsorbed bromine from the surface and grain boundaries prior to further handling and analysis. The washing step was found to be critical for achieving stability in air of electronic and transport properties in brominated FLG samples.

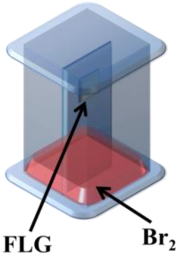

*Figure 3.14**:** Schematic of vapor exposure doping of FLG with bromine.*

3.3.3 Doping with Ferric Chloride

In **Chapter 6** and **Appendix C,** we discuss the intercalation doping of FLG using $FeCl_3$. Doping of FLG with $FeCl_3$ was carried out using the vapor transport method using the tube furnace described in **Appendix C** in a two-zone configuration. Anhydrous $FeCl_3$ (800 mg) was placed in a glass crucible at a distance of ~27 cm from the FLG sample inside an open-ended glass tube (having a diameter of 2 cm) which was inserted into the tube furnace, placing the $FeCl_3$ (upstream) and FLG (downstream) in different heating zones, as illustrated in **Figure 3.15**. The furnace was pumped down overnight to degas and reached a base pressure of 4.2×10^{-3} Torr. The tube furnace was subsequently sealed on both ends and the $FeCl_3$ powder side was heated to 320 °C while the FLG sample side was heated to a higher temperature of 360 °C. The tube was maintained at those temperatures for 6 hours, the time needed to reach a pressure of ~ 4.2 Torr, which was found to be sufficient to intercalate $FeCl_3$ between graphene sheets. The tube was vented by flowing N_2 gas, and the sample was taken out to rapidly cool down to room temperature in air. The doped FLG sample was washed with DI water (considering the hygroscopic nature of $FeCl_3$) to remove any weakly bound species on the surface, a step which was found to improve the air-stability of the electronic and transport properties of doped FLG. The optimization of $FeCl_3$ doping of FLG and characterization are discussed in more details in Appendix C.

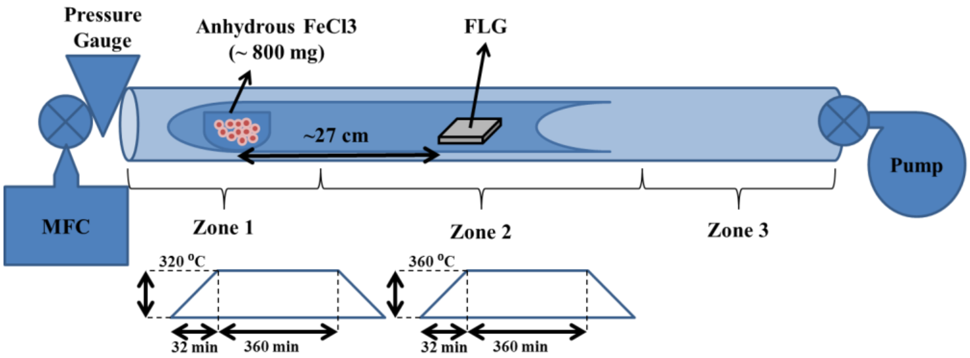

*Figure 3.15**:** Schematic of two-zone vapor transport of $FeCl_3$ intercalation into FLG.*

3.3.4 Doping with solution processed organic and metal-organic molecules

In **Chapter** 5, we discuss the surface doping using existing and novel organic and metal-organic molecules supplied by Prof. Seth Marder at the Georgia Institute of Technology. The soluble molecules are presented and illustrated in **Table 3.1**. For surface doping, solutions of 0.1 mg/mL of any of the dopants listed in Table 3.1 were prepared inside the stainless steel glove box. Toluene was used as the solvent for all dopants, except for Magic Blue, which is soluble in dichloromethane (DCM). FLG samples transferred to glass were dipped in dopant solutions inside the glove box as shown in **Figure 3.16**, either as is or after intercalation doping as described in the prior sections and in **Chapter 6**. The dopant uptake was controlled by the dipping time, which typically varied from 10 min to 180 min. All samples were subsequently rinsed with toluene (DCM in the case of Magic Blue) to remove any loosely bound molecules from the surface of graphene.

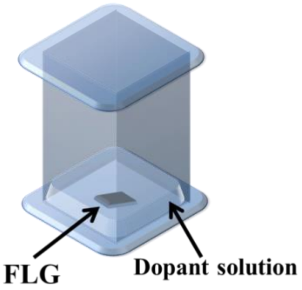

*Figure 3.16**:** Schematic of the FLG dipping into the dopant solution.*

*Table 3.1**:** Metal-organic and organic molecules used for surface doping of FLG in Chapter 5.*

Molecule name	Chemical Structure
ruthenium (pentamethylcyclopentadienyl)(mesitylene) dimer **(RuCp*mes)$_2$**	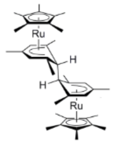
pentamethylrhodocene dimer **(RhCp*Cp)$_2$**	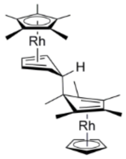
Molybdenum tris(1-phenyl-2-benzoyl-1,2-dithiolene) **Mo(PhBz-dt)3**	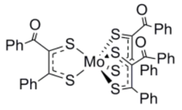
Molybdenum tris(1-(methoxycarbonyl)-2-(trifluoromethyl)ethane-1,2-dithiolene) **Mo(tfd-CO$_2$Me)$_3$**	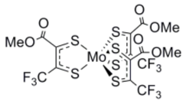
Molybdenum tris(1-(trifluoroacetyl)-2-(trifluoromethyl)ethane-1,2-dithiolene) **Mo(tfd-COCF$_3$)$_3$**	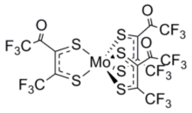
tris(4-bromophenyl)ammoniumyl hexachloroantimonate **Magic Blue**	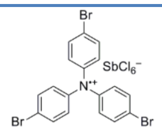

3.4 Characterization of pristine and doped graphene

In this section, the various characterization methods used to examine electrical transport, optical transmittance, surface morphology, chemical composition and the electronic structure of both pristine and doped graphene are described. An illustration of data analysis will also be provided along with the working principles of each tool and specific instrument description.

3.4.1 Optoelectronic characterization

As discussed in **Section 2.1.3**, the key properties defining the performance of graphene as TCE are the sheet resistance and optical transmittance, which are combined in **Equation 2.5** to calculate the FoM of TCE. The sheet resistance (R_s) in this work was measured via either a linear four-point probe or the Van der Pauw method. Furthermore, carrier density and mobility were obtained using Hall effect measurements, which are essential quantities to measure the extent of doping and better understand the changes in conductivity. Optical transmittance of graphene on glass was characterized using UV-Vis-IR spectrophotometry.

Linear four-point probe

Ohm's law defines the resistance (R) of a sample as the ratio of the voltage drop to the current flowing along the sample; however, such a quantity depends on the dimensions of the sample, thus is an extrinsic metric that doesn't define a material property. A material intrinsic property deduced from R is its resistivity (ρ) which excludes the sample length and cross-sectional area and hence is more suitable for comparisons and materials selection for specific applications. The resistivity is calculated by multiplying the resistance by the ratio of the cross-sectional area to the sample length, and thus has the units of Ω.m. For thin film samples typically used as TCEs, there is a general consensus of using the sheet resistance (R_s) as the metric to define their performance. The sheet resistance is defined simply by dividing ρ by the thickness of the film, where the sample is thought of being composed of squares having a unit area, and thus R_s is defined as the resistance of one square and thus has the units of Ω/□ as a convention despite the fact that it is actually equivalent to Ω.

The use of the four-point probe in contrast to the first generation measurements via two probes has the advantage of minimizing the effect of extrinsic sources of resistance in the measurement instrumentation which can lead to overestimating the measured resistivity of materials as elaborated in **Figure 3.17**. As the current passes through the film to be measured, it is impeded by the resistance of the film (R_f), the contact resistance (R_c) and the parasitic resistance from the instrument (R_p). For accurate determination of the resistance of the film, only the voltage drop due to the current passing through the film should be measured. In the two probes configuration, both the voltage and the current are measured using the same probe as shown in **Figure 3.17A**, and thus, contributions due to the contact between the probes and the film and the parasitic resistance from the circuit of the instrument would be significantly overestimating the measured resistance. This can be overcome through the use of the four probes configuration shown in **Figure 3.17B**, where the current is measured via the two exterior probes, and the voltage drop is measured through the interior probes using a high impedance voltmeter (typically on the order 10^{12} Ω or higher). Hence, the current passing through the voltmeter circuit (i) is significantly smaller than the input current (I), leading to negligible effect of R_c and R_p, as indicated by the circuit and equations in **Figure 3.17B**.

A Linear four-point probe typically consists of four equally spaced (s) co-linear probes, where the resistivity ρ is derived to equal;[242]

$$\rho = 2\pi s F \frac{V}{I} \qquad \textit{Equation 3.1}$$

Here F is a correction factor that accounts for samples edges, thickness and size.

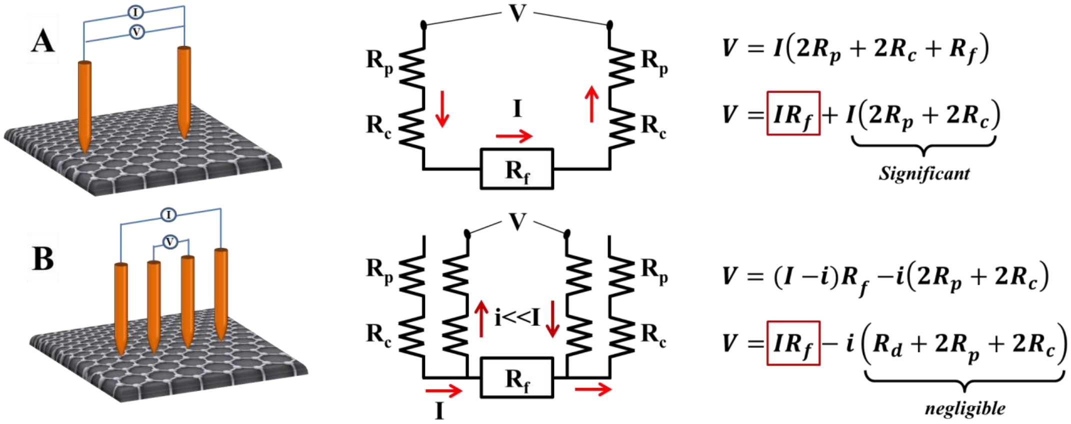

Figure 3.17: Schematics of (A) two-point probe and (B) linear four-point probe configurations for sheet resistance measurement, and the equivalent circuits and equations for the voltage drop.

For measurements away from the sample edges and for sample thickness $t < s/2$, which is valid in the case of graphene samples in this work which are significantly larger than the area of the probe, **Equation 3.1** is corrected to become;

$$\rho = 4.532 t \frac{V}{I} \qquad \textit{Equation 3.2}$$

And the sheet resistance is calculated using;

$$R_s = 4.532 \frac{V}{I} \qquad \textit{Equation 3.3}$$

Linear four-points probe measurements in this work were conducted using a hand-held cylindrical probe head, comprised of tungsten carbide co-linear probes that are equally separated with 1 mm spacing, with a tip radius of 500 μm from Jandel Engineering Limited. Sheet resistance measurements presented in this work were averaged over nine different points on the (1 cm × 1 cm) samples.

Hall effect measurement

A material carrying an electrical current along the direction of an applied electric field will develop a voltage in the transverse direction if placed in a magnetic field acting perpendicular to the applied electric field. This effect was discovered by Edwin Hall in 1879,[243] and was known since then as the Hall effect, and the generated transverse potential is known as the Hall voltage.

The Hall effect is a direct result of the Lorentz force, which is the force applied on a point charge due to its presence in an electromagnetic field and hence consists of both electric and magnetic force components. An electron moving in an electric field with the presence of a perpendicular magnetic field as shown in **Figure 3.18**, will experience a Lorentz force defined as;

$$\boldsymbol{F} = -e(\boldsymbol{E} + \boldsymbol{v} \times \boldsymbol{B}) \qquad \textit{Equation 3.4}$$

Here e is the elementary charge (1.602×10^{-19} C), E is the electric field, v is the particle velocity and B is the magnetic field. The direction of the magnetic force component "$-e(\boldsymbol{v} \times \boldsymbol{B})$", determined using the "right hand rule" (the index finger pointed along the direction of the carrier's drift velocity, and then is curled towards the direction of the magnetic field. The direction of the force acting on electrons would be the opposite of the direction of the thumb). It will be perpendicular to the direction of the electric field in the plane of the sample, which drives the electrons to curve towards the transvers direction of its original path, an hence accumulate on one side of the sample resulting in a potential drop across this direction which is the Hall voltage defined by the **Equation 3.5**,

$$V_H = \frac{IB}{end} \qquad \textit{Equation 3.5}$$

Here I is the current along the electric field, B is the magnetic field, e is the electron charge (1.602 ×10^{-19} C), n is the carriers density and d is the samples thickness. In case of two-dimensional samples, or where the thickness is unknown, the carrier's density term can be replaced with the sheet carrier density " $n_s = nd$".

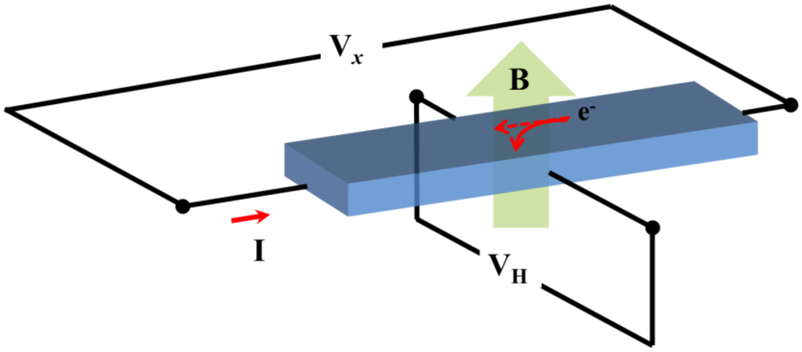

*Figure 3.18**:** Illustration of the Hall effect. Electrons driven by the electric field along the sample, will drift towards the transverse direction when a perpendicular magnetic field is applied, generating the Hall voltage.*

According to the discussion above, the Hall effect experiment allows for direct measurement of the Hall voltage from which the sheet carrier density can be calculated by using **Equation 3.5**. In a typical Hall effect measurement using the Van der Pauw setup, the sample is contacted as shown in **Figure 3.19**, where the contacts are numbered counter clockwise.

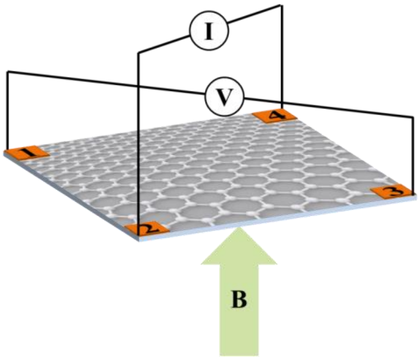

Figure 3.19: *Schematic of Hall effect measurement setup and contacts configuration.*

Eight data points for the Hall voltage are measured where the current is supplied along one diagonal of the sample and the voltage is measured along the other diagonal for each magnetic field direction. **Table 3.2** shows the set of measured data points.

Table 3.2: Data points measured to determine the Hall voltage in Hall effect measurement.

Measurement	Magnetic Field	Current	Voltage
A (-A)	Positive	$I_{31}(I_{13})$	$V_{42p}(V_{24p})$
B (-B)		$I_{42}(I_{24})$	$V_{13p}(V_{31p})$
C (-C)	Negative	$I_{31}(I_{13})$	$V_{42n}(V_{24n})$
D (-D)		$I_{42}(I_{24})$	$V_{13n}(V_{31n})$

The polarity reversal allows a direct determination of whether the sample is n- or p-type. For each pair of contacts, the difference in the voltage along the specific pair for positive and negative magnetic field is calculated, and then averaged to deduce the Hall voltage in accordance with **Equation 3.6**.

$$V_H = \frac{V_{13p} - V_{13n} + V_{31p} - V_{31n} + V_{24p} - V_{24n} + V_{42p} - V_{42n}}{8} \qquad \textit{Equation 3.6}$$

The sign of V_H will be negative if the major carriers are electrons (n-type) or positive if the major carriers are holes (p-type).

To determine the Hall mobility, measurement of the sheet resistance is required, which is related to the mobility by **Equation 3.7**;

$$\mu = \frac{V_H}{R_S I B} = \frac{1}{e n_s R_s} \qquad \textit{Equation 3.7}$$

A powerful technique that can be performed in parallel to the Hall effect measurement is the Van der Pauw technique, which allows the measurement of the sheet resistance of a uniform sample of arbitrary shape. Van der Pauw resistivity measurement requires four terminal leads to be placed on the sample and form Ohmic contacts. The contacts should be as close as possible to boundaries of the samples and their sizes should be as small as possible since measurement errors scale with the ratio of contact diameter to their separation.

Two characteristic resistances are determined during the measurement, namely R_A and $R_{B,}$ from which the sheet resistance of the sample can be calculated by solving **Equation 3.8** numerically;

$$e^{-\pi R_A/R_s} + e^{-\pi R_B/R_s} = 1 \qquad \textit{Equation 3.8}$$

Referring to **Figure 3.20** in which we consider square samples typically used in this work, eight measurements are performed by applying the current between a pair of the leads and then measuring the voltage across the opposite pair, followed by polarity reversal for each set of measurements. For example, the current I_{14} is injected from lead “1” and collected and lead “4” and then the voltage V_{23} is measured between lead “2” and “3” ($V_2 – V_3$), the resulting resistance from applying Ohm’s law is $R_{(14,23)}$.

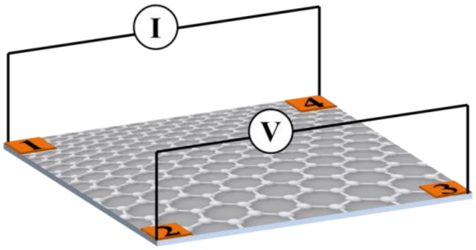

Figure 3.20: Schematic of Van der Pauw measurement setup and contacts configuration.

Theoretically, only two measurements are sufficient to calculate the resistance of the sample, in which the currents are applied along the vertical and horizontal edges. However, application of the reciprocity theorem which states that $R_{(ba,cd)} = R_{(cd,ba)}$ in addition to the polarity reversal in each case where $R_{(ba,cd)} = R_{(ab,dc)}$ allows for averaging each measurement over four points leading to the characteristic resistances R_A and R_B. Such averaging enhances the accuracy of the calculated resistance and cancels out potential sources of error, in addition to acting as a consistency check for the measurement setup. **Table 3.3** shows the eight measurements in a typical van der Pauw measurement.

Table 3.3: Data points measured to determine the characteristic resistances in Van der Pauw measurements.

Measurement	Current	Voltage	Resistance
A (-A)	$I_{21}(I_{12})$	$V_{34}(V_{43})$	$R_{[21,34]}$ $(R_{[12,43]})$
B (-B)	$I_{32}(I_{23})$	$V_{41}(V_{14})$	$R_{[32,41]}$ $(R_{[23,14]})$
C (-C)	$I_{43}(I_{34})$	$V_{12}(V_{21})$	$R_{[43,12]}$ $(R_{[34,21]})$
D (-D)	$I_{14}(I_{41})$	$V_{23}(V_{32})$	$R_{[14,23]}$ $(R_{[41,32]})$

The characteristic resistances are calculated using the following equations;

$$R_A = \frac{R_{[21,34]}+R_{[12,43]}+R_{[43,12]}+R_{[34,21]}}{4} \qquad \textit{Equation 3.9}$$

$$R_B = \frac{R_{[32,41]}+R_{[23,14]}+R_{[14,23]}+R_{[41,32]}}{4} \qquad \textit{Equation 3.10}$$

These equations are then substituted into **Equation 3.8** to determine the sheet resistance. Now that the carrier density and the sheet resistance are measured directly, the Hall mobility of the majority carriers can be determined using **Equation 3.7**.

A commercial Lakeshore 7700 system was used to conduct room temperature Hall effect measurements on graphene using the Van der Pauw configuration. Measurements were conducted by applying a reversible sweep of magnetic fields up to 20 kG using 1 mA excitation current. Contacts were fabricated using conductive silver paste to fix low strain Ag alloy wires (Lake Shore PN 671-260) which were soldered to the sample holder.

Optical transmittance measurement

The optical transmittance of graphene and doped graphene on glass were characterized using Cary 5000 UV-Vis-NIR spectrophotometer from Agilent Technologies, having a measurement range from 175 nm to 3300 nm. Transmittance measurements are based on passing a light of specific wavelength through the sample, and measuring how much of that light is absorbed.

The sample holder allows for the simultaneous measurement of a reference sample and the sample to be measured, so that the optical spectra from the reference sample are subtracted and thus the obtained spectra are representative for the coating supported on the reference sample. We have used a bare glass sample – the same one used to support graphene in this work – as a reference sample, so that the transmittance of graphene (excluding all absorption due to the substrate) is directly measured.

3.4.2 Morphological, structural and chemical characterization

Morphology characterization

Scanning electron microscopy (SEM), atomic force microscopy (AFM) and Scanning Tunneling Microscopy (STM) were used to study the morphology of pristine and doped graphene.

SEM relies on the interaction with high energy electron beam (1 – 40 kV) with the sample in UHV conditions. Once the electron beam hits the sample, it scatters either elastically generating backscattered electrons (BSE) having energy ranging from 50 eV up to the incident beam energy with large scattering angles, or inelastically generating secondary electrons (SE) having energy less than 50 eV with a small angle to the sample in a deflected trajectory. SEM images in this work were collected in SE mode, the signal of which is generated from a depth in the range of 5 to 50 nm, and is responsible for the topographic contrast in SEM images. Protrusions and edges not facing the detector would result in a lower number of SE and thus appear as darker regions in the image.

SEM images presented in this work were obtained using Quanta 200 FEG system from FEI, in SE collection mode, using 10 kV electron beam. Samples were prepared using a special holder with top contacting clips.

AFM is capable of directly probing the topography of samples by scanning the surface with a sharp tip, which detects near-field forces that are sensitive to the sample height. AFM can be operated in a static contact mode or dynamic tapping mode. In the static mode a cantilever holding the tip at its end is in direct contact with the sample, and thus is deflected depending on the height profile of the sample. On the other hand, the tapping mode oscillates above the sample without direct contact, where the oscillation frequency and its amplitude change based on interactions with the sample. Generally the tapping mode is preferred as it prevents damage to the sample and can provide contrasts other than the topographic contrast such as phase contrast.

AFM images in this work were collected using 5400 SPM from Agilent in tapping mode. Silicon tips (PPP-XYNCSTR-50) from Nanosensor having a resonance frequency of 76-263 kHz were used.

STM imaging was performed in ultrahigh vacuum conditions (5.0×10^{-10} mbar) in a variable temperature STM (VT-STM; Omicron Nanotechnology). Graphene samples were kept at room temperature during measurements. A chemically etched polycrystalline tungsten STM tip was used for imaging, which was further cleaned by electron bombardment in situ in UHV to reach atomically resolved imaging of HOPG. FLG samples on sputtered Ni on SiO_2/Si were mounted on a sample plate for STM studies. Sample bias of V_b and tunneling current of I_t will be specified in the caption of each image.

Raman Spectroscopy

Raman spectroscopy provides a facile method to identify the various types of carbon allotropes, and provide rich information on their structure, morphology, strain and doping. It has been favorable due to the non-destructive nature and speed of this method. Raman spectroscopy relies on the interaction of a monochromatic light with the material, leading to various transitions from the ground energy state including vibrational and electronic transitions, typically to virtual excited states. These transitions are then relaxed through emitting light in three possible ways as shown in **Figure 3.21**, (1) Rayleigh (elastic) scattering in which the emitted light has the same frequency as the incident light (ω_{inc}), (2) inelastic Stokes scattering where the frequency of the light is shifted to a lower value ($\omega_{inc} - \omega$), and (3) inelastic anti-Stokes scattering shifting the frequency of the light to higher values ($\omega_{inc} + \omega$). The shifts due to the inelastic scattering (both Stokes and anti-Stokes) are characteristic of the symmetry in the material and are the main scattering mechanism upon which Raman spectroscopy relies, to fingerprint materials.

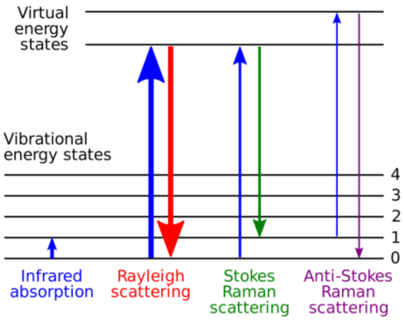

Figure 3.21: Light scattering mechanisms in Raman spectroscopy.

The Stokes Raman shifts are more intense than the anti-Stokes shifts, since in the latter only the pre-excited molecules contribute to the total intensity. However, the majority of molecules would be initially at the ground state. Accordingly, Stokes scattering is typically observed and reported in Raman spectroscopy. A Raman spectrum is presented by the intensity of the inelastically scattered light on the y-axis as a function of the frequency shift (typically labeled as Raman shift) in the units of wavenumber (cm^{-1}). A Raman process is considered first-order if it originates from a single scattering event, whereas it is labeled as a second-order peak if it involves two scattering events. Furthermore, if the laser energy was selected so that the electronic transitions correspond to a stationary state (rather than virtual), the process is generally known as resonant

Raman process which greatly enhances the intensity of the peaks due to electron-phonon coupling. The unique electronic structure of graphene characterized by the linear dispersion relation of the π-electrons with the absence of a band gap, leads to Raman scattering processes in graphene that are always resonant, making it useful to study the electronic structure as well as the lattice vibrations.[244]

The interpretation of Raman spectra of graphene is better understood in conjunction with its phonon dispersion relation. The unit cell of a monolayer graphene is comprised of two atoms, leading to six phonon branches – three of which are acoustic and the other three are optical) – as indicated in **Figure 3.22**.

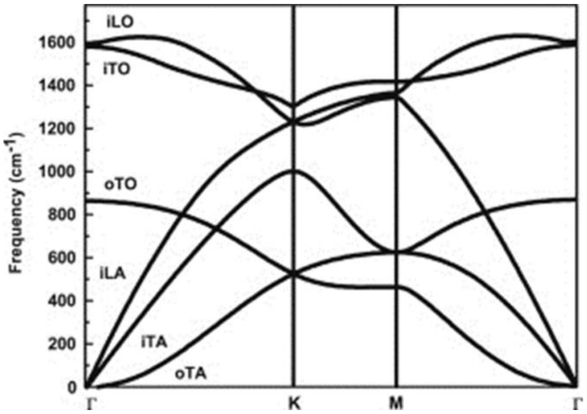

In-plane longitudinal optical phonon	iLO
In-plane transverse optical phonon	iTO
Out-of-plane transverse optical phonon	oTO
In-plane longitudinal acoustic phonon	iLA
In-plane transverse acoustic phonon	ITA
Out-of-plane transverse acoustic phonon	oTA

*Figure 3.22***:** *Phonon dispersion relation in graphene.*[245]

First-order Raman processes require the fulfillment of the fundamental selection rule, requiring the momentum of the phonon to be equal to zero (q=0) to achieve overall momentum conservation of the perturbed system,[246] which can only be satisfied by the phonon branches at the zone center Γ. Two optical phonons iLO and iTO are degenerate at ~1580 cm^{-1} and are Raman active giving rise to the G-peak in the spectra of graphene. The third optical phonon oTO appears at a lower energy around 800 cm^{-1}, however, it is IR active and doesn't contribute to the Raman spectra of graphene. It can also be seen that the three acoustic phonons are zero at the zone boundary and thus are not observed. This makes the G-peak the only first-order Raman active peak in graphene.

Second-order Raman processes involving two scattering processes (**Figure 3.23**), relaxes the fundamental selection rule, where the momentum can be conserved through two phonons at the K point with q and –q wave vectors. This process results in the 2D peak in graphene at ~2700 cm^{-1} arising from two iTO phonons occurring at the K point. Scattering in the second-order Raman process doesn’t need to arise from phonons, where scattering by defects in graphene such as edges, grain boundaries and point defects can contribute to the scattering of the photo-excited electrons along with the phonon scattering to conserve the momentum of the perturbed system. Scattering by defects is an elastic process which only affects the momentum of the electrons, and thus the Raman shift is governed by the frequency of the contributing phonon. The D-peak ~1350 cm^{-1}, typically appears in defective graphene, arise from a second-order process involving one iTO phonon at the K point and an elastic inter-valley scattering by defects. Another defect related peak is the D’ ~1620 cm^{-1} occurs from LO at the Γ and intravalley defect scattering.[247] Second-order processes in graphene are typically referred to as double resonance Raman peaks (DR), which involve resonant coupling between the involved phonons and the electron transitions from and back to the K point. It is this resonant process that accounts for the dispersive behavior of the D and 2D peaks where the peak position is a function of the laser energy used.

A typical Raman spectrum of monolayer graphene is comprised of two prominent peaks, the G-peak at ~1580 cm^{-1} and 2D-peak at ~2700 cm^{-1} at laser energy 473 nm, in addition to a small peak around 1350 cm^{-1} known as the D-peak, whose intensity increases with the increase of the amount of defects in the basal plane of graphene. Accordingly, the quality of graphene is typically assessed based on the intensity ratio of the D-peak to the G-peak.

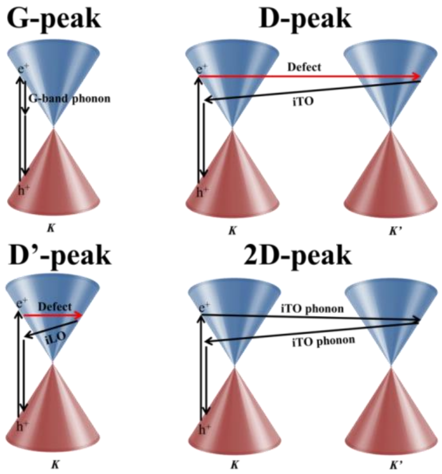

Figure 3.23: Scattering processes in graphene

Most sp^2 carbon materials show the G- and D-peaks whereas the 2D-peak is characteristic of graphene and graphite, and it changes in shape and intensity with the increase in the number of layers reflecting the changes in the electronic structure. The shape of the 2D-peak has been used to quantify the number of layers of mechanically exfoliated graphene.[248] Such samples exhibit AB-Bernal stacking, which maintains the electronic coupling between the sheets and thus the electronic structure would evolve as the number of layers increase, which is reflected by the changes in the shape of the 2D-peak. Monolayer graphene exhibits a characteristic single sharp Lorentzian peak (FWHM ~24 cm^{-1}), bilayers show a broad 2D-peak that can be fitted with four Lorentzian peaks each with FWHM ~24 cm^{-1}, whereas it would be fitted with six Lorentzians in trilayer graphene, and three in the case of four layers graphene. Increasing the layer number further, the 2D-peak shape will be indistinguishable from that in graphite in which it consists of two components; low energy peak ($2D_L$) and high energy peak ($2D_H$), having roughly ¼ and ½ the height of the G-peak.[245] The intensity ratio of the two component have been used to estimate the thickness of HOPG (ranging between 2 – 20 nm) crystals, where $2D_L$ increases in the intensity as the thickness decreases, lowering the intensity ratio $2D_H$ to $2D_L$ from ~3 in 20 nm discs to 1 in 2 nm discs.[83] In the case of rotationally faulted graphene films where AB stacking is absent, such as epitaxially grown FLG, the electronic coupling between the sheets is weak, and thus the shape of the 2D-peak would resemble that of a monolayer graphene. In turbostratic multilayer graphene, 2D-peak is a single Lorentzian peak similar to monolayer graphene, however, with a larger FWHM.

The intensity ratio between the 2D- and G-peak decreases as the number of the layers increases in CVD graphene, and thus is used to confirm monolayer growth by having a ratio of more than two.[80] Using the intensity ratio to identify the exact number of layers in CVD and turbostratic multilayer graphene has been attempted empirically, however, such approach isn’t accurate and should always be confirmed with other characterization tools.[157]

Instrumentation of Raman spectrometer is composed of a monochromatic light source, optics for illumination and collection of the scattered radiation, a spectrometer for radiation dispersion and a detector to measure the intensity of the collected signal. Gas lasers are generally used to generate monochromatic, linearly polarized small diameter beams of light, which made them the leading source of radiation in Raman spectrometers. As the laser beam is generated, it passes through a set of optics where first an interference filter is used to reduce the intensity of the radiation which is essential for heat sensitive samples, and then a set of mirrors and lenses that direct the radiation to the sample. The last stage prior to reaching the sample is passing through a focusing microscope objective, which controls the beam diameter and hence the spatial resolution of the measurement. The focal length of the lens is directly proportional to the spot size, and thus larger magnification objectives are generally used for Raman mapping. The inelastically scattered signal is then collected, passed through a notch filter to eliminate contributions of the elastically scattered and stray light and then directed to the spectrometer. The spectrometer is composed of gratings (1 to 3) that disperse the collected signal and allows resolving the collected signal to the involved wavelength shifts. The spacing between the grooves of the grating determines the spectral resolution of the system. The dispersed radiation is then detected by a CCD detector.

In this work, a LabRAM ARAMIS Raman spectrometer from Horiba Jobin Yvon, Inc. was used. The excitation source a 473 nm laser, which was focused using a 100X objective to a laser spot of 1 μm and 0.5 mW power. The signal was collected in backscattered geometry and dispersed with 1800 mm^{-1} grating.

X-ray Photoelectron Spectroscopy (XPS)

XPS is a powerful tool capable of probing core electronic levels of a material and perform quantitative characterization of the chemical composition, chemical state (bonding) and thickness of ultra-thin samples. It relies on the photoelectric effect whereby monochromatic X-rays are typically used to emit electrons from the elemental core levels. The emitted photoelectrons are then collected and counted as a function of their kinetic energy. An XPS spectrum is presented as electron counts per second (cps) versus the binding energy (BE) in eV, which typically appears as discrete peaks at the characteristic BE of electron orbitals and thus can be used for elemental identification. The relative area under the peaks is proportional to the atomic concentration, thus providing a direct quantitative analysis of the composition of the sample. Furthermore, the exact position and shape of each peak can be analyzed to deduce the chemical state and bonding configuration of each element including oxidation state, charge transfer and hybridization states.

XPS is a surface sensitive technique, with a nominal analysis depth in the range of 1 – 10 nm. The surface sensitivity is derived from the emission and collection of the emitted electrons since X-rays are capable of penetrating the sample up to few µm. The inelastic scattering of photoelectrons as they leave the bulk of the samples reduces their energy and changes their direction. The inelastic scattering of electrons is characterized by the inelastic mean free path (λ), which is the average distance traveled by electrons in the solid before being inelastically scattered which is on the order of few nanometers, and is typically a function of the electron energy and material type. The probability of electrons leaving the bulk of the sample is determined from the distance "x" from the sample surface where it is generated, λ and electron take-off angle (measured from the normal to the surface) according to $\exp(-x/(\lambda \cos \theta))$. The surface sensitivity can be generally increased by collecting the electrons at grazing angles from the surface of the sample.

As X-rays with a specific energy (hv) are absorbed by the sample, their energy is transferred to the core electrons leading to their excitation based on energy-conservation.

The excited electron (in the absence of scattering) would leave the surface of the sample once it possesses an energy that is sufficient to overcome its binding energy and the work function of the sample (Φ_s) as shown schematically in **Figure 3.24**. The excess energy allows the electron to travel towards the analyzer with a KE that is equal to ($KE = \text{h}\nu - \text{BE} - \Phi_s$)

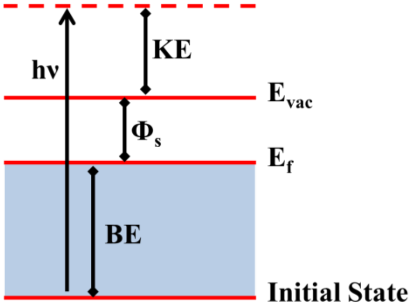

*Figure 3.24***:** *Photoelectric effect and various energy levels in the material.*

A very important practical aspect to be considered is the fact that the emitted electrons travel in vacuum towards the detector, and will have to overcome the work function of the analyzer (Φ_A) to be measured. Accordingly, the measured *KE* at the detector is different from that observed by the sample. The analyzer and the sample are electrically connected in the measurement setup so that the Fermi level of the sample is aligned with the Fermi level of the detector, making the difference between actual *KE* and the measured *KE* equal to $\Phi_A - \Phi_s$. The *BE* of photoelectrons is thus defined in terms of the measured *KE* and the Φ_A in accordance to

$$BE = \text{h}\nu - \text{KE} - \Phi_A \qquad \textit{Equation 3.11}$$

Φ_A is constant, and is typically calibrated upon installation and after major changes to the system such as venting and bake-out. The calibration of the Φ_A in this work, was conducted using a reference Ag single crystal that was Ar^+ sputter cleaned for 15 mins (1 keV, 10 μA) to remove surface contaminants which would otherwise affect the position of the peaks. Φ_A was set to the value 4.4 eV which aligns the Ag $3d_{5/2}$ to its expected binding energy of 368.2 eV.

The *KE* of the emitted electrons is most commonly resolved in a Hemispherical Sector Analyzer (HSA), which is preceded by a set of electrostatic lenses and followed by the detector. The function of the lenses is to sweep the value of *KE*, thus acting as a gate for electrons with specific energy to reach the analyzer. Ideally, only electrons having *KE* equal to the pass energy (E_p) of the analyzer are allowed to enter. E_p is determined by the geometry of the analyzer and the potential applied between the inner and outer hemispheres. However, electrons with $KE=E_p\pm\Delta E_A$ are typically transmitted through the analyzer, where ΔE_A defines the absolute resolution of the spectrum, and is determined by the geometry of the analyzer. Analyzers are designed to have a constant relative resolution of $\Delta E_A / E_p \sim 0.1$, and thus the resolution can be improved by using small E_p for a given system. Moreover, the intensity of XPS also varies with the choice of E_p, where a higher value E_p increases the intensity and thus the signal-to-noise ratio. Accordingly, the trade-off between resolution and signal-to-noise ratio shall be optimized based on the purpose of the measurement.

The most common operation mode for XPS measurements is to hold the pass energy constant while varying the sweep energy through the electrostatic lens system. This allows for a constant spectral resolution throughout the measured values of KE. For a quantitative compositional analysis, clearly defined intense peaks are needed over a large range of *KE* energy values that would reveal all of the elements which are potentially present, and thus the absolute resolution of the peaks is not a major concern. This is typically achieved by measuring the survey spectra, where large E_p is used in order to get a high signal-to-noise ratio over a short scanning time. On the other hand, if one is interested in resolving the chemical states and bonding configuration of a specific element, high-resolution spectra are measured around a single photoemission peak, over a narrow range of KE. In this case, the E_p used is much smaller so as to increase the spectral resolution. However, the collection of high-resolution spectra is done for longer durations and integrated over various sweeps to increase the signal-to-noise ratio.

XPS in this work was performed using an Omicron Nanotechnology (Taunusstein, Germany) UHV system with a monochromatic Al source (1486.7 eV). A hemispherical energy analyzer EIS-Sphera was used to measure the XPS spectra. Survey spectra were measured at a pass energy of 50 eV and a step size less than 0.5 eV. Core-level high-resolution scans were acquired at a pass energy of 20 eV and a step size of 0.05 eV. A base pressure of about 4.0×10^{-10} mbar was maintained throughout all measurements. The spectroscopic data were processed using CasaXPS software (Casa Software Ltd.).

(A) Chemical composition analysis

The identification of elements present in a sample can be achieved through a wide-range survey spectrum, and then comparing the peaks to the tabulated *BE* of elements, which is usually preinstalled with the XPS software. It is essential to point out that the presence of an element requires the presence of the XPS peaks from all orbitals, which should conform to the expected relative intensities of the peaks.

The relative atomic concentration can be calculated from the intensities of the peaks of the respective elements, by considering the contributions from the analyzer and the detector to these intensities in addition to differences in the λ and cross section (σ) of each orbital. The total flux of the photoelectrons leaving the surface of a sample (J^e) upon interaction with X-ray flux (F) depends on the photoemission probability defined by σ and the probability of the photoelectrons to leave the surface of the sample before being scattered as defined above. Assuming constant concentration across the sample (C_i), the total electron flux from orbital (i) can be presented as

$$J_i^e = F\sigma\lambda_i C_i \qquad \textit{Equation 3.12}$$

As photoelectrons travel in vacuum through the various lenses, analyzer and detector, the amount of electrons that would be transmitted towards the detector will be affected by various factors related to the instrument which determine the final intensity of the peak measured. The measured peak intensity would be related to the electron flux through,

$$I_i = AJ_i^e \qquad \textit{Equation 3.13}$$

Where A is a constant related to the analyzer transmission function, detector and instruments response functions. Combining **Equations 3.12** and **3.13**;

$$I_i = AF\sigma\lambda_i C_i \qquad \textit{Equation 3.14}$$

The instrument-related factors, cross-section and the inelastic mean free path, are combined in a single factor known as the sensitivity factor S_i, which is usually provided in a tabulated format for all the elements and is system specific.

$$I_i = FS_iC_i \qquad \textit{Equation 3.15}$$

Thus, the composition of a sample can be derived by calculating relative atomic concentration using **Equation 3.16**;

$$\frac{x_i}{x_j} = \frac{I_i/S_i}{I_j/S_j} \qquad \textit{Equation 3.16}$$

Typically the sensitivity factors are presented as relative sensitivity factors RSF, where the sensitivity factor of C 1s is taken as 1.

(B) Chemical State determination and peak fitting:

High-resolution XPS peaks can be used to deduce the elemental chemical state in addition to the direction of charge transfer in doped graphene. Changes in the chemical state of an element are reflected in the shape and position of its XPS peak, which should be carefully interpreted since other factors related to the photoemission process and subsequent events, such as the fate of the generated hole, can also contribute to the shifting and broadening of the peak. Generally speaking, if an element in the sample is present in a single chemical state, the whole peak will be shifted in accordance with the type of bonding, and the resulting partial charge in the valence band. Core electrons will sense the changes in the valence band, which would affect their binding energy; for example, a cation would appear at higher binding energy, whereas an anion of the same element would appear at a lower binding energy. This is due to electric screening of the charge of the nucleus by the absence/presence of an extra electron in the valence band, respectively. If an element is present in various chemical states and bonding environments, then its peak will be broadened, and peak fitting becomes important for the accurate determination of the relative amount of bonding.

(C) Calculating the thickness of FLG samples using XPS

XPS spectra of FLG samples have generally included signals from the underlying substrate, which indicates that all the layers in FLG are probed by the analyzer. Using intensity of the peaks of FLG (C 1s) and the underlying glass substrate (Si 2p) allows for the evaluation of the thickness of FLG. As discussed above, generated photoelectrons at a certain depth x in the sample, are attenuated depending on λ, which itself depends on the kinetic energy and on the sample, as illustrated in **Figure 3.25**.

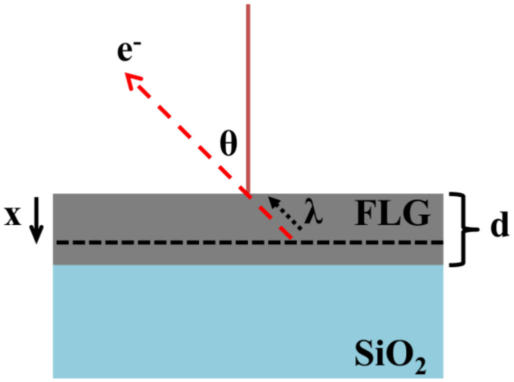

Figure 3.25: Illustration of the various parameters influencing photoelectron attenuation and FLG thickness measurement.

Hence, the observed intensity (I_{obs}) would be attenuated according to,

$$I_{obs} = I_s * exp\left(-\frac{x}{\lambda cos\theta}\right) \qquad \textit{Equation 3.17}$$

where I_s is the intensity that is collected from all generated photoelectrons inside the sample regardless of whether they leave the sample or not. The total signal of electrons that leave the surface of FLG from all the layers have a measured intensity I_{obs}^{C} that can be calculated by integrating **Equation 3.17** from the surface (*x=0*) to the thickness of the material (*d*). The intensity measured from the glass substrate I_{obs}^{Si} is obtained by the integration from a depth equal to the FLG thickness to infinity. Taking the ratio of these two signals can be used to measure the thickness of FLG;

$$\frac{I_{OBS}^{Si}}{I_{OBS}^{C}} = \frac{\rho_{Si} \int_d^\infty e^{-x/\lambda_{Si\,2p}} dx}{\rho_C \int_0^d e^{-x/\lambda_{C\,1s}} dx} \qquad \textit{Equation 3.18}$$

Note that "*cos θ*" is dropped as all the measurements were done at normal emission angle (*θ = 0*), and the materials' density ratio is included to account for the generated intensity which increases with increasing the number of atoms in the sampling volume. The mean free path values were obtained from reference [249], which allows the equation to be solved for "d" representing the thickness of our FLG films.

(D) Calculating the surface coverage of molecular dopants

In **Chapter 5**, the surface coverage of molecular dopants is calculated using the following procedure. First the C 1s intensity is adjusted to remove contributions from the carbon atoms in the dopant using **Equation 3.19**

$$I_{Graphene}^{C\,1s} = I_{OBS}^{M} * \left(\frac{I_{OBS}^{C\,1s}}{I_{OBS}^{M}} - \frac{C_{Dopant}}{M_{Dopant}}\right) \qquad \textit{Equation 3.19}$$

where I_{OBS}^{M} is the relative atomic intensity of a core level orbital belonging exclusively to the dopant molecule such as F 1s, Mo 3d, Ru 3p, or Rh 3d, C_{Dopant} is the number of carbon atoms in the dopant and M_{Dopant} is the number of atoms of the exclusive element found in the dopant. Note that in the case of the ionic dopant Magic Blue, the carbon-containing moiety tris(4-bromophenyl)ammoniumyl is assumed to have been neutralized and removed from the surface during the rinsing step (as evidenced by the absence of measureable Br or N core ionizations), so this adjustment is not required.

Then the graphene peak intensity is corrected to account for attenuation from the buried layers, and provide a more accurate estimation of the surface coverage. Based on **Equation 3.17**, photoelectrons generated at the surface (*x = 0*) are expected to be emitted at 100% probability. However, the probability decreases as we move deeper in the sample, for example, only 5% of the generated photoelectrons at *x* ~ 3λ are expected to leave the surface of the sample. The total intensity of a signal generated from the top surface to a depth of 3λ can be obtained by integrating **Equation 3.17** from 0→3λ thus leading to a peak intensity that is 95% of the generated photoelectrons. In the absence of attenuation, and for a sample thickness *d*, the total observed signal should be (100% × d) if the integration is taken from *x=0* to *x=d*. To account for the full signal coming from the buried graphene layers in FLG, and properly quantify the number of carbon atom, $I_{Graphene}^{C\,1s}$ is corrected using **Equation 3.20**:

$$\frac{I_{Corrected}^{C\,1s}}{I_{Graphene}^{C\,1s}} = \left(\frac{d}{\lambda_{C\,1s} * \left(1 - e^{-d/\lambda_{C\,1s}} \right)} \right) \qquad \textit{Equation 3.20}$$

Here, the denominator presents the integration of the attenuated signal for the whole thickness. $I_{Corrected}^{C\,1s}$ is used to determine Dopant/$C_{Graphene}$ based on the number of elements in the dopant, Dopant/nm^2 from the number of carbons in 1 nm^2 of SLG (38.17) multiplied by *d*/0.335, and monolayer coverage based on the numbers of dopants per nm^2 and the estimated area per dopant for a close-packed monolayer.

3.4.3 Work function characterization

Ultraviolet photoelectron spectroscopy (UPS)

UPS shares the same basic principle as explained for XPS above, in that it relies on the photoemission of electrons. However, the radiation source used is UV photons, having much lower energy as compared to X-rays in XPS, and is capable of probing the valence band of materials. UV sources are based on cold cathode capillary gas discharge typically using He I (21.22 eV) or He II (40.81 eV). Electrons near the Femi level are emitted with the highest kinetic energy, whereas a deep-lying electron would experience inelastic scattering and lose energy as it barely leaves the sample, and thus appears as a continuous band of secondary electrons, whose intensity would decrease abruptly at zero KE, and thus known as the secondary electron cut-off (SEC). Such electrons represent those who barely made it out of the surface of the sample after the various scattering events, and thus the distance between the Fermi level (BE = 0.0 eV) and the SEC is related to the work function of the material.

The work function can be calculated from UPS spectra taking the tangent at the SEC, and subtracting its binding energy from the energy of the UV photons.

An important practical concern in measuring UPS, is that additional secondary electrons are generated in the analyzer/detector as a result of the collisions of the emitted photoelectrons from the sample with the surface of the analyzer/detector, and thus they are superimposed over the real spectra of the sample obscuring the SEC. This is typically resolved by applying a bias between the sample and the analyzer that would accelerate the secondary electrons from the sample, and push the ones from the instrument away from the sample spectrum.

UPS spectra in this work were collected using He I (21.22 eV) source, with a bias ranging between -5 to -10 V. The UV photon flux was attenuated by 1/12 to prevent damage to the sample, and the signal was collected using pass energy of 2.0 eV and aperture 2.

Photoelectron Spectroscopy in Air (PESA)

Measurements of the work function were also conducted using PESA system AC-2 from RKI instruments Inc., which facilitates the measurement of the work function in air, thus having the benefit of easy operation and fast measurement. The measurement relies on the photoelectric effect described earlier. However, here, a tunable energy UV source comprised of deuterium lamp and a grating monochromator is utilized allowing the excitation energy to be scanned in the range of 3.40 to 6.20 eV. Once the photon energy reaches the threshold to excite electrons from the Fermi level to the vacuum level the photocurrent increases. The work function can be measured as the intersection of the slope of the electron yield with the x-axis which is the photon energy. A special detector capable of measuring the photoelectron signal in air, known as the open counter, is used. The open counter shown in **Figure 3.26** consists of an anode, quenching grid and suppressor grid. As electrons leave the sample, they are accelerated by applying an electric field between the grounded sample and the suppressor grid (+80 V), during which the electrons ionize the oxygen atoms. Ionized oxygen inside the detector is then accelerated again by a strong electric field between the quenching grid (+100V) and the anode (+2900 V), at which electrons are separated and multiplied producing a large number of negative charges and positive ions. Only the electrons are detected by the anode and thus increase the number of counts. To prevent positive ions from entering the detector during the detecting step a positive voltage is applied to the suppressor grid (+30 V) for 3 ms, which is sufficient to detect the electrons signal.

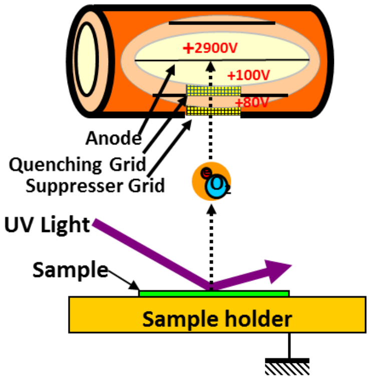

Riken Keiki Co. Ltd

*Figure 3.26***:** *Schematic of the PESA setup and the open-counter detector.*[250]

CHAPTER 4
Bromination of Graphene: A New Route to Making High-Performance TCEs with Low Optical Losses

Ahmed E. Mansour, Sukumar Dey, and Aram Amassian*,

Division of Physical Sciences and Engineering, KAUST Solar Center (KSC), King Abdullah University of Science and Technology (KAUST), Thuwal 23955-6900, Saudi Arabia

Minas H. Tanielian

Boeing Research and Technology, Seattle, Washington 98124-2499, United States

ACS Appl. Mater. Interfaces, 2015, 7 (32), pp 17692–17699
DOI: 10.1021/acsami.5b03274
Publication Date (Web): July 22, 2015

The unique optical and electrical properties of graphene have triggered great interest in its application as a transparent conducting electrode material and significant effort has been invested in achieving high conductivity while maintaining transparency. Doping of graphene has been a popular route for reducing its sheet resistance, but this has typically come at a significant cost in optical transmission. We demonstrate doping of few layers graphene with bromine as a means of enhancing the conductivity via intercalation without major optical losses. Our results demonstrate the encapsulation of bromine leads to air-stable transparent conducting electrodes with five-fold improvement of sheet resistance reaching ~180 Ω/□ at the cost of only 2-3% loss of optical transmission. The remarkably low tradeoff in optical transparency leads to the highest enhancements in the figure of merit reported thus far for FLG. Furthermore, we tune the work function by up to 0.3 eV by tuning the bromine content. These results should help pave the way for further development of graphene as a potential substitute to transparent conducting polymers and metal oxides used in optoelectronics, photovoltaics and beyond.

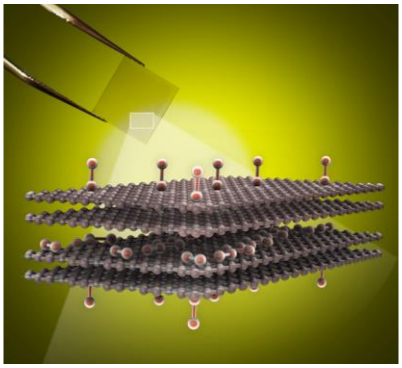

Figure 4.1: Schematic of bromine intercalation into FLG

4.1 Introduction

Bromine doping of carbon-based materials was reported decades ago, and has been demonstrated to increase the electrical conductivity of optically thick graphite,[251,252] carbon nanotubes[253,254]and polyacetylene.[255] Super-metallic conductivity of bromine-intercalated graphite has even been achieved via bromine vapor exposure of highly ordered pyrolytic graphite (HOPG).[225] The increase in conductivity was attributed to a parallel integration of weakly coupled p-doped graphene sheets. Bromine intercalation of graphitic compounds (Br-GIC) occurs as a stage 2 intercalation, meaning that intercalation occurs at every second layer.[213,222] The p-doping nature of bromine into graphene has been confirmed by density functional theory (DFT) studies, suggesting a charge transfer towards physically adsorbed bromine species on graphene without disrupting its basal plane.[224] Physically adsorbed bromine on graphene has been previously achieved via vapor exposure and intercalation has been observed for films more than 2 layers in thickness. Both mechanisms of adsorption and intercalation were found not to disrupt the basal plane of graphene and led to high p-type doping density.[222] Enhancement of the conductivity and up-shifting of the work function for thinner but still optically opaque multilayered graphene (30 – 60 layers) and thick graphite (10 μm) by bromine vapor exposure was also recently reported, implying a strong thickness dependence of conductivity enhancement as the thick graphite samples exhibited larger improvement than multilayer graphene.[221] Covalently bonded bromine on graphene has also been reported by a microwave spark assisted method, but this reduces the conductivity of pristine graphene.[256] Given the well-known reactivity and volatility of bromine, it is not surprising to find that bromination of SLG, layer-by-layer stacked graphene (LLG) and few layers graphene (FLG) has not been investigated experimentally, nor has the transparency of these layers been evaluated and compared with other graphene TCE doping schemes. Nevertheless, bromine is well-known to readily intercalate into graphite at room temperature due to the high vapor pressure of bromine, making it possible to minimize covalent bonding promoted at elevated temperature.[257] We therefore take the view that bromine may indeed intercalate into FLG films and be sufficiently stabilized by virtue of self-encapsulation under graphene to explore the electrical and optical benefits of bromine-intercalated FLG in the context of TCE applications.

Herein, we report the successful bromine doping of graphene in inert atmosphere resulting in air-stable transparent conducting electrodes with up to a five-fold increase in conductivity at the cost of only 2-3% loss of optical transmission in the case of FLG and 0.8% in case of SLG. The remarkably low tradeoff in optical transparency for the conductivity boost leads to the highest enhancements in FoM for any doping scheme reported thus far. The FLG (4 to 10 layers) samples show the best results in terms of FoM enhancement as well as doping stability, mainly due to the encapsulation of bromine by the intercalation process in between the graphene sheets, as demonstrated by scanning tunneling microscopy (STM) analysis. Moderate temperature and exposure conditions ensure bromine is mostly physically adsorbed, leading to charge transfer doping of graphene, rather than covalent bonding which disrupts the basal plane of the graphene sheets and reduces their conductivity.[256,258] These developments – at the crossroads of bulk graphite and graphene – should help pave the way for further development in the area of graphene-based highly transparent conducting electrodes for a wide range of optoelectronic and photovoltaic applications.

4.2 Results and discussion

Bromination on graphene was investigated on two types of samples, (1) FLG grown on Ni/SiO_2/Si and (2) stacked CVD monolayers (LLG) of graphene grown on a copper foil with varying number of layers from 1 to 3 layers. Our study was carried out in two different environments of varying degrees of moisture and O_2 content to elucidate the environmental effects on the bromine intercalation, more specifically mbraun glove box (Gbox) with <0.1 ppm O_2 and H_2O and a nitrogen filled glove bag (Gbag) with 2000 ppm O_2 and 2500 ppm H_2O. Graphene samples were lifted off the metal substrate to glass substrate using wet transfer method, which was then brominated by vapor exposure at room temperature as explained in details in **Chapter 3**. Importantly, all samples were washed with ethanol to remove excess and possibly weakly adsorbed bromine from the surface and grain boundaries prior to further handling and analysis, a condition we found to be very important for subsequent air stability of intercalated samples. The degree of bromination was systematically varied by controlling the vapor exposure time (60, 120 and 180 minutes).

Raman spectroscopy reveals no changes in the FLG structure after transfer from Ni to glass **Figure 4.2A**, where pristine FLG samples showed the typical Raman spectrum of CVD-grown graphene on nickel, with a G-band at 1580 cm^{-1} and a 2D-band at 2725 cm^{-1}. A very small D-peak is observed at 1350 cm^{-1}, indicating the presence of defects and grain boundaries in the graphene plane. These are believed to result from the patchy nature of the film and wrinkles present due to the difference in the thermal coefficient of expansion between graphene and the Ni foil.[37,38] Upon exposure to bromine, we observe a broadening of the G-peak which continues to broaden with increased exposure time, to a point where it splits after 180 minutes of exposure as shown in the close-up view in **Figure 4.2B**. The G-band doublet peak has been clearly observed in bromine intercalated graphite compounds (Br-GIC) and was reported to consist of a graphitic band at 1580 cm^{-1} resulting from graphite surrounded region (A_1), and a stiffened band at 1600 cm^{-1} from graphitic planes adjacent to bromine (A_2).[258] Even though these two bands aren't as clearly formed in FLG samples as in Br-GIC, we surmise that the fitted peaks in the G-band of our samples, having the same separation, result from a similar mechanism, strongly pointing to intercalation. The characteristic G-peak was fitted using two Gaussian peaks with areas A_1 and A_2, separated approximately by 20 cm^{-1} for all brominated samples (inset of Figure 1b). The increase of the intensity ratio A_2/A_1 with exposure time – even after ethanol wash – indicates increased bromine uptake by the sample with increasing exposure time (as shown in **Figure 4.2C**). The intensity ratio of A_2/A_1 peaks is sensitive to the relative number of the graphene-bound layers and Br-bound layers, as well as to the molecular alignment of bromine between the sheets of graphene. A higher degree of molecular alignment of Br is expected to promote the growth of the A_2 peak.[258] Since the FLG films are of a patchy nature and vary laterally in the number of layers from 4 to 10 and exhibit different in-plane orientations, they lead to non-uniform intercalated layer formations in terms of the number and orientation of molecules. The higher density of grain boundaries and edges in FLG films is expected to promote incorporation of bromine at these sites without any specific molecular orientation. All of these factors should diminish the A_2 peak intensity as compared to the A_1 peak and result in a less pronounced peak splitting in Br-FLG than in Br-GIC, where HOPG has uniformly extended sheets of graphene throughout the sample. These features may promote higher bromine density at these specific sites, while the graphitic band at 1580 cm^{-1} continues to dominate the spectrum. The graphitic peak of the G-band (A_1) is blue shifted in brominated graphene which is in line with previous Raman studies on doped graphene.[138] A Br-Br stretching mode peak appears in the spectrum at around 250 cm^{-1} (inset of **Figure 4.2A**) and is downshifted compared to that of free bromine molecules (323 cm^{-1}) and solid bromine (300 cm^{-1}).[258] This peak was previously reported around 240 cm^{-1} for both Br-GIC compounds and bromine doped mechanically exfoliated multilayer graphene.[222,259]At this position, the bromine peak can be related to either bromine molecules or to an anionic bromine mode. The blue shift of the G-band and the red shift in the Br_2 stretching mode at 250 cm^{-1} both point to charge transfer occurring between Br_2 molecules and graphene.

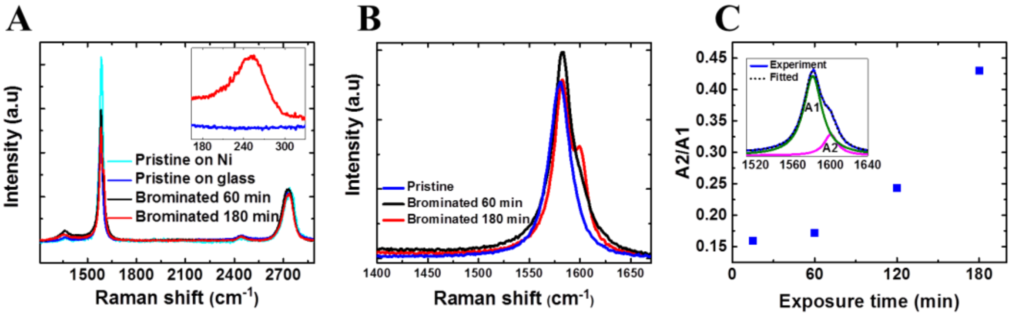

Figure 4.2: (A) Raman spectra taken of pristine FLG before and after transfer from a Ni film to a glass substrate and subsequently brominated (Gbag) for 60 and 180 minutes. The inset in (A) focuses on the region around the Br-Br stretching mode at 250 cm-1. (B) G-peak variation upon bromination and splitting in doublet peak. (C) The variation of the intensity ratio of the A2 to A1 components of a brominated FLG G-peak (shown in inset) with exposure time.

The doping of FLG with bromine is further confirmed by x-ray photoelectron spectroscopy (XPS) performed on samples exposed to bromine in both Gbox and Gbag environments. In **Figure 4.3A** we show a representative survey scan of a sample brominated for 180 minutes in glove box exhibiting a strong C 1s peak (graphene) and bromine peaks of Br 3s, Br 3p and Br 3d. The silicon peaks at 102.7eV (Si 2p) and 153.6eV (Si 2s) are related to the glass substrate carrying the FLG. The graphitic C 1s peaks for the brominated FLG samples were observed at 283.8eV, which is downshifted from that observed for the pristine sample at 284.1eV due to the Fermi level shift to a higher value in the negative direction as shown in **Figure 4.3B**. The C 1s peak shifts to a lower binding energy upon bromine doping; this is counter-intuitive to the fact that bromine acts as a p-dopant to graphitic materials due to its higher electronegativity (2.96) compared to that of Carbon (2.55). However, similar behavior has been previously observed on graphite intercalated compounds[225,260,261] and bromine doped double walled carbon nanotubes (DWCNT),[254] which was attributed to the fact that the final position of the C 1s peak is determined by two counteracting processes: the final state effect due to charge transfer and the Fermi level shifting, since binding energies in XPS are measured relative to the Fermi level. In p-doped (n-doped) materials, the charge transfer would shift the C 1s to a higher (lower) binding energy while the Fermi level shifts to a lower (higher) energy relative to the vacuum level. Brominated FLG in this work shifted by 0.3 eV to a lower binding energy indicating an increase in the Fermi Level in the negative direction. However, this shift cannot be used to deduce the energy of the Fermi level, since final state effects due to charge transfer also contribute to it. The shape of the C 1s peak doesn’t change except for a minor shoulder appearing at around 286 eV, which indicates a C-Br and/or C-O bond.[262] A high-resolution scan of Br 3d peak revealed the maximum at 69.4eV as shown in the inset of **Figure 4.3A**, which is higher than that of molecular Br_2 at (67.4eV) and anionic Br^- (68.5eV) and lower than covalently bonded C-Br (70.8eV). It has been reported that bromine adsorbed on the surface of graphene should have Br 3d peak centered at 69.2eV as compared to 70.8eV for covalently bonded bromine.[256] The Br 3d peak was deconvoluted into a set of three doublets using a Shirley background. The solid lines refer to the $3d_{5/2}$ peaks and dashed lines refer to $3d_{3/2}$ peaks, the doublets were constrained to an intensity ratio 3:2, respectively, with a separation of 1.05eV.[254] According to the fitted peaks, three forms of bromine are present; (1) C_n-Br_2 charge transfer complex (67.9eV), (2) physically adsorbed and anionic bromine (69.2eV) and (3) covalently bonded bromine to carbon (70.0eV).[262] Quantitative analysis of the fitted peaks reveals that after 180 minutes of exposure in Gbox, bromine species in FLG are generally intercalated as physically absorbed species (1.5 at.%) and charge transfer complexes (0.9 at.%) on and between the graphene sheets, with a relatively small, but non-negligible amount of covalently bonded bromine (0.4 at%) which is believed to be concentrated at the edges of the graphene sheets without disrupting the basal plane.

Since it is well established that bromine has an acceptor nature in graphitic materials as mentioned earlier, Br species on our brominated FLG films mostly consist of molecular Br_2 forming C_n-Br_2 complexes and anionic Br^- species that are physically adsorbed on the surface or intercalated between the graphene sheets rather than covalently bonded bromine. Hence, the increased binding energy as compared with molecular Br_2 and anionic Br^- is believed to result from the charge transfer towards Br rather than covalently bonded C-Br, which would disrupt the sp^2 planar structure of graphene. The absence of a significant peak in the C 1s spectrum at the position of covalently bonded C-Br (285.3eV) **(Figure 4.3B**) and the negligible increase of the D-peak in the Raman spectra upon bromine exposure support the fact that the majority of bromine is physically intercalated between the graphene sheets with the possibility of a smaller amount of bromine covalently bonded to carbon at defects and edge sites. The Br content (at. %) in FLG with different exposure times for samples brominated in Gbag and Gbox, are shown in **Figure 4.3C**. In both cases, the bromine content increases with increasing exposure time, which was limited to 180 minutes in the context of this study. However, samples treated in the Gbox exhibit higher bromine uptake indicating the influence of the exposure environment on the effectiveness of intercalation and doping processes.

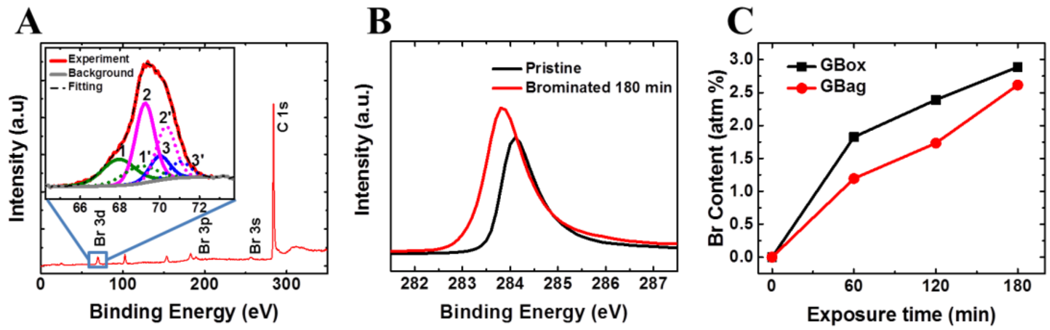

Figure 4.3: (A) XPS survey scan of a brominated FLG sample (Gbox) for 180 minutes. The inset shows a high-resolution view of the Br 3d peak. (B) A high-resolution scan of C 1s peak for pristine (black) and doped sample for 180 mins (C) Evolution of bromine content (at%) with increasing exposure time for bromination experiments performed inside the glove box (black) and the glove bag placed in a fume hood (red).

The higher presence of moisture in the Gbag can potentially react with anionic Br^- species on the graphene surface forming HBr in gaseous form which can further react with graphene, in addition to leaving –OH functionalities on the graphene surface and edges which was anticipated as a potential barrier to the intercalation processes and hence the lower uptake. To elucidate the effect of HBr-FLG interaction in Gbag, a control experiment of exposing FLG to HBr vapor in a similar setting to Bromine vapor exposure, while replacing bromine with hydrobromic acid and heating the enclosure to 175 ºC. Percent change in sheet resistance of FLG directly after 180 minutes vapor exposure (Br_2 or HBr) and after washing with ethanol is shown in **Figure 4.4A**. The sheet resistance was decreased for both Br_2 and HBr exposed samples but to a lower extent in the latter case. After washing with ethanol the sheet resistance increased by nearly 9% for Br_2 exposed samples and 35% for HBr exposed samples. These observations indicate that exposure to HBr vapor is generally less effective in improving the conductivity of FLG than Br_2 vapor. Also HBr effect is diminished after washing with ethanol, which indicates that the resulting doping species are less stable and are easily removed from the surface of graphene, resulting in bromine content of 0.5 at% compared to 2.6 at% in Br_2 exposed samples. **Figure 4.4B** shows the Br 3d peak for Br_2-FLG in Gbag and HBr-FLG, the difference in the peak positions indicate that the resulting species of HBr in Br_2-FLG interactions in Gbag are removed after washing with ethanol, otherwise, the peaks would have been similar.

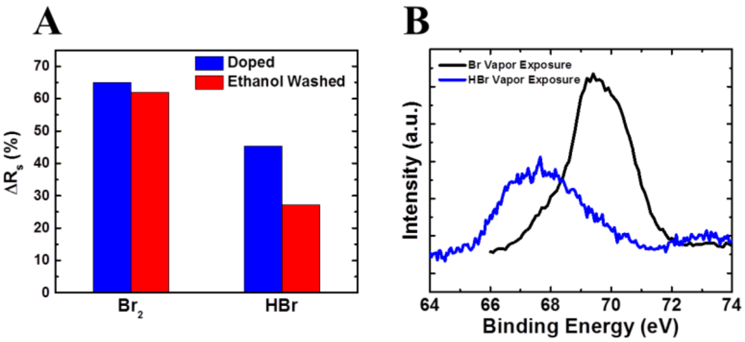

Figure 4.4: Comparison between the exposure of FLG to Br_2 and HBr vapors. (A) FLG sheet resistance changes relative to pristine sample upon exposure to vapors for 180 minutes before and after washing with ethanol. (B) High-resolution Br 3d peak for FLG exposed to Br_2 vapor (black) and HBr vapor (blue) for 180 minutes.

The pristine and brominated FLG samples were studied by STM, SEM, AFM, and micro-Raman imaging. The high-resolution surface morphology of the pristine FLG obtained by STM is shown in **Figure 4.5A**, demonstrating a stack of 4 layers of graphene. The apparent step height between the layers was obtained by taking a line profile, indicated by the black line (**Figure 4.5A**). It shows an average interlayer spacing of 0.27 nm in **Figure 4.5C**, and is in good agreement with previous STM measurements on graphene.[263–265]STM measurements performed on the brominated FLG for 180 minutes (Gbag), revealed the presence of bright features (marked with red arrows in **Figure 4.5B**) forming chain-like structures throughout the surface of graphene sheets. We attribute these to adsorbed Br species, in agreement with previous studies suggesting the formation of chain channels of bromine in intercalated graphite compounds.[40,45] Furthermore, the line profile comparison of pristine and brominated FLG (**Figure 4.5C**), shows an increased average value of apparent step height by 0.18 nm which matches closely with the atomic radius of bromine, and is direct evidence of Br intercalation beneath graphene sheets.

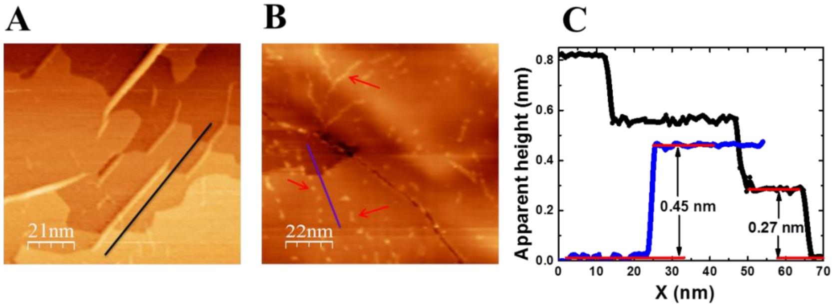

Figure 4.5: STM images (V_b= 0.5 V and I_t= 50 pA) of (a) pristine FLG and (b) brominated FLG (Gbag) for 180 minutes on nickel and (c) apparent height profiles for pristine FLG (black) and brominated FLG (blue) along the lines shown on (a) and (b), respectively.

The pristine FLG transferred to a glass substrate appears to be somewhat patchy and wrinkled, as can be seen in SEM (**Figure 4.6A**) and AFM (**Figure 4.6D**) images. Upon exposure to bromine for 180 minutes, the multilayer regions of the FLG exhibit new surface contrast under SEM, which might be related to topographic variations (**Figures 4.6B** and **C**). Similar features are also seen in AFM images (**Figures 4.6E** and **F**) leading to the conclusion that the graphene becomes locally swollen with bromine. Next, we seek to co-locate changes in graphene structure with the presence of bromine. Mapping of the G-peak to D-peak intensity ratio from Raman spectra for brominated sample **(Figure 4.6H)** over the area shown by the optical image in **Figure 4.6G** indicates that a high degree of order within the FLG is preserved after bromination, especially in areas showing thicker stacks of graphene. This implies that bromine intercalates into these sheets as expected without disrupting the basal planes. Mapping of the Br-Br stretching Raman peak intensity **(Figure 4.6I)** shows that a higher intensity is correlated with the thicker, more ordered regions of FLG, consistent with a greater degree of intercalation in thicker multilayer regions, as well as with more ordered chains of Br^-. The Br-Br stretching peak is observed all over the sample, as seen in **Figure 4.6I**, which indicates that bromine is aerially present everywhere in the FLG sample.

Pristine FLG samples on glass exhibited sheet resistance ranging between 750 and 930 Ω/□ and a transmittance of 76.3 and 77.8% in the middle of the visible (550 nm). This corresponds to a FoM ranging between 1.6 and 3.3. Upon exposure to bromine, the sheet resistance drops precipitously within the first hour of exposure and gradually saturates. The sample in the GBag decreases to 45% of its starting value (**Figure 4.6A**), whereas in the GBox it decreases to 20% of its starting value, yielding a sheet resistance as low as

~180 Ω/□. These differences are in line with XPS observations discussed earlier to the effect that the experimental environment can affect the outcome of the bromination process.

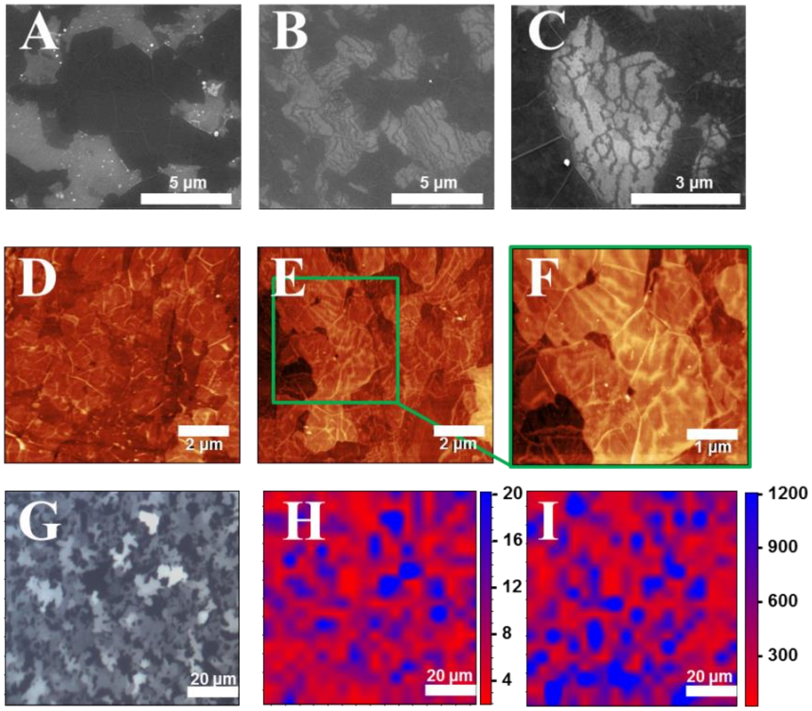

Figure 4.6: SEM images of (A) pristine FLG on glass and (B, C) brominated FLG (Gbag) for 180 minutes on glass. AFM images of (D) pristine FLG and (E, F) brominated FLG (Gbag) for 180 minutes on glass. (G) Optical micrograph of brominated FLG (Gbag) for 180 minutes and corresponding Raman maps of (H) I_G/I_D *and (I) Br-Br stretching mode peak intensity.*

In all cases, the transmittance decreased by only 2-3% of the pristine value (**Figure 4.7B**), resulting in an increase of the FoM to 3 and 7.7 for samples prepared in a GBag and a Gbox, respectively. The gradual changes of sheet resistance and transmittance with increasing exposure time generally agree with the Br content as measured by XPS. We also attempted bromination by exposure to liquid bromine. Liquid bromine was drop-cast on the surface of the FLG sample on glass and allowed to evaporate at room temperature inside the Gbag. The liquid bromine was found to dry within 10 minutes and the sample was washed with ethanol prior to sheet resistance measurement. We find the sheet resistance reaches the same level after 10 minutes of liquid bromination as was achieved after 180 minutes of vapor bromination, indicating the latter method can also be effective at doping graphene. We have also evaluated the vapor phase bromination of SLG and LLG samples (**Figure 4.7C**). In the case of SLG, the sheet resistance drops from 1548 Ω/□ for the pristine sample to 602 Ω/□ after exposure to bromine for 60 minutes. The transmittance decreased very slightly by 0.8% (**Figure 4.7B**), resulting in a FoM increase from 9.5 to 15.6. The sheet resistance decreases more modestly for two and three LLG samples. We have performed Hall effect measurements on brominated FLG samples (Gbag) and show the FLG becomes p-doped by bromination. Enhancement of the conductivity is shown to result from the doubling of the carrier concentration upon bromination (from 2.9×10^{13} to 5.7×10^{13} cm^{-2}), most likely due to charge transfer from FLG to bromine molecules. The carrier mobility doesn’t change significantly, as it drops from 266.2 $cm^2/(Vs)$ for the pristine sample to 255.4 $cm^2/(Vs)$ from brominated sample for 180 min. Bromination of FLG also modified the work function, increasing it from 4.84 eV to 5.10 eV after bromine vapor exposure for 180 minutes (**Figure 4.7D**). The upshift in the work function is believed to result from the shift in the Fermi energy level towards the valence band of FLG upon charge transfer to bromine.

The stability in ambient air of brominated SLG and FLG was evaluated by measuring sheet resistance after leaving samples in ambient air for ten days. In these conditions, bromine is expected to desorb with time towards its residue compound in a similar manner as intercalated graphite compounds.[213] FLG samples are found to remain stable in air, while the sheet resistance of SLG sample increases by 50% (**Figure 4.8A**).

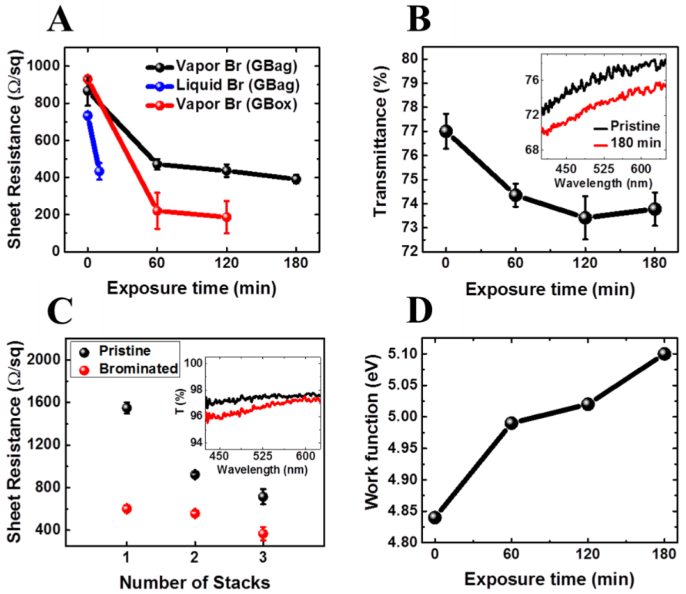

Figure 4.7: (A) Sheet resistance of FLG with respect to bromination time using vapor and liquid bromine sources in different inert environments. (B) Optical transmittance of vapor brominated FLG (Gbag) at 550 nm with respect to the exposure time. The inset shows the transmittance spectra for pristine (black) and vapor-brominated (red) FLG after 180 min treatment. (C) Sheet resistance of SLG, 2-LLG and 3-LLG before and after bromination for 60 min (Gbox). The inset shows the transmission spectra of SLG before and after bromination. (D) Work function of FLG with respect to bromine vapor exposure time (Gbag).

This indicates that intercalated bromine in the FLG sample is protected from desorption and reactivity, comparing very favorably to the aging in air of $AuCl_3$ doped graphene,[192] which degrades over time. As expected, SLG samples are probably more prone to loss of Br. We have further investigated the stability of brominated FLG samples by placing them on a hot plate for 10 min at fixed temperature in a nitrogen glove box and measuring their sheet resistance (**Figure 4.8B**). We find the sheet resistance increases slowly and monotonically up to 150°C toward the pristine FLG sheet resistance along with a decrease in the Br atomic content due to desorption. Beyond this temperature, the sheet resistance increases above the pristine value, hinting that graphene and bromine may potentially undergo a chemical reaction or structural changes resulting from a phase change at elevated temperature. Changes in the sheet resistance of Br-FLG with heating are reflected in the high-resolution XPS spectra of C 1s and Br 3p. C 1s peak shifts back to towards original position as shown in **Figure 4.8C**, while the Br 3p peak maintains its shape up to 150 °C heating, after which it broadens as clear from the peak shape at 180 °C as shown in **Figure 4.8D**.The decrease in the bromine at% with heating explains the initial increase in sheet resistance of brominated samples heated up to 150 °C, where we can imagine the intercalated and the adsorbed species on the surface leaving the sample as a result of heating. However, we expect that above 150 ºC other mechanisms are responsible for the increase in the sheet resistance rather than loss of bromine, especially that the sheet resistance values exceeds that of the pristine FLG and the fact that the loss of bromine from 150 °C to 300 °C isn't large as compared to that in the first regime (**Figure 4.8B**). We propose two possible mechanisms for the heating region above 150 °C, chemical changes in the bonding between bromine and carbon and/or structural changes due to a phase change of intercalated bromine. Changes in chemical bonding between bromine and carbon in graphene at elevated temperature can be inferred from the broadening of the Br 3p XPS peak.

We believe that heating above 150 °C causes some of the adsorbed bromine (182.55 and 182.85 eV) to become covalently bonded (183.65) and/or form C_n-Br_2 complexes (181.05).[262] Structural changes can be responsible for the changes in sheet resistance above 150 °C. It has been reported in early work on bromine intercalated graphite that phase transitions can occur at temperatures around 266 °C represented by a change of stage or interlayer ordering.[213]

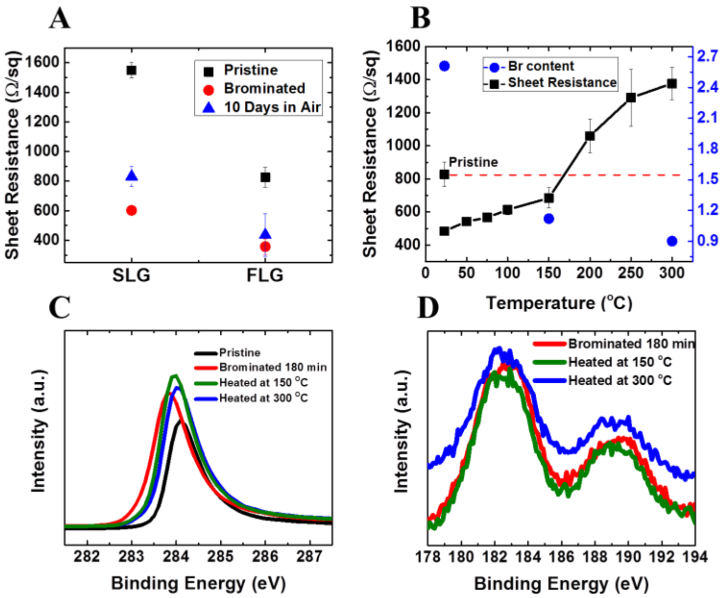

Figure 4.8: Stability of brominated graphene (Gbox). (A) Sheet resistance of brominated SLG and FLG after leaving for 10 days in air at room temperature and (B) Sheet resistance of FLG graphene after thermal annealing in a Gbox for 10 min heating intervals at each temperature and corresponding bromine. The samples were allowed to cool down to room temperature before measuring the sheet resistance. High-Resolution XPS peaks. (C) C 1s peak and (D) Br 3p peak for samples exposed to bromine for 180 minutes (red) and heated at 150 ºC (green) and 300 ºC (blue).

4.3 Conclusion

Our results have thus far indicated that bromine doping of graphene electrodes can result in a large enhancement of conductivity with minor cost in optical transmittance, but without quantitatively comparing them to other doping schemes reported previously. We have plotted in **Figure 4.9A** the ratio of the decrease of sheet resistance with respect to the change in transmittance ($\Delta R_S/\Delta T$) of brominated graphene samples and compared it with various other treatments reported in the literature, including metal chlorides, acid doping and other approaches. [185,186,192,212,266]The raw data of sheet resistance and transmittance before and after treatment are shown in the inset of **Figure 4.9A**, with a line linking the data points to highlight the differences in the steepness of the slope. We find that bromine doping of graphene outperforms in terms of $\Delta R_S/\Delta T$ almost all results in the literature for both SLG (shaded bars) and FLG (solid bars), with the exception of acid-doped graphene.[212] In **Figure 4.9B**, we have plotted the percentage change of FoM for a wide range of results in the literature which provide sheet resistance and transmission change data and compared it to bromine doping of SLG and FLG graphene. The results indicate that we have achieved the highest enhancement of FoM when compared to other doping schemes for FLG. The performance enhancement of FLG was greater than that of SLG. We attribute this to the ability of bromine to decorate the surface, grain boundaries, step edges and intercalate between the layers of FLG, whereas in SLG it is mainly adsorbed on the surface and at grain boundaries. In summary, we have successfully demonstrated p-doping of graphene with bromine, resulting in a significant reduction of sheet resistance at minimal cost to optical transmission. The air stability of the bromination approach for FLG in ambient conditions indicates this method may be technologically applicable. Comparison and benchmarking of the performance of Br-doped graphene in terms of $\Delta R_S/\Delta T$ and FoM with previously reported doping schemes reveals that bromination is significantly more effective than most previously reported methods, making this approach potentially suitable for a wide range of optoelectronic applications requiring highly transparent conducting electrodes.

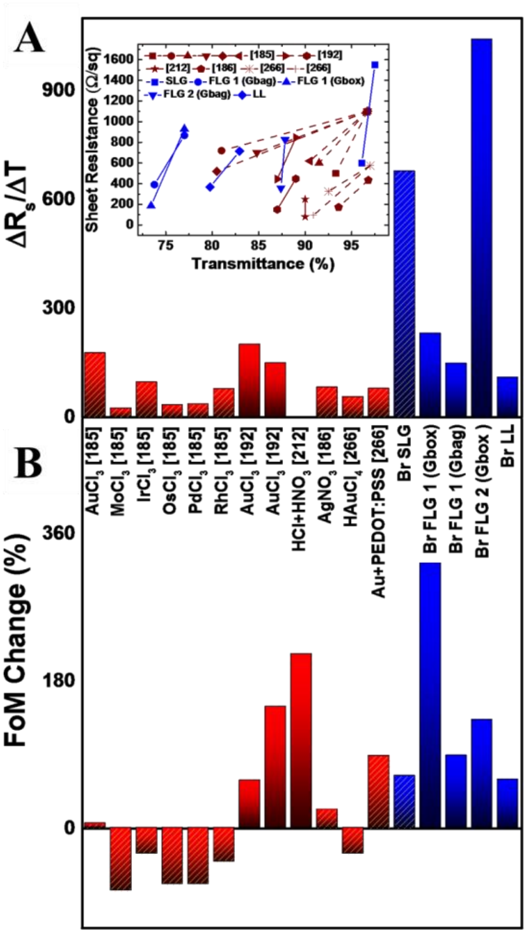

Figure 4.9: (A) The decrease in sheet resistance with respect to the change of transmittance for several doping methods reported in the literature (red) and in this work (blue). The inset shows the raw sheet resistance and transmittance data. (B) Percentage change of the figure of merit (FoM) for different doping methods reported in the literature (red) and in this work (blue). Hash patterns in (A) and (B) correspond to SLG with all the rest referring to FLG samples. ΔRS/ΔT is not shown for acid doping (ref. [212]) because ΔT was reported to be zero.

CHAPTER 5
Facile Doping and Work-function Modification of Few-Layer Graphene Using Molecular Oxidants and Reductants

A. E. Mansour, S. Dey, H. Hu, R. Munir, A. Amassian*

King Abdullah University of Science and Technology (KAUST), KAUST Solar Center
(KSC), and, Division of Physical Sciences and Engineering (PSE), Thuwal, 23955-6900,
Saudi Arabia

M. M. Said, S. Zhang, Y. Zhang, K. Moudgil, S. Barlow, S. R. Marder

Center for Organic Photonics & Electronics and School of Chemistry & Biochemistry,
Georgia Institute of Technology, Atlanta, GA,30332-0400, USA

Advance Functional Materials. DOI: *10.1002/adfm.201602004 (in press)*

Doping of graphene is a viable route towards enhancing its electrical conductivity and modulating its work function for a wide range of technological applications. In this work, we demonstrate facile, solution-based, non-covalent surface doping of few-layer graphene (FLG) using a series of molecular metal-organic and organic species of varying n- and p-type doping strengths. In doing so we tune the electronic, optical and transport properties of FLG. We modulate the work function of graphene over a range of 2.4 eV (from 2.9 to 5.3 eV) – unprecedented for solution-based doping – via surface electron transfer. A substantial improvement of the conductivity of FLG is attributed to increasing carrier density, slightly offset by a minor reduction of mobility via Coulomb scattering. The mobility of single layer graphene has been reported to decrease significantly more via similar surface doping than FLG, which has the ability to screen buried layers. The dopant dosage influences the properties of FLG and reveals an optimal window of dopant coverage for the best transport properties, wherein dopant molecules aggregate into small and isolated clusters on the surface of FLG. This study shows how soluble molecular dopants can easily and effectively tune the work function and improve the optoelectronic properties of graphene.

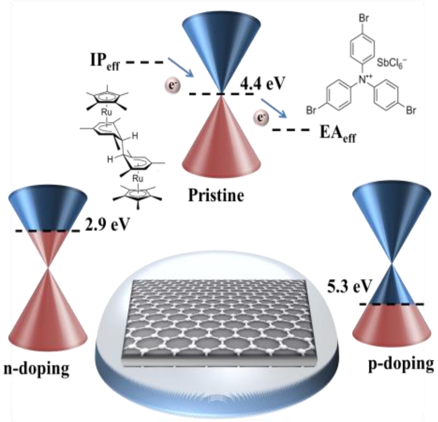

Figure 5.1: Schematic of work function modulation in FLG using p- and n- dopants.

5.1 Introduction

Surface molecular dopants have been investigated theoretically and experimentally in the context of SLG. Examples of organic and metal-organic p-dopants that have been used include 2,3,5,6-tetrafluoro-7,7,8,8-tetracyanoquinodimethane, F_4-TCNQ,[198] and molybdenum tris(1-(trifluoroacetyl)-2-(trifluoromethyl)ethane-1,2-dithiolene), Mo(tfd-$COCF_3)_3$,[139] respectively. n-Dopants include 2-(2-methoxyphenyl)-1,3-dimethyl-2,3-dihydro-1*H*-benzimidazole, MeO-DMBI,[199] and the pentamethylrhodocene dimer, $(RhCp^*Cp)_2$.[139] These species have been shown to dope SLG without disrupting its basal structure.

A molecule capable of p-doping graphene by a simple one-electron redox process will have an electron affinity (EA) greater than the work function (Φ) of undoped graphene (Φ = ca. 4.43 eV). Similarly, the ionization potential (IP) of a simple one-electron n-dopant should be smaller than the work function of graphene.[32] Accordingly, if variations in the electrostatic interactions between dopant ions and the graphene and between adjacent dopant ions are ignored, the thermodynamic strength of molecular p- and n-dopants for graphene can be approximated as EA(dopant) – Φ(graphene) and Φ(graphene) – IP(dopant), respectively, where a larger positive value in each case indicates a stronger dopant. The six dopants used in this study are shown in **Figure 5.2**. However, since the doping is carried out in solution and since solid-state EA/IP values have not been determined for all six compounds (and, in any case, would not be appropriate for the two n-dopants, which, as discussed below, are not simple one-electron reductants), we define the dopant strength using the solution redox potentials of the molecular dopants; **Figure 5.2** plots these potentials vs. ferrocenium/ferrocene ($FeCp_2^{+/0}$). As well as redox potential, dopants were also selected considering molecular size and shape; dopants forming large three-dimensional molecular ions were selected where possible in order to minimize Coulombic interactions between contributed charge carriers and dopant ions and to minimize π interactions between dopants and graphene. For example, the 2D F_4-TCNQ was not included in the present study. Instead, three molybdenum tris(dithiolene) derivatives Mo(tfd-$COCF_3$)$_3$, Mo(tfd-CO_2Me)$_3$, and Mo(PhBz-dt)$_3$ were used as p-dopants; these compounds resemble molybdenum tris[1,2-bis(trifluoromethyl)ethane-1,2-dithiolene], Mo(tfd)$_3$, which has been used as a vacuum-processable dopant for organic semiconductors that shows less tendency to diffuse within organic films than F_4-TCNQ,[200,201] but their different substituents lead to increased solubility and allow their reduction potentials to be varied from +0.39 to –0.38 V (a range that includes the reduction potential of F_4-TCNQ). Mo(tfd-$COCF_3$)$_3$ has, as noted above, previously been used to dope SLG,[139] Mo(tfd-CO_2Me)$_3$ has been used for the solution doping of poly(3-hexylthiophene),[208] and Mo(PhBz-dt)$_3$ is a new compound. In addition, tris(4-bromophenyl)ammoniumyl hexachloroantimonate (Magic Blue), was selected to extend the range of redox potentials to +0.70 V.[267] Magic Blue has also been used as a p-dopant for organic semiconductors[268] and has recently been demonstrated to raise the work function of trilayer MoS_2 by 0.8 eV,[269] and SLG (up to 5.1 eV) for application in mid-infrared hyperbolic metamaterials.[270] Unlike the other dopants examined, Magic Blue is a salt of an oxidizing cation and its use is anticipated to result in the formation of neutral tris(4-bromophenyl)amine, which is expected to be washed away from a substrate during rinsing, leaving $SbCl_6^-$ counterions on the doped surface.[267,269]

Strong one-electron molecular n-dopants necessarily have low IP and so can be highly air-sensitive. The n-dopants used in this work –pentamethylrhodocene dimer, $(RhCp^*Cp)_2$ and ruthenium (pentamethylcyclopentadienyl)(mesitylene) dimer, $(RuCp^*mes)_2$ – are *not* simple one-electron reductants; these compounds react with oxidants to form the corresponding monomeric cations; the potentials for this reaction (both ca. –2 V), shown in **Figure 5.2**, are obtained according to:

$$E(M^+/0.5M_2) = E(M^+/M) + \Delta G_{Diss}(M_2)/2F \qquad \textit{Equation 5.1}$$

where $E(M^+/M)$ is obtained from the cyclic voltammetry (CV) of the corresponding monomer cation and $\Delta G_{Diss}(M_2)$ is estimated from DFT calculations.[271] This coupling of electron-transfer and bond cleavage processes results in materials that are moderately air stable, despite their strongly reducing character. Both of these compounds have been used as dopants for organic semiconductors[272–274] and for reducing the work function of oxide electrodes.[275,276] Pentamethylrhodocene dimer has also been recently demonstrated to dope SLG, causing the work function to decrease by 1.29 eV.[139]

The hypothetical potential corresponding to the work function of pristine FLG, determined to be 4.43 eV in this work, is represented by a gray box in **Figure 5.2**, the vertical height of which represents experimental uncertainties in determining the absolute potential of $FeCp_2^{+/0}$ relative to vacuum.

In this study, we investigate the solution-doping of FLG samples using the six molecular p- and n-dopants shown in **Figure 5.2** and evaluate the extent to which the strength of the dopant and dosage can tune the electronic, optical and transport properties of FLG and its FoM as a TCE. Our study of solution-doped FLG shows the ability to tune the work function of graphene over a very large range of 2.4 eV (between 2.9 to 5.3 eV), while improving the transport properties and FoM of FLG commensurately with the doping strength of the metal-organic molecular dopants.

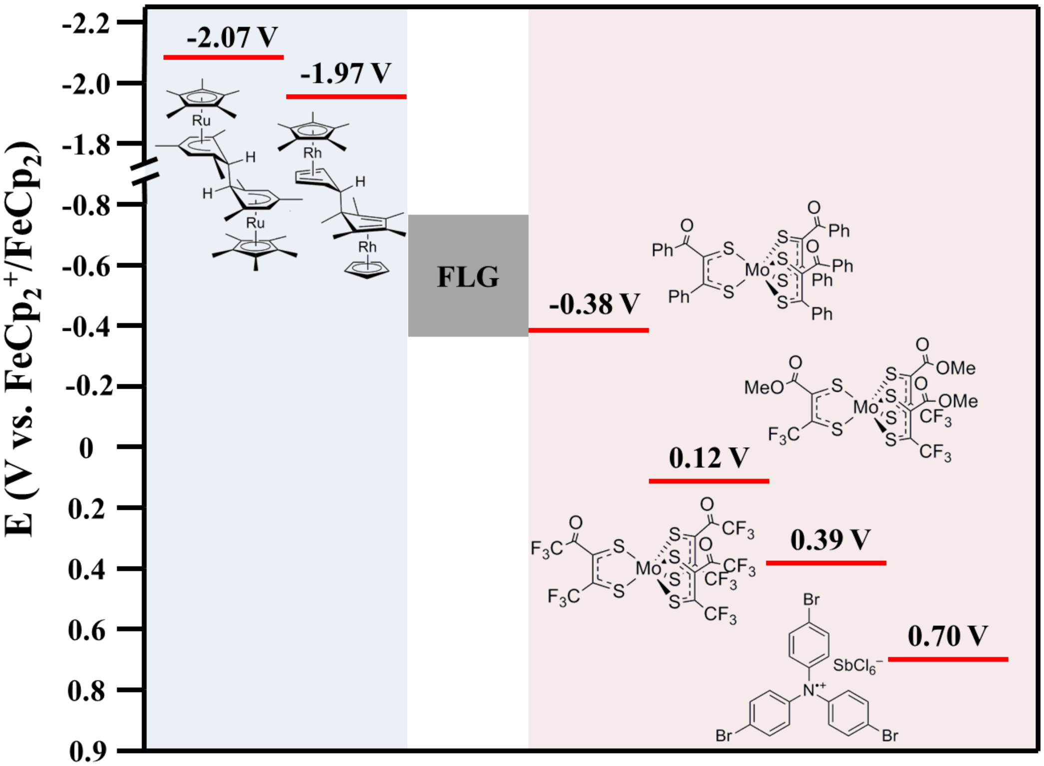

Figure 5.2: The chemical structures of dopants used in this work and their redox potential vs. the ferrocenium/ferrocene couple. The strength of the dopants is defined by the separation of these levels from the EF of graphene in either direction. The FLG value represents the effective potential of pristine graphene is based on –Φ/e, where Φ is the work function determined by UPS, allowing for the uncertainty in the absolute value of the ferrocenium / ferrocene vs. vacuum (–4.8 to –5.2 eV).

5.2 Results and Discussion

5.2.1 Surface coverage of dopants on FLG

Doping was achieved by immersing FLG on glass in dichloromethane (Magic Blue) or toluene (other dopants) solutions of the dopant for multiple durations (more detail is given in **Chapter 3**). The immersion allows for dopant-induced electron transfer at the surface, which is anticipated to produce charged dopant ions adhered to the oppositely charged FLG surface, but can also potentially result in the strong physisorption of neutral species, which would not contribute to the carrier density. Subsequent rinsing of the substrate is expected to remove weakly physisorbed neutral dopants, but, depending on the strength of dopant-graphene interactions some more strongly unreacted material may remain (as seen for example in SLG heavily n-doped with $(RhCp^*Cp)_2$).[139]

For the molybdenum-based p-dopants, the doping step does not result in a change in dopant composition. With Magic Blue, however, the hole injection to the graphene neutralizes the ammoniumyl species which, no longer coulombically bound to either the FLG surface or the hexachloroantimonate counterion, can leave the adhered anion behind. For the n-dopants, the initial doping of the graphene results in the decoupling of dimers followed by a second reduction, but with no net change in atomic composition.

X-ray photoelectron spectroscopy (XPS) was used to determine dopant surface coverage; the results are shown in **Table 5.1**. Integrating the expected signal attenuation due to the inelastic scattering of photoelectrons from the C 1s and Si 2p ionizations allows us to estimate the effective thickness of the FLG on the glass substrate, which typically gives a thickness corresponding to 8-10 layers. Adjusting the C 1s intensity for the number of layers and assuming a uniform FLG thickness, we can estimate the surface coverage of dopants using the atomic ratio of $M/C_{graphene}$, where M is an element exclusive to the particular dopant. The methodology of these calculations is described in more detail in **Chapter 3**.

For all the dopants examined, surface coverage increases with immersion time, although the number of dopants per unit area of FLG shows strong dopant-to-dopant variability as shown in **Figure 5.3**. For example, the weak dopant Mo(PhBz-dt)$_3$ is deposited to afford a coverage of 0.212 Dopants/nm^2 after 180 minutes, while the slightly stronger dopant Mo(tfd-CO$_2$Me)$_3$ only yields 0.0363 Dopants/nm^2 after the same time period. In this particular comparison it is likely that there is some physisorption of neutral species for the weaker dopant (as suggested by UPS data, see below), perhaps due to interactions between its phenyl substituents and the surface.

Table 5.1: Calculation of the dopants coverage for various dipping durations from XPS.

Dopant Treatment	Effective Thickness (nm)	Dopants/C$_{Graphene}$	Dopants/nm^2	Monolayer (%)
Magic Blue				
10 minutes	3.54	0.00134	0.542	25.4
60 minutes	3.43	0.00256	1.00	46.9
180 minutes	3.50	0.00431	1.72	80.8
Mo(tfd-COCF$_3$)$_3$				
60 minutes	2.63	0.000244	0.0731	12.1
180 minutes	2.97	0.000501	0.170	28.1
Mo(tfd-CO$_2$Me)$_3$				
60 minutes	2.51	0.0000976	0.0279	4.6
180 minutes	2.69	0.000118	0.0363	6.0
Mo(PhBz-dt)$_3$				
60 minutes	-	-	-	-
180 minutes	2.66	0.000698	0.212	35.2
(RuCp*mes)$_2$				
60 minutes	2.99	0.00523	1.78	130.1
(RhCp*Cp)$_2$				
60 minutes	2.95	0.0152	5.17	373.5

More generally, for most of the dopants, the XPS data do not enable us to reliably determine the redox state of the dopant and so the relative contributions of neutral and ionic species to the observed surface coverages. However, in the case of Magic Blue, the XPS clearly shows only the elements from the $SbCl_6^-$ counterion and no evidence for any cationic or neutral N- and Br-containing oxidant, suggesting that the Sb coverage can be equated to the number of electrons removed from the graphene. It is worth noting that there is significant discussion in the literature of the distinction between the level of hole or electron transfer to a material and the number of free carriers that are actually generated. Several studies suggest that the free-carrier concentration is substantially lower than would be expected based solely on the number of holes or electrons that appear to have been injected into a material as judged by quantification of the number of compensating ions that would be associated with those charges.[277] Therefore, care must be taken when comparing carrier concentrations determined by measurement of electrical properties of the materials to those that one could simplistically infer by assuming one free carrier being injected per compensating ion.[277] The importance of this distinction will become more apparent below.

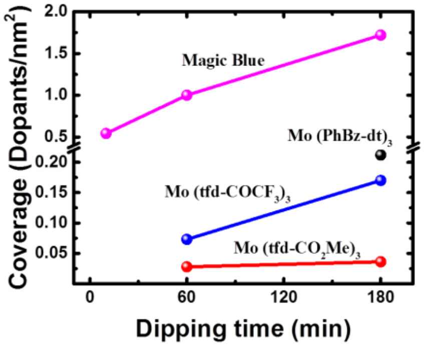

Figure 5.3: Surface coverage of the p-dopants per nm^2 of graphene as a function of dipping time.

5.2.2 Electronic properties of solution-doped FLG

Ultraviolet photoelectron spectroscopy (UPS) was used to measure the changes in FLG work function upon solution-doping. In **Figure 5.4A**, we show the secondary electron cut-off (SEC) of pristine FLG and solution-doped FLG for 60 min (moderate exposure and optimal conditions for transport measurements, as will be shown in below). The SEC shifts to a lower binding energy for p-dopants where the graphene valence band is expected to be depopulated as a result of electron transfer to the dopant molecules (or, in the case of Magic Blue, molecular cations), whereas the opposite trend is observed for n-dopants with electrons transferring from the dimeric dopants into the graphene conduction band. The electron transfer in doped FLG is evident from the shift in carbon core level (C 1s) measured using XPS as shown in **Figure 5.4B** for p-doped FLG, where the peak shifts to a lower binding energy. The peak shift is due to lowering of the Fermi level of graphene into its valence band as a result of electrons being transferred to the p-dopants, which causes the core levels to appear at a lower binding energy.[260] The shift in the C 1s peak increases with the increase of the dopant strength as shown qualitatively in **Figure 5.4B** and more quantitatively in **Figure 5.5B**. The data show a good correlation between the Fermi level shift and the p-dopant redox potential, as expected.

The work function, Φ, was calculated from the measured SEC (Φ = 21.22-SEC) for all samples and is shown in **Figure 5.4C**, along with the work function of pristine FLG (Φ = 4.43 eV). Generally, we find that the shifts in Φ are larger with increasing dopant strength, consistent with expectations that more electrons will be transferred if the difference between the redox potential energy of the dopant and the E_F of graphene is larger.[235] For Mo(PhBz-dt)$_3$ the XPS data suggests a much greater surface coverage than for the other Mo p-dopants, despite its weaker dopant strength and in apparent contradiction to the observed work function shifts. Presumably, this dopant absorbs relatively strongly to graphene in its neutral form, as well as an anion. The work function of FLG was increased by up to 0.6 eV for the strongest p-dopant (Magic Blue) and decreased by 1.5 eV for the strongest n-dopant (RuCp*mes dimer), which to the best of our knowledge, is the largest work-function shift reported to date for solution-based doping of graphene.[139] Overall the work function of graphene can be tuned over a broad range of 2.1 eV from 2.9 eV to 5.0 eV using this moderate exposure time.

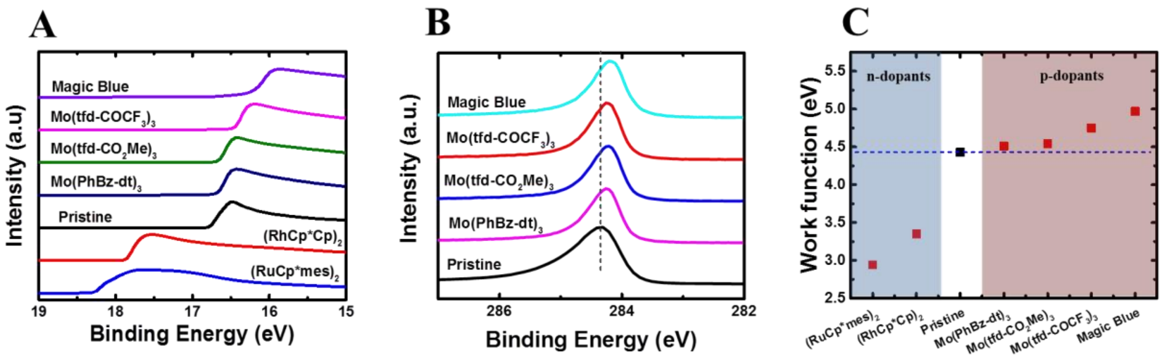

Figure 5.4: Photoelectron spectroscopy on doped FLG. (A) UPS secondary electron cut-off (SEC) of pristine FLG and doped FLG with various n- and p-dopants. (B) XPS C 1s peak for pristine FLG and p-doped FLG. (C) Work function deduced from UPS data in (A) [Φ = 21.22-SEC] for pristine FLG and doped FLG for 60 minutes.

The results reported thus far pertain to a solution-doping time of 60 min. Extending the exposure time further increases the dopant coverage, as evidenced by the increase in the intensity of the dopant-related XPS peaks. These lead to additional shifts of the work function which, however, appear to be minor and dopant-dependent. In **Figure 5.5A**, we have plotted the work function of p-doped FLG for solution-doping times of 60 min and 180 min (extended exposure). The shift seems to increase with dopant strength and appears to be more pronounced in the case of Magic Blue, where the total shift of 0.83

eV after 180 min is considerably higher than the 0.6 eV shift observed at 60 min. The change in work function of doped graphene can result from a Fermi level shift due to the change in the band population resulting from electron-transfer reactions[167,185,235] and/or from a vacuum level shift due to the formation of surface dipoles, as will be discussed in more detail in the Discussion section.[139,233] We have compared the changes of the work function (**Figure 5.5A**) and the shifts of the sp^2 component of the C 1s peak measured by XPS **(Figure 5.5B**) for FLG p-doped for 60 and 180 min. The shifts in the XPS core level (correlated to the Fermi level shift) are smaller than the observed changes in the work function and are not affected significantly by prolonging doping time, indicating that the vacuum level shift dominates the work function shift at longer exposure times, consistent with previous studies. The extended exposure time expands the work-function window achievable for graphene to a very large value of 2.4 eV (from 2.9 to 5.3 eV).

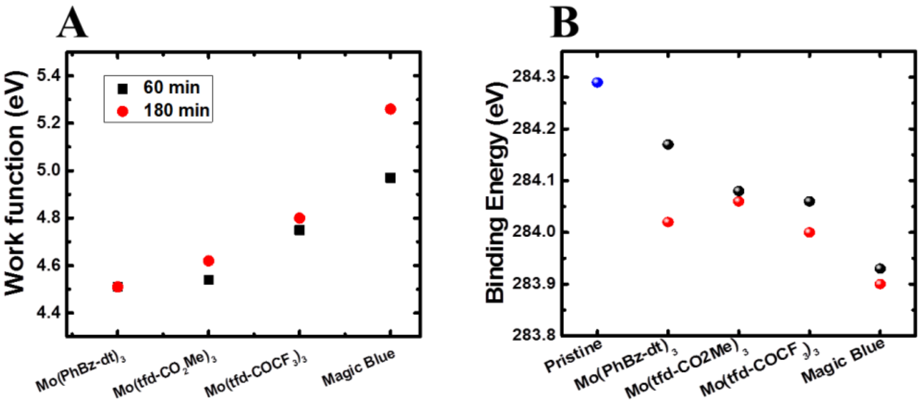

Figure 5.5: (A) Work function of p-doped FLG treated and (B) binding energy of the fitted sp^2 component in the C 1s XPS peak for p-doped FLG for 60 and 180 minutes

The unique electronic structure and underlying phonon-electron resonant Raman scattering processes in graphene make the position, intensity and full width at half maximum (FWHM) of its Raman bands sensitive to the presence of dopant molecules and to changes in the charge-carrier density. Raman spectra of pristine and p-doped FLG

(60 min) are shown in **Figure 5.6A**, showing the two characteristic peaks of graphene, namely the G-peak around 1580 cm^{-1} and the 2D-peak centered around 2750 cm^{-1}.[244] The Raman spectra of p-doped FLG show a shift in the position of the G-peak and 2D-peak towards a higher energy, in agreement with previous results on electrical,[278] electrochemical,[138] and chemical[279] p-doping of graphene. The G-peak of doped graphene always shifts to a higher energy regardless of the type of induced carriers due to the non-adiabatic removal of the Kohn anomaly from the Γ point, while the 2D-peak shift direction depends on the type of doping, where p-type doping causes a shift towards higher energy due to lattice contractions caused by the withdrawal of electrons from graphene.[138]

In **Figure 5.6B and C** we show the Raman shift of the G-peak and 2D-peak, respectively, for pristine and p-doped FLG. The shift in the position of the G-peak is correlated with the strength of the dopant, as shown in **Figure 5.6B**. The largest shift (1.75 cm^{-1}) is observed for FLG doped with Magic Blue. The shift of the 2D peak to a higher wave number as shown in **Figure 5.6C** confirms p-doping of graphene.

For the determination of these Raman shifts, the G-peak was fitted with a single Lorentzian line shape, while the 2D-peak was fitted with two Lorentzian components, a high-energy peak denoted as $2D^H$ (ca. 2746 cm^{-1}) and a low-energy peak denoted as $2D^L$ (ca. 2712 cm^{-1}). We observe that the position of $2D^H$ appears to be insensitive to doping, in contrast to $2D^L$, the position of which generally shifts to higher energy as shown in **Figure 5.7.**

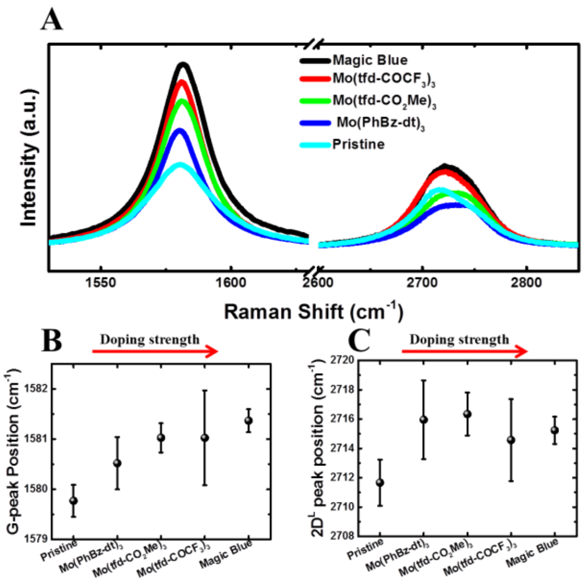

Figure 5.6 (A) Raman spectra of pristine and doped FLG showing the evolution of G-peak (left) and 2D-peak (right) of various p-dopants for 60 minutes dipping time. (B) G-peak position of FLG p-doped for 60 minutes and (C) $2D^L$ peak position of FLG p-doped for 60 minutes.

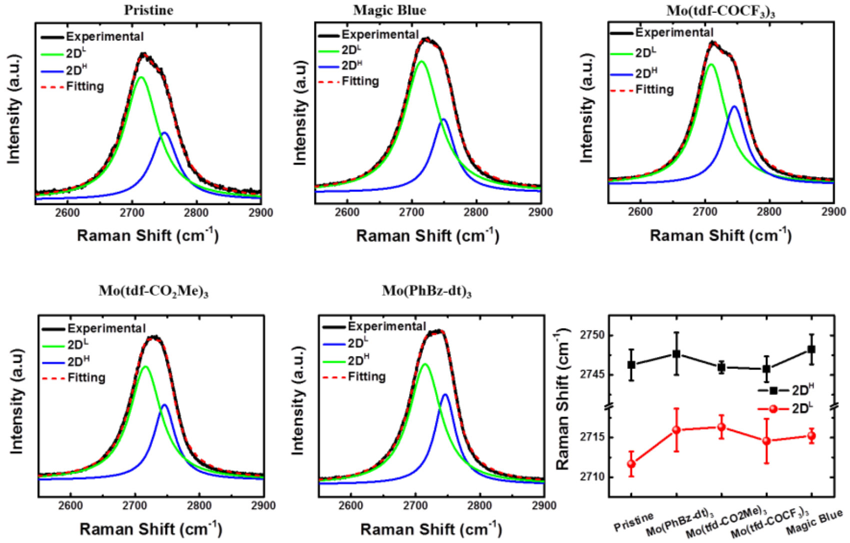

Figure 5.7: Fitting of Raman 2D peak of pristine FLG and p-doped FLG for 60 min and the shift of the fitted components as a function of the dopant strength.

In addition to the energy shift of the G-peak and 2D-peaks, the intensity ratio I(2D)/I(G) decreases as shown in the middle row of **Figure 5.8** with doping for all exposure conditions, in agreement with previous reports on doped FLG.[279]

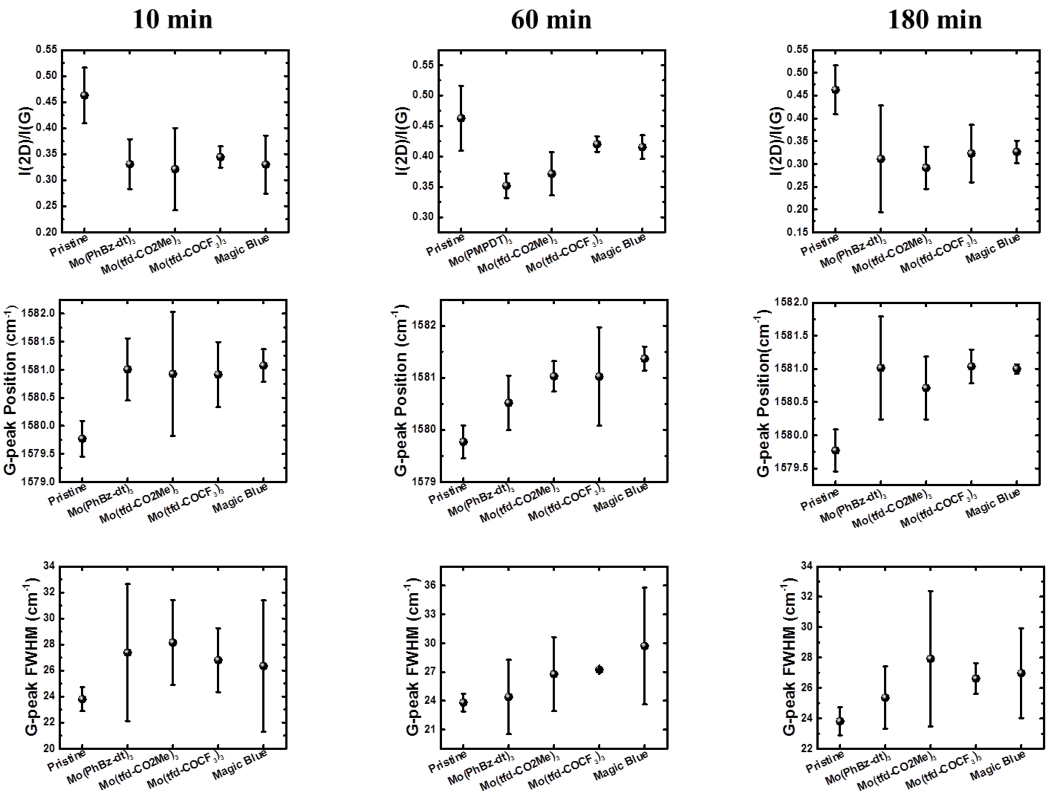

Figure 5.8: The variation of I(2D)/I(G) (top row), G-peak position (middle row) and G-peak FWHM (bottom row) for Pristine and p-doped FLG at 10 min (left column), 60 min (middle column) and 180 min (right column) dipping time.

The doping of SLG has generally resulted in significantly larger shifts as compared with FLG. For instance, doping SLG with Mo(tfd-COCF$_3$)$_3$ yielded a shift of ca. 10 cm^{-1},[139] an order-of-magnitude greater than when doping FLG (this work). The small shift of G-peak was recently interpreted as a lower degree of charge transfer (weaker doping effect) in FLG as compared to SLG.[192] We believe this interpretation may be inaccurate. FLG in this work shows a strong doping effect, as indicated by large shifts in work function and further substantiated by transport measurements in the next section. Instead, we attribute the weak shift of the G-peak to the fact that the Raman signal is a superposition of all layers of the FLG, whereas doping is expected to take place solely on the top-most exposed 1 or 2 layers and is not expected to affect the bulk of the FLG sample as the charge transfer is screened by the neighboring sheets. The stiffening of the G-peak resulting from the transfer of charge carriers to/from the top layers is counteracted by the pristine G-peak signals coming from the bulk. This is supported by the observed increase in the FWHM of the G-peak shown in the bottom row of **Figure 5.8** for all exposure conditions.

5.2.3 Transport properties of solution-doped FLG

Next, we investigate the influence of molecular doping on the transport properties of FLG. The average sheet resistance of pristine FLG measured in our lab is 917 ± 66 Ω/□. As expected, it generally decreases upon both n- and p-doping (**Figure 5.9A**), although the weaker p-dopants Mo(tfd-CO_2Me)$_3$ and Mo(PhBz-dt)$_3$ have minimal effects. The drop in sheet resistance correlates well with the strength of the dopant for both dopant types. The lowest values were observed for p-dopant Magic Blue, reaching a value of 403 ± 35 Ω/□, while it was 427 ± 9 Ω/□ for the n-dopant (RuCp*mes)$_2$.

We compare the FoM of the pristine and doped FLG in **Figure 5.9B**. The FoM nearly doubles for both the strongest p-dopant (Magic Blue) and the strongest n-dopant ((RuCp*mes)$_2$). The increase of FoM is attributed to the significant decrease in the sheet resistance at the cost of only 8% reduction in transmission as compared to the pristine sample. To elucidate the factors influencing the changes in sheet resistance, we have performed Hall effect measurements. These measurements were performed in air; however, the Van der Pauw conductivities determined were very similar to those from the linear four-point probe measurements conducted in an inert atmosphere (**Table 5.2**); thus, we believe that the Hall effect results are not significantly affected by the reactivity of doped graphene with oxygen or water.

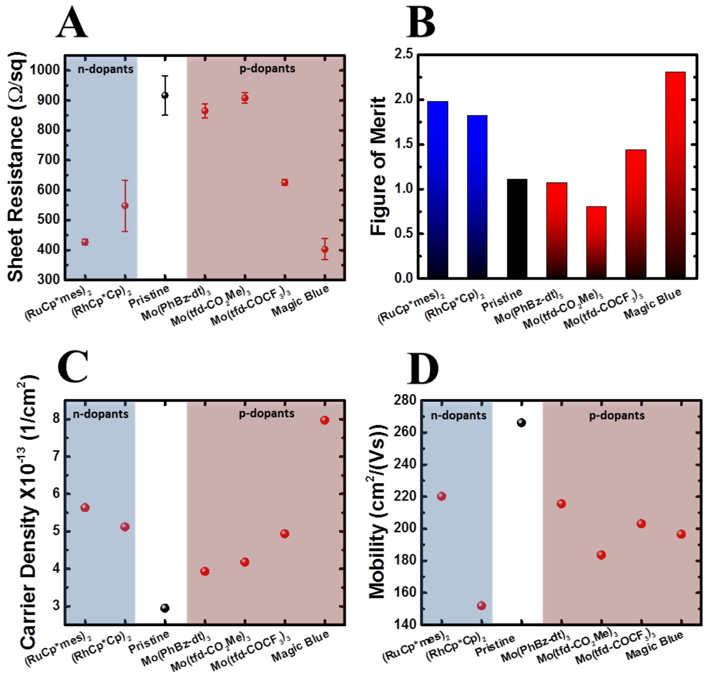

Figure 5.9: Transport properties of pristine FLG and doped FLG for 60 minutes dipping time. (A) Sheet resistance, (B) FoM of pristine sample (black), p-doped FLG (red) and n-doped FLG (blue) (C) carrier density and (D) Hall mobility for pristine FLG, n-doped FLG (blue shaded) and p-doped FLG (red shaded).

Table 5.2: Comparison between the sheet resistance measured by a 4-pt probe in the glove box and that measure using Van der Pauw method in air.

Dopant treatment	10 minutes		60 minute		180 minutes	
	4-pt probe	Van der Pauw	4-pt probe	Van der Pauw	4-pt probe	Van der Pauw
	Ω/□					
Magic Blue	520 ± 44	583	403 ± 35	413	465 ± 26	497
Mo(tfd-COCF$_3$)$_3$	979 ± 15	940	626 ± 10	649	833 ± 5.5	814
Mo(tfd-CO$_2$Me)$_3$	1069 ± 55	891	908 ± 17	847	1108 ± 19	1000
Mo(PhBz-td)$_3$	1078 ± 33	1010	865 ± 23	772	951 ± 54	923

In **Figure 5.9C**, we plot the charge-carrier density of solution-doped FLG samples, where it is observed to consistently increase with increasing dopant strength in agreement with the trend of reduced sheet resistance. Pristine FLG exhibits p-type characteristics with a carrier concentration of ca. 3×10^{13} cm^{-2} and a mobility of 266 $cm^2/(Vs)$. The characteristics of p-type doping of as-prepared graphene have been previously observed, and have been linked to unintentional hole doping due to PMMA residues from the transfer process, in addition to environmental contamination.[112] The measured mobility of pristine CVD FLG is consistent with values reported for CVD graphene,[144,153] and is significantly lower than in mechanically exfoliated graphene,[141] due to the polycrystalline nature and higher defects density of the former. Molecular doping of graphene via electron transfer increases the carrier density while leaving the dopant ions on the surface, which can act as charged impurities that increase the scattering of carriers and hence reduce the mobility as shown in **Figure 5.9D**. The Hall mobility decreases moderately for doped samples, but, for most of the dopants, is more than compensated for by a larger increase in carrier density, which explains the net increase of the conductivity ($\sigma = en\mu$) and measured decrease of the sheet resistance. We confirm the type of doping through the sign of the Hall coefficient (shown in **Table 5.3**), which is then used to deduce the charge carrier density and subsequently the Hall mobility.

The moderate reduction of the mobility in doped FLG in this work (24% and 17% for the strongest p- and n-dopants, respectively) can be contrasted to the larger reductions of mobility in doped SLG (26–80%) as summarized in **Table 5.4**.[180,181,210,280–282] This difference can be attributed to the fact that charged impurities can be screened by each additional graphene layer,[144] so that Coulomb scattering of the charged dopant ions on the surface of FLG doesn't significantly affect the mobility of the buried layers of FLG.

The smaller decrease in mobility for FLG on doping, therefore, less significantly offsets the accompanying increase in carrier density than in SLG. Importantly these results indicate that the transport properties of FLG are more robust to doping and work function modification than those of SLG.

Table 5.3: Sheet Hall coefficient of doped FLG

Sheet Hall coefficient [cm^2/C]							
Pristine	Time	n-dopants		p-dopants			
		$(RuCp^*mes)_2$	$(RhCp^*Cp)_2$	Mo(PhBz-td)$_3$	Mo(tfd-CO$_2$Me)$_3$	Mo(tfd-COCF$_3$)$_3$	Magic Blue
2.1×10^5	10 min	-1.1×10^5	-1.2×10^5	2.4×10^5	2.3×10^5	3.0×10^5	1.3×10^5
	60 min	-	-	1.6×10^5	1.5×10^5	1.3×10^5	7.8×10^4
	180 min	-	-	1.9×10^5	2.3×10^5	2.2×10^5	1.1×10^5

Surface coverage estimates from XPS are in reasonable agreement with the order of magnitude of the calculated carrier densities from Hall measurements, and are similar to those observed for SLG by Paniagua *et al*.[139] For example, Mo(tfd-CO$_2$Me)$_3$, Mo(tfd-COCF$_3$)$_3$, and Magic Blue display coverages of 0.28×10^{13}, 0.73×10^{13} and 10×10^{13} Dopants/cm^2 after 60 minutes, which are roughly comparable to the increases in carrier density.

Discrepancies can arise due to some of the dopant species being physisorbed as neutral species rather than undergoing electron transfer (although, as discussed above, this is not significant in the case of Magic Blue) and/or to some of the dopants reacting with impurities or defects on the surface, or with portions of the graphene that are electrically isolated from the bulk by defects, and, therefore, not generating carriers detectable in the Hall effect measurements. An example of the former effect is presumably occurring with the weakest p-dopant, Mo(PhBz-dt)$_3$, which demonstrates higher coverage but a very low contribution to the carrier density. The n-dopants also display a much lower carrier contribution relative to their surface coverage, which could be due to oxidation from air exposure just prior to the Hall effect measurement. The extremely high coverage of (RhCp*Cp)$_2$ does assist in explaining the drop in mobility of this sample, if the oxidized dopants are indeed acting as scattering sites.

Table 5.4: Reduction in mobility in non-covalently doped SLG presented as the ratio of the change in mobility upon doping $\Delta\mu$ to the mobility in pristine SLG μ_o in each reference.

Dopant	**type**	**$\Delta\mu/\mu_o$**	**Reference**
Mo(tfd-COCF$_3$)$_3$	p	-61%	[139]
Pentaethylenehexamine (PEHA)	n	-48%	[180]
Poly(ethyleneimine) (PEI)	n	-62%	
Triethylene tetramine (TETA)	n	-26%	[181]
Nitric Acid (HNO$_3$)	p	-78%	[282]
Hydrazine	n	-37%	
Poly(ethyleneimine) (PEI)	n	-67%	
Tetraacyanoethylene (TCNE)	p	-80%	[210]
Gold Chloride (AuCl$_3$)	p	-37%	[281]
NH$_2$-SAMs	n	-53%	[280]
Impurities on SiO$_2$ substrate	p	-64%	

The air-stability of surface doped FLG was examined by monitoring the changes in the sheet resistance of FLG doped with Magic Blue over 7 days, while storing the sample at the ambient pressure and temperature. **Figure 5.10** shows that the sheet resistance increases by ~12%, which is generally considered stable as compared to other surface dopants such as $AuCl_3$ which would increase by ~40%.[196] While the surface-doped electrode degrades in air, it is not expected to behave this way when buried inside a device that is in addition encapsulated. This demonstration is outside the scope of this study.

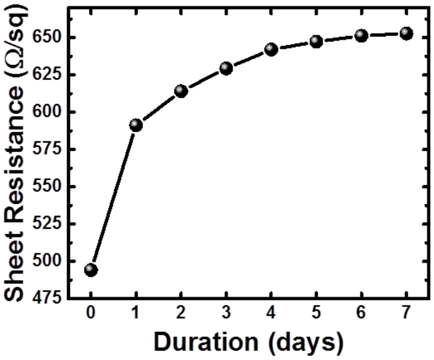

Figure 5.10: Changes in the sheet resistance of Magic Blue doped FLG over 7 days in air at ambient pressure and temperature.

5.2.4 Effect of doping time on the transport properties of solution-doped FLG

Aiming to determine the optimum dopant amount to yield the best performance of FLG as a TCE, we have varied the dipping time of samples in the dopant solutions and then characterized the transport properties and surface morphology. In **Figure 5.11A**, we plot the sheet resistance with respect to solution-dipping time for all p-dopants. Dipping the samples for 10 min (mild exposure) generally yields no significant reduction in the sheet resistance compared to the pristine sample with the exception of Magic Blue, the strongest p-dopant.

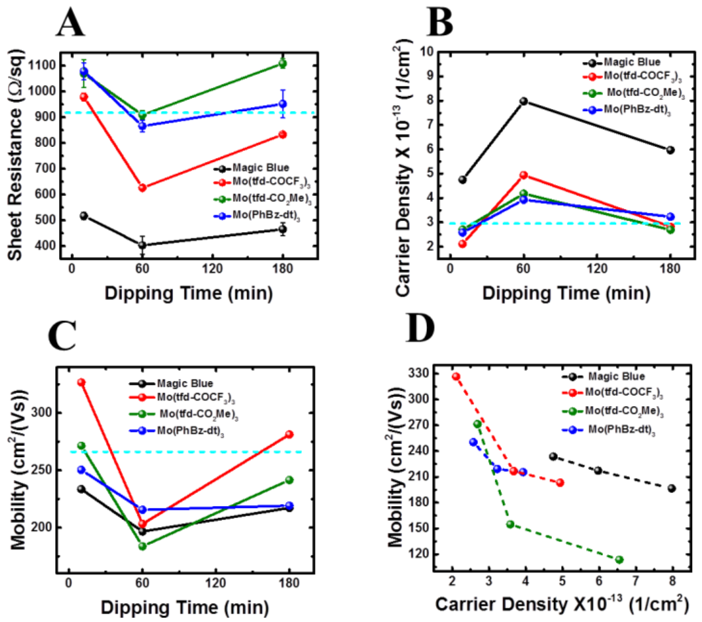

Figure 5.11: Effect of doping time on the transport properties of FLG. (A) Variation in Sheet resistance, (B) carrier density and (C) Hall mobility for p-doped FLG with various doping time (10, 60 and 180 minutes). The light blue dashed line represents the corresponding value of the pristine FLG sample for comparison. (D) Mobility vs. Carriers density of p-doped FLG.

The sheet resistance dips to a minimum at the 60 min mark, after which it rises steadily for all dopants. This trend can be understood by measuring the variations in the carrier density and Hall mobility, plotted in **Figure 5.11B** and **C**, respectively. The data show a poor doping level initially for mild exposure time (10 min) which, increases with dipping time up to 60 min. Longer exposure to the dopant solution reduces the carrier density indicated by the Hall effect measurements and increases the mobility, suggesting less efficient generation of free carriers. This will be discussed in the next section.

To gain insight into the dominant scattering mechanism in molecular-doped FLG, we have plotted the mobility as a function of carrier concentration for p-dopants (**Figure 5.11D**). The observation of a universal negative correlation for all dopants suggests that charged impurity scattering (i.e., scattering by the charged dopant ions present on the surface) is the main scattering mechanism. However, the role of defects and phonon scattering cannot be completely excluded, since heavily p- and n-doped graphene could be reactive to nucleophiles and electrophiles respectively, and potentially such species could be present in solvent as trace impurities or even in glovebox atmosphere.

5.2.5 Effect of doping on the surface morphology of FLG

We examine the surface morphology of doped FLG via scanning tunneling microscopy (STM) for clues about the adsorption and aggregation behavior of molecular dopants for different solution-doping durations of 10, 60 and 180 min. In **Figure 5.12**, we show the STM topographic images of pristine FLG (**Figure 5.12A)** and FLG-doped with the Magic Blue p-dopant (**Figure 5.12B-D**). The dopant appears as bright spots on the surface of FLG as indicated by the red arrow in **Figure 5.12B**. At the lowest exposure time of 10 min (**Figure 5.12B**), we observe the formation of a disjointed molecular wire, presumably of $SbCl_6^-$ dopant ions or small clusters thereof, extended several tens of nanometers across the sample. Presumably, like-charged dopant ions would not aggregate on a completely uniform graphene surface for Coulombic reasons and the aggregation here may be driven by inhomogeneities (e.g. grain boundaries) in the underlying electrostatic landscape of the FLG. Increasing the solution-doping time to the optimum 60 min duration results in a uniform distribution of nanoclusters and nanowires across the entire sample surface (**Figure 5.12C**). At the extended solution-doping time (180 min), the surface appears to be covered with molecules as we no longer see the isolated bright spots, indicating nearly full coverage of the FLG surface. Visually, these images correspond well to calculated monolayer coverage (assuming hexagonal close-packing of

$SbCl_6$ ions) of ca. 25, 47, and 81% of a monolayer for the 10, 60, and 180 minutes immersed samples respectively, keeping in mind that these values may not indicate a continuous monolayer (i.e. clusters and bare patches may exist) and that well-dispersed single dopant molecules might not be observable by STM.

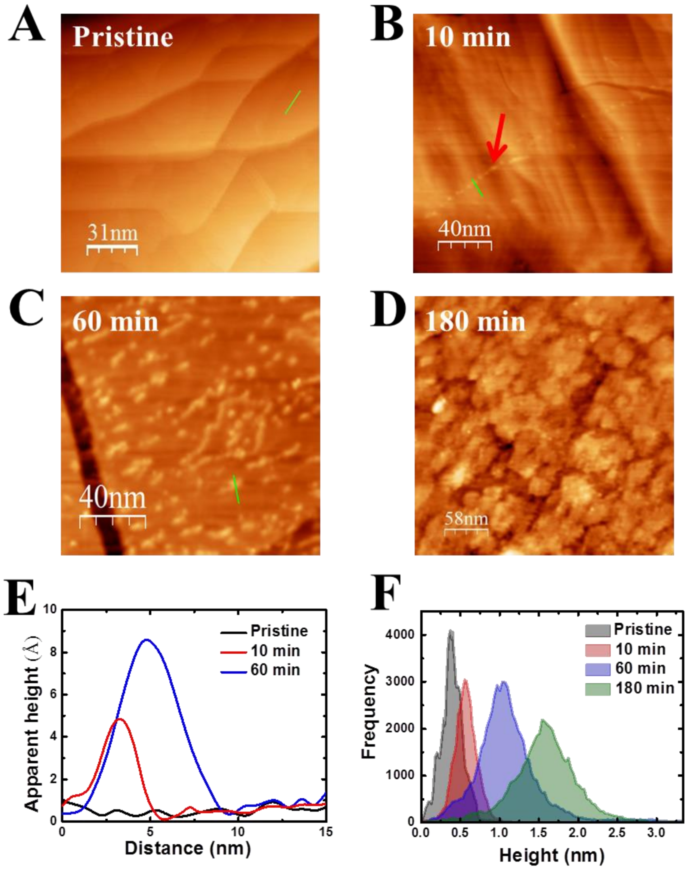

Figure 5.12: STM images (V_b = 0.6 V, I_t = 0.3 nA) of (A) pristine and p-doped FLG with Magic Blue for (B) 10 min with the red arrow pointing to dopants, (C) 60 min, (D) 180 min and (E) line profiles along for pristine FLG and Magic Blue-doped FLG for 10 min and 60 min along the green lines shown in a, b and c (F) corresponding height distributions of pristine FLG and Magic Blue-doped FLG for various exposure times.

Topographic line scans (**Figure 5.12E**) confirm the surface features become increasingly taller and coarser, as an indication of clustering of the dopant ions over time. This is further supported by the statistical distribution of apparent surface height shown in

Figure 5.12F, which exhibits an increase in the mean apparent height and the width of the distribution.

5.2.6 Discussion

Theoretical and experimental studies have identified Coulomb impurity scattering as the dominant scattering mechanism in graphene, rather than other common scattering mechanisms, such as short-range (defect) and phonon scattering.[135] In pristine graphene, random impurities providing both negative and positive charges coexisting on the surface of graphene and in the underlying substrate are believed to generate electron-hole puddles that form the main scattering mechanism.[144] Due to the presence of the electron-hole puddles in pristine graphene, the initial stage of doping has been reported to act as a neutralizing stage for such impurities, which results in no increase in the carrier density in graphene.[136] In addition, the mobility either increases or minimally decreases in that regime, contrary to what is expected for the charge-impurity scattering mechanism explained above. This regime resembles the behavior of solution-doped FLG for the shortest dipping time (10 min). Here, dipping the FLG in the dopant solutions (toluene and DCM) inside the glovebox is likely to further clean the surface from PMMA residues and environmental contaminants, hence leading to a more intrinsic pristine FLG mostly by eliminating the p-type characteristic of FLG ascribed to its preparation and transfer, rather than to molecular doping alone. Indeed, the p-doping resulted in no increase in the carrier density in FLG and the measured mobility was either unchanged or slightly higher than pristine graphene, depending on the dopant used. An apparent exception to this behavior was that of Magic Blue, which has the highest redox potential and can presumably also dope the FLG in a shorter time scale due to its higher doping strength.

The initial increase in mobility reported for some molecular dopants has been observed before[162] and was theorized to result from a compensation effect of the random charged impurities between the graphene and the substrate where the molecules push such impurities farther from the graphene surface.[136]

Upon increasing the dipping time to 60 min, the induced charge-carrier density increases in accordance with dopant strength, while the mobility drops due to charge-impurity scattering as discussed earlier. This regime presents the optimum condition for FLG doping, as the reduction in mobility is compensated by the larger increase in the carrier concentration and hence yields the lowest sheet resistance values.

Further increasing the doping time (180 min), reverses the positive trend in conductivity, where the carrier concentration decreases while the mobility increases and was recently reported to universally occur for various dopants on graphene.[281] Increasing the concentration of dopants can either cause more clustering of dopants[191] – as we have observed in **Figure 5.12B** and **C** – or change their orientation and can even promote the layer-by-layer growth of multilayered structures, which we suspect is occurring in **Figure 5.12D**.[232] Layering of the dopant may decrease the likelihood of forming additional charged impurity scattering centers and may in fact decrease the scattering as compared to FLG doped for 60 min as the dopants would lie farther from the graphene surface due to dopant-dopant interactions, which would explain the increase in mobility at this stage. Surprisingly, the transport measurements (**Figure 5.11**) show a decrease in carrier densities at higher dipping times despite a higher surface coverage of dopant species. While previous studies have found that longer exposure times can result in a lower doping efficiency, i.e., a lower % of the dopants present undergoing electron transfer, the absolute number of carriers still increases.[139] Moreover, at least in the case of Magic Blue, XPS analysis indicates the presence of increased levels of Sb and Cl on the surface (and the absence of Br and N), suggesting more $SbCl_6^-$ is present and, therefore, that more holes are introduced at longer exposure times. The work function continues to shift as well with increased dipping time, an effect which is more prominent in the case of Magic Blue (**Figure 5.5A**). It is believed that the vacuum level shift contribution due to dipole formation may dominate at this stage, since the shift in the Fermi level, as deduced from the shifts in the XPS C1s peak, appear to be negligible between doping times of 60 and 180 min for most dopants as shown in **Figure 5.5B**. Note that this is generally expected, since the relative importance of vacuum level shift vs. band filling / emptying increases with dopant coverage, as the former is proportional to the number of dopants that react whereas the latter is a function of the square root of the number of dopants that react.[139] The explanation for this behavior is not clear at the present stage, but the data imply that at higher exposure times, a large portion of the carriers expected to be generated by the dopant is not able to contribute to the Hall current.

These results reveal that while molecular doping can be effective in its current form, challenges remain to understand the effects of long exposure time and of high dopant coverage and to obtain further improvement in the FoM. The described effects of the dopant coverage on the transport properties and morphology of FLG, are summarized in **Figure 5.12**.

5.3 Conclusion

We have demonstrated the effect of molecular doping on FLG using solution-processed and stable metal-organic n- and p-dopants exhibiting a wide range of doping strengths as measured by their redox potentials, compared approximately to the potential of electrons at the Fermi level of pristine FLG. The effect of dopants on the work function, sheet resistance, carrier density and Hall mobility was presented and generally showed a direct correlation with the dopant strength. The wide tunability range of the work function of doped FLG combined with minor reductions in the carrier mobility as compared with SLG, where there is no screening of Coulomb scattering from the charged dopants, allows for the opportunity to produce FLG layers with high mobility and broadly tunable work function for utilization in electrode applications and beyond. Doping is shown to occur via electron transfer between FLG and the dopants, leaving the latter as a charged ion (charged impurity) on the surface. This is shown to have a neutralizing effect on the substrate-induced impurities at low dopant concentration leading to a slight change of the mobility, which even increased in some cases. At moderate doping levels, the dopant species on the FLG surface lead to charge-impurity scattering and consequently to a decreased mobility. However, due to the large induced carrier density, the sheet resistance is minimized at this stage and the FoM of FLG increases in all instances. With prolonged exposure, the sheet resistance increases and the number of free carriers in the FLG decrease in apparent contradiction to what can be inferred from XPS and UPS, presumably suggesting that a large proportion of the contributed carriers are immobile. The sheet resistance values presented for doped FLG are suitable for touch screen applications which typically require values $< 500\ \Omega/\square$. However, our finding of markedly different behavior in different doping regimes emphasizes the necessity of experimental methods of controlling the amount of molecular doping in FLG, which can play an important role towards enhancing the FoM for utilization of FLG as a TCE in optoelectronic and photovoltaic applications.

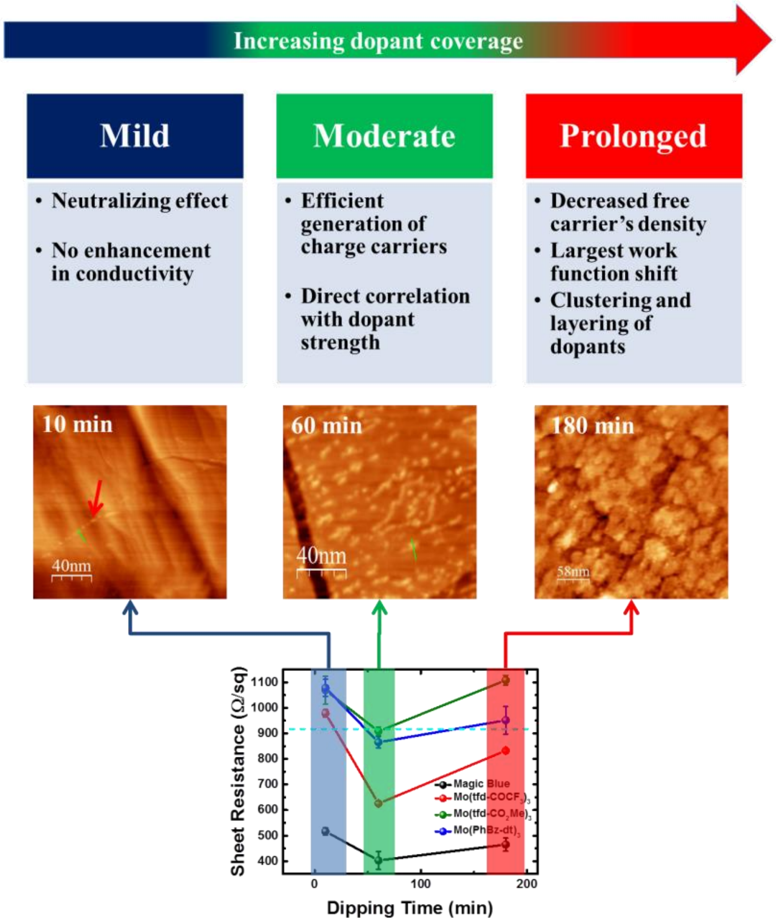

Figure 5.13: Doping mechanism of FLG as a function of coverage and its effect on the transport properties and morphology of doped FLG.

CHAPTER 6
Novel Hybrid Doping Strategy of FLG via a Combination of Intercalation and Surface Doping

Ahmed E. Mansour, Ahmad R. Kirmani, Aram Amassian*

King Abdullah University of Science and Technology (KAUST), KAUST Solar Center (KSC), Division of Physical Sciences and Engineering (PSE), Thuwal, 23955-6900, Saudi Arabia

Stephen Barlow, Seth R. Marder

Center for Organic Photonics & Electronics and School of Chemistry & Biochemistry, Georgia Institute of Technology, Atlanta, GA, 30332-0400, USA

In preparation

Chemical doping of graphene is a promising route towards facilitating its use as a TCE in various applications. Most studies of chemical doping have focused on the use of surface molecular dopants, which undergo charge transfer with graphene leading to improved conductivity and a significant shift of the work function. However, the resulting conductivity is still below the industrial standards for TCE applications. In addition, the dopants are exposed at the surface, making them more prone to the surrounding environment which can jeopardize the long-term stability of the TCE. As shown in this thesis, FLG can be intercalated with various species leading to low sheet resistance and extremely high carrier density. The intercalation doping maximizes the number of layers being doped in FLG in addition to the intercalants being encapsulated between the graphene layers, enhancing their long-term stability. In this work, the combination of the benefits presented of these two doping modalities in FLG is presented in a facile multi-modal doping strategy (hybrid doping). FLG intercalated with Br_2 *or* $FeCl_3$ *have been further doped with surface molecular dopants, leading to lower sheet resistance and larger tunability in the work function. Angle-resolved XPS was used to locate the position of the dopants being either on the surface of in the bulk. The further increase in the conductivity is attributed to the increase in the carrier density due to additional charge transfer with the surface dopants, while the mobility is not affected as evident by Hall effect measurements. The work function increases further after surface doping, which was attributed to contributions from shifts in the vacuum energy level as a result of surface dipoles resulting from the charge transfer.*

6.1 Introduction

FLG offers a unique platform pertinent to the modulation of the electrical and electronic properties by doping. Being amenable to intercalation of small molecules in a manner similar to GIC, allows for effective doping of the bulk of FLG depending on the staging of the intercalate molecules,[213,214] thereby achieving high carrier density on the order of 10^{15} cm^{-2},[64,125] a regime which isn't accessible with the conventional molecular surface doping of both SLG and FLG. Moreover, the intercalation process eliminates the electronic coupling between graphene sheets, thus the overall conductivity results from doped individual layers acting as parallel channels for the charge carriers[225] thereby decreasing the sheet resistance to values as low as 8.8 Ω/□ for mechanically exfoliated FLG.[125] Molecular surface doping of graphene has proven to be an effective route to modulate its work function,[181,198,232,235] in addition to increasing the conductivity which, however, is limited by the significant decrease in the carrier mobility due to Coulomb scattering by charged molecules (after electron transfer),[181,210,235,282] an effect that was shown to be minimized in FLG due to screening of such charges by the additional layers in the bulk as discussed in **Chapter 5**. Work function modulation generally occurs via two mechanisms; (1) shift of the Fermi level as a result of electron transfer to/from graphene for n- and p-doping, respectively, and (2) shift of the vacuum level due to the resulting surface dipoles.[139] These two mechanisms can be combinedly achieved via a combination of the two doping modalities just described, namely, bulk intercalation and molecular surface doping, thus have the potential to provide larger tunability of the work function in addition to achieving low sheet resistance.

Herein, we report the first results of such combination using CVD-FLG, that was p-doped through intercalation with either Br_2 or $FeCl_3$ followed by surface p-doping using tris(4-bromophenyl)ammoniumyl hexachloroantimonate “Magic Blue” and molybdenum tris(1-(trifluoroacetyl)-2-(trifluoromethyl)ethane-1,2-dithiolene) “Mo-(tfd-$COCF_3$)$_3$”, or surface n-doping using ruthenium (pentamethylcyclopentadienyl)(mesitylene) dimer “(RuCp*mes)$_2$” and pentamethylrhodocene dimer “(RhCp*Cp)$_2$”. We employ angle-resolved XPS (ARXPS) to gain insights into the position of the dopants in the doped FLG. We find that the intercalants are encapsulated beneath the surface and into the bulk layers of FLG, while the surface dopants are present only at the surface. This compartmentalizes the different dopants which do not mix unfavorably or interact chemically in any meaningful way. Systematic characterization of the electrical transport properties shows that the enhancement of the conductivity is dominated by the increase of the carrier density from ~ 3×10^{13} cm^{-2} to ~ 6×10^{14} cm^{-2} , thus compensating the decrease in the mobility from 289 $cm^2/(Vs)$ to ~ 90 $cm^2/(Vs)$ with a significant contribution coming from the intercalant dopant. The surface dopants are observed to additionally increase the carrier density, without affecting the mobility since the related Coulomb scattering is screened by the topmost graphene layers. Accordingly, an overall increase in the conductivity is achieved using the hybrid approach with the sheet resistance dropping from ~ 863 Ω/□ to ~ 100 Ω/□. We show that the work function is further increased with surface doping of intercalated FLG up to 5.43 eV shifting by 0.55 eV as compared to the shift of ~ 0.40 due to intercalation alone. This is due to additional contribution from the vacuum level shift due to the formation of surface dipoles from surface dopants. The presented approach allows for fine tuning of the optoelectronic properties and the work function of graphene-based TCEs to meet the specific requirements of a broad range of applications.

6.2 Results and Discussion

CVD grown FLG on nickel was transferred to a glass substrate using the modified PMMA transfer procedure detailed in **Chapter 3** and **Appendix B**. The samples were first intercalated with either $FeCl_3$ using the two-zone vapor transport process for 360 mins or Br_2 using vapor exposure at room temperature for 180 mins (intercalated). Surface doping was then carried out by dipping the intercalated FLG (bulk-doped) in solutions of either the p-dopants Magic blue (hybrid A) or Mo-(tfd-$COCF_3$)$_3$ (hybrid B) or the n-dopants (RuCp*mes)$_2$ (hybrid C) and (RhCp*Cp)$_2$ (hybrid D) for 60 mins.

The intercalation process was carried out as the first step to prevent potential chemical reactions with the intercalant and the surface dopants, considering the reactivity of both $FeCl_3$ and Br_2, in addition to the high-temperature processing involved in the former (360 ^{o}C). Interaction of the surface molecular dopants is limited to the surface of graphene and thus is not expected to interact with the intercalants since they are encapsulated in between the graphene layers as illustrated in **Figure 6.1**. A crucial step in the doping procedure is the washing step of intercalated FLG aiming to remove unreacted and weakly adsorbed intercalants from the surface so that the following surface doping step using can proceed without unfavorable interactions with the intercalants on the surface of FLG. $FeCl_3$-FLG was washed with DI water considering the hygroscopic nature of $FeCl_3$, and Br_2-FLG was washed with ethanol which was demonstrated to be efficient in removing weakly adsorbed bromine from FLG surface in **Chapter 4**. It is worth mentioning that Br_2 can potentially bind covalently with carbon,[124,256] and thus its presence on the surface cannot be excluded. Such a covalent binding will reduce the available interaction surface for surface dopants as will be discussed below.

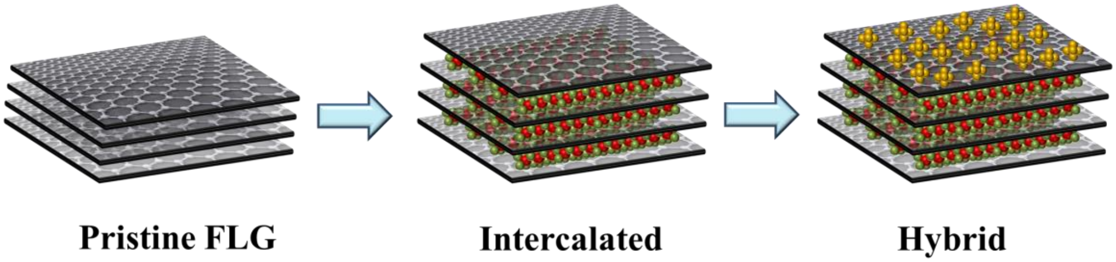

Figure 6.1: Schematic of the hybrid doping approach, showing $FeCl_3$ *intercalants encapsulated in between the graphene layers in FLG, while the* $SbCl^{-6}$ *ions from the surface dopant Magic blue are exclusively present at the surface in hybrid doped FLG.*

6.2.1 Doping effect and the chemical composition of the hybrid-doped FLG

Figure 6.2A shows survey XPS spectra of pristine, $FeCl_3$ intercalated and hybrid doped FLG with Magic blue as the surface dopant (hybrid A1). The coexistence of bulk and surface doping is evident by the mutual appearance of Sb 4d (surface) and Fe 3p (bulk) peaks in the hybrid doped sample as shown in the inset of **Figure 6.2A**. Similarly, the survey XPS spectra of Br_2 intercalated and hybrid doped FLG shown in **Figure 6.2B** indicates the coexistence of bromine intercalant (Br 3d) and antimony (Sb 4d) from the surface dopant. High-resolution XPS C 1s peak shifts to a lower binding energy from 284.10 eV for pristine FLG to ~ 283.85 eV for $FeCl_3$ intercalated FLG and further to 283.70 eV once the surface dopant Magic blue is added, which is a consequence of p-doping as shown in **Figure 6.2C**. Br_2 intercalated FLG shows a similar trend, but with smaller shifts, where the C 1s downshifts to 283.90 eV after intercalation, where it slightly shifts after surface doping as shown in **Figure 6.2D**. The further decrease in the C 1s binding energy in hybrid doped FLG, indicates that surface doping can additionally p-dope the intercalated FLG and additionally lower the Fermi level. This points to the fact that the surface dopant increases the carriers density of intercalated FLG since the shifts in the Fermi energy are directly related to the square root of the induced charge carriers into graphene.[139]

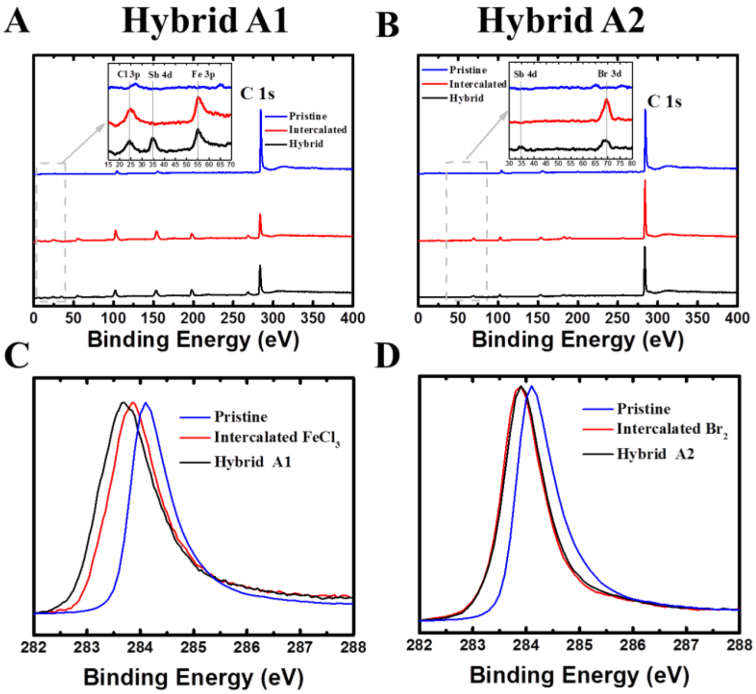

Figure 6.2: Survey XPS spectra showing the coexistence of bulk intercalants and surface dopants (A) $FeCl_3$ intercalation with Magic blue surface dopant –hybrid A1– and (B)Br_2 intercalation with Magic blue surface dopant –hybrid A2–. And high-resolution XPS spectra of core level C 1s peak for pristine, intercalated and hybrid doped FLG for (C) hybrid A1 and (B) hybrid A2.

The larger down-shift of C 1s for the $FeCl_3$ intercalation points to its higher p-doping effect than Br_2 probably due to its ability to form stage-1 intercalation compounds with FLG and thus dopes larger number of graphene layers, whereas bromine can only form a maximum of stage-2 intercalation compounds.[213] This shift of the core level C 1s peak, however, is counter-intuitive to the expected upshift in the binding energy of core level peaks once they lose electrons, since the positive charge of the nucleus becomes less screened and thus increases its binding with the remaining core electrons.

However, such downshift is attributed to the lowering of Fermi energy level in p-doped materials which aligns to the Fermi energy level of the detector in photoelectron spectroscopy instrumentation, to which the XPS spectrum is referenced, as has been previously observed for p-doped graphite,[225,260,261] carbon nanotubes[254] and graphene.[124]

The atomic content of the Sb (surface dopant) gradually increases as the take-off angle decreases (increasingly surface sensitive) as shown in **Figure 6.3A** for hybrid A1 and **Figure 6.3B** for hybrid A2. This confirms the exclusive existence of the molecular dopant (magic blue) on the surface of the intercalated FLG. However, for larger take-off angles (such as 90^o), the measurements are bulk-sensitive and therefore the Sb/C atomic ratio would be expected to be lower as shown in **Figure 6.3A** and **B**. $FeCl_3$ intercalant gradually decreases with increasing surface sensitivity, where the atomic ratio of Fe with respect to C decreases as shown in **Figure 6.3A**, whereas Br_2 intercalant shows a nearly constant atomic content at all electron take-off angles which would be expected for uniformly bulk-doped FLG. We conducted a control measurement on only intercalated FLG and a similar trend in the atomic content of iron for $FeCl_3$ intercalation (**Figure 6.3C**). This indicates the absence of $FeCl_3$ on the surface of FLG and demonstrates the effectiveness of the washing step in our experimental procedure. Moreover, this leads to the conclusion that intercalation of $FeCl_3$ is more concentrated at the bottom surface of FLG closer to the substrate and that a fully stage 1 intercalated FLG has not been achieved, which is currently a limitation for the intercalation of CVD FLG due to intrinsic differences in crystallinity and layers coupling from HOPG. Recent reports on $FeCl_3$ intercalated FLG have shown that full intercalation could only be achieved for mechanically exfoliated FLG which closely resembles the structure of graphite,[125,216,217] whereas in the case of CVD FLG, non-uniform and incomplete intercalation has been reported under the same processing conditions.[238] Additionally, the trend of the atomic content of iron in **Figure 6.3C** could be explained by the fact that desorption of intercalant would be easier from the outer surface of the layers away from the substrate as has been recently demonstrated for $FeCl_3$ intercalated FLG.[216] On the other hand, bromine content in only Br_2 intercalated FLG shown in in **Figure 6.3D** confirms the nearly constant bromine content observed in the hybrid A2 samples, which can be contrasted to the case of $FeCl_3$ intercalated FLG by the fact bromine can potentially form covalent bonds with the basal plane of the topmost layer, and the edges of the sheets throughout the bulk which was demonstrated in **Chapter 4**.[124] A comparison of the total amount of the surface dopant (magic blue) in the hybrid A1 and hybrid A2, shows that the former exhibits a higher atomic content of Sb ~5 at%, while the latter exhibits a significantly smaller amount of ~0.5 at%. This is expected to result from the presence of covalently Br_2 atoms on the surface and edges which are not removed by the washing step, and thus could prevent the surface dopant from interacting with FLG. This is further confirmed by the uniform atomic content of Br with respect to carbon as a function of electron take-off angle where it slightly increases for the lowest angle (20°) indicating the presence of bromine on the surface.

Figure 6.4A shows Raman spectra of pristine and intercalated FLG with either Br_2 or $FeCl_3$. Pristine FLG shows the two main peaks of graphitic materials, namely, the G-peak at ~1580 cm^{-1} originating for the in-plane stretching mode (E_{2g}) originating from the optical phonon near the Γ point, and the second order 2D-peak at ~2743 cm^{-1} arising from two optical phonons at the K point. The D-peak which typically appears at ~1350 cm^{-1} is activated by the presence of defects, exhibits very low intensity indicating the high quality of the graphene domains in our samples.[244]

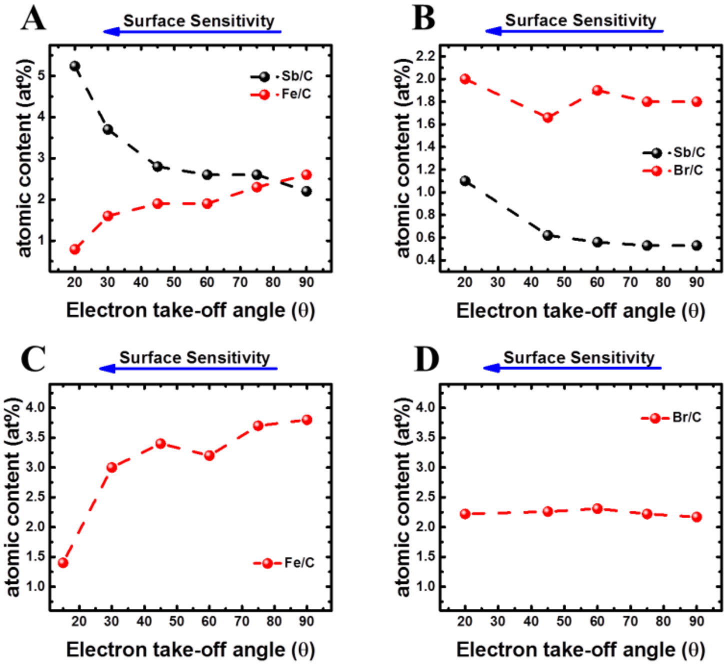

Figure 6.3: Angle-resolved XPS for (A) hybrid A1, (B) hybrid A2, (C) $FeCl_3$ intercalated FLG and (D) Br_2 intercalated FLG. The electron-take off angle (θ) shown on the x-axis determines the surface sensitivity of the measurement, where the smaller value indicates increasingly surface sensitive spectra as indicated by the blue arrow.

The shape of the 2D-peak depends on the electronic structure of graphene films and reflects the stacking order and the number of graphene layers. SLG typically exhibits a single and sharp Lorentzian peak which splits into various components in AB-Bernal stacked graphene layers until it resembles that of HOPG where it is composed of two components, with the lower energy component having approximately ¼ the intensity of the high energy component. However, in the case of turbostratic graphite, the 2D-peak resembles the shape of that for SLG with single Lorentzian peak indicating the absence of layer coupling and resemblance to the electronic structure of SLG.[245] The 2D-peak in our samples could be fitted with two Lorentzian peaks, with the lower energy component being as intense as the high energy component, which is attributed to randomly rotated stacking and agrees with previous results on epitaxially grown FLG.[83]

Upon exposure to the intercalants, the G-peak splits into a doublet as shown in **Figure 6.4A**, with the lower energy peak positioned around that of the pristine FLG and originates from graphene layers not adjacent to intercalant, and a higher energy peak from intercalant bound graphene layers, the position of which is generally dependent on the degree of intercalation and the doping strength of the intercalant.[213,216,257] Raman shifts in the low energy G-peak position are shown in **Figure 6.4B**, with the inset showing the high energy G-peak shifts for intercalated and hybrid doped FLG. Both G-peak components upshift with intercalation and the subsequent hybrid doping, which is a signature of doped graphene.[138] It can be seen that the shift is larger in the case of $FeCl_3$ intercalation indicating a larger doping effect due to its ability to intercalate into every interlayer spacing in FLG (stage 1).[213] This is in agreement with XPS results of the higher atomic content of iron as compared to bromine in **Figure 6.3** and the larger downshifts of C 1s peaks in the case of $FeCl_3$ intercalation (**Figure 6.2).** Furthermore, the upshift of both components of the G-peak continues to increase upon adding the surface dopant to intercalated FLG as shown in **Figure 6.4B**. The same trend is observed for the low energy fitted components of the 2D-peak shown in **Figure 6.4C**, which is more sensitive to doping effects as demonstrated in **Chapter 5**. The additional shifts in the Raman peaks, once the intercalated FLG is treated with the surface dopants, is in agreement with the XPS observation in that the hybrid doping approach contributes towards more efficient doping of all available layers in FLG where the Fermi level additionally shifts as reflected by the additional upshift in the Raman G- and 2D-peaks.The upshift in the G-peak has been observed for doped graphene reflecting the changes in the Fermi energy level and results from the non-adiabatic removal of the Kohn anomaly at the Γ point in addition to changes in the lattice constant where it contracts in the case of electron removal in p-doping and thus stiffens the phonon mode or expands in the case of adding electrons in n-doping and thus softening the phonons.[138,216] In the case of acceptor intercalants, these two mechanisms work together and an overall upshift in the G-peak is always observed. On the other hand, the fact that 2D-peak originates from phonons away from the Γ point, its shifting is only attributed to the latter mechanism, where the upshift is a signature of p-doping due to phonon stiffening as a result of lattice contraction that accompanies the electron transfer away from graphene.

6.2.2 Electrical transport properties of hybrid-doped FLG

The sheet resistance of pristine FLG on glass is 863±81 Ω/□ as measured from linear 4-point probe. Upon intercalation with Br_2 the sheet resistance decreases to 391±13 Ω/□ which is further reduced in hybrid A2 doped FLG to 237±35 Ω/□ as shown in **Figure 6.5A**. A similar trend is observed for the Hybrid A1 doped FLG where $FeCl_3$ intercalation results in a sheet resistance reduction to 137.6±6.4 Ω/□ which further decreases with surface doping to 100.1±3.3 Ω/□.

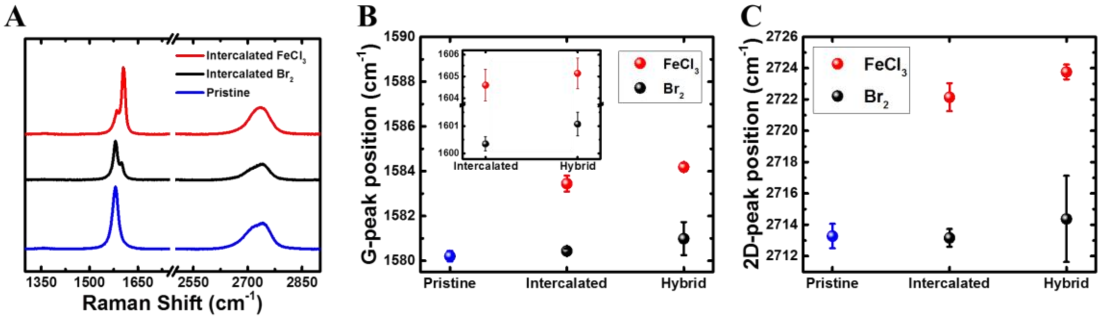

Figure 6.4: (A) Raman spectra of pristine and intercalated FLG with either Br_2 or $FeCl_3$. Changes of the Raman shift of (B) the G-peak components and (C) the 2D-peak low energy component for intercalated and hybrid doped FLG.

We show the sheet resistance of only surface doped sample FLG with Magic blue, which results in a sheet resistance of 414.6±19 Ω/□, demonstrating that the combination of both surface and intercalation doping of FLG is crucial for achieving the highest electrical conductivity. However, it seems that the choice of the surface dopant is important to result in desirable conductivity of the doped sample, since using Mo(tfd-$COCF_3$)$_3$ with $FeCl_3$ intercalated FLG has caused an increase in the sheet resistance to 165.38±9.3 Ω/□, since the effect of the surface dopants results from a balance between the injected charge carriers and the reduction of carrier mobility due to Coulomb scattering as previously described in **Chapter 5**.

To elucidate the effect of the presented doping modalities on the transport properties, we conducted Hall effect measurements on the various stages towards hybrid doped FLG. **Figure 6.5B** shows the changes in the carrier density, which significantly increase after $FeCl_3$ intercalation from 3.05×10^{13} cm^{-2} for pristine FLG to 4.78×10^{14} cm^{-2} nearly an order of magnitude higher that the value obtained for surface doping only with Magic blue (7.98×10^{13} cm^{-2}). The effective doping of a significant number of the graphene layers in the bulk with intercalation is responsible for such high increase in the carrier density as compared to surface doping. However, for Br_2 intercalated FLG the carrier density moderately increases to 5.7×10^{13} cm^{-2} in line with the lower atomic content of bromine as compared with $FeCl_3$ as shown in **Figure 6.3** due to the lower expected staging. For the hybrid doped FLG, the carrier density further increases to 5.91×10^{14} cm^{-2} in the case of hybrid A1, whereas it increases to 8×10^{13} cm^{-2} in the case of hybrid A2, in indication to the cumulative doping effect of both doping modalities. **Figure 6.5C** shows the changes in the charge carrier mobility where it significantly reduces from the pristine FLG value of 289.1 cm^{2}/(Vs) to 89.2 cm^{2}/(Vs) for $FeCl_3$ intercalated FLG due to the Coulomb scattering by charged dopants and the fact that $FeCl_3$ is present throughout the bulk of the sample. The scattering effect has been demonstrated to be minimal in the case of surface doped sample especially for FLG, where the charge dopant molecules (after electron transfer) would be screened by the additional graphene layers in FLG as discussed in details in **Chapter 5**; where the mobility decreases to 196.63 cm^{2}/(Vs) in the case of magic blue doped FLG as shown in **Figure 6.5C**. The addition of the surface dopants to the intercalated FLG in hybrid A1 doped sample does not seem to deteriorate the carrier mobility, which, at 91.4 cm^{2}/(Vs) is nearly equal to that of the $FeCl_3$ intercalated FLG.

Despite the fact that the charge carrier mobility decreases by more than 65%, the carrier density sees an enormous increase by more than 1800% and thus an overall increase in the resulting conductivity is achieved for the hybrid A1 doped FLG. Bromine intercalation, however, shows a moderate effect on the carrier mobility, where the mobility reduces to 255.4 cm^{2}/(Vs) upon intercalation, with a further reduction after the surface dopant is added to a value of 219.5 cm^{2}/(Vs).

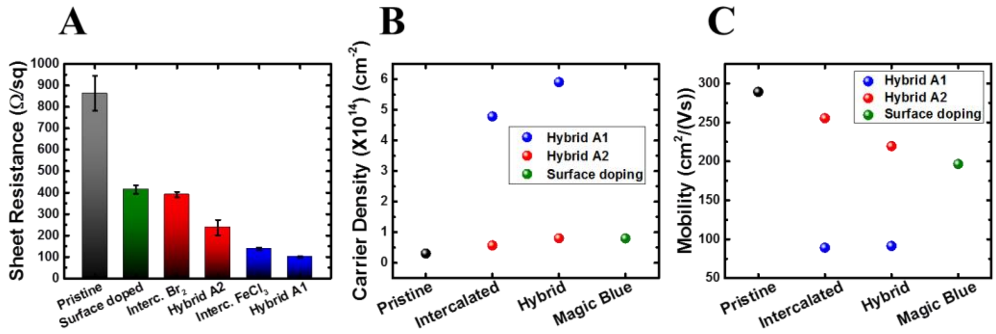

Figure 6.5: Electrical Transport properties. (A) Sheet resistance, (B) Sheet carrier density and (C) and carrier mobility, for pristine, surface doped with magic blue, intercalated with either $FeCl_3$ or Br_2 and hybrid doped FLG.

6.2.3 Work function shifts in hybrid-doped FLG

The effect of the various dopant modalities and their combination on the work function is shown in **Figure 6.6**. The work function was measured using photoelectron spectroscopy in air (PESA), where pristine FLG exhibited a value of 4.88 eV as shown in **Figure 6.6A**. Upon intercalation with bromine (**Figure 6.6B**), the work function increases to 5.08 eV consistent with values obtained in **Chapter 4**. For $FeCl_3$ intercalated FLG, larger work function shift is observed, with an absolute value of 5.29 eV as shown in **Figure 6.6D**. The larger increase in the work function for the case of $FeCl_3$ intercalated as compared to Br_2 agrees with the previously demonstrated XPS, Raman and Hall effect measurement results, which indicates a qualitatively larger shift in the Fermi energy level for the former. Treating intercalated FLG with surface dopants has demonstrated tunability and an additional increase in the work function. The surface doping of Br_2-FLG with magic blue (hybrid A2) further increases the work function to 5.27 eV once the surface dopant magic blue is applied as shown in **Figure 6.6C**. The work function corresponding to the addition of the surface molecular dopants Mo-(tfd-$COCF_3$)$_3$ (hybrid B1) and Magic blue (hybrid A1) to $FeCl_3$ intercalated FLG are shown in **Figures 6.6E** and **F**, respectively.

Hybrid B1 shows a moderate change in the work function of 0.05 eV whereas hybrid A1 leads to a larger shift of 0.14 eV with a work function value of 5.43 eV. Such larger shifts in the latter are attributed to the larger doping strength of magic blue as explained in **Chapter 5**.

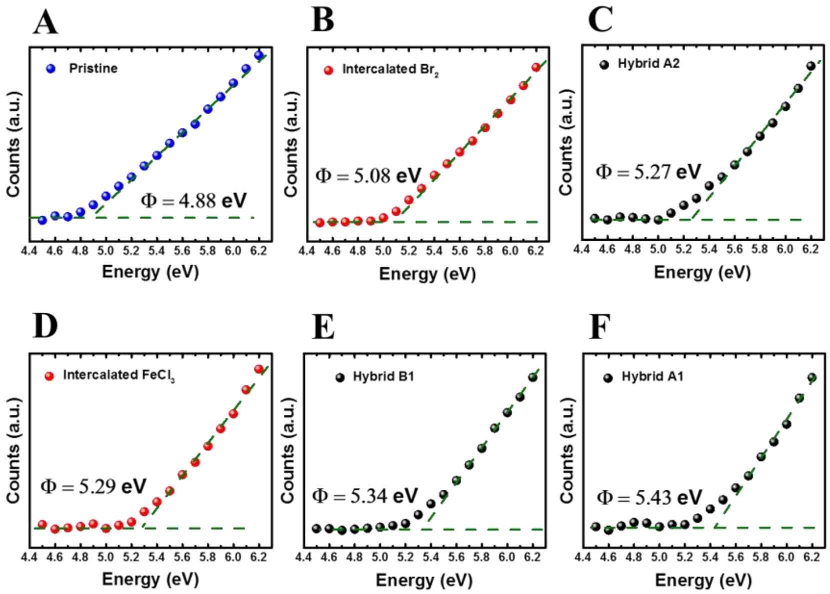

Figure 6.6: Photoelectron spectroscopy in air spectra and the deduced work function for (A) Pristine FLG, (B) Br2 intercalated FLG, (C) Hybrid A2 doped FLG, (D) FeCl3 intercalated FLG, (E) hybrid B1 FLG and (F) hybrid A1 doped FLG.

A comparison between the shifts of the Fermi level approximated from the sp^2 fitted peak in the XPS C 1s core level peaks, and the shifts in the work function obtained from PESA is shown in **Figure 6.7**. The total change in the work function of graphene results from changes in the Fermi energy level as a result of electron transfer and the changes in vacuum level resulting from dipole formation. [139] For $FeCl_3$ intercalation and the hybrid A1 doped FLG (**Figure 6.7A**), the differences between the work function and the Fermi level shifts always exist and are an indication of significant surface dipole contribution to the total work function change.

However, in the case of Br_2 intercalated sample shown in **Figure 6.7B** the shifts in the work function seem to coincide with the shift in the Fermi energy level, where a considerable difference exists once the surface dopants are applied (hybrid A2), indicating that the additional shift comes from vacuum level shifts due to the formation of surface dipoles. The presence of vacuum level shift for $FeCl_3$ intercalated sample in contrast to its absence for the Br_2 intercalated sample may be explained by the fact that the surface dipole dominates the changes in work function at large carrier density due to the linear dependence of such contribution on the carriers density (n) involved in the charge transfer (proportional to n), whereas the Fermi level shift contribution has a weaker dependence (proportional to $n^{1/2}$) **Chapter 2**. Thus, the larger increase in the carrier density for $FeCl_3$ intercalation as compared to Br_2 intercalation as shown in **Figure 6.4B** may lead to considerable molecular dipole buried in the bulk of FLG. For the hybrid doped FLG (A1 and A2), it seems that the additional shifts in the work function are dominated by vacuum level shift contribution, which explains the large changes in the work function as compared to the changes in the sheet carrier density.

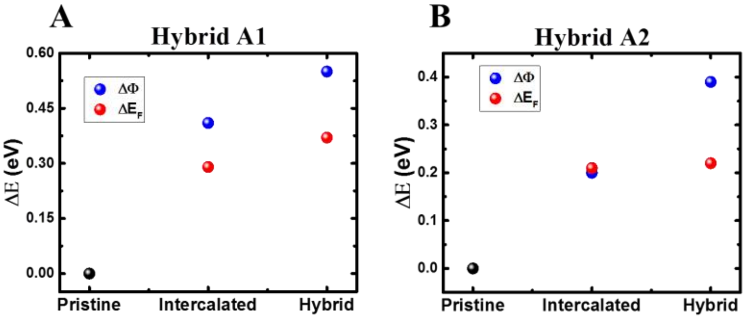

Figure 6.7: Comparison of the changes in the work function and shifts of the sp^2 *carbon peak from XPS C 1s core level for (A) Hybrid A1 doped FLG and (B) Hybrid A2 doped FLG.*

6.2.5 Combining surface n-dopants with bulk p-type intercalants

Aiming to achieve a tunable work function towards a lower energy (decreasing Φ) we have attempted hybrid doping using intercalated FLG with FeCl$_3$ and surface metal-organic dimers (RuCp*mes)$_2$ (hybrid C1) and (RhCp*Cp)$_2$ (hybrid D1), which are strong n-dopants as discussed in **Chapter 5**. Schematics of these structures are shown in **Figure 6.8A** and **B**, respectively. The sheet resistance has increased significantly after applying the surface dopants as shown in **Figure 6.8D and C**, where it increases from 137.6 ± 6.4 Ω/□ for FeCl$_3$ intercalated FLG to 293.9 ± 6.4 Ω/□ for hybrid C1 and to 344.6 ± 31.4 Ω/□ for hybrid D1.

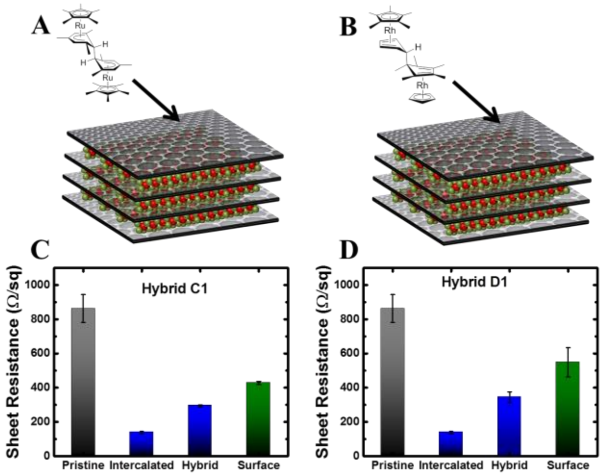

Figure 6.8: Schematics of the hybrid doping of (A) hybrid C1 and (B) hybrid D1. The sheet resistance of FeCl$_3$ intercalated FLG treated with surface n-dopants for (C) hybrid C1 and (D) hybrid D1.

Hall effect measurement was performed on hybrid C1 to elucidate the increase in the sheet resistance. **Figure 6.9A** shows that the surface dopant does not result in any increase in the carrier density, indicating the surface n-dopants are not effectively doping the intercalated FLG. In fact, the charge transfer from surface dopants is expected to decrease the carrier density since electrons will neutralize the hole doped FLG. We attribute the absence of such effects, to the fact that $FeCl_3$ intercalated FLG is heavily p-doped, and thus n-doping would have a minimal effect. However, exposing $FeCl_3$ intercalated FLG to surface n-dopant $(RuCp^*mes)_2$ has resulted in decreasing the carrier mobility as shown in Figure 6.9B, where it decreases from 89.2 $cm^2/(Vs)$ for intercalated FLG to 50.3 $cm^2/(Vs)$ for hybrid C1. This reduction in the mobility can be attributed to the introduction of charged molecules on the surface leading to additional Coulomb scattering.

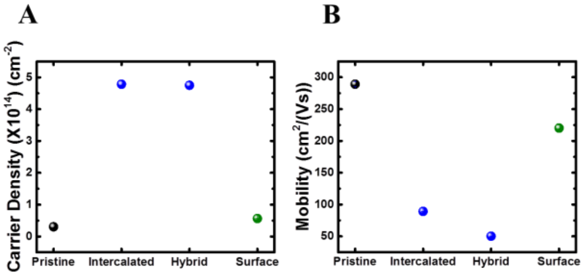

Figure 6.9: Hall effect measurement on hybrid C1 FLG. (A) Carrier density and (B) carrier mobility.

The work function was nearly unchanged for the hybrid C1 and D1 doped FLG, as shown in **Figures 6.10B** and **C**, respectively. The large shift in the Fermi level resulting from p-doping of the bulk may be the reason of the unchanged work function in hybrid doped FLG with n-doping surface molecules. The latter would shift the vacuum level to a direction that would reduce the work function; however, this would be shaded by the significantly large Fermi level shift (towards increasing work function) resulting from bulk doping.

Accordingly, the hybrid doping approach of combining bulk p-dopants with surface n-dopants shows no clear benefits at this stage since the conductivity significantly decreases without resulting in a considerable shift in the work function, and thus defying the main objective of the hybrid doping approach.

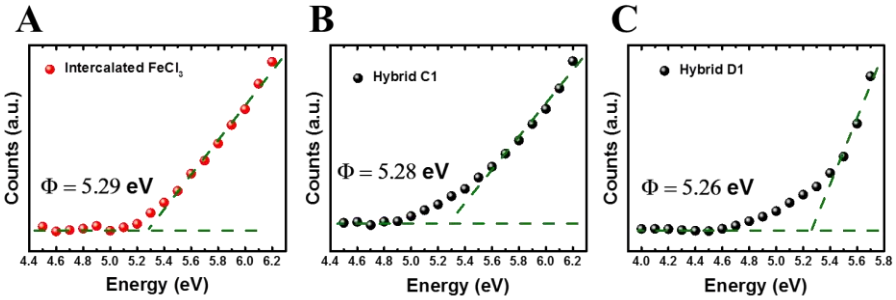

Figure 6.10: *Photoelectron spectroscopy in air spectra and the deduced work function for (A) FeCl3 intercalated FLG, (B) Hybrid C1 doped FLG, (C) Hybrid D1 doped FLG.*

6.3 Conclusion

In conclusion, a novel and general hybrid doping strategy for CVD grown FLG was presented, enabling efficient doping of all the layers in FLG through a combination of molecular surface dopants and bulk intercalation with small molecules. The variation of the chemical composition of hybrid doped FLG with its thickness, reveals the existence of intercalants in the bulk of the films, which dope the interior graphene layers, while the surface dopants are found to be exclusively present on the exposed FLG surface. It is demonstrated that the two doping modalities (intercalation and surface) work in tandem in tuning the electrical transport and electronic properties of FLG. Further p-doping effect was observed after surface doping of intercalated FLG. However, the intercalation has dominated the enhancement in the electrical conductivity. On the other hand, surface dopants have further increased the work function of intercalated FLG, via surface dipole formation. At the current stage, our doping strategy shows work function tunability towards increasing the work function. Attempts to tune the work function to the opposite direction have been attempted by exposing p-doped intercalated FLG to n-doping surface species. However, this results in increasing the sheet resistance without changing the work function. This work introduces a novel hybrid doping strategy for large-scale CVD-FLG that uniquely allows for precise control over the energetics of the bulk and the surface, separately, thereby pushing towards the development of graphene-based TCEs towards photovoltaics and optoelectronic applications.

CHAPTER 7
Conclusion and Future Perspective

The ever increasing cost of ITO as a result of increasing demand in conjunction with its chemical stability issues, and its lack of mechanical flexibility have motivated the search for alternative TCEs. Graphene as a potential replacement for ITO, is a promising emerging TCE, thanks to its high optical transmittance, electrical conductivity, flexibility and chemical stability. While CVD is the most promising route towards large-scale production of graphene as we expound in **Chapter 2**, the state-of-the-art CVD process combined with transfer methods that are prone to introduce defects inevitably result in polycrystalline and defective graphene (either SLG or FLG). This results in inferior conductivity as compared to ITO and to the theoretical predictions regarding the maximum achievable conductivity for graphene, clearly impeding graphene’s potential as an emerging TCE.

The work presented in this thesis, contributes to the efforts of enhancing the conductivity of CVD graphene via different chemical doping modes without significant losses in optical transmittance. A key strategy adopted in this work, is the elimination of the cumbersome layer stacking and interlayer doping processes that limit the applicability of graphene TCEs and impede the objective of the industrial-scale realization of the material. Thus, CVD-FLG, which readily grows on thin films of nickel (300 nm) with conditions similar to those used for SLG on copper foils, was used as the main platform for the demonstration of the various results presented. This led to obtaining an increased number of layers and the benefit of reduced sheet resistance as compared to SLG, without the need of the tedious process of repeated transfer of SLG layers to form stacks, which inevitably introduces additional defects and contaminants. In addition, FLG is amenable to spontaneous and facile intercalation of small guest molecules in the bulk between graphene layers, and thus can achieve an efficient doping similar to the interlayer doping process achieved when sequential transfer and doping cycles of SLG are employed. Furthermore, beyond the issues just mentioned regarding layers stacking, the stability of the dopant during the transfer process constitutes an additional bottleneck. This rationale of our choice of CVD-FLG is further supported by the additional advantages in comparison to CVD-SLG presented in **Chapter 2**. Our work demonstrates that CVD-FLG qualifies as the most suitable graphene form as a candidate emerging TCE towards ITO replacement.

The results presented in **Chapters 4** and **6** have shown that intercalation of FLG, in a similar manner to GIC, is an effective doping route of graphene. We have shown that the number of graphene layers that undergo doping by charge transfer is maximized because dopants can infiltrate and intercalate between graphene sheets in the bulk of FLG film. The insertion of the dopants in between the sheets, leads to higher air stability as dopants that are present on the surface are more prone to degrade. In **Chapter 4**, we have demonstrated the intercalation of bromine at room temperature in CVD-FLG. Through bromination, we achieved highly-stable TCEs with five-fold improvement in sheet resistance at the cost of only 2-3% loss of optical transmission. Evaluation of the changes in the FoM shows that the improvement between pristine and intercalated FLG exceeds that for all other doping strategies.

Furthermore, we have used surface molecular dopants to study the effect of doping on FLG whereas most reports in the literature focus on SLG. The common misconception that molecular dopants would be less effective in doping FLG as contrasted to SLG was also addressed in this thesis. We have shown in **Chapter 5**, using a set of organic and metal-organic molecules with a wide range of doping strength as n- and p-dopants, that FLG is effectively doped with surface dopants as suggested by the reductions in the sheet resistance exceeding 50% for the strongest dopants. This is attributed to the increase in carrier density in doped-FLG in correlation with the strength of the dopant, and the minimal reduction in mobility, as compared to the significant reductions encountered in doped-SLG. The minimal reduction in the mobility was explained as originating from the screening of the Coulomb scattering effect of the charged molecules by the additional layers in FLG. One of the main findings of this work is the dependence of the transport properties of doped FLG on the coverage of the surface dopants, and showing that *'more is not good'* in the case of molecularly doped FLG. Three doping regimes differing by the doping mechanism were identified. The initial stage of doping would result in no enhancement in the conductivity in FLG, whereas optimal transport properties were obtained at moderate exposures. In contrast prolonged exposure would actually lead to adverse effects on the conductivity owing to morphological changes in the dopant molecules on the surface of FLG.

An important aspect of doping that has been discussed in detail in this thesis is the modulation of the work function of graphene. In **Chapter 5**, we have shown that the changes in the work function of FLG are directly correlated to the strength of the surface molecular dopants. Furthermore, the use of surface molecular dopants has resulted in work function modulation over an unprecedented range for solution-processed dopants. The work function of FLG was varied over a range of 2.4 eV (from 2.9 to 5.3 eV), making surface doping an optimal route for controlling the energetics at the interface of graphene in devices. A comparison between bulk doping of FLG via bromine intercalation, and surface doping by molecular species, reveal that the changes in the work function are smaller in the former (~0.3 eV as compared to ~0.8 eV for the strongest surface dopant). It was shown that such differences are due to the large contribution of the induced molecular surface dipole in the latter, thus shifting the vacuum level in FLG and adding to the shift in the Fermi level induced by charge transfer.

The culmination of our doping work is the development of a novel doping scheme which we called “hybrid doping”. It combines in one doping scheme the benefits of large enhancements in electrical conductivity resulting from the bulk doping modality via intercalation (**Chapter 4**) and the wide-range of work function modulation achieved via surface molecular doping modality (**Chapter 5**). FLG was both intercalated and surface doped as demonstrated in **Chapter 6**, achieving a low sheet resistance FLG down to100 Ω/□ with the main contribution coming from intercalation, with a work function that is tuned up to 5.43 eV thanks to the surface dipoles resulting from the molecular surface dopants.

The universality of the hybrid doping approach has been demonstrated using two different intercalants (Br_2 and $FeCl_3$) and surface dopants (organic and metal-organic molecular), showing the significance of the presented approach in its ability of making graphene-based TCEs that would meet the requirements of a wide range of applications, by simply making the appropriate choice of materials for each doping modality.

Limitations faced in the presented work, include the inability to achieve full intercalation of CVD-FLG, which has been achieved in HOPG. This is attributed to the intrinsic differences between the polycrystalline and patchy nature of CVD-FLG, in addition to being rotationally faulted without a specific stacking order, in contrast to the crystalline AB-Bernal stacked HOPG. In addition, it is expected that the thermodynamics and kinetics of intercalation would differ with sample thickness and graphene flake size. Furthermore, to fully capture the advantages of the hybrid doping approach, lowering of the work function independently from the conductivity of FLG needs to be demonstrated, beyond further increasing the work function (and improving the conductivity) as presented in this work.

The outcomes of the presented study motivate future work in this direction. The well-established intercalation studies and optimal conditions on HOPG have been adapted to FLG intercalation in the recent reports. However, this thesis along with the current reports proves that full intercalation has not been achieved in CVD-FLG using such conditions. To secure the complete benefits of intercalation bulk doping of FLG, a comprehensive study of the thermodynamics and kinetics of intercalation of CVD-FLG is needed, aiming towards defining the optimized conditions, such as the threshold pressure of intercalation, and the rate of intercalation for ultrathin and polycrystalline graphene films, towards the attainment of full intercalation of graphene-based materials.

Additionally, for large-scale applications, reaching the intrinsic limits of graphene properties is a challenge that should be addressed. This would be achieved by further optimization of the CVD process towards growth of FLG with larger crystalline and continuous domains. A significant effort has been already placed on the growth process optimization of CVD-SLG, without considering CVD-FLG. This effort needs to be extended to the latter, considering the obvious advantages presented in this work.

Future development of the hybrid doping approach can be realized through the investigation of additional combinations of intercalates and surface dopants. The need for modulating the work function of FLG without affecting the conductivity could be addressed by the use of surface dopant exhibiting intrinsic dipole, that wouldn’t require a charge transfer as the dopants used in this study. In addition, such dopants should be limited to non-covalent attachments to graphene, due to the well-known adverse effect of covalent bonding that disrupts the basal plane of graphene and adversely affects its conductivity.

The implications of this would provide a clear definition of the structure-property-performance relationship of doped-FLG, and enable the selection of the intercalants, and surface dopants based on the desired conductivity and work function for each application.

BIBLIOGRAPHY

[1] R. G. Gordon, *MRS Bull.* **2000**, *25*, 52.

[2] B. Kippelen, J.-L. Brédas, *Energy Environ. Sci.* **2009**, *2*, 251.

[3] P. W. M. Blom, V. D. Mihailetchi, L. J. A. Koster, D. E. Markov, *Adv. Mater.* **2007**, *19*, 1551.

[4] D. S. Hecht, L. Hu, G. Irvin, *Adv. Mater.* **2011**, *23*, 1482.

[5] CientificaResearch, "Wearables, Smart Textiles and Nanotechnology Applications Technologies and Markets," can be found under http://www.cientifica.com/research/market-reports/wearables-smart-textiles-nanotechnologies-markets/, **2016**.

[6] S. Bae, S. J. Kim, D. Shin, J.-H. Ahn, B. H. Hong, *Phys. Scr.* **2012**, *T146*, 14024.

[7] I. Hamberg, C. G. Granqvist, *J. Appl. Phys.* **1986**, *60*, R123.

[8] K. Yu, J. Chen, *Mater. Matters* **2014**, *9*, 6.

[9] H. Zervos, *The Market for Touch Screens and ITO Replacement*, **2012**.

[10] K. Ghaffarzadeh, R. Das, *Transparent Conductive Films (TCF) 2016-2026: Forecasts, Markets, Technologies*, **2016**.

[11] T. D. Kelly, G. R. Matos, Comps., *Indium Statistics [through 2014; Last Modified January 28, 2016] Historical Statistics for Mineral and Material Commodities in the United States (2016 Version)*, **2016**.

[12] A. J. Hurd, R. L. Kelley, R. G. Eggert, M.-H. M.-H. Lee, *MRS Bull.* **2012**, *37*, 405.

[13] M. P. De Jong, L. J. Van Ijzendoorn, M. J. A. De Voigt, *App. Phys. Lett.* **2000**, *77*, 2255.

[14] F. Bonaccorso, Z. Sun, T. Hasan, A. C. Ferrari, *Nat. Photonics* **2010**, *4*, 611.

[15] K. Ellmer, *Nat. Photonics* **2012**, *6*, 809.

[16] A. Kumar, C. Zhou, *ACS Nano* **2010**, *4*, 11.

[17] Polinares: Eu Policy on Natural Resources, *Fact Sheet: Indium*, **2012**.

[18] K. S. Novoselov, a K. Geim, S. V Morozov, D. Jiang, Y. Zhang, S. V Dubonos, I. V Grigorieva, A. A. Firsov, *Science (80-.).* **2004**, *306*, 666.

[19] W. Lu, P. Soukiassian, J. Boeckl, *MRS Bull.* **2012**, *37*, 1119.

[20] C. Lee, X. Wei, J. W. Kysar, J. Hone, *Science* **2008**, *321*, 385.

[21] S. V. Morozov, K. S. Novoselov, M. I. Katsnelson, F. Schedin, D. C. Elias, J. A. Jaszczak, A. K. Geim, *Phys. Rev. Lett.* **2008**, *100*, 16602.

[22] R. R. Nair, P. Blake, A. N. Grigorenko, K. S. Novoselov, T. J. Booth, T. Stauber, N. M. R. Peres, A. K. Geim, *Science (80-.).* **2008**, *320*, 1308.

[23] H.-Z. Geng, K. K. Kim, K. P. So, Y. S. Lee, Y. Chang, Y. H. Lee, *J. Am. Chem. Soc.* **2007**, *129*, 7758.

[24] L. Hu, H. S. Kim, J. Y. Lee, P. Peumans, Y. Cui, *ACS Nano* **2010**, *4*, 2955.

[25] D. Langley, G. Giusti, C. Mayousse, C. Celle, D. Bellet, J.-P. Simonato, *Nanotechnology* **2013**, *24*, 452001.

[26] C. J. M. Emmott, A. Urbina, J. Nelson, in *Sol. Energy Mater. Sol. Cells*, **2012**, pp. 14–21.

[27] C. Mattevi, H. Kim, M. Chhowalla, *J. Mater. Chem.* **2011**, *21*, 3324.

[28] X. Li, C. W. Magnuson, A. Venugopal, J. An, J. W. Suk, B. Han, M. Borysiak, W. Cai, A. Velamakanni, Y. Zhu, L. Fu, E. M. Vogel, E. Voelkl, L. Colombo, R. S. Ruoff, *Nano Lett.* **2010**, *10*, 4328.

[29] M. Losurdo, M. M. Giangregorio, P. Capezzuto, G. Bruno, *Phys. Chem. Chem. Phys.* **2011**, 20836.

[30] Q. Yu, L. a Jauregui, W. Wu, R. Colby, J. Tian, Z. Su, H. Cao, Z. Liu, D. Pandey, D. Wei, T. F. Chung, P. Peng, N. P. Guisinger, E. a Stach, J. Bao, S.-S. Pei, Y. P. Chen, *Nat. Mater.* **2011**, *10*, 443.

[31] S. Bhaviripudi, X. Jia, M. S. Dresselhaus, J. Kong, *Nano Lett.* **2010**, *10*, 4128.

[32] H. Pinto, A. Markevich, *Beilstein J. Nanotechnol.* **2014**, *5*, 1842.

[33] T. Kuila, S. Bose, A. K. Mishra, P. Khanra, N. H. Kim, J. H. Lee, *Prog. Mater. Sci.* **2012**, *57*, 1061.

[34] H. Y. Mao, Y. H. Lu, J. D. Lin, S. Zhong, A. T. S. Wee, W. Chen, *Prog. Surf. Sci.* **2013**, *88*, 132.

[35] A. Kasry, M. a. Kuroda, G. J. Martyna, G. S. Tulevski, A. a. Bol, *ACS Nano* **2010**, *4*, 3839.

[36] J. Du, S. Pei, L. Ma, H. Cheng, *Adv. Mater.* **2014**, *26*, 1958.

[37] Clark I. Bright, in *50 Years Vac. Coat. Technol. Growth Soc. Vac. Coaters* (Eds.: D.M. Mattox,

V.H. Mattox), Society Of Vacuum Coaters, **2007**, pp. 38–45.
[38] T. Minami, *Semicond. Sci. Technol.* **2005**, *20*, S35.
[39] T. J. Coutts, T. O. Mason, J. D. Perkins, D. S. Ginley, in *Photovoltaics 21st Century Proc. Int. Symp. (Pp. 274-286). Electrochem. Soc.*, Philadelphia, PA, USA, **1999**.
[40] D. S. Ginley, C. Bright, *MRS Bull.* **2011**, *25*, 15.
[41] K. Badeker, *Ann. Phys.(Leipzig)* **1907**, *22*, 749.
[42] H. A. McMaster, *Conductive Coating for Glass and Method of Application*, **1947**, US2429420 A.
[43] J. T. Littleton, *Insulator*, **n.d.**, US2118795 A.
[44] John M Mochel, *Electrically Conducting Coatings on Glass and Other Ceramic Bodies*, **1951**, US2564707 A.
[45] History.com, "Energy crises (1970S)," can be found under http://www.history.com/topics/energy-crisis, **2010**.
[46] Terry Macalister, *Guard.* **2011**.
[47] D. S. Ginley, Ed. , *Handbook of Transparent Conductors*, Springer US, Boston, MA, **2011**.
[48] K. Ellmer, *Nat. Photonics* **2012**, *6*, 808.
[49] C. Guillén, J. Herrero, in *Org. Photovoltaics Mater. Device Physics, Manuf. Technol.*, **2009**, pp. 399–423.
[50] C. Renouf, *Nat. Chem.* **2012**, *4*, 862.
[51] S. De, T. M. Higgins, P. E. Lyons, E. M. Doherty, P. N. Nirmalraj, W. J. Blau, J. J. Boland, J. N. Coleman, *ACS Nano* **2009**, *3*, 1767.
[52] S. I. Na, S. S. Kim, J. Jo, D. Y. Kim, *Adv. Mater.* **2008**, *20*, 4061.
[53] M. Vosgueritchian, D. J. Lipomi, Z. Bao, *Adv. Funct. Mater.* **2012**, *22*, 421.
[54] D.-S. Leem, A. Edwards, M. Faist, J. Nelson, D. D. C. Bradley, J. C. de Mello, *Adv. Mater.* **2011**, *23*, 4371.
[55] T. M. Barnes, J. D. Bergeson, R. C. Tenent, B. A. Larsen, G. Teeter, K. M. Jones, J. L. Blackburn, J. van de Lagemaat, *Appl. Phys. Lett.* **2010**, *96*, 243309.
[56] R. V. Salvatierra, C. E. Cava, L. S. Roman, A. J. G. Zarbin, *Adv. Funct. Mater.* **2013**, *23*, 1490.
[57] H. Park, S. Chang, M. Smith, S. Gradečak, J. Kong, *Sci. Rep.* **2013**, *3*, 1581.
[58] H. Park, S. Chang, X. Zhou, J. Kong, T. Palacios, S. Gradečak, *Nano Lett.* **2014**, *14*, 5148.
[59] X. Wang, L. Zhi, K. Müllen, *Nano Lett.* **2008**, *8*, 323.
[60] G. Haacke, *J. Appl. Phys.* **1976**, *47*, 4086.
[61] D. B. Fraser, H. D. Cook, *J. Electrochem. Soc.* **1972**, *119*, 1368.
[62] S. De, J. N. Coleman, *ACS Nano* **2010**, *4*, 2713.
[63] S. Bae, H. Kim, Y. Lee, X. Xu, J.-S. Park, Y. Zheng, J. Balakrishnan, T. Lei, H. Ri Kim, Y. Il Song, Y.-J. Kim, K. S. Kim, B. Özyilmaz, J.-H. Ahn, B. H. Hong, S. Iijima, *Nat. Nanotechnol.* **2010**, *5*, 574.
[64] W. Bao, J. Wan, X. Han, X. Cai, H. Zhu, D. Kim, D. Ma, Y. Xu, J. N. Munday, H. D. Drew, M. S. Fuhrer, L. Hu, *Nat. Commun.* **2014**, *5*, DOI 10.1038/ncomms5224.
[65] R. Arvidsson, D. Kushnir, S. Molander, B. A. Sandén, *J. Clean. Prod.* **2016**, *132*, 289.
[66] L. Banszerus, M. Schmitz, S. Engels, J. Dauber, M. Oellers, F. Haupt, K. Watanabe, T. Taniguchi, B. Beschoten, C. Stampfer, *Sci. Adv.* **2015**, *1*, 1500222.
[67] B. N. Chandrashekar, B. Deng, A. S. Smitha, Y. Chen, C. Tan, H. Zhang, H. Peng, Z. Liu, *Adv. Mater.* **2015**, *27*, 5210.
[68] D. Wei, J. Kivioja, *Nanoscale* **2013**, *5*, 10108.
[69] H. P. Boehm, R. Setton, E. Stumpp, *Carbon N. Y.* **1986**, *24*, 241.
[70] R. Saito, M. Fujita, G. Dresselhaus, M. S. Dresselhaus, *Phys. Rev. B* **1992**, *46*, 1804.
[71] I. Forbeaux, J.-M. Themlin, J.-M. Debever, *Phys. Rev. B* **1998**, *58*, 16396.
[72] R. Saito, G. Dresselhaus, M. S. Dresselhaus, *J. Appl. Phys.* **1993**, *73*, 494.
[73] S. Wang, S. Yata, J. Nagano, Y. Okano, H. Kinoshita, H. Kikuta, T. Yamabe, *J. Electrochem. Soc.* **2000**, *147*, 2498.
[74] A. Bianco, H. M. Cheng, T. Enoki, Y. Gogotsi, R. H. Hurt, N. Koratkar, T. Kyotani, M. Monthioux, C. R. Park, J. M. D. Tascon, J. Zhang, *Carbon N. Y.* **2013**, *65*, 1.
[75] P. Wick, A. E. Louw-Gaume, M. Kucki, H. F. Krug, K. Kostarelos, B. Fadeel, K. A. Dawson, A. Salvati, E. Vázquez, L. Ballerini, M. Tretiach, F. Benfenati, E. Flahaut, L. Gauthier, M. Prato, A. Bianco, *Angew. Chemie Int. Ed.* **2014**, *53*, 7714.

[76] A. K. Geim, K. S. Novoselov, *Nat. Mater.* **2007**, *6*, 183.

[77] K. S. Novoselov, *Science (80-.).* **2004**, *306*, 666.

[78] K. S. Novoselov, D. Jiang, F. Schedin, T. J. Booth, V. V Khotkevich, S. V Morozov, a K. Geim, *Proc. Natl. Acad. Sci. U. S. A.* **2005**, *102*, 10451.

[79] M. Yi, Z. Shen, *J. Mater. Chem. A* **2015**, *3*, 11700.

[80] X. Li, W. Cai, J. An, S. Kim, J. Nah, D. Yang, R. Piner, A. Velamakanni, I. Jung, E. Tutuc, S. K. Banerjee, L. Colombo, R. S. Ruoff, *Science* **2009**, *324*, 1312.

[81] H. Yamaguchi, G. Eda, C. Mattevi, H. Kim, M. Chhowalla, *ACS Nano* **2010**, *4*, 524.

[82] E. Vesapuisto, W. Kim, S. Novikov, H. Lipsanen, P. Kuivalainen, *Phys. Status Solidi Basic Res.* **2011**, *248*, 1908.

[83] C. Faugeras, a. Nerrière, M. Potemski, a. Mahmood, E. Dujardin, C. Berger, W. a. de Heer, *Appl. Phys. Lett.* **2008**, *92*, 11914.

[84] K. V Emtsev, A. Bostwick, K. Horn, J. Jobst, G. L. Kellogg, L. Ley, J. L. McChesney, T. Ohta, S. a Reshanov, J. Röhrl, E. Rotenberg, A. K. Schmid, D. Waldmann, H. B. Weber, T. Seyller, *Nat. Mater.* **2009**, *8*, 203.

[85] T. Ohta, A. Bostwick, T. Seyller, K. Horn, E. Rotenberg, *Science* **2006**, *313*, 951.

[86] C. Berger, Z. Song, T. Li, X. Li, A. Y. Ogbazghi, R. Feng, Z. Dai, A. N. Marchenkov, E. H. Conrad, P. N. First, W. A. de Heer, *J. Phys. Chem. B* **2004**, *108*, 19912.

[87] S. Park, R. S. Ruoff, *Nat. Nanotechnol.* **2009**, *4*, 217.

[88] D. C. Marcano, D. V Kosynkin, J. M. Berlin, A. Sinitskii, Z. Sun, A. Slesarev, L. B. Alemany, W. Lu, J. M. Tour, *ACS Nano* **2010**, *4*, 4806.

[89] A. E. Karu, *J. Appl. Phys.* **1966**, *37*, 2179.

[90] S. D. ROBERTSON, *Nature* **1969**, *221*, 1044.

[91] B. C. BANERJEE, T. J. HIRT, P. L. WALKER, *Nature* **1961**, *192*, 450.

[92] F. J. Himpsel, K. Christmann, P. Heimann, D. E. Eastman, P. J. Feibelman, *Surf. Sci.* **1982**, *115*, L159.

[93] P. W. Sutter, J.-I. Flege, E. A. Sutter, *Nat. Mater.* **2008**, *7*, 406.

[94] V. Yong, H. T. Hahn, *CrystEngComm* **2011**, *13*, 6933.

[95] G. W. Cushing, V. Johánek, J. K. Navin, I. Harrison, *J. Phys. Chem. C* **2015**, *119*, 4759.

[96] L. Gao, W. Ren, H. Xu, L. Jin, Z. Wang, T. Ma, L.-P. Ma, Z. Zhang, Q. Fu, L.-M. Peng, X. Bao, H.-M. Cheng, *Nat. Commun.* **2012**, *3*, 699.

[97] H. Ago, Y. Ito, N. Mizuta, K. Yoshida, B. Hu, C. M. Orofeo, M. Tsuji, K. Ikeda, S. Mizuno, *ACS Nano* **2010**, *4*, 7407.

[98] Q. Yu, J. Lian, S. Siriponglert, H. Li, Y. P. Chen, S.-S. Pei, *Appl. Phys. Lett.* **2008**, *93*, 113103.

[99] H. J. Park, J. Meyer, S. Roth, V. Skákalová, *Carbon N. Y.* **2010**, *48*, 1088.

[100] K. S. Kim, Y. Zhao, H. Jang, S. Y. Lee, J. M. Kim, K. S. Kim, J.-H. Ahn, P. Kim, J.-Y. Choi, B. H. Hong, *Nature* **2009**, *457*, 706.

[101] A. Reina, X. Jia, J. Ho, D. Nezich, H. Son, V. Bulovic, M. S. Dresselhaus, J. Kong, *Nano Lett.* **2009**, *9*, 30.

[102] L. Liu, H. Zhou, R. Cheng, Y. Chen, Y.-C. Lin, Y. Qu, J. Bai, I. a. Ivanov, G. Liu, Y. Huang, X. Duan, *J. Mater. Chem.* **2012**, *22*, 1498.

[103] A. Kumar, C. Huei, in *Adv. Graphene Sci.*, InTech, **2013**.

[104] A. Ismach, C. Druzgalski, S. Penwell, A. Schwartzberg, M. Zheng, A. Javey, J. Bokor, Y. Zhang, *Nano Lett.* **2010**, *10*, 1542.

[105] M. P. Levendorf, C. S. Ruiz-Vargas, S. Garg, J. Park, *Nano Lett.* **2009**, *9*, 4479.

[106] Y. H. Lee, J. H. Lee, *Appl. Phys. Lett.* **2010**, *96*, 22.

[107] Z. Y. Juang, C. Y. Wu, A. Y. Lu, C. Y. Su, K. C. Leou, F. R. Chen, C. H. Tsai, *Carbon N. Y.* **2010**, *48*, 3169.

[108] E. S. Polsen, D. Q. McNerny, B. Viswanath, S. W. Pattinson, A. John Hart, *Sci. Rep.* **2015**, *5*, 10257.

[109] J. Kang, D. Shin, S. Bae, B. H. Hong, *Nanoscale* **2012**, *4*, 5527.

[110] J.-Y. Choi, *Nat. Nanotechnol.* **2013**, *8*, 311.

[111] L. Jiao, B. Fan, X. Xian, Z. Wu, J. Zhang, Z. Liu, *J. Am. Chem. Soc.* **2008**, *130*, 12612.

[112] A. Pirkle, J. Chan, A. Venugopal, D. Hinojos, C. W. Magnuson, S. McDonnell, L. Colombo, E. M. Vogel, R. S. Ruoff, R. M. Wallace, *Appl. Phys. Lett.* **2011**, *99*, 122108.

[113] Y.-C. Lin, C.-C. Lu, C.-H. Yeh, C. Jin, K. Suenaga, P.-W. Chiu, *Nano Lett.* **2012**, *12*, 414.

[114] X. Li, Y. Zhu, W. Cai, M. Borysiak, B. Han, D. Chen, R. D. Piner, L. Colombo, R. S. Ruoff, *Nano Lett.* **2009**, *9*, 4359.

[115] S. J. Kang, B. Kim, K. S. Kim, Y. Zhao, Z. Chen, G. H. Lee, J. Hone, P. Kim, C. Nuckolls, *Adv. Mater.* **2011**, *23*, 3531.

[116] J. Song, F.-Y. Kam, R.-Q. Png, W.-L. Seah, J.-M. Zhuo, G.-K. Lim, P. K. H. Ho, L.-L. Chua, *Nat. Nanotechnol.* **2013**, *8*, 356.

[117] W. a. de Heer, *MRS Bull.* **2011**, *36*, 632.

[118] I. V Antonova, S. V Mutilin, V. a Seleznev, R. a Soots, V. a Volodin, V. Ya Prinz, *Nanotechnology* **2011**, *22*, 285502.

[119] A. J. Hong, E. B. Song, H. S. Yu, M. J. Allen, J. Kim, J. D. Fowler, J. K. Wassei, Y. Park, Y. Wang, J. Zou, R. B. Kaner, B. H. Weiller, K. L. Wang, *ACS Nano* **2011**, *5*, 7812.

[120] Y. Ouyang, H. Dai, J. Guo, *Nano Res.* **2010**, *3*, 8.

[121] T. Yu, E. Kim, N. Jain, B. Yu, *MRS Proc.* **2012**, *1407*, mrsf11.

[122] X. W. Fu, Z. M. Liao, J. X. Zhou, Y. B. Zhou, H. C. Wu, R. Zhang, G. Jing, J. Xu, X. Wu, W. Guo, D. Yu, *Appl. Phys. Lett.* **2011**, *99*, 3.

[123] K. Nagashio, T. Nishimura, K. Kita, A. Toriumi, *Jpn. J. Appl. Phys.* **2010**, *49*, 51304.

[124] A. E. Mansour, S. Dey, A. Amassian, M. H. Tanielian, *ACS Appl. Mater. Interfaces* **2015**, *7*, 17692.

[125] I. Khrapach, F. Withers, T. H. Bointon, D. K. Polyushkin, W. L. Barnes, S. Russo, M. F. Craciun, *Adv. Mater.* **2012**, *24*, 2844.

[126] P. R. Wallace, *Phys. Rev.* **1947**, *71*, 622.

[127] P. Avouris, *Nano Lett.* **2010**, *10*, 4285.

[128] "Quantum interference phenomena in transport," can be found under http://www.fkf.mpg.de/538305/70_Quantum-Transport, **2016**.

[129] K. S. Novoselov, A. K. Geim, S. V Morozov, D. Jiang, M. I. Katsnelson, I. V Grigorieva, S. V Dubonos, A. A. Firsov, *Nature* **2005**, *438*, 197.

[130] S. Adam, E. H. Hwang, V. M. Galitski, S. Das Sarma, *Proc. Natl. Acad. Sci. U. S. A.* **2007**, *104*, 18392.

[131] Y. W. Tan, Y. Zhang, K. Bolotin, Y. Zhao, S. Adam, E. H. Hwang, S. Das Sarma, H. L. Stormer, P. Kim, *Phys. Rev. Lett.* **2007**, *99*, 10.

[132] E. H. Hwang, S. Adam, S. Das Sarma, *Phys. Rev. Lett.* **2007**, *98*, 2.

[133] X. Du, I. Skachko, A. Barker, E. Y. Andrei, *Nat. Nanotechnol.* **2008**, *3*, 491.

[134] S. Das Sarma, E. H. Hwang, *Phys. Rev. B - Condens. Matter Mater. Phys.* **2013**, *87*, 1.

[135] S. Das Sarma, S. Adam, E. H. Hwang, E. Rossi, *Rev. Mod. Phys.* **2011**, *83*, 407.

[136] E. H. Hwang, S. Adam, S. Das Sarma, *Phys. Rev. B - Condens. Matter Mater. Phys.* **2007**, *76*, 1.

[137] Y.-J. Yu, Y. Zhao, S. Ryu, L. E. Brus, K. S. Kim, P. Kim, *Nano Lett.* **2009**, *9*, 3430.

[138] A. Das, S. Pisana, B. Chakraborty, S. Piscanec, S. K. Saha, U. V Waghmare, K. S. Novoselov, H. R. Krishnamurthy, A. K. Geim, A. C. Ferrari, A. K. Sood, *Nat. Nanotechnol.* **2008**, *3*, 210.

[139] S. A. Paniagua, J. Baltazar, H. Sojoudi, S. K. Mohapatra, S. Zhang, C. L. Henderson, S. Graham, S. Barlow, S. R. Marder, *Mater. Horiz.* **2014**, *1*, 111.

[140] J.-H. Chen, C. Jang, S. Adam, M. S. Fuhrer, E. D. Williams, M. Ishigami, *Nat. Phys.* **2008**, *4*, 377.

[141] J.-H. Chen, C. Jang, S. Xiao, M. Ishigami, M. S. Fuhrer, *Nat. Nanotechnol.* **2008**, *3*, 206.

[142] T. Stauber, N. M. R. Peres, F. Guinea, *Phys. Rev. B* **2007**, *76*, 205423.

[143] S. Fratini, F. Guinea, *Phys. Rev. B* **2008**, *77*, 195415.

[144] W. Zhu, V. Perebeinos, M. Freitag, P. Avouris, *Phys. Rev. B - Condens. Matter Mater. Phys.* **2009**, *80*, 1.

[145] E. H. Hwang, S. Das Sarma, *Phys. Rev. B - Condens. Matter Mater. Phys.* **2009**, *79*, 1.

[146] J. H. Chen, W. G. Cullen, C. Jang, M. S. Fuhrer, E. D. Williams, *Phys. Rev. Lett.* **2009**, *102*, 1.

[147] E. H. Hwang, S. Das Sarma, *Phys. Rev. B* **2008**, *77*, 115449.

[148] K. I. Bolotin, K. J. Sikes, Z. Jiang, M. Klima, G. Fudenberg, J. Hone, P. Kim, H. L. Stormer, *Solid State Commun.* **2008**, *146*, 351.

[149] J. Moser, A. Barreiro, A. Bachtold, *Appl. Phys. Lett.* **2007**, *91*, 163513.

[150] A. Kumari, N. Prasad, P. K. Bhatnagar, P. C. Mathur, A. K. Yadav, C. V. Tomy, C. S. Bhatia, *Diam. Relat. Mater.* **2014**, *45*, 28.

[151] X. Li, C. W. Magnuson, A. Venugopal, R. M. Tromp, J. B. Hannon, E. M. Vogel, L. Colombo, R. S. Ruoff, *J. Am. Chem. Soc.* **2011**, 3.

[152] N. Petrone, C. R. Dean, I. Meric, A. M. van der Zande, P. Y. Huang, L. Wang, D. Muller, K. L. Shepard, J. Hone, *Nano Lett.* **2012**, *12*, 2751.

[153] H. S. Song, S. L. Li, H. Miyazaki, S. Sato, K. Hayashi, A. Yamada, N. Yokoyama, K. Tsukagoshi, *Sci. Rep.* **2012**, *2*, 337.

[154] O. V Yazyev, S. G. Louie, *Nat. Mater.* **2010**, *9*, 806.

[155] F. Wooten, *Optical Properties of Solids*, Academic Press, Inc, New York, **1972**.

[156] A. B. Kuzmenko, E. Van Heumen, F. Carbone, D. Van Der Marel, *Phys. Rev. Lett.* **2008**, *100*, 2.

[157] S. Zhu, S. Yuan, G. C. A. M. Janssen, *A Lett. J. Explor. Front. Phys.* **2014**, *108*, 1.

[158] L. a. Falkovsky, *J. Phys. Conf. Ser.* **2008**, *129*, 12004.

[159] Z. Q. Li, E. a. Henriksen, Z. Jiang, Z. Hao, M. C. Martin, P. Kim, H. L. Stormer, D. N. Basov, *Nat. Phys.* **2008**, *4*, 6.

[160] F. Wang, Y. Zhang, C. Tian, C. Girit, A. Zettl, M. Crommie, Y. R. Shen, *Science (80-.).* **2008**, *320*, 206.

[161] K. F. Mak, M. Y. Sfeir, Y. Wu, C. H. Lui, J. a. Misewich, T. F. Heinz, *Phys. Rev. Lett.* **2008**, *101*, 2.

[162] F. Schedin, a K. Geim, S V Morozov, E. W. Hill, P. Blake, M. I. Katsnelson, K. S. Novoselov, *Nat. Mater.* **2007**, *6*, 652.

[163] A. Peigney, C. Laurent, E. Flahaut, R. R. Bacsa, A. Rousset, *Carbon N. Y.* **2001**, *39*, 507.

[164] L. Yan, Y. B. Zheng, F. Zhao, S. Li, X. Gao, B. Xu, P. S. Weiss, Y. Zhao, *Chem Soc Rev* **2012**, *41*, 97.

[165] F. Schwierz, *Nat. Nanotechnol.* **2010**, *5*, 487.

[166] H. Yuan, S. Chang, I. Bargatin, N. C. Wang, D. C. Riley, H. Wang, J. W. Schwede, J. Provine, E. Pop, Z.-X. Shen, P. A. Pianetta, N. A. Melosh, R. T. Howe, *Nano Lett.* **2015**, *15*, 6475.

[167] J.-K. Chang, W.-H. Lin, J.-I. Taur, T.-H. Chen, G.-K. Liao, T.-W. Pi, M.-H. Chen, C.-I. Wu, *ACS Appl. Mater. Interfaces* **2015**, *7*, 17155.

[168] T. S. Sreeprasad, V. Berry, *Small* **2012**, 341.

[169] V. Georgakilas, M. Otyepka, A. B. Bourlinos, V. Chandra, N. Kim, K. C. Kemp, P. Hobza, R. Zboril, K. S. Kim, *Chem. Rev.* **2012**, *112*, 6156.

[170] J. M. Englert, C. Dotzer, G. Yang, M. Schmid, C. Papp, J. M. Gottfried, H.-P. Steinrück, E. Spiecker, F. Hauke, A. Hirsch, *Nat Chem* **2011**, *3*, 279.

[171] J. T. Robinson, M. Zalalutdinov, E. S. Snow, J. W. Baldwin, Z. Wei, P. Sheehan, B. H. Houston, *Nano Lett.* **2008**, *8*, 3441.

[172] R. Balog, B. Jørgensen, L. Nilsson, M. Andersen, E. Rienks, M. Bianchi, M. Fanetti, E. Laegsgaard, A. Baraldi, S. Lizzit, Z. Sljivancanin, F. Besenbacher, B. Hammer, T. G. Pedersen, P. Hofmann, L. Hornekaer, *Nat. Mater.* **2010**, *9*, 315.

[173] Z. Luo, J. Shang, S. Lim, D. Li, Q. Xiong, Z. Shen, J. Lin, T. Yu, *Appl. Phys. Lett.* **2010**, *97*, 233111.

[174] C. K. Chua, M. Pumera, *Chem. Soc. Rev.* **2013**, *42*, 3222.

[175] T. Wu, H. Shen, L. Sun, B. Cheng, B. Liu, J. Shen, *New J. Chem.* **2012**, *36*, 1385.

[176] B. Guo, Q. Liu, E. Chen, H. Zhu, L. Fang, J. R. Gong, *Nano Lett.* **2010**, *10*, 4975.

[177] D. Wei, Y. Liu, Y. Wang, H. Zhang, L. Huang, G. Yu, *Nano Lett.* **2009**, *9*, 1752.

[178] R. Lv, Q. Li, A. R. Botello-Méndez, T. Hayashi, B. Wang, A. Berkdemir, Q. Hao, A. L. Elías, R. Cruz-Silva, H. R. Gutiérrez, Y. A. Kim, H. Muramatsu, J. Zhu, M. Endo, H. Terrones, J.-C. Charlier, M. Pan, M. Terrones, *Sci. Rep.* **2012**, *2*, 15.

[179] B. Cai, S. Zhang, Z. Yan, H. Zeng, *ChemNanoMat* **2015**, *1*, 542.

[180] I. Jo, Y. Kim, J. Moon, S. Park, J. S. Moon, W. B. Park, J. S. Lee, B. H. Hong, *Phys. Chem. Chem. Phys.* **2015**, *17*, 29492.

[181] Y. Kim, J. Ryu, M. Park, E. S. Kim, J. M. Yoo, J. Park, J. H. Kang, B. H. Hong, *ACS Nano* **2014**, *8*, 868.

[182] X. Dong, D. Fu, W. Fang, Y. Shi, P. Chen, L. J. Li, *Small* **2009**, *5*, 1422.

[183] Q. Su, S. Pang, V. Alijani, C. Li, X. Feng, K. Müllen, *Adv. Mater.* **2009**, *21*, 3191.

[184] T. O. Wehling, K. S. Novoselov, S. V. Morozov, E. E. Vdovin, M. I. Katsnelson, a. K. Geim, a. I. Lichtenstein, *Nano Lett.* **2008**, *8*, 173.

[185] K. C. Kwon, K. S. Choi, S. Y. Kim, *Adv. Funct. Mater.* **2012**, *22*, 4724.

[186] D. H. Shin, K. W. Lee, J. S. Lee, J. H. Kim, S. Kim, S.-H. Choi, *Nanotechnology* **2014**, *25*, 125701.

[187] S. Watcharinyanon, C. Virojanadara, L. I. Johansson, *Surf. Sci.* **2011**, *605*, 1918.

[188] K. Pi, K. M. McCreary, W. Bao, W. Han, Y. F. Chiang, Y. Li, S. W. Tsai, C. N. Lau, R. K. Kawakami, *Phys. Rev. B - Condens. Matter Mater. Phys.* **2009**, *80*, 1.

[189] I. Gierz, C. Riedl, U. Starke, C. R. Ast, K. Kern, *Nano Lett.* **2008**, *8*, 4603.

[190] G. Giovannetti, P. a. Khomyakov, G. Brocks, V. M. Karpan, J. Van Den Brink, P. J. Kelly, *Phys. Rev. Lett.* **2008**, *101*, 4.

[191] C. Straßer, B. M. Ludbrook, G. Levy, a. J. Macdonald, S. a. Burke, T. O. Wehling, K. Kern, A. Damascelli, C. R. Ast, *Nano Lett.* **2015**, *15*, 2825.

[192] K. K. Kim, A. Reina, Y. Shi, H. Park, L.-J. Li, Y. H. Lee, J. Kong, *Nanotechnology* **2010**, *21*, 285205.

[193] K. C. Kwon, B. J. Kim, J.-L. Lee, S. Y. Kim, *J. Mater. Chem. C* **2013**, *1*, 2463.

[194] K. C. Kwon, K. S. Choi, C. Kim, S. Y. Kim, *J. Phys. Chem. C* **2014**, *118*, 8187.

[195] K. C. Kwon, K. S. Choi, C. Kim, S. Y. Kim, *Phys. Status Solidi* **2014**, *211*, 1794.

[196] F. Güneş, H. Shin, C. Biswas, G. H. Han, E. S. Kim, S. J. Chae, J.-Y. Choi, Y. H. Lee, *ACS Nano* **2010**, *4*, 4595.

[197] K. C. Kwon, B. J. Kim, J.-L. Lee, S. Y. Kim, *J. Mater. Chem. C* **2013**, *1*, 253.

[198] W. Chen, S. Chen, D. C. Qi, X. Y. Gao, A. T. S. Wee, C. Q. Dong, Y. G. Xing, A. T. S. Wee, *J. Am. Chem. Soc.* **2007**, *129*, 10418.

[199] P. Wei, N. Liu, H. R. Lee, E. Adijanto, L. Ci, B. D. Naab, J. Q. Zhong, J. Park, W. Chen, Y. Cui, Z. Bao, *Nano Lett.* **2013**, *13*, 1890.

[200] J. Drechsel, M. Pfeiffer, X. Zhou, A. Nollau, K. Leo, *Synth. Met.* **2002**, *127*, 201.

[201] X. Zhou, M. Pfeiffer, J. Blochwitz, A. Werner, A. Nollau, T. Fritz, K. Leo, *Appl. Phys. Lett.* **2001**, *78*, 410.

[202] Y. Nosho, Y. Ohno, S. Kishimoto, T. Mizutani, *Nanotechnology* **2007**, *18*, 415202.

[203] J. T. Sun, Y. H. Lu, W. Chen, Y. P. Feng, a. T. S. Wee, *Phys. Rev. B* **2010**, *81*, 155403.

[204] S. Duhm, I. Salzmann, B. Bröker, H. Glowatzki, R. L. Johnson, N. Koch, *Appl. Phys. Lett.* **2009**, *95*, DOI 10.1063/1.3213547.

[205] Z. Q. Gao, B. X. Mi, G. Z. Xu, Y. Q. Wan, M. L. Gong, K. W. Cheah, C. H. Chen, *Chem. Commun.* **2008**, 117.

[206] Y. Qi, T. Sajoto, S. Barlow, E. G. Kim, J. L. Brédas, S. R. Marder, A. Kahn, *J. Am. Chem. Soc.* **2009**, *131*, 12530.

[207] Y. Qi, T. Sajoto, M. Kröger, A. M. Kandabarow, W. Park, S. Barlow, E. G. Kim, L. Wielunski, L. C. Feldman, R. a. Bartynski, J. L. Brédas, S. R. Marder, A. Kahn, *Chem. Mater.* **2010**, *22*, 524.

[208] A. Dai, Y. Zhou, A. L. Shu, S. K. Mohapatra, H. Wang, C. Fuentes-Hernandez, Y. Zhang, S. Barlow, Y. L. Loo, S. R. Marder, B. Kippelen, A. Kahn, *Adv. Funct. Mater.* **2014**, *24*, 2197.

[209] S. A. Paniagua, J. Baltazar, H. Sojoudi, S. K. Mohapatra, S. Zhang, C. L. Henderson, S. Graham, S. Barlow, S. R. Marder, *Mater. Horiz.* **2014**, *1*, 111.

[210] L. Chen, L. Wang, Z. Shuai, D. Beljonne, *J. Phys. Chem. Lett.* **2013**, *4*, 2158.

[211] C. L. Hsu, C. Te Lin, J. H. Huang, C. W. Chu, K. H. Wei, L. J. Li, *ACS Nano* **2012**, *6*, 5031.

[212] Y. Wang, S. W. Tong, X. F. Xu, B. Ozyilmaz, K. P. Loh, *Adv. Mater.* **2011**, *23*, 1514.

[213] M. S. Dresselhaus, G. Dresselhaus, *Adv. Phys.* **2002**, *51*, 1.

[214] H. Selig, L. B. Ebert, *Adv. Inorg. Chem. Radiochem.* **1980**, *23*, 281.

[215] M. Inagaki, *J. Mater. Res.* **1989**, *4*, 1560.

[216] W. Zhao, P. H. Tan, J. Liu, A. C. Ferrari, *J. Am. Chem. Soc.* **2011**, *133*, 5941.

[217] D. Zhan, L. Sun, Z. H. Ni, L. Liu, X. F. Fan, Y. Wang, T. Yu, Y. M. Lam, W. Huang, Z. X. Shen, *Adv. Funct. Mater.* **2010**, *20*, 3504.

[218] X. Qi, J. Qu, H.-B. Zhang, D. Yang, Y. Yu, C. Chi, Z.-Z. Yu, *J. Mater. Chem. A* **2015**, *3*, 15498.

[219] D. J. Wehenkel, T. H. Bointon, T. Booth, P. Bøggild, M. F. Craciun, S. Russo, *Sci. Rep.* **2015**, *5*, 7609.

[220] a. Yaya, C. P. Ewels, I. Suarez-Martinez, P. Wagner, S. Lefrant, a. Okotrub, L. Bulusheva, P. R. Briddon, *Phys. Rev. B* **2011**, *83*, 45411.

[221] K. Ueno, R. Kosugi, K. Imazeki, A. Aozasa, Y. Matsumoto, H. Miyazaki, N. Sakuma, A. Kajita, T. Sakai, *Jpn. J. Appl. Phys.* **2014**, *53*, 05GC02.

[222] N. Jung, N. Kim, S. Jockusch, N. J. Turro, P. Kim, L. Brus, *Nano Lett.* **2009**, *9*, 4133.

[223] O. Jankovský, P. Šimek, K. Klimová, D. Sedmidubský, S. Matějková, M. Pumera, Z. Sofer, *Nanoscale* **2014**, *6*, 6065.

[224] X. Fan, L. Liu, J.-L. L. Kuo, Z. Shen, *J. Phys. Chem. C* **2010**, *114*, 14939.

[225] S. Tongay, J. Hwang, D. B. Tanner, H. K. Pal, D. Maslov, A. F. Hebard, *Phys. Rev. B* **2010**, *81*, 115428.

[226] Y. Song, W. Fang, A. L. Hsu, J. Kong, *Nanotechnology* **2014**, *25*, 395701.

[227] Y. Shi, K. K. Kim, A. Reina, M. Hofmann, L. J. Li, J. Kong, *ACS Nano* **2010**, *4*, 2689.

[228] D. Kim, D. Lee, Y. Lee, D. Y. Jeon, *Adv. Funct. Mater.* **2013**, *23*, 5049.

[229] H. Park, J. a Rowehl, K. K. Kim, V. Bulovic, J. Kong, *Nanotechnology* **2010**, *21*, 505204.

[230] H. Ishii, K. Sugiyama, E. Ito, K. Seki, *Adv. Mater.* **1999**, *11*, 605.

[231] S. Braun, W. R. Salaneck, M. Fahlman, *Adv. Mater.* **2009**, *21*, 1450.

[232] C. Christodoulou, a. Giannakopoulos, M. V. Nardi, G. Ligorio, M. Oehzelt, L. Chen, L. Pasquali, M. Timpel, a. Giglia, S. Nannarone, P. Norman, M. Linares, K. Parvez, K. Müllen, D. Beljonne, N. Koch, *J. Phys. Chem. C* **2014**, *118*, 4784.

[233] C. Christodoulou, A. Giannakopoulos, G. Ligorio, M. Oehzelt, M. Timpel, J. Niederhausen, L. Pasquali, A. Giglia, K. Parvez, K. Müllen, D. Beljonne, N. Koch, M. V. Nardi, *ACS Appl. Mater. Interfaces* **2015**, *7*, 19134.

[234] K. C. Kwon, H. J. Son, Y. H. Hwang, J. H. Oh, T.-W. Lee, H. W. Jang, K. Kwak, K. Park, S. Y. Kim, *J. Phys. Chem. C* **2016**, *120*, 1309.

[235] H.-J. Shin, W. M. Choi, D. Choi, G. H. Han, S.-M. Yoon, H.-K. Park, S.-W. Kim, Y. W. Jin, S. Y. Lee, J. M. Kim, J.-Y. Choi, Y. H. Lee, *J. Am. Chem. Soc.* **2010**, *132*, 15603.

[236] J. Baltazar, H. Sojoudi, S. A. Paniagua, J. Kowalik, S. R. Marder, L. M. Tolbert, S. Graham, C. L. Henderson, *J. Phys. Chem. C* **2012**, *116*, 19095.

[237] K. C. Kwon, K. S. Choi, B. J. Kim, J.-L. Lee, S. Y. Kim, *J. Phys. Chem. C* **2012**, *116*, 26586.

[238] T. H. Bointon, G. F. Jones, A. De Sanctis, R. Hill-Pearce, M. F. Craciun, S. Russo, *Sci. Rep.* **2015**, *5*, 16464.

[239] MTI-Corp., *EQ-GSL-4Z: Four Channel Gas Control System for Tube Furnaces with Precision Mass Flow Meters and Valves Operation Manual*, **2016**.

[240] W. Liu, H. Li, C. Xu, Y. Khatami, K. Banerjee, *Carbon N. Y.* **2011**, *49*, 4122.

[241] J. Fischer, J. Bingle, *J. Am. Chem. Soc.* **1955**, *77*, 6511.

[242] Dieter K. Schroder, *Semiconductor Material and Device Characterization*, Wiley-IEEE Press, **2006**.

[243] E. H. Hall, *Am. J. Math.* **1879**, *2*, 287.

[244] A. C. Ferrari, *Solid State Commun.* **2007**, *143*, 47.

[245] L. M. Malard, M. a. Pimenta, G. Dresselhaus, M. S. Dresselhaus, *Phys. Rep.* **2009**, *473*, 51.

[246] A. Ferrari, D. Basko, *Nat. Nanotechnol.* **2013**, *8*, 235.

[247] R. Saito, M. Hofmann, G. Dresselhaus, *Adv. Phys.* **2011**, *8732*, 37.

[248] a. C. Ferrari, J. C. Meyer, V. Scardaci, C. Casiraghi, M. Lazzeri, F. Mauri, S. Piscanec, D. Jiang, K. S. Novoselov, S. Roth, a. K. Geim, *Phys. Rev. Lett.* **2006**, *97*, 1.

[249] M. P. Seah, W. A. Dench, *Surf. Interface Anal.* **1979**, *1*, 2.

[250] Y. Nakajima, in *Org. PV Summit Japan 09*, Riken Keiki, Tokyo, **2009**.

[251] G. Hennig, *J. Chem. Phys.* **1952**, *20*, 1443.

[252] T. Sasa, Y. Takahashi, T. Mukaibo, *Bull. Chem. Soc. Jpn.* **1970**, *43*, 34.

[253] R. S. Lee, H. J. Kim, J. E. Fischer, A. Thess, *Nature* **1997**, *388*, 255.

[254] L. G. Bulusheva, A. V. Okotrub, E. Flahaut, I. P. Asanov, P. N. Gevko, V. O. Koroteev, Y. V. Fedoseeva, a. Yaya, C. P. Ewels, *Chem. Mater.* **2012**, *24*, 2708.

[255] I. Ikemoto, Y. Cao, M. Yamada, H. Kuroda, I. Harada, H. Shirakawa, S. Ikeda, *Bull. Chem. Soc. Jpn.* **1982**, *55*, 721.

[256] J. Zheng, H.-T. Liu, B. Wu, C.-A. Di, Y.-L. Guo, T. Wu, G. Yu, Y.-Q. Liu, D.-B. Zhu, *Sci. Rep.* **2012**, *2*, 662.

[257] J. J. Song, D. D. L. Chung, P. C. Eklund, M. S. Dresselhaus, *Solid State Commun.* **1976**, *20*, 1111.

[258] J. Li, L. Vaisman, G. Marom, J. K. Kim, *Carbon N. Y.* **2007**, *45*, 744.

[259] P. Eklund, N. Kambe, G. Dresselhaus, M. Dresselhaus, *Phys. Rev. B* **1978**, *18*, 7069.

[260] G. K. Wertheim, P. T. T. M. Van Attekum, S. Basu, *Solid State Commun.* **1980**, *33*, 1127.

[261] Z. Yan, Z. Zhuxia, L. Tianbao, L. Xuguang, X. Bingshe, *Spectrochim. Acta. A. Mol. Biomol. Spectrosc.* **2008**, *70*, 1060.

[262] E. Papirer, R. Lacroix, J. Donnet, G. Nanse, P. Froux, *Carbon N. Y.* **1994**, *32*, 1341.

[263] X. Feng, M. Salmeron, *Appl. Phys. Lett.* **2013**, *102*, 53116.

[264] S. W. Poon, W. Chen, A. T. S. Wee, E. S. Tok, *Phys. Chem. Chem. Phys.* **2010**, *12*, 13522.

[265] Q. Wang, W. Zhang, L. Wang, K. He, X. Ma, Q. Xue, *J. Phys. Condens. Matter* **2013**, *25*, 95002.

[266] Z. Liu, J. Li, Z.-H. Sun, G. Tai, S.-P. Lau, F. Yan, *ACS Nano* **2012**, *6*, 810.

[267] N. G. Connelly, W. E. Geiger, *Chem. Rev.* **1996**, *96*, 877.

[268] A. Yamamori, C. Adachi, T. Koyama, Y. Taniguchi, *Appl. Phys. Lett.* **1998**, *72*, 2147.

[269] A. Tarasov, S. Zhang, M.-Y. Tsai, P. M. Campbell, S. Graham, S. Barlow, S. R. Marder, E. M. Vogel, *Adv. Mater.* **2015**, *27*, 1175.

[270] Y. Chang, C.-H. Liu, C. Liu, S. Zhang, S. R. Marder, E. E. Narimanov, Z. Zhong, T. B. Norris, *Nat. Commun.* **2016**, *7*, 10568.

[271] S. K. Mohapatra, A. Fonari, C. Risko, K. Yesudas, K. Moudgil, J. H. Delcamp, T. V. Timofeeva, J.-L. Brédas, S. R. Marder, S. Barlow, *Chem. - A Eur. J.* **2014**, *20*, 15385.

[272] Y. Qi, S. K. Mohapatra, S. Bok Kim, S. Barlow, S. R. Marder, A. Kahn, *Appl. Phys. Lett.* **2012**, *100*, 83305.

[273] S. Guo, S. B. Kim, S. K. Mohapatra, Y. Qi, T. Sajoto, A. Kahn, S. R. Marder, S. Barlow, *Adv. Mater.* **2012**, *24*, 699.

[274] A. Higgins, S. K. Mohapatra, S. Barlow, S. R. Marder, A. Kahn, *Appl. Phys. Lett.* **2015**, *106*, 163301.

[275] A. J. Giordano, F. Pulvirenti, T. M. Khan, C. Fuentes-Hernandez, K. Moudgil, J. H. Delcamp, B. Kippelen, S. Barlow, S. R. Marder, *ACS Appl. Mater. Interfaces* **2015**, *7*, 4320.

[276] K. Akaike, M. V. Nardi, M. Oehzelt, J. Frisch, A. Opitz, C. Christodoulou, G. Ligorio, P. Beyer, M. Timpel, I. Pis, F. Bondino, K. Moudgil, S. Barlow, S. R. Marder, N. Koch, *Adv. Funct. Mater.* **2016**, *26*, 2493.

[277] I. Salzmann, G. Heimel, M. Oehzelt, S. Winkler, N. Koch, *Acc. Chem. Res.* **2016**, *49*, 370.

[278] S. Pisana, M. Lazzeri, C. Casiraghi, K. S. Novoselov, A. K. Geim, A. C. Ferrari, F. Mauri, **2007**, *6*, 3.

[279] R. Voggu, B. Das, C. S. Rout, C. N. R. Rao, *J. Phys. Condens. Matter* **2008**, *20*, 472204.

[280] J. Park, W. H. Lee, S. Huh, S. H. Sim, S. Bin Kim, K. Cho, B. H. Hong, K. S. Kim, *J. Phys. Chem. Lett.* **2011**, *2*, 841.

[281] M. Hofmann, Y. Hsieh, K. Chang, H. Tsai, T. Chen, *Sci. Rep.* **2015**, *5*, 17393.

[282] J. B. Bult, R. Crisp, C. L. Perkins, J. L. Blackburn, *ACS Nano* **2013**, *7*, 7251.

APPENDICES

Appendix A
Optimization process of CVD growth of SLG

Initial attempts of CVD growth of SLG using the conditions described in **Chapter 3**, resulted in highly defective films as indicated by the prominent D-peak (1350 cm^{-1}) in Raman spectra, shown in **Figure A.1**. In addition, SEM micrographs revealed defects in the surface morphology of the films, with the appearance of speckles across the surface as shown in **Figures A.1b** and **c**.

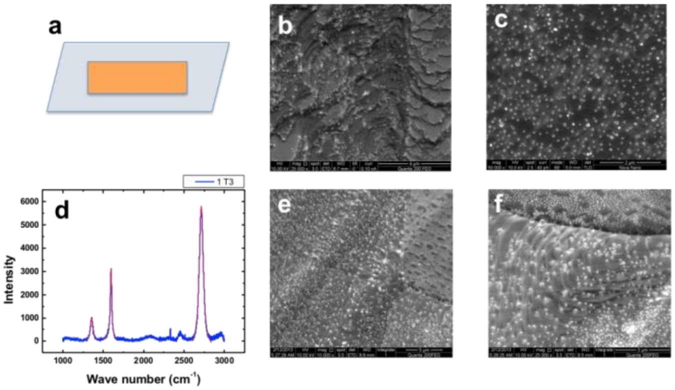

Figure A.1: Conventional chemical vapor deposition of graphene. (a) Schematic showing the configuration of a copper foil used for graphene growth on a fused quartz sample holder. (b, c) SEM micrographs of graphene films on copper foil. (d) Raman spectra of the resulting graphene film on copper foil and (e, f) SEM micrographs of a bare copper foil after annealing in the same configuration as (b, c) in a methane-free ambient

This issue has persisted even after a thorough optimization process in which the flow rate, growth pressure, temperature and the source of the copper foil used were varied. We hypothesized that the white spots and the irregular surface result from the reconstruction of copper grains and the sublimation of copper. To elucidate this, we annealed the copper foil under the same conditions without the introduction of methane (CH_4). Similar defects were observed on the annealed copper foils proving the assumption that such features resulted from the sublimation and restructuring of copper surface at high processing temperature of 1000 °C and low pressure of 1.8 mTorr - since the sublimation of copper is known to be suppressed at high pressures - as shown in **Figures A.1e** and **f**.

Growth at a higher pressure to suppress the sublimation of copper was attempted to resolve this issue without success. However, we found out accidentally that high-quality SLG simultaneously grew on the bottom surface of the copper foil facing the fused quartz holder as evident by both SEM and Raman spectrum of **Figure A.2**, which compares the graphene grown on the top and bottom surface under same conditions.

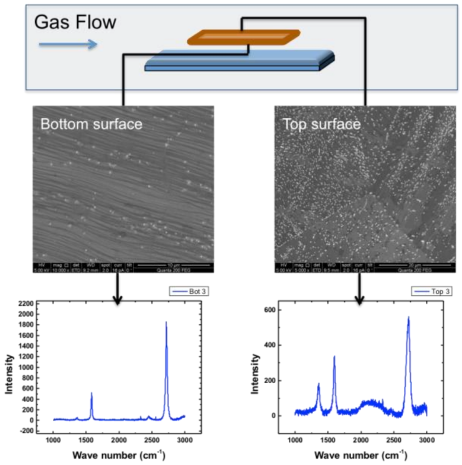

Figure A.2: Higher quality monolayer graphene films on the copper surface facing the fused quartz sample holder the exposed surface on the top.

The confined space between the foil and the quartz sample holder appears to locally impose higher growth pressure, preventing the sublimation and reconstruction of the copper foil and hence leading to a uniform growth of graphene. Based on this observation, we have developed a modified CVD process, where the copper foil was sandwiched between two quartz plates to reproduce the conditions at the bottom surface, successfully reproducing the growth of high-quality CVD graphene as shown in **Figure A.3**.

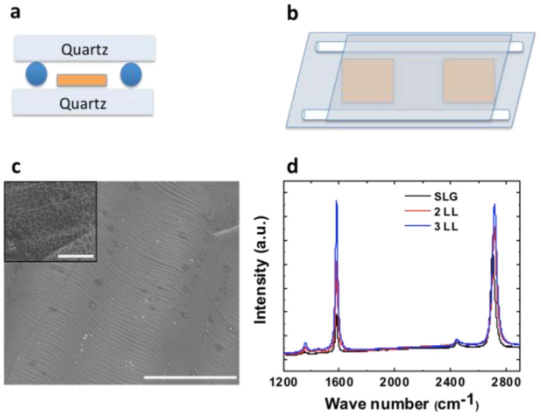

Figure A.3: Modified chemical vapor deposition of graphene. (a, b) schematics of the configuration of the sample holder with the copper foil sandwiched between two fused quartz foils. (c) SEM images of the grown monolayer graphene. The inset shows a graphene grown with conventional CVD under the same conditions, scale bar is 20 µm.(d) Raman spectra of the grown SLG, and Layer-by-Layer transferred graphene films of 2 layers (red) and 3 layers (blue)

Appendix B
The effect of annealing after PMMA transfer method

As discussed in **Chapter 3**, the conventional process of removing PMMA from the transferred graphene isn’t sufficient to fully clean its surface. PMMA residues almost always reside on the graphene surface due to the strong covalent bond between PMMA and graphene.

In this appendix, the results of the control experiment showing the need of an annealing step, to further remove and clean the graphene surface are discussed. Thermal annealing was done at a temperature of 450 °C under a reducing protective atmosphere of H_2 and Ar in the tube furnace at a pressure of 18 Torr for 90 minutes. This step was adopted in every transfer process used in this work.

Figure B.1 illustrates the changes in high-resolution *C 1s* XPS peak for graphene transferred on SiO_2 substrate before and after annealing. The peak appearing at 289 eV is related to C-O bond and indicates the presence of PMMA residues after the acetone wash step. This peak disappeared from the spectrum after the annealing. AFM images also demonstrate the importance of the annealing step in improving the quality of graphene, where the roughness decreases by almost 50% after the annealing step.

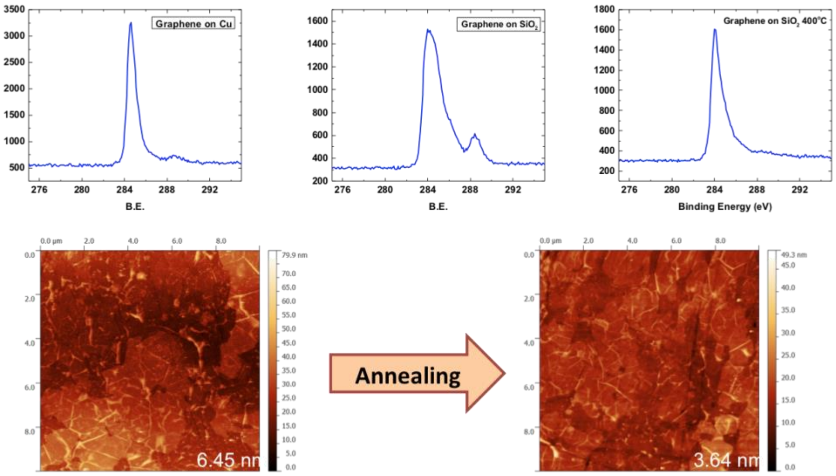

Figure B.1: Effect of the annealing process on transferred graphene samples. High-resolution C 1s XPS peaks on copper, transferred to SiO_2 and annealed at 400 °C. AFM of FLG graphene with the RMS roughness before and after annealing.

Appendix C

Bulk doping of CVD few layers graphene via $FeCl_3$ intercalation

Optimization of two-zone vapor transport process for $FeCl_3$ intercalation of FLG

As explained in **Chapter 3**, the intercalation of FLG with $FeCl_3$ was performed using a standard two-zone vapor transport process adopted from the intercalation of GIC.[213] A schematic of the process was shown in **Figure 3.15**. Anhydrous $FeCl_3$ was placed upstream and heated at 320 ^{o}C, while FLG is located ~25 cm downstream heated at a higher temperature of 360 ^{o}C inside a smaller tube (1.5 cm in diameter) that is opened at one end. The tube furnace was pumped down to a base pressure of 1.3×10^{-2} Torr and then sealed at both ends. The heating process lasted for 6 hours, the time needed for the pressure to reach ~4.2 Torr. Sealing of the tube at both ends was crucial for developing such high pressure that would facilitate the intercalation of $FeCl_3$ as evident by the comparison of the sheet resistance shown in **Figure C.1A**. The cooling conditions of the sample in which $FeCl_3$ was intercalated, seemed to affect the sheet resistance of the resulting films. For instance, taking the sample out of the hot furnace and exposing it to air at room temperature was shown to yield lower sheet resistance values and longer air-stability as shown in **Figure C.1B**. This is attributed to the fact that intercalated $FeCl_3$ is more stable in air than in vacuum, in agreement with recent results on $FeCl_3$ intercalated mechanically exfoliated FLG.[216] Due to the hygroscopic nature of $FeCl_3$, the surface of the as-prepared sample appeared to be wet, requiring the addition of a washing step with water in order to remove adsorbed $FeCl_3$ from the surface. This procedure only slightly increased the sheet resistance as shown in **Figure C.1C**, however, was essential to achieve long-term air-stability.

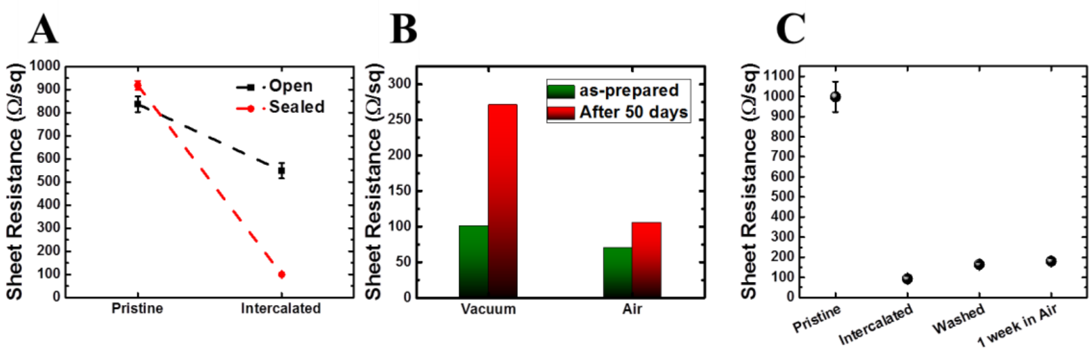

Figure C.1: Optimization conditions for FeCl3 intercalation into CVD-FLG, by comparing the sheet resistance. (A) Sealed vs. opened tube, (B) cooling in vacuum vs. cooling in air, and (C) effect of washing with water after intercalation.

Surface doping of FLG by dipping into $FeCl_3$ solutions

To compare the effect of intercalation vs. surface doping with $FeCl_3$, dipping of FLG in an aqueous solution of $FeCl_3$ (2%) at room temperature was experimented. At these conditions, intercalation is not expected to occur, as the reduction in the sheet resistance was significantly smaller as compared to the two-zone vapor transport process. **Figure C.2** shows the sheet resistance of doped FLG after various dipping durations, where a washing step with water was applied after every cycle. The sheet resistance moderately drops from ~950 Ω/□ (for pristine FLG) to ~650 Ω/□ after overnight dipping conditions.

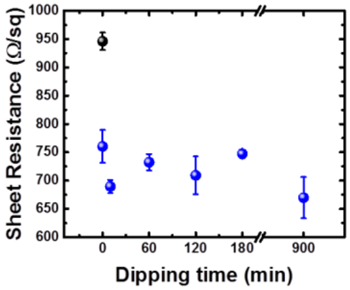

Figure C.2: Doping FLG by dipping in an aqueous solution of the $FeCl_3$ for various durations.

Optoelectronic properties of $FeCl_3$ intercalated FLG

Using the optimized intercalation process described above, the sheet resistance of CVD-FLG (~830.5±8.8 Ω/□) was significantly reduced to values as low as ~69.2±4.2 Ω/□), which was highly reproducible as shown in Figure C.3 showing the histogram for the sheet resistance values, calculated over 81 points over 9 samples. Furthermore, the sheet carrier density was significantly increased from 3.1×10^{13} cm^{-2} for the pristine sample to 9.9×10^{14} cm^{-2} as a result of charge transfer p-doping, while the mobility decreased from 284.1 $cm^2/(Vs)$ for the pristine sample to 100.9 $cm^2/(Vs)$ due to coulomb scattering, as deduced from Hall effect measurements. However, the large increase in the carrier density more than compensates the losses in the carrier mobility, and results in a large reduction in the sheet resistance.

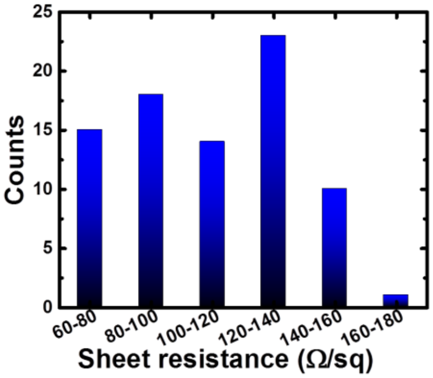

Figure C.3: Histogram of the sheet resistance of $FeCl_3$ intercalated FLG, calculated using 81 data points, and measured over 9 different samples. The minimum value was 63.1 Ω/□, and the maximum value was 164.7 Ω/□. The average sheet resistance was calculated to be 109.5 Ω/□ with a standard deviation of 26.3 Ω/□.

Figure C.4 shows the optical transmittance spectra for pristine and intercalated FLG in the visible and near infrared regions. Intercalation causes an insignificant loss in transmittance of ~1%.The minimal loss in the optical transmission and the significant reduction in the sheet resistance results in more than 800% improvement in the FoM of

TCEs. Interestingly, the transmittance increases by more than 10% in the near infrared region as shown in **Figure C.4**. This is attributed to the large increase in the carrier density leading to the shift of the Fermi level, so that interband electronic transitions are blocked since the condition $E_{ph} > 2E_F$ cannot be satisfied as discussed in **Section 2.3.3**.

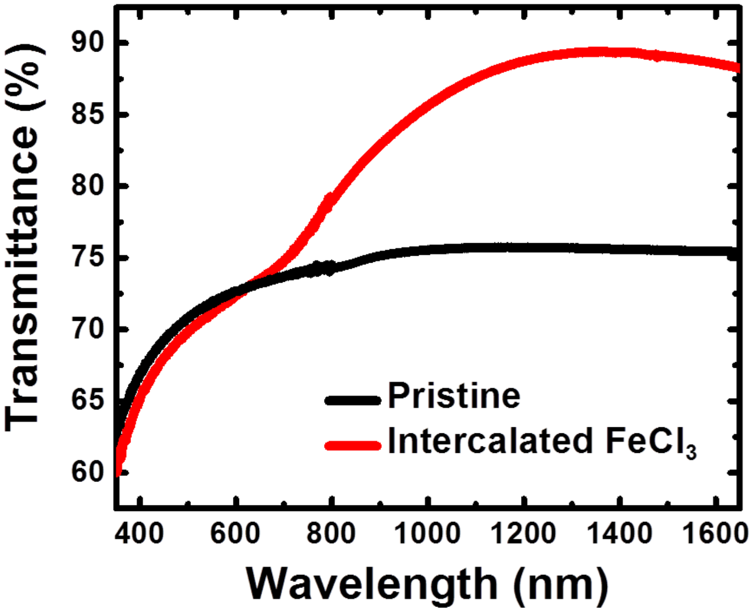

Figure C.4: Optical transmission of pristine and $FeCl_3$ *intercalated FLG.*